Quantum optomechanics at room temperature

THÈSE N^{O} 8134 (2017)

PRÉSENTÉE LE 24 NOVEMBRE 2017
À LA FACULTÉ DES SCIENCES DE BASE
LABORATOIRE DE PHOTONIQUE ET MESURES QUANTIQUES (SB/STI)
PROGRAMME DOCTORAL EN PHYSIQUE

ÉCOLE POLYTECHNIQUE FÉDÉRALE DE LAUSANNE

POUR L'OBTENTION DU GRADE DE DOCTEUR ÈS SCIENCES

PAR

Hendrik SCHÜTZ

acceptée sur proposition du jury:

Prof. R. Houdré, président du jury
Prof. T. Kippenberg, directeur de thèse
Prof. L. Novotny, rapporteur
Prof. P. Verlot, rapporteur
Prof. V. Savona, rapporteur

ÉCOLE POLYTECHNIQUE
FÉDÉRALE DE LAUSANNE

Suisse
2017

It always seems impossible
until it’s done.
— Nelson Mandela

To my parents…

Acknowledgements

I was fortunate to work with many people, whose help and support were indispensable to the success of this thesis. I want to thank all of them for their individual contributions.

First and foremost, I am sincerely thankful to my advisor, *Professor Tobias Kippenberg*, for giving me the opportunity to become part of his group. His unbridled enthusiasm and enormous optimism, but also his persistence, is what made the results in this thesis possible in the first place. Without his relentless support, the outcome of the experiments would have been quite different, not to say inferior. The myriad of ideas guided me especially in the beginning, but, in combination with his continuous interest in the project, also throughout my entire time in the group. I am also grateful for his encouragement and support to present my work to experts in the field at a number of conferences and workshops around the world.

When originally joining the He3-team, the post-docs *Nicolas Piro* and *Dalziel Wilson* introduced me to the experimental details of optomechanics. I have great appreciation for the time they devoted to me and their patience, but also for the numerous hours spent debugging my setup.

I am very grateful to *Vivishek Sudhir*, whom I thank for always making sure that I understand the theory behind and for sharing his Mathematica skills, a priceless aid in the data analysis. Even beyond his time in this lab, he provided his invaluable help for the final steps of my thesis to make sure it would be a success. Outside the lab, he was so kind to invite a few of us to his wedding in India, which for me was an unforgettable experience.

A special thank goes to my fellow PhD student *Ryan Schilling*. This is not only due to the fact that he supplied the ”hero" sample that made this thesis a success, but also for the numerous hours he joined me in the lab, to either assemble vacuum chambers or for uncountable characterization measurements. Other colleagues also keep spreading the rumor that we occasionally went to the Satellite bar, having good conversations about science and similarly interesting matter.

I am also thankful to *Sergey Fedorov* who joined the experiment before the main data for this thesis was taken. He helped out with countless sample characterizations and supported me in the acquisition of the lengthy measurement campaigns. With him, we had the most productive time during the quiet hours of the weekends which guaranteed us nearly vibration-free data during these quiet hours. After hunting it down together, it was him who took the initiative of solving the fiber vibration issues – by breaking parts of the sample. He still claims, this was an

accident…

The latest addition to our team is post-doc *Nils Engelsen*. Although having only shared little lab time together, I am grateful to him not only for the valuable advice on thesis writing he provided, but also for the many fun and entertaining stories he shared from his PhD studies. This made my writing period a lot more diversified and I hope for my successors that he has many more to share.

I also want to mention my (former) office buddies *Erwan Lucas*, *Nathan Bernier* and *Junqiu Liu*, as well as my other colleagues *Clément Javerzac-Galy*, *John Jost*, *Caroline Lecaplain* and the rest of the group, for many fun and interesting discussions, be it on scientific topics or not.

I am also thankful to the group's assistants *Hélène Laurens*, *Antonella Ragnelli* and *Nicole Bouendin*. They all have been very helpful for any administrative challenges that I faced during my time in the group, be it travel arrangements, overdue invoices or grant reports.

Last but not least, my parents have been very supportive to me throughout my entire education in uncountable ways, for which I am sincerely grateful. I also very much enjoyed their regular visits to Switzerland together with my siblings. During these times, we went on several breathtaking hikes or just enjoyed some quality time at one of the many beautiful Swiss lakes. Very special thanks also to my wonderful girlfriend as well as all my friends for making sure I maintain a life apart from optomechanics and outside the lab. I happily look back to the great times spent together at the lakes, in the mountains (be it on foot, snow shoes, skis or bikes), or somewhere lost in the vineyards with some good wine.

Lausanne, August 2017 Hendrik Schütz

Abstract

Why are classical theories often sufficient to describe the physics of our world even though everything around us is entirely composed of microscopic quantum systems? The boundary between these two fundamentally dissimilar theories remains an unsolved problem in modern physics. Position measurements of small objects allow us to probe the area where the classical approximation breaks down. In quantum mechanics, Heisenberg's uncertainty principle dictates that any measurement of the position must be accompanied by measurement induced back-action—in this case manifested as an uncertainty in the momentum.

In recent years, cavity optomechanics has become a powerful tool to perform precise position measurements and investigate their fundamental limitations. The utilization of optical microcavities greatly enhances the interaction between light and state-of-the-art nanomechanical oscillators. Therefore, quantum mechanical phenomena have been successfully observed in systems far beyond the microscopic world. In such a cavity optomechanical system, the fluctuations in the position of the oscillator are transduced onto the phase of the light, while fluctuations in the amplitude of the light disturb the momentum of the oscillator during the measurement. As a consequence, correlations are established between the amplitude and phase quadrature of the probe light.

However, so far, observation of quantum effects has been limited exclusively to cryogenic experiments, and access to the quantum regime at room temperature has remained an elusive goal because the overwhelming amount of thermal motion masks the weak quantum effects. This thesis describes the engineering of a high-performance cavity optomechanical device and presents experimental results showing, for the first time, the broadband effects of quantum back-action at room temperature. The device strongly couples mechanical and optical modes of exceptionally high quality factors to provide a measurement sensitivity $\sim 10^4$ times below the requirement to resolve the zero-point fluctuations of the mechanical oscillator. The quantum back-action is then observed through the correlations created between the probe light and the motion of the nanomechanical oscillator. A so-called "variational measurement", which detects the transmitted light in a homodyne detector tuned close to the amplitude quadrature, resolves the quantum noise due to these correlations at the level of 10% of the thermal noise over more than an octave of Fourier frequencies around mechanical resonance. Moreover, building on this result, an additional experiment demonstrates the ability to achieve quantum enhanced metrology. In this case, the generated quantum correlations are used to cancel quantum noise in the measurement record, which then leads to an improved relative signal-to-noise ratio in measurements of an external force.

In conclusion, the successful observation of broadband quantum behavior on a macroscopic object at room temperature is an important milestone in the field of cavity optomechanics. Specifically, this result heralds the rise of optomechanical systems as a platform for quantum physics at room temperature and shows promise for generation of ponderomotive squeezing in room-temperature interferometers.

Keywords: quantum measurement, room temperature cavity optomechanics, measurement back-action, quantum correlations

Zusammenfassung

Warum können wir unsere Welt mittels der Theorien klassischer Physik beschreiben, obwohl sie gänzlich aus mikroskopischen Quantensystemen zusammengesetzt ist? Der Verlauf der Grenze zwischen diesen beiden fundamental gegensätzlichen Theorien stellt bis heute ein ungelöstes Problem der modernen Physik dar. Als Lösung ermöglichen Messungen des Aufenthaltsortes winziger Objekte den Zugang zu einem Bereich, an dem die klassischen Näherungen versagen. Jedoch schreibt die Quantenmechanik vor, dass die Messung der Position durch eine Messrückwirkung auf das System begleitet wird — in diesem Fall manifestiert als Störung des Impulses.

Innerhalb der letzten Jahre hat sich die noch junge Forschung der Resonator-Optomechanik zu einem bedeutenden Werkzeug für präzise Positionsmessungen und der Erforschung der fundamentalen Beschränkungen jener entwickelt. Durch die Verwendung von optischen Mikroresonatoren, welche die Wechselwirkung zwischen Licht und hochmodern gefertigten nanomechanischen Oszillatoren deutlich steigern, konnten quantenmechanische Effekte an Systemen weit jenseits des Mikrokosmos nachgewiesen werden. Zur Messung der Auslenkung in einem solchen optomechanischen System prägt sich die Schwingung des Oszillators auf die Phase des zirkulierenden Lichts, während Fluktuationen der Lichtamplitude den Impuls der Schwingung beeinflussen. In Konsequenz führt dies zu messbaren Korrelationen zwischen der Amplituden- und Phasenquadratur des ausgekoppelten Lichts.

Bis dato konnte ein erfolgreicher Nachweis der Quantenmessrückwirkung lediglich unter Tieftemperaturbedingungen erbracht werden, wohingegen dies bei Raumtemperatur ein bisher unerreichtes Ziel blieb. Grund hierfür ist, dass die schwachen Quanteneffekte hier durch die sehr große thermische Bewegung der mechanischen Schwingung überschattet werden. Diese Dissertation beschreibt den Prozess der Entwicklung eines besonders leistungsstarken optomechanischen Systems, mit dessen Hilfe erstmalig der breitbandige Effekt der Messrückwirkung bei Raumtemperatur nachgewiesen wurde. Das System zeichnet sich hierbei durch eine hohe optomechanische Wechselwirkung zwischen mechanischer und optischer Resonanzen außerordentlich hoher Güten aus. Somit wurde eine Messempfindlichkeit erreicht, die um einen Faktor $\sim 10^4$ unterhalb der Grundzustandsfluktuationen des mechanischen Oszillators liegt. Die Messrückwirkung kann als Folge dessen anhand der Korrelationen zwischen Oszillator und Licht nachgewiesen werden. Mittels homodyner Detektion nahe der Amplitudenquadratur wurde das so entstehende Quantenrauschen gemessen, das in den hier beschriebenen Messungen bis zu 10% des thermischen Rauschens erreicht. Die Korrelationen spannen dabei mehr als eine Oktave an Fourierfrequenzen rund um die Resonanzfrequenz. Des Weiteren wurden in einem zweiten Experiment die entstandenen Quantenkorrelationen dazu genutzt, das Quantenrauschen des Messvorgangs auszulöschen und so eine erhöhte Messempfindlichkeit des relativen Signal-Rausch-Verhältnisses einer externen Kraft erreicht.

Zusammenfassend markiert die erfolgreiche Beobachtung des breitbandigen Quanteneffekts einen wichtigen Meilenstein in der Resonator-Optomechanik. Weiterhin untermauert dieses Resultat die allgemeine Bedeutung von optomechanischen Systemen als Plattform für quantenphysikalische Experimente und gilt als vielversprechende Lösung, gequetschtes Licht in Raumtemperatur-Interferometern zu erzeugen.

Stichwörter: Quantenmessung, Raumtemperatur Resonator-Optomechanik, Messrückwirkung, Quantenkorrelationen

Résumé

Pourquoi les théories classiques sont-elles souvent suffisantes pour décrire la physique de notre monde, alors même que celui-ci est entièrement composé de systèmes quantiques microscopiques ? La frontière entre ces deux théories fondamentalement dissemblables reste un problème non résolu de la physique moderne. Mesurer la position d'objets mesoscopiques nous permet de sonder le domaine où l'approximation classique échoue. En mécanique quantique, le principe d'incertitude de Heisenberg impose que toute mesure de la position doit s'accompagner d'une action en retour, induite par la mesure—qui se manifeste, dans ce cas, comme une incertitude sur la quantité de mouvement.

Au cours de ces dernières années, l'opto-mécanique en cavité est devenue un outil puissant pour effectuer des mesures de position très précises et étudier leurs limites fondamentales. En utilisant des micro-cavités optiques, qui augmentent considérablement l'interaction entre la lumière et des oscillateurs nanomécaniques à la pointe de la technologie, des phénomènes quantiques ont pu être observés dans des systèmes dépassant largement l'échelle microscopique. Dans une cavité opto-mécanique, les fluctuations de position de l'oscillateur influencent la phase de la lumière tandis que les variations d'amplitude de la lumière perturbent la quantité de mouvement de l'oscillateur durant la mesure. En conséquence, des corrélations s'établissent entre les quadratures d'amplitude et de phase de la lumière de sonde.

Cependant, l'observation des effets quantiques est restée, jusqu'à présent, exclusivement limitée aux expériences cryogéniques. Accéder au régime quantique à température ambiante est resté un objectif inatteignable en raison de la quantité écrasante de mouvement thermique, qui masque les subtils effets quantiques. Cette thèse décrit la conception d'un système d'opto-mécanique en cavité de haute performance et présente des résultats expérimentaux montrant, pour la première fois à température ambiante, les effets quantiques de l'action en retour sur une large bande. Le dispositif couple fortement des modes mécaniques et optiques aux facteurs de qualité exceptionnellement élevés, pour fournir une sensibilité de mesure $\sim 10^4$ fois inférieure à celle nécessaire pour résoudre les fluctuations du point zéro de l'oscillateur mécanique. L'action en retour quantique est alors mise en évidence à travers les corrélations créées entre la lumière de la sonde et le mouvement de l'oscillateur nanomécanique. Une «mesure variationnelle», qui détecte la lumière transmise dans un montage homodyne sélectionnant la quadrature d'amplitude, permet de résoudre le bruit quantique lié à ces corrélations à un niveau de 10% du bruit thermique sur une plage fréquentielle de plus d'une octave autour de la résonance mécanique. De plus, en se basant sur ce résultat, une expérience supplémentaire démontre la capacité d'améliorer la métrologie par effet quantique. Dans ce cas, les corrélations quantiques générées sont utilisées pour annuler le bruit quantique dans l'enregistrement mesuré, ce qui conduit à l'amélioration du rapport signal / bruit relatif pour la mesure d'une force externe.

En conclusion, l'observation sur une large bande du comportement quantique d'un objet macroscopique à température ambiante est une étape importante dans le domaine de l'opto-mécanique en cavité. Plus précisément, ce résultat préfigure l'éminence des systèmes opto-mécaniques en tant que plate-forme permettant l'étude de la physique quantique à température ambiante et démontre leur potentiel prometteur pour la génération d'états pondéromoteurs compressés dans des interféromètres à température ambiante.

Mots clefs : mesure quantique, opto-mécanique en cavité à température ambiante, mesure de l'action en retour, corrélation quantique

Contents

Acknowledgements **i**

Abstract (English/Français/Deutsch) **iii**

List of figures **xiii**

List of symbols **xv**

1 Introduction **1**
- 1.1 Radiation pressure forces . . . 2
- 1.2 Cavity optomechanics . . . 4
  - 1.2.1 Optomechanical systems in practice . . . 5
  - 1.2.2 Quantum cavity optomechanics at room temperature: this thesis . . . 6

2 Foundations of cavity optomechanics **9**
- 2.1 Optical microresonators . . . 9
  - 2.1.1 Whispering-gallery modes . . . 10
  - 2.1.2 Quality factor and optical loss mechanisms . . . 11
  - 2.1.3 Resonator-waveguide coupling . . . 14
- 2.2 Nanomechanical oscillators . . . 19
  - 2.2.1 Mechanical motion . . . 20
  - 2.2.2 Silicon nitride nanobeam mechanical oscillators . . . 23
- 2.3 Cavity optomechanics . . . 25
  - 2.3.1 Classical description . . . 26
  - 2.3.2 Quantum mechanical formulation . . . 31
- 2.4 Optomechanical readout of motion . . . 36
  - 2.4.1 Quantum noise limitations in displacement sensing . . . 37
  - 2.4.2 Standard quantum limit . . . 38
  - 2.4.3 Laser noise . . . 41
  - 2.4.4 Photodetection of noise spectra . . . 42

3 High-cooperativity near-field optomechanical transducer **49**
- 3.1 Device design . . . 50
  - 3.1.1 Nanomechanical beam . . . 50
  - 3.1.2 Optical microdisk . . . 52

3.1.3 Evanescent optomechanical coupling 53
3.2 Fabrication details 57
3.2.1 Microdisk fabrication 57
3.2.2 Planarized sacrificial layer 58
3.2.3 Nanobeam fabrication 59
3.2.4 Structural release 61
3.3 Characterization measurements 61
3.3.1 Experimental setup 62
3.3.2 Calibrated thermal noise measurement 63
3.3.3 Gas damping 65
3.3.4 Optical spring effect 66
3.3.5 g_0 and C_0 versus lateral beam position 68
3.3.6 g_0 and C_0 versus beam width and disk thickness 69
3.3.7 g_0 versus mechanical mode order 69
3.4 Displacement sensitivity 70
3.5 Structural damping 72
3.6 Conclusion 74

4 Quantum correlations of light at room temperature **77**
4.1 Theoretical background 78
4.1.1 Theoretical model for optomechanically induced quantum correlations 78
4.1.2 Analysis of the correlation magnitude 81
4.1.3 Quantum-enhanced force sensitivity 82
4.2 Experimental results 86
4.2.1 Concept of the experiment 87
4.2.2 Observation of quantum correlations 90
4.2.3 Quantum-noise cancellation for force sensing 94
4.3 Experimental details 96
4.3.1 Experimental platform 96
4.3.2 Measurement setup 97
4.3.3 Data acquisition and analysis 99
4.3.4 Laser noise 101
4.3.5 Effect of homodyne phase fluctuations 104
4.3.6 Excess detection noise due to taper vibrations 106
4.4 Conclusion 107

5 Outlook **109**
5.1 Future directions 109
5.1.1 Phononic crystal nanobeams 110
5.1.2 Nanobeams with ultra-high stress 113
5.2 Conclusion 113

A Experimental setup **115**

B Ti-sapphire laser operation **119**

C (Ultra-)High vacuum chambers **121**
C.1 Cleaning 122
C.2 Assembly of a UHV system 123
C.3 Bake-out of a vacuum chamber 125

D Setup and operation of a balanced homodyne interferometer **127**

E Sample design and characterization **131**

F Degradation of the mechanical quality factor **135**

G Two-level systems in cavity optomechanical systems **137**

Bibliography **153**

Curriculum Vitae **155**

List of Figures

1.1 Radiation pressure effect on the tail of a comet 1
1.2 Nichols radiometer 2
1.3 LIGO interferometer 4
1.4 The Thing 5
1.5 Survey of various cavity optomechanical systems. 6

2.1 Whispering gallery modes 10
2.2 Wedged SiO_2 microdisk resonator 11
2.3 Wavelength sweep over several free spectral ranges 15
2.4 Illustration and measurement of different coupling regimes 16
2.5 Transmission and reflection for counter-propagating modes 18
2.6 Thermal spectrum of a mechanical oscillator 22
2.7 Mechanical eigenmodes of a nanobeam 24
2.8 Principle of cavity optomechanics 26
2.9 Optical cavity response 27
2.10 Cavity response in an optomechanical system 36
2.11 Quantum noise contributions and the SQL 40
2.12 Measured noise spectrum 45
2.13 Homodyne detection principle 47

3.1 Q-factor and $Q \times$ frequency product of flexural modes of a nanobeam 51
3.2 Measurement results of optical quality factors 52
3.3 Simulation of the evanescent optomechanical coupling 54
3.4 False-colored SEM of the device 55
3.5 Fabrication process flow 57
3.6 Selective etch of the microdisk 58
3.7 Microscope image of the defined nanobeam and mesa 60
3.8 Characterization setup and measurements 62
3.9 Calibration of modulation index 65
3.10 Gas damping measurement 66
3.11 Optical spring measurement 67
3.12 Characterization measurements for swept sample parameters 68
3.13 Displacement sensitivity measurement 71

3.14 Structural damping measurement 73
3.15 Tethered beam design 75

4.1 Model of the homodyne photocurrent spectrum 81
4.2 Theoretical quantum-enhanced sensitivity to thermal force 85
4.3 Optomechanical quantum correlations 86
4.4 Asymmetry in homodyne spectrum 90
4.5 Asymmetry in homodyne spectrum as a function of quadrature angle 92
4.6 Visibility of quantum correlations versus laser power 93
4.7 Quantum-enhanced external force estimation 95
4.8 False colored scanning electron micrograph of the device 97
4.9 Schematic of the experimental setup 98
4.10 Asymmetry ratio for different offsets and integration bandwidths 100
4.11 Choice of integration bands for the external force measurements 101
4.12 Phase and amplitude noise of the lasers used in the experiments 105
4.13 Excess noise due to taper vibrations 106
4.14 Broadband measurement of taper excess noise: 107

5.1 Quality factor measurements of micropatterned nanobeams 111
5.2 Near-field setup 112
5.3 Ultraviolet thermal processing 114
5.4 Ultraviolet thermal processing setup 114

A.1 Picture of the vacuum setup 116
A.2 Layout of the experiment 117

B.1 MSquared SolsTiS laser 120
B.2 Frequency stability of the SolsTiS laser 120

C.1 Ultra-high vacuum chamber 122
C.2 Near-field setup 124
C.3 Pumpdown of the vacuum chamber 125

D.1 Balanced homodyne detection layout 127
D.2 Length balancing of a homodyne interferometer 128
D.3 Homodyne lock and residual phase noise 130

E.1 Sample chip 131
E.2 Sample chip 132
E.3 Characterization data 133

F.1 Degradation of mechanical quality factor 136

G.1 Two-level systems in optomechanical systems 138
G.2 Optical and mechanical properties of microsphere resonators 139

List of Symbols

Symbol	Meaning
ω_c	Cavity resonance frequency
ω_L	Laser frequency
Δ	Laser detuning, $\Delta = \omega_\mathrm{l} - \omega_\mathrm{c}$
κ_0	Intrinsic loss rate of the cavity
κ_ex	Loss rate of the cavity from external coupling
κ	Total cavity decay rate, $\kappa = \kappa_0 + \kappa_\mathrm{ex}$
η_c	Optical coupling efficiency, $\eta_\mathrm{c} = \kappa_\mathrm{ex}/\kappa$
n_c	Intracavity photon number
Ω_m	Mechanical resonance frequency
Γ_m	Mechanical damping rate
Q_m	Mechanical quality factor, $Q_\mathrm{m} = \Omega_\mathrm{m}/\Gamma_\mathrm{m}$
n_th	Phonon occupation in thermal equilibrium, $n_\mathrm{th} = (e^{\hbar\Omega_\mathrm{m}/(k_\mathrm{B}T)} - 1)^{-1} \approx k_\mathrm{B}T/(\hbar\Omega_\mathrm{m})$
m_eff	Effective mass of the mechanical oscillation
$\chi_x(\Omega)$	Mechanical susceptibility, $\chi_x(\Omega) = \left(m_\mathrm{eff}(\Omega_\mathrm{m}^2 - \Omega^2 - i\Omega\Gamma_\mathrm{m})\right)^{-1}$
x_ZPF	Zero-point fluctuations of the mechanical resonator, $x_\mathrm{ZPF} = \sqrt{\hbar/(2m_\mathrm{eff}\Omega_\mathrm{m})}$
G	Optical frequency shift per displacement, $G = \partial\omega_\mathrm{c}/\partial x$
g_0	Single-photon optomechanical coupling strength, $g_0 = G \cdot x_\mathrm{ZPF}$
C_0	Single-photon cooperativity, $C_0 = 4g_0^2/(\kappa\Gamma_\mathrm{m})$
C	Multi-photon cooperativity, $C = C_0 n_\mathrm{c}$
Γ_eff	Effective damping rate in the case of dynamical back-action (DBA)
Ω_eff	DBA spring shift
n_imp	Imprecision noise expressed in phonon-equivalent units, $n_\mathrm{imp} = (16\eta_\mathrm{c}C_0 n_\mathrm{c})^{-1}$
n_ba	(Quantum) Back-action noise expressed in phonon-equivalent units, $n_\mathrm{qba} = C_0 n_\mathrm{c}$
$S_{aa}(\Omega)$	Double-sided spectral density, $S_{aa}(\Omega) = \int_{-\infty}^{\infty} \mathrm{d}\tau\, \langle a(t)a(t+\tau)\rangle\, e^{i\Omega\tau}$
$\bar{S}_{aa}$	Symmetrized spectral density, $\bar{S}_{aa} \equiv (S_{aa}(\Omega) + S_{aa}(-\Omega))/2$
S_a	Single-sided spectral density, $S_a(\Omega) = 2 \cdot \bar{S}_{aa}(\Omega)$ (only evaluated for $\Omega > 0$)

1 Introduction

For most species on this planet, light as the visible part of the electromagnetic spectrum is the primary way of perceiving the surrounding environment with us humans being no exception. Throughout history, the vision has always been our primary tool of observing and understanding the laws of nature. This holds true until today where the optical perception still constitutes the main mechanism for studying phenomena in both biological and physical sciences.

It was only logical that the desire to understand the concepts of light itself would eventually arise. Until the mid 19th century, both, wave and particle theories competed with each other attempting to describe the nature of light. The alleged solution was brought with the formulation of an early version of Maxwell's equations in 1862 that led to the comprehension of light as electromagnetic waves capable of describing observations such as interference and polarization effects. However, evidence for the particle character of light remained omnipresent. Hertz and Hellwachs discovered the photoelectric effect in 1887 where they made the observation that the energy of the emitted electrons is proportional to the frequency of the incident light while their number merely depends on the light's intensity [2]. This effect, standing in contrast to the classical wave theory and supporting a particle nature of light, was later on in 1905 described by Einstein in one of his annus mirabilis papers with his postulation of the quantum nature of light in form of localized par-

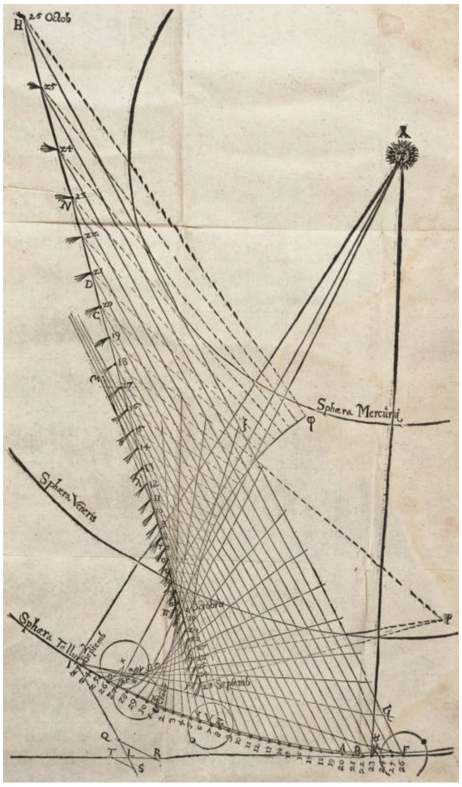

Figure 1.1 – **Radiation pressure effect on the tail of a comet.** Original drawing by Kepler from 1619 [1].

ticles with discrete energies proportional to the light's frequency [3]. This eventually led to the formulation of the theory of quantum mechanics [4] describing both, the particulate character of light waves as well as the complimentary wave character of - until then thought of as pure - particles (e.g. atoms, electrons etc.).

1.1 Radiation pressure forces

The fact that light also carries momentum leads to the concept of a *radiation pressure* force, the underlying fundamental mechanism for this thesis. The first reference to this effect dates back to as early as 1619 when Kepler studied the phenomenon that the tails of comets always seem to point away from the sun [1]. This is illustrated in his original drawing in fig. 1.1 where he suggested an outward solar radiation pressure acting on the tails of the comets as explanation, a claim which remained unsubstantiated for more than two centuries due to a lack of a quantitative theory. The assertion of light being able to exert this kind of pressure force first followed as a consequence from Maxwell's equations that required electromagnetic radiation to carry momentum.

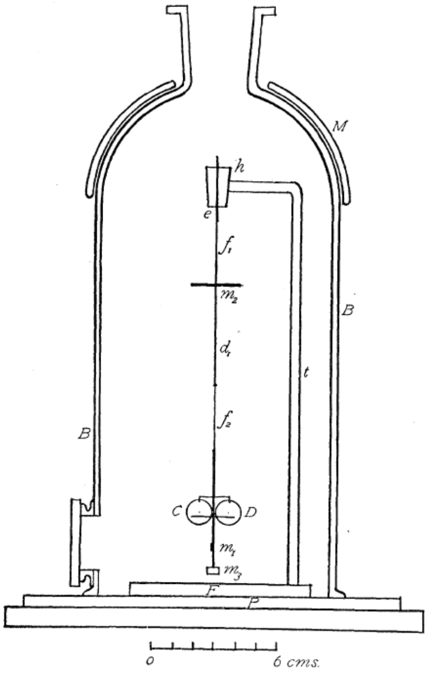

Figure 1.2 – **Nichols radiometer** [5]. The apparatus consists of a torsion balance in which two silvered mirrors (C and D) are suspended by a thin wire. One mirror is illuminated by a high intensity light source while the other is used to measure the rotation caused by the radiation pressure. This is carried out by reflecting a weaker light beam off the other mirror, similar to a galvanometer. The apparatus is placed inside an evacuated glass cylinder to avoid thermal effects as in Crookes' attempt [6].

Inspired by Cavendish's precision measurement of the gravitational force between two masses using a torsion balance [7], in 1873 William Crookes presented his invention that targeted the first observation of direct evidence of the radiation pressure of light: the radiometer [6]. Indeed, the apparatus consisting of a low-friction spindle with several vertical lightweight vanes responded to a photo-induced force and rotated when illuminated. By investigating the observations made by Crookes more carefully, it quickly became clear that the rotation of the vanes was solely caused by a thermal effect through impacting gas molecules. In addition, the rotation direction was opposite of what was expected from radiation pressure forces. The first successful observations of a pure radiation pressure effect were eventually realized by Lebedew in 1900 [8], and independently by Nichols and Hull using a Nichols radiometer in the following year [5]. A drawing of this device is shown in fig. 1.2. The essential difference to Crooke's device was that here, the torsion apparatus was placed inside an evacuated glass cylinder, therefore eradicating the main flaw of Crooke's radiometer.

After the first theoretical analysis of the statistics of radiation pressure force fluctuations by Einstein in 1909, more than half a century had to pass until further investigation of this effect was conducted at a lab scale [1]. A powerful tool hereby turned out to be the in 1960 newly invented lasers, although they were at first considered as a "solution looking for a problem" [12]. However, relying on quantum mechanical principles, with the laser it was finally possible to provide the required high-intensity, monochromatic, collimated light fields necessary to further study light forces. It was first within the context of *laser cooling* that the effects of radiation pressure forces of light were experimentally demonstrated. To understand the fundamental principle behind laser cooling, one first has to go back to the discovery made by Brown, a botanist who in 1827 observed a random motion of pollen grains in water[2]. Einstein in 1905, in another annus mirabilis paper, explained this observation with the kinetic theory of gases that, highly controversial at that time, describes a gas as a large ensemble of submicroscopic particles, i.e. atoms or molecules [13]. He conjectured that a large object that is placed into a gas will experience kicks from the gas particles with the amount of these kicks being proportional to the magnitude of thermal motion, establishing a link to the temperature. This immediately rose the question whether the Brownian motion would vanish by bringing the object of interest to zero temperature. The answer to this question is indeed a complete suppression of the thermal motion, leaving the object only to its vacuum fluctuations. When performing a measurement however, quantum mechanics dictates a disturbance of the object in the order of the vacuum fluctuations, imparting additional motion onto the object: this process is referred to as the *measurement back-action* effect. The aim of the first laser cooling experiments was the “refrigeration,” or cooling, of the thermal motion of atomic-scale matter as well as controlling and trapping neutral particles [14–17]. Since the first experiments, laser cooling has become an exceptionally important technique in quantum optics and has enabled the study of low-temperature many-body systems as well as applications such as optical clocks.

It was the pioneering work of Braginsky who first investigated the impact of radiation pressure forces on larger scale objects, i.e. the *optomechanical* effects, by considering a harmonically suspended end mirror of an optical cavity. His theoretical study predicted the so-called ponderomotive effect of light, meaning the ability to cool or amplify the periodic motion of a mechanically oscillating object with light due to the retarded nature of the radiation pressure force which he eventually also succeeded to demonstrate experimentally [18, 19]. Later on, Braginsky also studied the impact of quantum fluctuations in the radiation pressure force limiting the sensitivity of a position measurement of a mirror [20, 21]. Applying this to interferometric measurements, further detailed analysis of this quantum noise eventually established the so-called *standard quantum limit* (SQL) for a continuous position measurement using an interferometer [22–24].

---

[1] For the field of astronomy, the concept of radiation pressure forces was of high relevance since the beginning as it delivered explanations for various, until then unsolved, observations [9–11]

[2] Brown made the same observation also on inorganic matter, directly ruling out any life-related processes.

1.2 Cavity optomechanics

Braginsky's findings soon led to the emergence of the new research field of *cavity optomechanics* [25]. Based on his work described above, cavity optomechanics studies the properties and effects of radiation pressure interactions between light and matter. For this, the light is confined inside an optical cavity and interacts during its circulation with a mechanically compliant object. Each photon recirculates inside the cavity, and therefore is able to interrogate the state of the mechanical object multiple times before exiting the cavity. This leads to a greatly enhanced measurement sensitivity and enables the most precise displacement measurements ever performed.

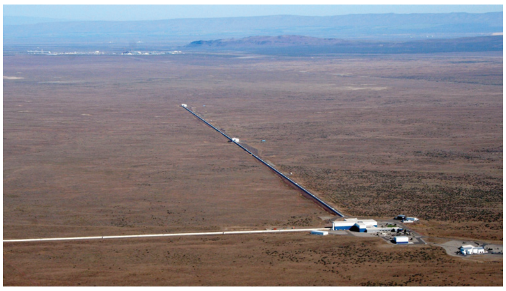

Figure 1.3 – **LIGO interferometer:**. Aerial view of the Laser Interferometer Gravitational-Wave Observatory in Hanford, WA, USA. The interferometer arms measure 4 km in length.

Prominent examples that harnesses this extreme sensitivity are the gravitational wave interferometers. With the Laser Interferometer Gravitational-Wave Observatory (LIGO) in the USA leading the way, the LIGO collaboration has recently detected the very first gravitational-wave signal and therefore proven their existence. An aerial view of one of the LIGO facilities is shown in fig. 1.3. LIGO utilizes an optical interferometer to detect space-time fluctuations caused by gravitational waves, which are passing through the interferometer arms. Owing to its exceptionally high strain sensitivity of $10^{-23}/\sqrt{\text{Hz}}$, a transient gravitational-wave signal caused by two merging black holes about 10^9 ly away from Earth could very recently be observed for the very first time at LIGO [26]. The gravitational wave strain for this event was 10^{-21}, resulting in a change of path length in the order of 10^{-18} m in one of the 4 km long interferometer arms. This corresponds to the one-thousandth diameter of a proton. Already predicted by Einstein about a century ago, this direct evidence of gravitational waves marks a breakthrough discovery providing new ways of understanding our universe and giving astrophysicists the ability to observe objects that otherwise would remain invisible. Consequently, the Nobel Prize in Physics 2017 was awarded to the LIGO project for the successful observation of gravitational waves.

As an interesting remark, the first example of an optomechanical resonator (though not operating at optical frequencies) surfaced long before the first dedicated experiments: ”The Thing". In 1945, the Soviets presented a carved wooden plaque of the Great Seal of the United States to the US ambassador as a ”gesture of friendship". Hidden inside this plaque was a diaphragm coupled to a UHF cavity. Figure 1.4 shows a replica of the Great Seal which is displayed in a museum in the USA. The device invented by Léon Theremin served as a passive bug to eavesdrop on possibly confidential conversations [27]. The principle was very similar to Braginsky's work: vibrations of the diaphragm modulate the resonance frequency of the cavity and thereby transmit sound in the room via radio waves if the cavity was driven with the correct UHF frequency from a distant transmitter. The device was not found before seven

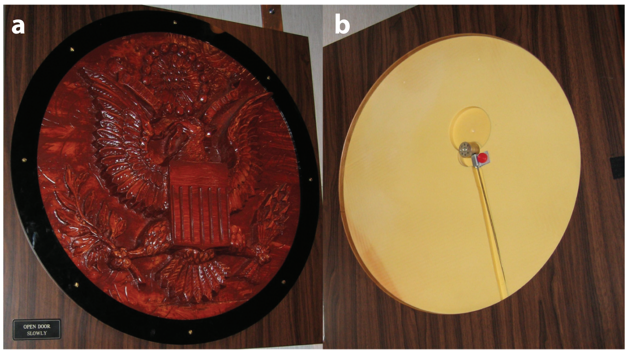

Figure 1.4 – **The Thing.** Replica of "The Thing", on display at the NSA's National Cryptologic Museum in Annapolis Junction, MD, USA. It contained a listening device hidden inside the Great Seal, which was used by the Soviets to spy on the American ambassador to Russia between 1945 and 1952, when it was finally exposed.

years of successful spying had passed. Whether or not it is a coincidence that Braginsky's first optomechanics experiments also took place at UHF frequencies, is up to the reader to decide for himself.

1.2.1 Optomechanical systems in practice

Eventually, advances in microfabrication helped substantially to boost the rise of the field of cavity optomechanics. Photons became a powerful tool for quantum-limited measurements, as the field of a laser-driven cavity can be quantum-noise limited even at room temperature, and hence constitutes an ideal mechanical transducer. Moreover, the finite build-up time of the cavity field allows it to perform work on the mechanical element, enabling low-noise optical cooling and amplification [28]. Investigation of these effects has led to two paradigmatic goals: cooling of a solid-state mechanical oscillator to its quantum ground state and, concomitantly, read-out of its zero-point motion with the minimal disturbance allowed by the Heisenberg uncertainty principle due to measurement back-action (radiation-pressure shot noise (RPSN) [22]).

The first goal, ground-state cooling, has been achieved by several cryogenic optomechanical [34, 45] and electromechanical systems [71] (via resolved-sideband cooling [72]).

The second goal, measuring at the standard quantum limit (SQL) [21], remains outstanding; however, readout noise far below the zero-point displacement has been reported [59, 73], as well as RPSN dominating the thermal force in a cryogenic environment [74, 75]. Reaching the SQL ultimately requires a 'Heisenberg-limited' displacement sensor for which the product of the read out noise and the total force noise is the minimum allowed by the uncertainty principle. Several cryogenic systems have come within an order of magnitude of this goal [71, 73] and operating within this regime has allowed measurement-based feedback protocols for cooling [73, 76] and squeezing [77] of an oscillator.

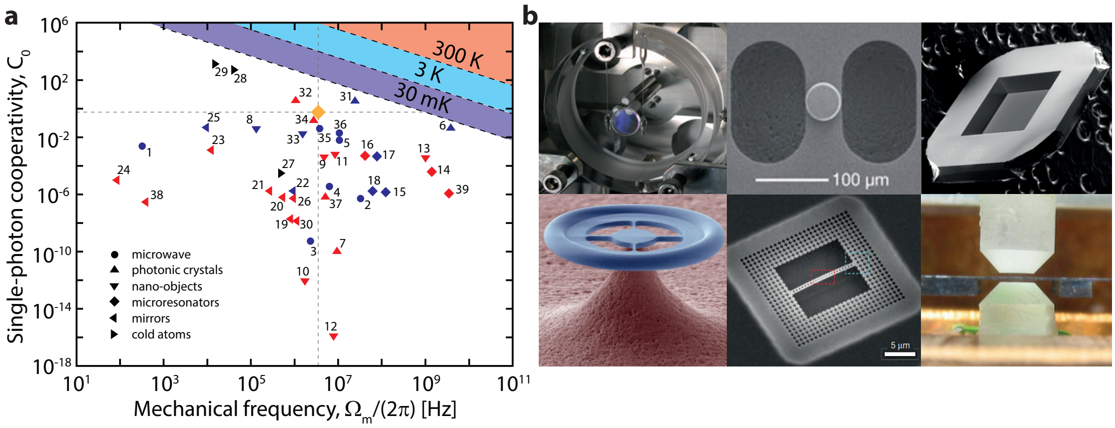

Figure 1.5 – **Survey of various cavity optomechanical systems.** (a) Single-photon cooperativity C_0 for various cavity optomechanical systems plotted versus mechanical frequency. C_0 is an important figure of merit in optomechanics, describing the efficiency of the coupling between photons and phonons. Blue and red data correspond to cryogenic (typically $T < 10$ K) and room temperature experiments, respectively. Diagonal lines indicate the condition for $C_0 = n_{\mathrm{th}} \approx k_B T/\hbar\Omega_m$, for various T. The device used for the main results reported in this thesis (see chapter 4) is highlighted in orange at the intersection of the dashed gray lines. All other systems correspond to published results in (in the numbering order) [29–67]. (b) Examples of optomechanical systems covering ranges from the kilogram scales to atom mass. The illustration includes macroscopic [68] and microscopic suspended mirrors [54], suspended membranes inside an optical cavity [36], microtoroids [45], phoxonic crystals [69] and cold atoms coupled to an optical cavity [70].

Efficient cavity optomechanical transduction involves co-localization of optical and mechanical modes with high Q/(mode volume) and high optical power handling capacity. Moreover, it is desirable that the cavity supports a mechanism for efficient input/output coupling. A diverse zoo (fig. 1.5) of micro- and nanoscale cavity optomechanical systems has been designed to meet these challenges, ranging from cantilevers [51] and membranes [36] coupled to Fabry-Pérot cavities to mechanically-compliant whispering-gallery-mode (WGM) microcavities [44] and photonic crystals [41, 69]. They generally employ one of two types of radiation pressure force coupling: either traditional scattering-type coupling, in which the cavity field exchanges energy with the mechanical element via momentum transfer, or gradient force coupling [78], in which energy is exchanged via induced-dipole coupling to a field gradient. The net effect is a parametric coupling between the cavity resonance frequency and the mechanical degree of freedom. The actual device used in the experiments presented in this thesis is marked in fig. 1.5 and detailed in chapter 3.

1.2.2 Quantum cavity optomechanics at room temperature: this thesis

The very recent arrival of optomechanical systems in the quantum regime opens the door to an entirely new class of measurements. Quantum control schemes already established for atoms and ions could now be applied to tangible macroscopic objects. While all cavity optomechanics experiments that were able to operate in the quantum regime so far were limited to cryogenic environments, the work presented in this thesis marks one of the first successful ventures into this promised land at room temperature by being able to observe the quantum back-action – the fluctuating force due to the random arrival of photons that drives additional motion during a displacement measurement. Emphasizing the room-temperature aspect, our advances signal a paradigm shift in the practical applicability of quantum optomechanics.

To achieve this, this thesis details the engineering and optimization of an optomechanical near-field system for room temperature experiments, featuring both high quality factors for optics and mechanics as well as large optomechanical interaction. The result is a high-performance device that allows for mechanical displacement measurements with a sensitivity several orders below that at the standard quantum limit, even at room temperature. Performing a strong (i.e. at relatively large optical powers) ”variational" measurement [79], we observe the generation of quantum correlations between the quadratures of the light that has interacted with the mechanical oscillator.

These correlations are a direct consequence of strong quantum measurement back-action and could eventually lead to ponderomotive squeezing. In this regime, the quantum back-action induced motion dominates over the thermal motion and leads to suppression of the fluctuations on the output optical field below the shot-noise level, however, at the expense of increasing fluctuations in the orthogonal quadrature. Squeezed light is known to constitute a resource for sensitivity improvements beyond usual quantum limits, as has been demonstrated already in gravitational wave observatories [80, 81]. In contrast to ongoing methods of squeezed light generation, optomechanically generated squeezing is uniquely powerful as it is capable of enhancing the displacement measurement of the same mechanical object that generated it. This situation is, for instance, very relevant to gravitational wave detectors that are limited by radiation-pressure shot noise [82, 83].

This thesis describes the first-time broadband observation of these optomechanically generated quantum correlations at room temperature, spanning over an octave around the mechanical resonance frequency. In an additional experiment, the working principle behind a quantum-enhanced force measurement is demonstrated, in which the quantum back-action is canceled in the measurement record. Finally, the thesis provides an outlook of current efforts to further increase the efficiency of the optomechanical interaction and hence approach the regime of ponderomotive squeezing.

In particular, this thesis is structured into four following chapters. First, the thesis begins with the foundations of cavity optomechanics (chapter 2): here, the necessary theoretical background to understand the observed effects is provided. Following that is a discussion of the engineering and optimization of our particular optomechanical platform and its properties (chapter 3). Chapter 4 is devoted to the main experimental results, in which we first observe the effects of quantum measurement back-action at room temperature, and then use this result to achieve a quantum-enhanced estimation of an external force. Finally, an outlook is given discussing ongoing work on improving the device parameters to further enhance its performance (chapter 5).

2 Foundations of cavity optomechanics

In this chapter, the basic formalism used to describe optomechanical systems and effects will be introduced, with an eye towards the main experimental results of this thesis which are presented in chapters 3 and 4.

To begin with, section 2.1 covers the relevant physics of optical cavities and whispering-gallery mode microresonators. Section 2.2 introduces the properties of nanomechanical oscillators before section 2.3 combines optics and mechanics in order to convey the principles and foundations of the field of cavity optomechanics. Section 2.4 finally details the formalism of optical readout and describes the detection mechanisms used in this work.

2.1 Optical microresonators

Silica microresonators have a rich history in the field of quantum optics. A prominent example is the microsphere resonator, which is fabricated by melting the tip of an optical fiber. Owing to the extremely high optical quality factors of microspheres in excess of 10^9 in combination with their small mode volume [84–86], they have been established as a powerful tool to study effects of non-linear optics [84, 87], low-threshold Raman lasers [87–89], cavity quantum electrodynamics [90], and molecule- and biosensing [91–93].

The downside with these microsphere resonators is, however, that their exact geometry cannot be precisely controlled during fabrication. In addition, this process is not compatible with fabrication techniques developed in microelectronics, rendering a potential integration with other mechanical or electrical components impossible. This changed with the development of the microtoroid [94] which combines the high quality factors of microspheres with an on-chip fabrication scheme, finally allowing for chip-based integration.

This section describes the fundamentals of silica optical microresonators and their properties, as used in this work. Section 2.1.1 introduces the concept of whispering-gallery modes and their properties, followed by the analysis of the different loss channels and definition of the quality factor, an important measure for optical cavities (section 2.1.2). Section 2.1.3 presents

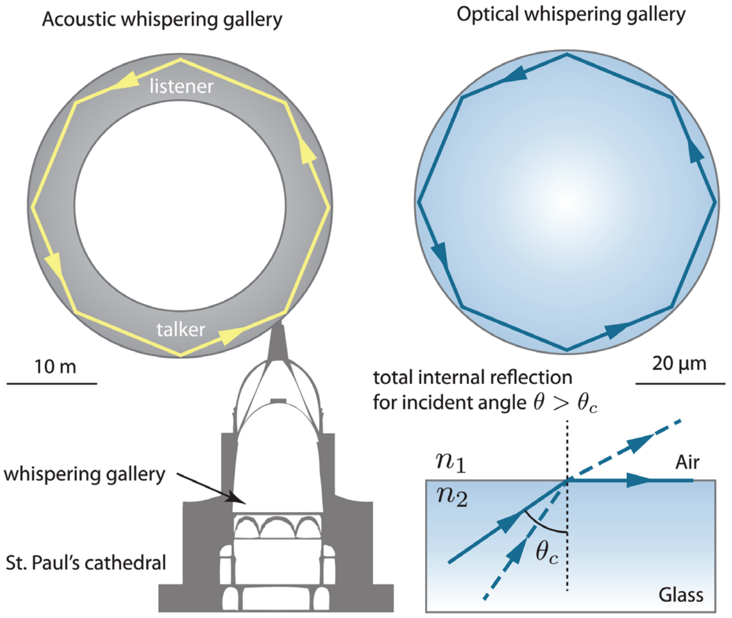
Acoustic whispering gallery
Optical whispering gallery
listener
talker
10 m
20 µm
whispering gallery
St. Paul's cathedral
total internal reflection
for incident angle $\theta > \theta_c$
n_1
n_2
Air
θ_c
Glass

Figure 2.1 – **Whispering gallery modes:** Total internal reflection of acoustic (left) and optical (right) waves inside a circular resonator. A mode is supported if the optical path along the circumference is an integer multiple of the wavelength. Image adapted from [97].

the mathematics behind the process of coupling light in and out of an optical cavity and defines the observables measured in an experiment under different coupling conditions.

2.1.1 Whispering-gallery modes

The term ”whispering-gallery mode" (or ”whispering-gallery wave") was first mentioned in 1878, when Lord Rayleigh used it to describe an acoustic phenomenon occurring in the dome of St. Paul's Cathedral [95]. There, whispers can be heard across the 32 m gallery on the opposite site when placing the ear close to the wall. He explained this effect with multiple reflections of the sound waves off the dome's circumferential wall and further developed theories stating that, based on wave interference, only certain pitches of sound experience this effect, the so-called *modes* [96].

When investigating light scattering from spherical particles, Mie in 1908 predicted sharp resonances for certain wavelengths of the incident light [98], corresponding to optical resonances (modes) of the spheres. The light was found to propagate inside the sphere close to the surface, which Mie subsequently linked to the concept of the acoustic whispering-gallery modes (WGM). In this simple picture, the light rays inside the sphere repeatedly bounce off the glass-air interface at a shallow angle due to total internal reflection, and are contained within the perimeter, similar to the acoustic WGMs. The strongest scattering is observed if the optical path length of a round trip is an integer multiple of the wavelength, corresponding to a supported mode, or more precisely, a whispering-gallery mode. The concept of acoustic and optical WGMs is illustrated in fig. 2.1. A detailed mathematical description can be found

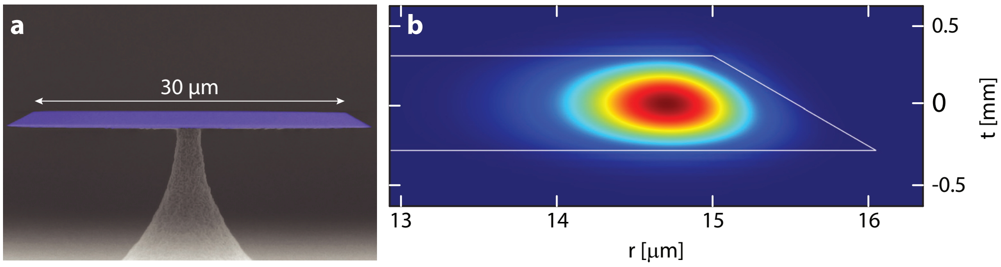

Figure 2.2 – **Wedged SiO_2 microdisk resonator:** (a) SEM of a wedged microdisk; blue and gray indicate SiO_2 and Si, respectively. (b) Finite-element calculated electric field intensity distribution of a WGM for a disk with 40 μm diameter, 600 nm thickness and 30° wedge angle. For fabrication details, see section 3.2.

in [99].

Throughout the experiments presented in this work, silica microdisk resonators, as shown in fig. 2.2a, are used. Due to a completely MEMS compatible fabrication process, the disks enable the on-chip integration with a mechanical oscillator to form an optomechanical system in which optical and mechanical resonator are separated. This novel concept of having integrated on-chip optomechanical devices where mechanics and optics are completely separated obviously bears the advantage that specific materials and designs can be chosen independently for each element. A second advantage is that in an integrated device no relative positioning after the fabrication process is required, nullifying instabilities caused by external vibrations, for example. Together, these two aspects enabled a significant boost of the performance of the samples.

The microdisks, however, lack a key advantage compared to spheres and toroids – the silica is not reflowed and therefore has a less smooth surface. However, by fabricating a wedge, the cavity mode can be spatially isolated from the surface of the disk and equally high quality factors can be achieved. Responsible for this is the wedge that spatially isolates the mode from the surface of the disk. Figure 2.2b shows a finite-element simulation (using COMSOL) of the whispering-gallery mode and its location inside the disk resonator. The fabrication process of the microdisks and measurements of the quality factor are detailed in chapter 3.

2.1.2 Quality factor and optical loss mechanisms

To mathematically describe optical microresonators, the Fabry-Pérot cavity constitutes a straightforward example to introduce useful quantities. Such a resonator consists of two highly reflective mirrors facing each other at a distance L, and hence supports resonances characterized by their angular frequency,

$$\omega_{\mathrm{c,m}} \approx m \cdot \pi \frac{c}{L}, \tag{2.1.1}$$

with the integer mode number m. The spectral separation of two adjacent modes is named the free spectral range (FSR) of the oscillator and is given by,

$$\Delta\omega_{\mathrm{FSR}} = \pi\frac{c}{L}. \tag{2.1.2}$$

Note that in the following, the focus is on a single optical mode denoted as ω_{c}.

An ideal resonator with perfectly reflecting mirrors would have no losses besides the light that is intentionally coupled back out of the resonator. Due to different loss mechanisms however, the energy stored in a cavity mode decays over a characteristic timescale τ, or more frequently described at a loss rate κ,

$$\kappa = \tau^{-1}. \tag{2.1.3}$$

A useful quantity proportional to the average number of cavity round-trips of the photons before exiting through one of the loss channels is the *optical Finesse* $\mathscr{F}$ given by,

$$\mathscr{F} = \Delta\omega_{\mathrm{FSR}}\tau = \frac{\Delta\omega_{\mathrm{FSR}}}{\kappa} = \frac{2\pi\tau_{\mathrm{rt}}^{-1}}{\kappa} = \pi\frac{c}{L\kappa}, \tag{2.1.4}$$

where τ_{rt} denotes the cavity round-trip time of light. Therefore, the optical Finesse can be understood as the power enhancement factor and describes the ratio between intracavity and injected power. In line with this, another very important parameter of an optical cavity is its *quality factor* Q that compares the oscillation period of the field inside a cavity with the photon life time,

$$Q = \omega_{\mathrm{c}}\tau = \frac{\omega_{\mathrm{c}}}{\kappa}. \tag{2.1.5}$$

To understand the limitations in the quality factor, the total loss rate needs to be decomposed into the individual contributions that each reduce the photon storage time τ of the cavity. In general, the cavity decay rate κ is separated into two major parts, one describing internal losses, κ_0, and the other denoting losses due to the intentional input and output coupling, κ_{ex}. In the case of a Fabry-Pérot cavity, κ_{ex} represents losses due to the coupling, while κ_0 combines internal loss channels inside the cavity, such as transmission losses at the second mirror as well as scattering and absorption losses during the circulation. For silica microresonators, the intrinsic loss rate κ_0 consists of absorption and bulk Rayleigh scattering of the material κ_{mat}, scattering losses due to residual surface inhomogeneities $\kappa_{\mathrm{s.s}}$, absorption due to surface contaminations κ_{cont}, and radiation loss κ_{rad}. The total loss rate of the cavity can then be expressed as,

$$\kappa = \kappa_0 + \kappa_{\mathrm{ex}} = \kappa_{\mathrm{mat}} + \kappa_{\mathrm{s.s}} + \kappa_{\mathrm{cont}} + \kappa_{\mathrm{rad}} + \kappa_{\mathrm{ex}}, \tag{2.1.6}$$

and an intrinsic quality factor Q_0 of the cavity can be defined as,

$$Q_0^{-1} = \left(\frac{\omega_{\mathrm{c}}}{\kappa_0}\right)^{-1} = Q_{\mathrm{mat}}^{-1} + Q_{\mathrm{s.s}}^{-1} + Q_{\mathrm{cont}}^{-1} + Q_{\mathrm{rad}}^{-1}. \tag{2.1.7}$$

The losses due to material absorption in ultra-clean silica are very low for wavelengths in the visible (390 – 700 nm) and near-infrared (700 – 2500 nm) regime. For a given absorption coefficient α, Q_{mat} can be approximated by [99],

$$Q_{\mathrm{mat}} \approx \frac{4.3 \cdot 10^3}{\alpha} \frac{2\pi n}{\lambda}. \tag{2.1.8}$$

For silica (refractive index $n = 1.45$, $\alpha = 0.17$ dB/km) at a wavelength $\lambda = 780$ nm, a material limited quality factor as high as $Q_{\mathrm{mat}} \approx 10^{11}$ is predicted and values approaching this limit have been observed in microsphere resonators [100, 101].

The magnitude of the loss channel caused by scattering from surface inhomogeneities, described by the scattering quality factor $Q_{\mathrm{s.s}}$, is derived from calculations of Rayleigh scattering by molecular-sized surface clusters under grazing incidence and total internal reflection [100, 102]. For microsphere resonators this estimate yields,

$$Q_{\mathrm{s.s}} = \frac{\lambda^2 D}{2\pi^2 \sigma^2 B}, \tag{2.1.9}$$

where D is the diameter of the resonator, and σ and B denote the root-mean-square surface roughness and correlation length of surface inhomogeneities, respectively. Values reported for glass surfaces are $\sigma = 0.3$ nm and $B = 3$ nm. The exact loss rate also depends on the ratio of the light intensity at the surface to the total modal energy. For large microsphere resonators, quality factors of up to $8 \cdot 10^9$ have been observed, approaching the surface loss limit of $Q_{\mathrm{s.s}} \approx 10^{10}$ if $D \approx 100$ μm. However, optical silica micro resonators are in general scattering-loss limited at quality factors of 10^8 due to their small mode volume [103].

Intrinsic radiation (curvature) losses due to lack of confinement of the optical mode by the curved surface of the resonator are typically negligible for resonators with dimensions used in this work. Spheres and microdisks with diameters larger than 20 μm experience radiation losses in the order of $Q_{\mathrm{rad}} > 10^{11}$ at visible and near-infrared wavelengths [104], as radiation losses exponentially decrease with increasing size [100].

Finally, since silica is highly hygroscopic, losses due to chemically adsorbed water molecules on the surface are important. When measuring the quality factors of large microspheres (up to 800 μm in diameter) under ambient conditions, the quality factors were limited to $Q = 8 \cdot 10^9$ [86]. Particularly at telecommunication wavelengths around 1.5 μm where water absorption peaks, even a mono-layer of water on the surface leads to a significant increase of losses [103]. Investigating the adsorption, a degradation of the optical quality factor in microsphere resonators due to a water layer has been observed after exposure to air for a time period as short as 100s. Therefore, κ_{cont} is the dominant loss contribution for experiments under ambient conditions [100]. However, the quality factors can be recovered by baking out the sample at $400°C$ (see appendix F).

2.1.3 Resonator-waveguide coupling

When investigating the properties of an optical resonator, light is coupled into it using some type of input wave, for example light inside a waveguide. To study both the steady states and temporal dynamics of the coupled system, the input-output formalism described in [105] provides a powerful tool for the modeling of quantum fluctuations from any coupling port and also includes the treatment of a possible coherent laser drive at angular frequency ω_L. In this formalism, the complex scalar mode amplitude $a(t)$ is introduced, which is normalized such that $|a(t)|^2$ equals the mode energy (or equivalently the photon number with a proportionality factor of $1/(\hbar\omega_\mathrm{L})$). Based on the Heisenberg equations of motion, the time evolution of $a(t)$ inside the cavity can be derived [105, 106] and its equation of motion is given as,

$$\frac{\mathrm{d}a}{\mathrm{d}t} = -i\omega_\mathrm{c} a(t) - \left(\frac{\kappa_0}{2} + \frac{\kappa_\mathrm{ex}}{2}\right) a(t) + \sqrt{\kappa_\mathrm{ex}} s_\mathrm{in}(t), \tag{2.1.10}$$

with $s_\mathrm{in}(t)$ describing the input field amplitude due to a laser drive (coupled to the cavity, for example via an optical fiber). This quantity is normalized such that $|s_\mathrm{in}(t)|^2$ is the optical power (or equivalently the photon flux) of the driving light field. Typically, the drive is supplied by a harmonic oscillation at an angular frequency ω_L, resulting in $s_\mathrm{in}(t) \equiv \hat{s}_\mathrm{in}(t) e^{-i\omega_\mathrm{L} t}$. For a convenient further analysis, transformation into a frame rotating at the drive frequency using $a(t) \equiv \hat{a}(t) e^{-i\omega_\mathrm{L} t}$ leads to the modified equation of motion,

$$\frac{\mathrm{d}\hat{a}}{\mathrm{d}t} = i\Delta \hat{a}(t) - \frac{\kappa}{2}\hat{a}(t) + \sqrt{\kappa_\mathrm{ex}}\hat{s}_\mathrm{in}(t), \tag{2.1.11}$$

with the detuning of the laser field $\Delta = \omega_\mathrm{L} - \omega_\mathrm{c}$ and the total losses $\kappa = \kappa_0 + \kappa_\mathrm{ex}$ as introduced in the previous section. Positive (negative) detuning means blue (red) detuning from the cavity. The solution of this first-order ordinary differential equation for a constant drive amplitude $\hat{s}_\mathrm{in}(t) = \bar{s}$ is given by,

$$\hat{a}(t) = \underbrace{\hat{A}_0 e^{-\frac{1}{2}t(\kappa + 2i\Delta)}}_{\text{damped part}} + \underbrace{\frac{\sqrt{\kappa_\mathrm{ex}}\bar{s}}{-i\Delta + \kappa/2}}_{\text{steady state}}, \tag{2.1.12}$$

with a complex amplitude $\hat{A}_0$. For times $t \gg \kappa^{-1}$, only the steady state $\bar{a} \equiv \frac{\sqrt{\kappa_\mathrm{ex}}\bar{s}}{-i\Delta+\kappa/2}$ is of relevance and the power circulating in the cavity, $\left|\bar{p}\right|^2$, can be derived as,

$$\begin{aligned} \left|\bar{p}\right|^2 &= \frac{|\bar{a}|^2}{\tau_\mathrm{rt}} = \frac{1}{\tau_\mathrm{rt}} \frac{\kappa_\mathrm{ex}|\bar{s}|^2}{\Delta^2 + (\kappa/2)^2} \\ &= \frac{4\eta_\mathrm{c}}{\tau_\mathrm{rt}\kappa} \frac{|\bar{s}|^2}{1 + 4\Delta^2/\kappa^2} = 2\eta_\mathrm{c} \frac{\mathscr{F}}{\pi} \frac{|\bar{s}|^2}{1 + 4\Delta^2/\kappa^2}. \end{aligned} \tag{2.1.13}$$

Here, the coupling parameter $\eta_\mathrm{c} \equiv \frac{\kappa_\mathrm{ex}}{\kappa}$ describes the cavity-waveguide coupling efficiency. The last equation highlights the meaning of the cavity finesse. For a symmetric cavity in which $\kappa_\mathrm{ex} = \kappa_0$ (i.e. $\eta_\mathrm{c} = 1/2$), the intracavity power on resonance ($\Delta = 0$) is enhanced by a factor of $\left|\bar{p}/\bar{s}\right|^2 = \mathscr{F}/\pi$. The steady-state intracavity field also gives rise to the mean photon number n_c

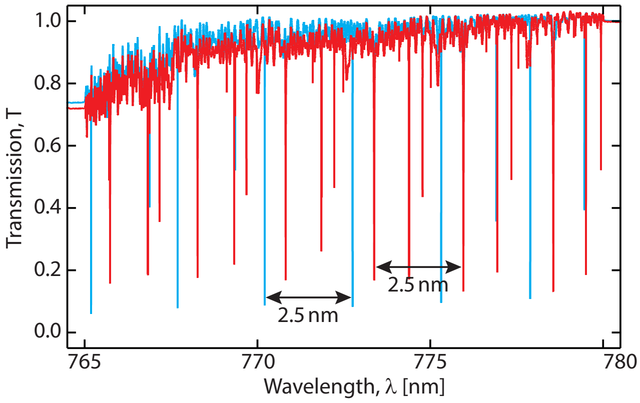

Figure 2.3 – **Wavelength scan across several free spectral ranges of a microdisk resonator:** Measurement of the transmission T versus laser wavelength for sample AE/L2/A2/23. The red and blue traces are measurements of the two different polarizations (TE and TM). The free spectral range can be easily read off to be ~2.5 nm. The background noise is caused by fluctuations of the input power (e.g. due to output power fluctuations of the laser or etalons in the optical path).

inside the cavity,

$$n_c = |\bar{a}|^2 = \frac{4\eta_c}{\kappa}\frac{P_{in}}{\hbar\omega_L}\frac{1}{1+4\Delta^2/\kappa^2}. \tag{2.1.14}$$

Here, $P_{in} = \hbar\omega_L\,|\bar{s}|^2$ is the input power launched into the waveguide.

To estimate the transmission amplitude detected at the output of the waveguide, the input-output relation for the transmission amplitude $s_{out} = s_{in} - \sqrt{\kappa_{ex}}a$ is used. In the steady state, the transmission coefficient T is can be found as,

$$T(\Delta) \equiv \left|\frac{\bar{s}_{out}}{\bar{s}}\right|^2 = \frac{\Delta^2 + (\kappa_0/2 - \kappa_{ex}/2)^2}{\Delta^2 + (\kappa_0/2 + \kappa_{ex}/2)^2} = 1 - \frac{\eta_c(1-\eta_c)\kappa^2}{\Delta^2 + (\kappa/2)^2}, \tag{2.1.15}$$

corresponding to a Lorentzian suppression when approaching resonance ($|\Delta| \to 0$) with FWHM linewidth κ.

Figure 2.3 shows a measurement of the optical spectrum of a microdisk resonator for the two different input polarizations of the light, TE and TM. For this, the laser wavelength was slowly tuned over its entire range from 765 – 780 nm while monitoring the transmission of the fiber. By investigating the periodicity of the acquired transmission signal, we gain access to the free spectral range ~2.5 nm in this example, which is equivalent to a free spectral range $\Delta\omega_{FSR} \approx 2\pi\cdot 1.3$ THz. From this result, we can calculate the radius R of the microdisk resonator by (cf eq. (2.1.2)),

$$\Delta\omega_{FSR} = \pi\frac{c}{2n\pi R} \Leftrightarrow R = \frac{c}{2n\Delta\omega_{FSR}} \approx 15\,\mu\text{m}, \tag{2.1.16}$$

with the refractive index of SiO_2, $n = 1.45$.

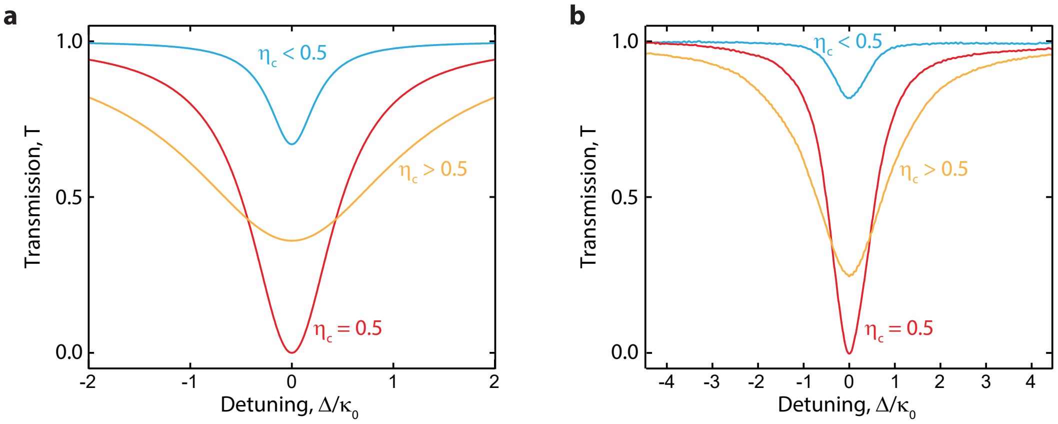

Figure 2.4 – **Coupling regimes:** (a) Model and (b) measurement of the transmission T versus cavity detuning Δ for the undercoupled (blue traces, $\eta_c = 0.1$), critically coupled (red traces, $\eta_c = 1$) and overcoupled case (orange traces, $\eta_c = 0.8$). The measurements were taken with sample M2/CU/T/BD. See text for details regarding the experiment.

Coupling regimes

The coupling parameter η_c can be continuously tuned by varying the strength of the external coupling κ_{ex}, for example by changing the distance between the optical waveguide and the cavity in case of WGM resonators. This grants access to three different coupling regimes: undercoupled, critically coupled and overcoupled [107].

In the first regime, the total losses of the cavity are dominated by the intrinsic loss rate. The cavity is hence operated in the *undercoupled regime*. It is characterized by $\kappa_0 > \kappa_{ex}$, leading to a coupling parameter $\eta_c < 1/2$. In this case, the magnitude of the light coupled back from the cavity is smaller than the field propagating in the optical fiber. This regime is useful for measuring the intrinsic linewidth of the optical resonator.

The second regime of *critical coupling* describes the case where the intrinsic loss rate equals the external coupling rate, $\kappa_0 = \kappa_{ex} \Leftrightarrow \eta_c = 1/2$. On cavity resonance, the light field coupled back from the cavity equals the field propagating in the optical fiber in magnitude. However, due to their phase difference of π, this results in zero transmitted power of the system.

A further increase of the external coupling strength leads to the *overcoupled regime* in which $\kappa_0 < \kappa_{ex}$. Here, $\eta_c > 1/2$, leading to a larger magnitude of the outcoupled light compared to the field propagating in the fiber.

The different coupling regimes are illustrated in fig. 2.4. The measurements were taken for a fundamental optical mode of a microdisk WGM resonator with an intrinsic loss rate of $\kappa_0 \approx 2\pi \cdot 500$ MHz, a typical value for the experiments carried out in this thesis. The data was acquired by directly measuring the transmission $T(\Delta)$ at the end of an optical fiber on the output side of the cavity. To this end, a widely tunable external cavity diode laser at a wavelength of 780 nm is coupled into a tapered fiber which is positioned in the evanescent near-field of the microdisk. By varying the gap between fiber and resonator, κ_{ex}, and hence the coupling efficiency, η_c, can be precisely controlled and tuned through the different regimes. Sweeping the laser frequency across the whispering-gallery mode allows for the recording of $T(\Delta)$. The relative detuning between laser and cavity is calibrated by directing a fraction of the laser light into a fiber-loop cavity of known FSR. The intrinsic linewidth of the cavity is accessed in the strongly undercoupled regime in which the total losses κ are dominated by κ_0.

Experiments generally operate close to the critically coupled regime $\eta_c \sim 0.5$, as this means that the signal that is eventually measured on the output side is almost only composed of light that has entered and circulated in the cavity, yielding a high measurement efficiency, while keeping the deterioration of the optical quality factor at a reasonable level.

Coupling of counter-propagating modes in bi-directional cavities

Due to the frequency degeneracy of counter-propagating modes in whispering-gallery mode resonators the direction of the light propagation is determined by the propagation direction of light in the tapered fiber. Light scattering processes due to inhomogeneities in the bulk and on the surface however cause an excitation of the mode propagating in the opposite direction [108, 109]. This effect is described using a simple coupled harmonic oscillator model [109]. The field amplitudes of the excited clockwise (cw) mode and the unpumped counter-clockwise (ccw) that are coupled to each other at a rate γ evolve following the equations of motion,

$$\frac{\mathrm{d}a_{\mathrm{cw}}}{\mathrm{d}t} = -i\omega_{\mathrm{c}} a_{\mathrm{cw}} - \left(\frac{\kappa_0}{2} + \frac{\kappa_{\mathrm{ex}}}{2}\right) a_{\mathrm{cw}} + i\frac{\gamma}{2} a_{\mathrm{ccw}} + \sqrt{\kappa_{\mathrm{ex}}}\, s_{\mathrm{in}}(t), \tag{2.1.17}$$

$$\frac{\mathrm{d}a_{\mathrm{ccw}}}{\mathrm{d}t} = -i\omega_{\mathrm{c}} a_{\mathrm{ccw}} - \left(\frac{\kappa_0}{2} + \frac{\kappa_{\mathrm{ex}}}{2}\right) a_{\mathrm{ccw}} + i\frac{\gamma}{2} a_{\mathrm{cw}}. \tag{2.1.18}$$

Again transforming to a frame that rotates at the driving frequency ($a_{\mathrm{cw(ccw)}} = \hat{a}_{\mathrm{cw(ccw)}} e^{-i\omega_{\mathrm{L}} t}$) and taking $\kappa = \kappa_0 + \kappa_{\mathrm{ex}}$ leads to the modified equations of motion,

$$\frac{\mathrm{d}\hat{a}_{\mathrm{cw}}}{\mathrm{d}t} = \left(i\Delta - \frac{\kappa}{2}\right) \hat{a}_{\mathrm{cw}} + i\frac{\gamma}{2} \hat{a}_{\mathrm{ccw}} + \sqrt{\kappa_{\mathrm{ex}}}\, \hat{s}_{\mathrm{in}}, \tag{2.1.19}$$

$$\frac{\mathrm{d}\hat{a}_{\mathrm{ccw}}}{\mathrm{d}t} = \left(i\Delta - \frac{\kappa}{2}\right) \hat{a}_{\mathrm{ccw}} + i\frac{\gamma}{2} \hat{a}_{\mathrm{cw}}. \tag{2.1.20}$$

In the steady state, the solutions for these equations are given by,

$$\bar{a}_{\mathrm{cw}} = \frac{1}{2}\left(\frac{1}{\kappa/2 - i(\Delta + \gamma/2)} + \frac{1}{\kappa/2 - i(\Delta - \gamma/2)}\right) \sqrt{\kappa_{\mathrm{ex}}}\, \bar{s}, \tag{2.1.21}$$

$$\bar{a}_{\mathrm{ccw}} = \frac{1}{2}\left(\frac{1}{\kappa/2 - i(\Delta + \gamma/2)} - \frac{1}{\kappa/2 - i(\Delta - \gamma/2)}\right) \sqrt{\kappa_{\mathrm{ex}}}\, \bar{s}. \tag{2.1.22}$$

Under these conditions, the eigenfrequencies ω_c become non-degenerate and are split due to the modal coupling by $\pm\gamma/2$. By considering the time derivative of the energy stored in the cavity it can be verified in a straightforward manner that the cross-coupling term $i\gamma/2$ does

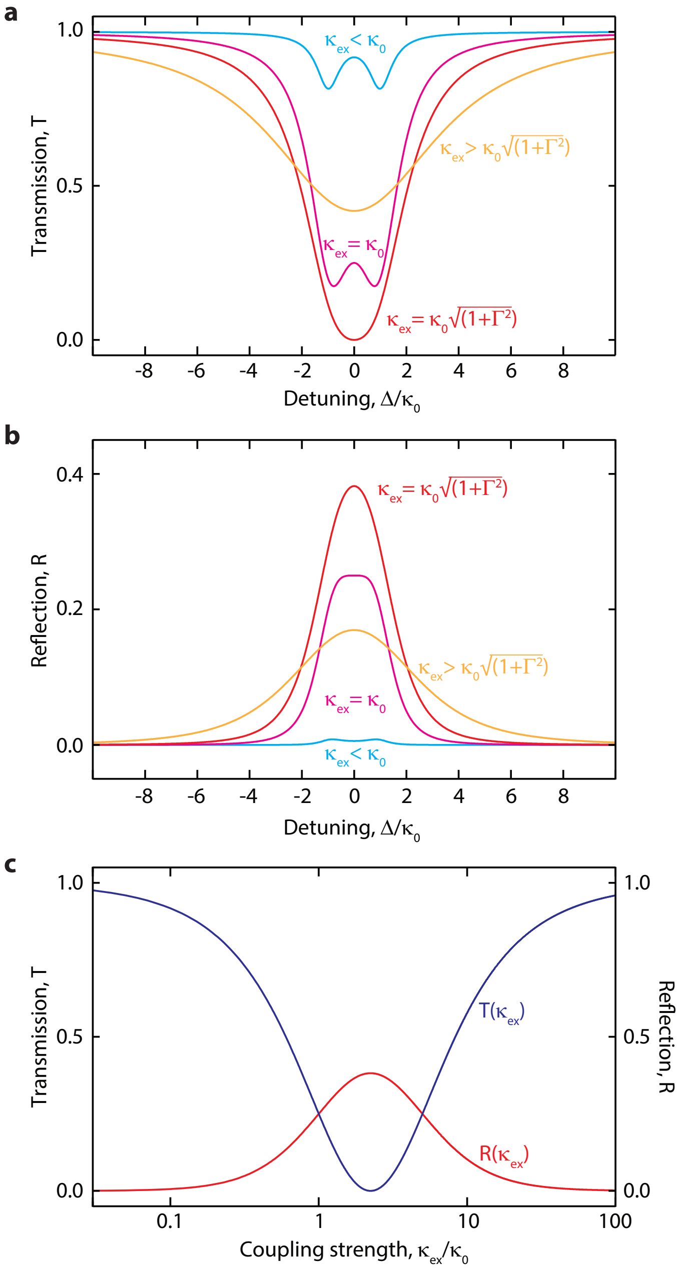

Figure 2.5 – **Transmission and reflection for counter-propagating modes:** (a,b) Transmission T and reflection R coefficient versus cavity detuning Δ for the cases of (i) undercoupled ($\kappa_{\text{ex}} < \kappa_0$), (ii) $\kappa_{\text{ex}} = \kappa_0$, (iii) critically coupled ($\kappa_{\text{ex}} = \kappa_0\sqrt{1+\Gamma^2}$), and (iv) overcoupled case ($\kappa_{\text{ex}} > \kappa_0\sqrt{1+\Gamma^2}$). (c) Transmission T and reflection R versus coupling strength κ_{ex} on resonance ($\Delta = 0$). For all these illustrations, a modal coupling rate $\gamma = 3\kappa_0$ was assumed.

not cause a loss in optical power, as the result is independent of γ:

$$\frac{\mathrm{d}}{\mathrm{d}t}\left[|a_{\text{cw}}|^2 + |a_{\text{ccw}}|^2\right] = -\kappa\left(|a_{\text{cw}}|^2 + |a_{\text{ccw}}|^2\right) + \kappa_{\text{ex}}\,|a_{\text{cw}}s|\,. \tag{2.1.23}$$

In addition to the transmitted field $s_{\text{out}} = s_{\text{in}} - \sqrt{\kappa_{\text{ex}}} a_{\text{cw}}$ due to the clockwise mode, a reflected field $r = -\sqrt{\kappa_{\text{ex}}} a_{\text{ccw}}$ from the counter-clockwise mode is also coupled back into the fiber. The transmission and reflection coefficients on resonance are found to be,

$$T(\Delta) = \left|\frac{\bar{s}_{\text{out}}}{\bar{s}}\right|^2 = \left|\frac{(2i\Delta+\kappa)^2+\gamma^2-(4i\Delta+2\kappa)\kappa_{\text{ex}}}{(2i\Delta+\kappa)^2+\gamma^2}\right|^2 \overset{\Delta=0}{=} \frac{\left(\gamma^2-\kappa_{\text{ex}}^2+\kappa_0^2\right)^2}{\left(\gamma^2+(\kappa_{\text{ex}}+\kappa_0)^2\right)^2}, \tag{2.1.24}$$

$$R(\Delta) = \left|\frac{\bar{r}}{\bar{s}}\right|^2 = \left|\frac{2i\kappa_{\text{ex}}\gamma}{(2i\Delta+\kappa)^2+\gamma^2}\right|^2 \overset{\Delta=0}{=} \frac{4\gamma^2\kappa_{\text{ex}}^2}{\left(\gamma^2+(\kappa_{\text{ex}}+\kappa_0)^2\right)^2}. \tag{2.1.25}$$

The mode splitting also causes a modification of the coupling conditions. In particular, zero transmission (critical coupling) now occurs when the external coupling is $\kappa_{\text{ex}} = \kappa_0\sqrt{1+\Gamma^2}$ with the modal coupling parameter $\Gamma = \gamma/\kappa_0$. The reflected signal reaches its maximum at this critical point and is given by,

$$R(\Delta=0) = \frac{\Gamma^2}{\left(1+\sqrt{1+\Gamma^2}\right)^2}. \tag{2.1.26}$$

Figure 2.5 illustrates the transmission and reflection coefficients in dependence of the detuning and coupling strength. Note that for strong modal coupling, $\Gamma \gg 1$, the reflection coefficient approaches unity.

Finally, the stored optical energy in the cavity is given by,

$$\begin{aligned} E &= |a_{\text{cw}}|^2 + |a_{\text{ccw}}|^2 \\ &= \frac{4s^2\kappa_{\text{ex}}\left(\gamma^2+4\Delta^2+(\kappa_{\text{ex}}+\kappa_0)^2\right)}{\left((\gamma-2\Delta)^2+(\kappa_{\text{ex}}+\kappa_0)^2\right)\left((\gamma+2\Delta)^2+(\kappa_{\text{ex}}+\kappa_0)^2\right)} \\ &\overset{\Delta=0}{=} \frac{4s^2\kappa_{\text{ex}}}{\gamma^2+(\kappa_{\text{ex}}+\kappa_0)^2}. \end{aligned} \tag{2.1.27}$$

2.2 Nanomechanical oscillators

This section provides the properties of the second ingredient of any cavity optomechanical system: the nanomechanical oscillator. Nanomechanical oscillators are sensitive to weak forces and have large zero-point fluctuations, rendering them an attractive platform for both precision sensing technology [110–112] and basic quantum science [113]. To try to use this precision sensing in the electrical domain, great efforts have been devoted to making transducers from mechanical motion to the electrical domain, including single-electron transistors [114], atomic point contacts [115], and superconducting microwave cavities [31].

In the first part of this section, the relevant properties and useful quantities of mechanical motion are discussed in general (section 2.2.1), before section 2.2.2 covers the reasons for choosing silicon nitride nanobeams as the mechanical element in the system used in this work

2.2.1 Mechanical motion

The displacement $x(t)$ of a harmonic mechanical oscillator at mechanical frequency Ω_m is described by the equation of motion,

$$\frac{\mathrm{d}^2x(t)}{\mathrm{d}t^2}+\Gamma_\mathrm{m}\frac{\mathrm{d}x(t)}{dt}+\Omega_\mathrm{m}^2x(t)=\frac{F(t)}{m_\mathrm{eff}}. \tag{2.2.1}$$

Here $F(t)$ denotes the combined forces, that are acting on the oscillator. The effective mass, m_eff, is introduced to account for the displacement profile of a finite-sized mechanical oscillator, as eq. (2.2.1) is only valid for point-like masses. With an effective mass that is in general smaller than the physical mass of the system, eq. (2.2.1) holds true for arbitrary oscillator geometries. The expression also includes the energy dissipation rate Γ_m, quantifying the loss rate of mechanical excitations. A very important quantity characterizing the ratio between stored and dissipated energy of the oscillator is the mechanical quality factor,

$$Q_\mathrm{m}=\frac{\Omega_\mathrm{m}}{\Gamma_\mathrm{m}}. \tag{2.2.2}$$

There are different mechanisms that contribute to the overall mechanical dissipation [116, 117] that can be divided into extrinsic and intrinsic loss channels. The extrinsic sources include viscous damping due to interactions with surrounding gas molecules, Γ_gas, and clamping losses, Γ_cl, caused by radiation into the substrate through the supports of the oscillator. The intrinsic loss mechanisms, Γ_0, comprise fundamental anharmonic effects, such as thermoelastic damping and phonon-phonon interactions, as well as material-induced losses due to bulk and surface imperfections. All these processes contribute independently to the total losses and result in the total dissipation rate $\Gamma_\mathrm{m}=\sum_i\Gamma_i$, or quality factor $Q_\mathrm{m}^{-1}=\sum_i Q_i^{-1}$, where i labels the individual loss channels [25].

Another useful quantity of a mechanical oscillator is its thermal decoherence rate. This rate corresponds to the inverse time for one quantum from the environment to enter the system. Considering an oscillator that is coupled to a high-temperature bath (at a temperature T) with phonon occupation $\bar{n}_\mathrm{th}$, the average phonon number, $\bar{n}$, of the oscillator evolves as,

$$\frac{\mathrm{d}\bar{n}}{\mathrm{d}t}=-\Gamma_\mathrm{m}(\bar{n}-\bar{n}_\mathrm{th}). \tag{2.2.3}$$

Starting from an initial ground state $\bar{n}(t=0)=0$ (neglecting the zero-point energy of $1/2\hbar\Omega_\mathrm{m}$), a simple time dependence of the occupation $\bar{n}(t)=\bar{n}_\mathrm{th}(1-e^{-\Gamma_\mathrm{m}t})$ is obtained. The thermal decoherence rate is then found to be the rate at which the oscillator is heated out of the ground state,

$$\left.\frac{\mathrm{d}\bar{n}(t)}{\mathrm{d}t}\right|_{t=0}=\bar{n}_\mathrm{th}\Gamma_\mathrm{m}\approx\frac{k_\mathrm{B}T}{\hbar Q_\mathrm{m}}, \tag{2.2.4}$$

where the approximation denotes the high-temperature limit $\bar{n}_{\mathrm{th}} \approx \frac{k_{\mathrm{B}}T}{\hbar\Omega_{\mathrm{m}}}$. To achieve a low decoherence rate, a high quality factor (and a low-temperature bath) is essential. The decoupling of a mechanical oscillator from its thermal environment is given by its number of coherent oscillations in the presence of thermal decoherence,

$$\frac{\Omega_{\mathrm{m}}}{\bar{n}_{\mathrm{th}}\Gamma_{\mathrm{m}}} = Q_{\mathrm{m}} f_{\mathrm{m}} \frac{h}{k_{\mathrm{B}}T}, \tag{2.2.5}$$

highlighting the meaning of the often mentioned $Q-f$ product of a mechanical oscillator.

When attempting a measurement of the motion of a mechanical oscillator, a signal randomly time-varying in both amplitude and phase would be observed due to the presence of damping [25]. For this reason, the interest lies in general in a frequency-domain description of the mechanical oscillator. To this end, eq. (2.2.1) can be solved in frequency space by performing a Fourier transformation via $x(\Omega) = \int_{-\infty}^{\infty} \mathrm{d}t\, x(t) e^{i\Omega t}$ to obtain,

$$x(\Omega) = \chi_x(\Omega) F(\Omega). \tag{2.2.6}$$

This linear expression links the external force $F(\Omega)$ to the displacement $x(\Omega)$, mediated by the mechanical susceptibility[1],

$$\chi_x(\Omega) = \frac{m_{\mathrm{eff}}^{-1}}{\Omega_{\mathrm{m}}^2(1 - i\phi(\Omega)) - \Omega^2}, \tag{2.2.7}$$

where $\phi(\Omega)$ is the frequency-dependent loss angle. In an experiment, the measured quantity is not $x(\Omega)$ but rather the associated spectrum $S_{xx}(\Omega)$. Following the Wiener-Khinchin theorem, the spectrum for a given quantity $a(t)$ is obtained by taking the Fourier transform of the autocorrelation function [118],

$$S_{aa}(\Omega) = \int_{-\infty}^{\infty} \mathrm{d}\tau\, \langle a(t) a(t+\tau) \rangle\, e^{i\Omega\tau}, \tag{2.2.8}$$

where $\langle \ldots \rangle$ denotes the statistical mean. Such a spectrum has units of $[a]^2\ \mathrm{Hz}^{-1}$ and gives information about the spectral density of the Fourier components of the measured quantity. In case of a known Fourier transform of the quantity in question, the spectrum can be obtained by,

$$S_{aa}(\Omega) = \langle a(\Omega) a(-\Omega) \rangle. \tag{2.2.9}$$

Therefore, the mechanical displacement spectrum $S_{xx}(\Omega)$ follows as,

$$S_{xx}(\Omega) = \left|\chi_x(\Omega)\right|^2 S_{FF}(\Omega), \tag{2.2.10}$$

whereas S_{FF} denotes the power spectrum of the sum of the forces acting on the mechanical oscillator. In the absence of any other external driving forces, $F(\Omega)$ is simply the thermal Langevin force leading to the thermal Brownian motion of the oscillator [13]. The caused fluctuations in

---

[1] The response at low frequency is given by $\chi_x(0) = (m_{\mathrm{eff}}\Omega_{\mathrm{m}}^2)^{-1} = 1/k$ with the spring constant k.

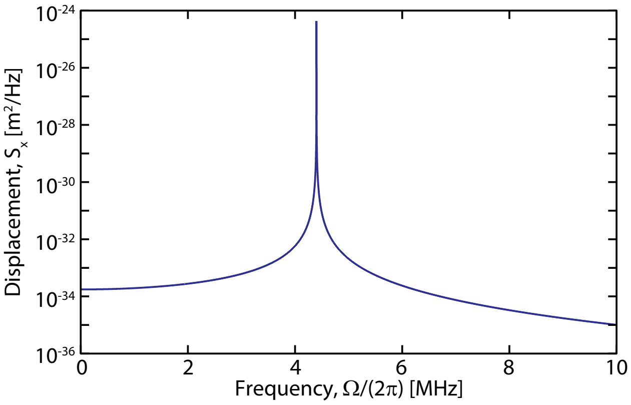

Figure 2.6 – **Thermal spectrum of a mechanical oscillator.** Symmetrized single-sided displacement spectrum $S_x^{\text{th}}(\Omega)$ of a mechanical oscillator versus Fourier frequency. The oscillator is modeled using typical values as presented throughout this work, leading to a resonance frequency $\Omega_\text{m} = 2\pi \cdot 4.4\,\text{MHz}$ and dissipation rate $\Gamma_\text{m} = 2\pi \cdot 10\,\text{Hz}$.

displacement in any system with dissipation can be expressed with the fluctuation-dissipation theorem (FDT) [119, 120]. Applying the FDT, the (double-sided) spectrum of the thermal force S_{FF}^{th} is obtained [121]:

$$S_{FF}^{\text{th}}(\Omega) = -\frac{2k_\text{B}T}{\Omega}\text{Im}\left(\chi_x(\Omega)^{-1}\right). \tag{2.2.11}$$

Generally in literature, frequency-independent (white) thermal noise is considered for mechanical oscillators, corresponding to a linear loss dispersion $\phi(\Omega) = Q^{-1}\Omega/\Omega_\text{m}$. In the further considerations throughout this chapter, this assumption is followed. Consequently, the susceptibility and the thermal force spectrum is given by,

$$\chi_x(\Omega) = \frac{1}{m_\text{eff}(\Omega_\text{m}^2 - \Omega^2 - i\Omega\Gamma_\text{m})}, \tag{2.2.12}$$

$$S_{FF}^{\text{th}} = 2m_\text{eff}\Gamma_\text{m}k_\text{B}T, \tag{2.2.13}$$

depending on the ambient temperature T, dissipation rate and effective mass. The associated displacement spectrum S_{xx}^{th} is then expressed as,

$$S_{xx}^{\text{th}}(\Omega) = \frac{2\Gamma_\text{m}k_\text{B}T}{m_\text{eff}\left[(\Omega_\text{m}^2 - \Omega^2)^2 + \Gamma_\text{m}^2\Omega^2\right]} = \frac{2n_\text{th}\hbar\Omega_\text{m}\Gamma_\text{m}}{m_\text{eff}\left[(\Omega_\text{m}^2 - \Omega^2)^2 + \Gamma_\text{m}^2\Omega^2\right]}, \tag{2.2.14}$$

with the thermal phonon occupation in the high-temperature limit $n_\text{th} = \frac{k_\text{B}T}{\hbar\Omega_\text{m}}$. This spectrum represents a Lorentzian peak around the resonance frequency Ω_m and full width at half maximum of Γ_m, as illustrated in fig. 2.6. For this model, values typical for experiments carried out in this thesis have been assumed, namely $\Omega_\text{m} = 2\pi \cdot 4\,\text{MHz}$, $\Gamma_\text{m} = 2\pi \cdot 10\,\text{Hz}$, $m_\text{eff} = 10\,\text{pg}$ and ambient conditions ($T = 295\,\text{K}$). At frequencies far below the mechanical resonance, the noise spectrum is frequency-independent, and at large frequencies it shows a Ω^{-4} scaling. The peak value of the thermal spectrum reaches $S_{xx}^{\text{th}}(\Omega_\text{m}) = 2k_\text{B}T/(m_\text{eff}\Omega_\text{m}^2\Gamma_\text{m})$. High displacement sensitivities in the readout (see section 2.4) can therefore be achieved through decreasing m_{eff} and Γ_{m}, which is equivalent to maximizing the $Q_{\mathrm{m}}/m_{\mathrm{eff}}$ ratio [122].

Integration of the displacement spectrum allows the calculation of the oscillator's energy. The equipartition theorem states that the stored displacement energy of a harmonic oscillator should amount to half of its thermal energy, specifically $\frac{1}{2}m_{\mathrm{eff}}\Omega_{\mathrm{m}}^2\left\langle x_{\mathrm{th}}^2\right\rangle = \frac{1}{2}k_{\mathrm{B}}T$. When calculating the root-mean-square of the thermal motion $\left\langle x_{\mathrm{th}}^2\right\rangle$ from eq. (2.2.14), it indeed confirms the equipartition theorem as it results in,

$$\left\langle x_{\mathrm{th}}^2\right\rangle = \int_{-\infty}^{\infty}\frac{\mathrm{d}\Omega}{2\pi}S_{xx}^{\mathrm{th}}(\Omega) = \frac{k_{\mathrm{B}}T}{m_{\mathrm{eff}}\Omega_{\mathrm{m}}^2}. \tag{2.2.15}$$

Note that the chosen factor of 2 in eq. (2.2.11) ensures that the entire energy is contained in the double-sided spectrum which explains the integration boundaries. In experiments, instruments only analyze the positive half of the frequency spectrum because the spectrum of a real-world signal is generally symmetrical around DC. Therefore, the measured quantity of the single-sided spectral density, S_a, follows from the symmetrized spectral density, $\bar{S}_{aa}$, as,

$$\bar{S}_{aa}(\Omega) = \frac{1}{2}\left(S_{aa}(+\Omega) + S_{aa}(-\Omega)\right), \tag{2.2.16}$$

$$S_a(\Omega) = 2\bar{S}_{aa}(\Omega), \tag{2.2.17}$$

and is only evaluated at positive frequencies.

2.2.2 Silicon nitride nanobeam mechanical oscillators

The frequency band of interest in an experiment is usually around the mechanical resonance frequency. One reason for operating a nanoscale oscillator becomes obvious when considering, that the mechanical susceptibility at resonance is proportional to the inverse of the effective mass, $\chi_x(\Omega_{\mathrm{m}}) = \frac{i}{m_{\mathrm{eff}}\Omega_{\mathrm{m}}\Gamma_{\mathrm{m}}}$. To increase the responsiveness to external forces, both the dissipation rate as well as the effective mass need to be decreased. An increase of the $Q_{\mathrm{m}}/m_{\mathrm{eff}}$ ratio also brings a second advantage into play, as it causes a reduction of the magnitude of the thermal force (eq. (2.2.13)). The thermal motion sets the sensitivity limit for transducer applications, as it cannot be distinguished from motion induced by another external force. In addition, as the resonance frequency scales with the dimension of the oscillator, a nanometer scale resonator means a high fundamental resonance frequency, resulting in lower phonon occupation at a given temperature which is advantageous for experiments in the quantum regime.

The canonical example of a nanoscale oscillator is the nanobeam. The mechanical quality factors of these beams are set by their intrinsic elasticity (which can be enhanced by high stress) and extrinsic factors such as the clamping conditions. The total motion of the beam is composed by a number of eigenmodes, each with a distinct resonance frequency and displacement profile, which are obtained by solving the characteristic elastic equations for a

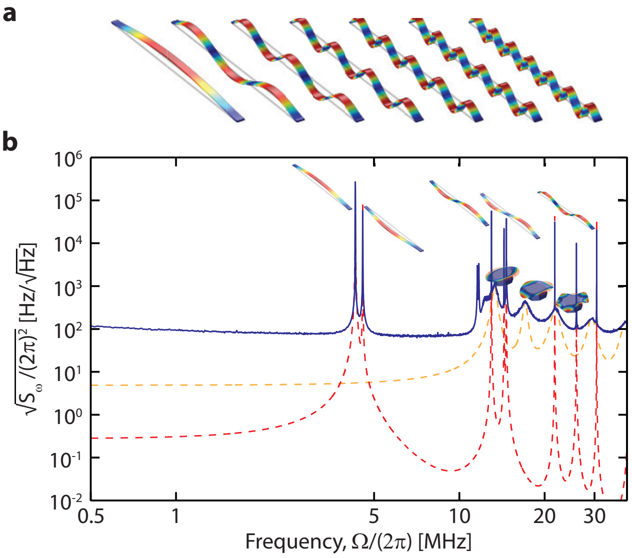

Figure 2.7 – **Mechanical eigenmodes of a nanobeam.** (a) Finite-element simulation results for a doubly-clamped nanobeam. Shown are the displacement profiles of the fundamental out-of-plane mode and the first six odd-numbered harmonics from left to right. The number of nodes for each harmonic increases by two. (b) Blue trace shows the measured frequency noise spectrum S_ω for a nanobeam (sample M2/CU/T/-1) showing the first three odd-ordered modes for in-plane and out-of-plane motion. The red dashed line is a fit based on FEM simulations. Also noticeable are the mechanical modes of the microdisk with their fit shown as the orange dashed line.

specific geometry. This can be done either analytically for simple geometries, or by simulation utilizing the finite-element method (FEM) for more complex architectures and designs. For a simple nanobeam geometry, the displacement profiles of the fundamental out-of-plane vibrational mode and its first six harmonics are shown as a FEM solution in fig. 2.7a, as these are the modes of interest in the experiments presented in this thesis. Figure 2.7b shows a measured noise spectrum of a nanobeam with typical dimensions. The emphasis lies on the fact that the spectrum around the fundamental mode, which is the mode of interest for the experiments conducted here, is extremely clean. The dimensions of the nanobeam samples are therefore carefully chosen to ensure large spectral separation between the individual modes, such that each can be modeled as a simple harmonic oscillator as discussed in the previous section[2].

Historically, the readout mechanisms of mechanical motion are mostly based on the electrical or magnetic properties of the nanomechanical oscillator, forging the field of nanoelectromechanical systems (NEMS) [117, 125]. Specific examples for readout mechanisms include magnetomotive readout [126], piezoresistive readout [127], readout via a single-electron transistor [114], and capacitative readout of a carbon nanotube [128]. While all of these techniques allow for reasonable readout sensitivities in the range of $\mathrm{fm}\cdot\mathrm{Hz}^{-1/2}$, the quality factors of the mechanical motion is generally limited to only $Q_\mathrm{m} \sim 10^4$ which can be explained by the fact that the choice of materials is limited due to the requirements of the readout mechanisms.

---

[2] Mechanical modes with small spectral separation have also been studied with the aim to demonstrate interference and avoided crossings [123, 124].

Also, often additional material needs to be deposited on a mechanical resonator to enable a specific readout in the first place.

To overcome the sensitivity limitations of these conventional readout mechanisms, a high-Q, low-mass oscillator is required that allows for efficient readout (and control) at room temperature. To this end, a doubly-clamped high-stress silicon nitride (Si_3N_4) nanobeam oscillator has been developed, combining an exceptionally high mechanical quality factor in excess of 10^6 at room temperature with a low mass in the picogram range [129, 130]. Since silicon nitride is a dielectric material, the readout in those experiments is realized interferometrically by focusing laser light onto the beam and monitoring its reflection. This method does not grant very high sensitivity (the dimension of the oscillators are typically below the diffraction limit), but laid the foundation for the field of cavity optomechanics which uses an optical cavity for enhanced-sensitivity readout of mechanical motion [25]. We adopt the high-stress silicon nitride nanobeam oscillator in our experiments as, besides the advantages already discussed, this geometry can be precisely positioned into the evanescent near-field of an optical microdisk whispering-gallery mode resonator, creating a high-sensitivity cavity optomechanical system. See chapter 3 for details about the integrated system and its fabrication process.

2.3 Cavity optomechanics

Combining an optical cavity with a mechanical degree of freedom defines the research field of cavity optomechanics [25, 28]. With the use of recirculating photons, the cavity provides a large enhancement in readout and control of the mechanical motion with exceptionally high sensitivity.

This section provides the formalism used to describe any cavity optomechanical system. The first part (section 2.3.1) presents a classical description, an illustrative way to understand the basic concepts of cavity optomechanics. This is followed by the quantum mechanical description in section 2.3.2 required to describe and understand quantum mechanical effects in optomechanical measurements.

Cavity optomechanics is most intuitive when considering the canonical optomechanical system illustrated in fig. 2.8a. It consists of a Fabry-Pérot cavity in which one of the end mirrors is suspended by a spring. The design relevant for this thesis is shown in fig. 2.8b and consists of a nanostring as the mechanical resonator in the near-field of an optical WGM microresonator. In both cases, the mechanical degree of freedom can be described by its one-dimensional position variable $x(t)$. Consequently, the resonance frequency of the optical cavity at a given time $\omega_c(t)$ depends linearly on the displacement of the mechanical oscillator and is given by the expression,

$$\omega_c(t) = \omega_c + Gx(t). \tag{2.3.1}$$

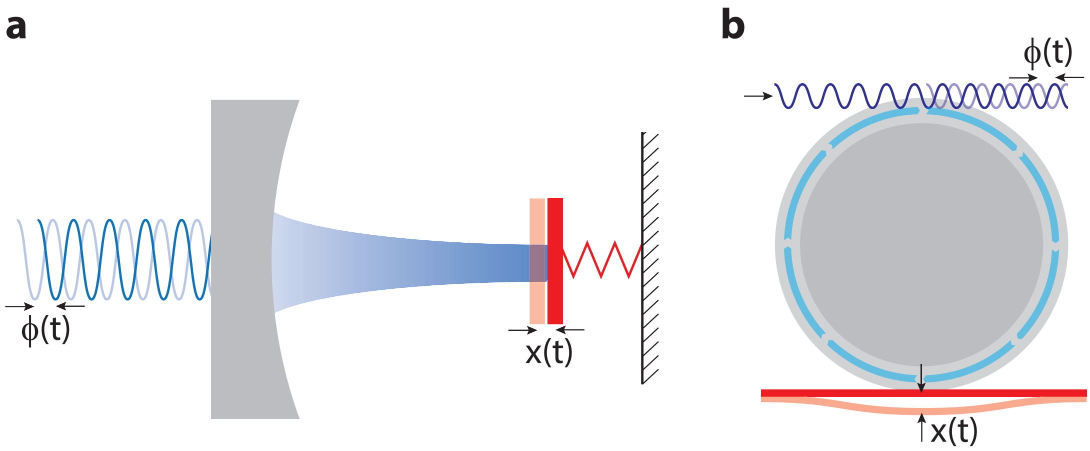

Figure 2.8 – **Principle of cavity optomechanics.** (a) Canonical optomechanical system: A Fabry-Pérot cavity with one of its end mirrors suspended by a spring and thus free to oscillate. (b) Architecture relevant to this thesis: The optical cavity is a WGM microresonator with a nanostring acting as the mechanical oscillator.

Here ω_c denotes the cavity resonance frequency for $x = 0$ and

$$G = \frac{\partial \omega_\mathrm{c}(t)}{\partial x} \tag{2.3.2}$$

is the optomechanical coupling parameter (also frequency pull parameter) describing optical frequency shift per displacement. For a Fabry-Pérot cavity, the coupling is given as, $G = -\omega_\mathrm{c}/L$.

2.3.1 Classical description

Effects of an oscillating mirror on an optical cavity

For now, disregarding any back-action effect of the light through radiation-pressure forces on the mechanical degree of freedom, the equation of motion for the cavity amplitude following eq. (2.1.10) becomes,

$$\frac{\mathrm{d}a}{\mathrm{d}t} = \left(-i\left(\omega_\mathrm{c} + Gx(t)\right) - \frac{\kappa}{2}\right) a(t) + \sqrt{\eta_\mathrm{c}\kappa}\,\bar{s}e^{-i\omega_\mathrm{L}t} \tag{2.3.3}$$

Assuming that the mechanical degree is moving with a sinusoidal oscillation with small amplitude x_0 and angular frequency Ω_m such that $x(t) = x_0 \sin(\Omega_\mathrm{m} t)$, the intracavity field

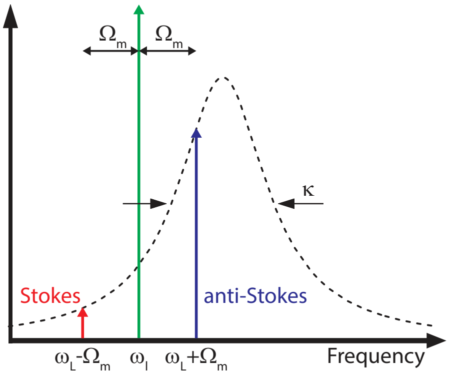

Figure 2.9 – **Optical cavity response:** Build-up of anti-Stokes and Stokes sidebands in a driven optical cavity at frequencies $\omega_\mathrm{L}+\Omega_\mathrm{m}$ and $\omega_\mathrm{L}-\Omega_\mathrm{m}$, weighted by the Lorentzian of the cavity.

amplitude can be approximated as [131],

$$\begin{aligned} a(t) &\approx a_0(t)+a_1(t)\\ a_0(t) &= \frac{\sqrt{\eta_\mathrm{c}\kappa}\,\bar{s}}{-i\Delta+\kappa/2}e^{-i\omega_\mathrm{L}t}\\ a_1(t) &= \frac{Gx_0}{2}\frac{\sqrt{\eta_\mathrm{c}\kappa}\,\bar{s}}{-i\Delta+\kappa/2}\left(\underbrace{\frac{e^{-i(\omega_\mathrm{L}+\Omega_\mathrm{m})t}}{-i(\Delta+\Omega_\mathrm{m})+\kappa/2}}_{\text{anti-Stokes}}-\underbrace{\frac{e^{-i(\omega_\mathrm{L}-\Omega_\mathrm{m})t}}{-i(\Delta-\Omega_\mathrm{m})+\kappa/2}}_{\text{Stokes}}\right). \end{aligned} \tag{2.3.4}$$

From the above expression it is obvious that the resulting mode amplitude consists of the contribution $a_0(t)$ due to the laser drive at frequency ω_L but also of a pair of sidebands $a_1(t)$ at frequencies $\omega_\mathrm{L}\pm\Omega_\mathrm{m}$. Consequently, the oscillating boundary can be understood as a modulator that builds up what is commonly referred to as the anti-Stokes and Stokes sidebands [28]. Depending on the detuning Δ and mechanical frequency Ω_m, their amplitude is weighted by the cavity Lorentzian, as illustrated in fig. 2.9.

Considering $|a(t)|^2$, it becomes evident that the presence of the sidebands correspond to a modulation of the intracavity stored energy. Specifically, the calculation yields

$$\begin{aligned} |a(t)|^2 \approx & |a_0(t)|^2+a_0(t)a_1^*(t)+a_0^*(t)a_1(t)\\ =&\frac{\eta_\mathrm{c}\kappa|\bar{s}|^2}{\Delta^2+(\kappa/2)^2}\Bigg(1+\\ & Gx_0\left(\frac{\Delta+\Omega_\mathrm{m}}{(\Delta+\Omega_\mathrm{m})^2+(\kappa/2)^2}+\frac{\Delta-\Omega_\mathrm{m}}{(\Delta-\Omega_\mathrm{m})^2+(\kappa/2)^2}\right)\sin(\Omega_\mathrm{m}t)+\\ & Gx_0\left(\frac{\kappa/2}{(\Delta+\Omega_\mathrm{m})^2+(\kappa/2)^2}-\frac{\kappa/2}{(\Delta-\Omega_\mathrm{m})^2+(\kappa/2)^2}\right)\cos(\Omega_\mathrm{m}t)\Bigg). \end{aligned} \tag{2.3.5}$$

and includes an in-phase ($\propto \sin(\Omega_\mathrm{m}t)$) as well as an out-of-phase quadrature ($\propto \cos(\Omega_\mathrm{m}t)$). In the above approximation, the term $|a_1(t)|^2$ has been neglected under the assumption that the amplitude x_0 is small.

Radiation-pressure back-action: static effect

To fully describe an optomechanical system, it is not sufficient to only consider the effects of the mechanical oscillation on the optical field. For a complete description, the mutual coupling between the optical and mechanical degrees of freedom has to be taken into account. The effect of the light on the moving cavity boundary is referred to as *back-action* and arises due to radiation pressure. For a movable mirror of a Fabry-Pérot cavity, the radiation-pressure force is a consequence of the momentum flips of the photons being reflected from the mirror surface and is given as,

$$F_{\mathrm{rp}}(t) = 2\hbar k \frac{|a(t)|^2}{\tau_{\mathrm{rt}}} = \hbar \frac{\omega_{\mathrm{c}}}{L} |a(t)|^2 = -\hbar G |a(t)|^2, \tag{2.3.6}$$

with the cavity round-trip time $\tau_{\mathrm{rt}} = \frac{2L}{c}$, $|a(t)|^2$ normalized to the photon number, and the photon momentum $\hbar k$ where $k = \frac{\omega_{\mathrm{c}}}{c}$. Therefore, $\hbar \frac{\omega_{\mathrm{c}}}{L} = \hbar G$ represents the radiation-pressure force exerted per photon. In general, optomechanical coupling can arise due to different mechanisms. One way is by direct momentum transfer, as described in this example and also observed in systems such as microtoroids [132]. Other methods are based on coupling via dispersive shift of the resonance frequency, as used in membrane-in-the-middle experiments [133] or levitating nanoparticles [134], or by near-field effects with a mechanical oscillator in the evanescent field of an optical cavity [135]. The latter concept is realized with the system described in chapter 3 which is used to achieve the main results of this thesis (see chapter 4). Note that the introduction of G in the last step in eq. (2.3.6) generalizes the expression for F_{rp} and thus makes it a valid statement for different types of optomechanical systems. The coupled equations of motion for describing the optomechanical system, assuming a viscous damping rate Γ_{m}, become (in a frame rotating by ω_{L}),

$$\dot{a}(t) = \left(i\,(\Delta - Gx(t)) - \frac{\kappa}{2}\right) a(t) + \sqrt{\eta_{\mathrm{c}}\kappa}\, s_{\mathrm{in}}(t) \tag{2.3.7}$$

$$\ddot{x}(t) + \Gamma_{\mathrm{m}} \dot{x}(t) + \Omega_{\mathrm{m}}^2 x(t) = -\hbar G \frac{|a(t)|^2}{m_{\mathrm{eff}}}, \tag{2.3.8}$$

where $|s_{\mathrm{in}}(t)|^2$ is normalized to denote the photon flux. For a constant drive with amplitude $s_{\mathrm{in}}(t) = \bar{s}$, stable solutions $a(t) = \bar{a}$ and $x(t) = \bar{x}$ can be found as a first step which read,

$$\bar{a} = \frac{1}{-i(\Delta - G\bar{x}) + \kappa/2} \sqrt{\eta_{\mathrm{c}}\kappa}\, \bar{s} \tag{2.3.9}$$

$$\bar{x} = -\frac{\hbar G |\bar{a}|^2}{m_{\mathrm{eff}} \Omega_{\mathrm{m}}^2}. \tag{2.3.10}$$

The solution $\bar{x}\left(|\bar{a}|^2\right)$ of these two expressions can be understood as a static displacement $\bar{x}$ mapped to an intracavity photon number $|\bar{a}|^2$. For sufficiently large optical input powers, multiple stable solutions are possible and a well-known bistable behavior arises which results in a hysteresis in the cavity transmission for swept detuning or variation in the input power [136].

Radiation-pressure back-action: dynamic phenomena

More interesting than the static consequences of the radiation pressure force is the dynamical response of an optomechanical system around its equilibrium. These fluctuations not only introduce new physics into the system, but also have a significant impact on the experiment, in particular the ultra-sensitive gravitational wave interferometers [18]. To dynamics of the system can be described by considering small fluctuations $\delta a(t)$ and $\delta x(t)$ around the equilibrium states $\bar{a}$ and $\bar{x}$ which are caused by a small applied force $\delta F(t)$ to the mechanical oscillator. Definition of the equilibrium detuning,

$$\bar{\Delta} \equiv \omega_{\mathrm{L}} - (\omega_{\mathrm{c}} + G\bar{x}), \tag{2.3.11}$$

and insertion of $a(t) = \bar{a} + \delta a(t)$ and $x(t) = \bar{x} + \delta x(t)$ into eqs. (2.3.7) and (2.3.8) together with the above definitions for $\bar{a}$ and $\bar{x}$ yield the linearized equations,

$$\delta \dot{a}(t) = \left(i\bar{\Delta} - \frac{\kappa}{2}\right)\delta a(t) - iG\bar{a}\delta x(t) \tag{2.3.12}$$

$$m_{\mathrm{eff}}\left(\delta\ddot{x}(t) + \Gamma_{\mathrm{m}}\delta\dot{x}(t) + \Omega_{\mathrm{m}}^2\delta x(t)\right) = -\hbar G\bar{a}\left(\delta a(t) + \delta a^*(t)\right) + \delta F(t). \tag{2.3.13}$$

To obtain these results, second-order terms $\propto \delta a(t)\delta x(t)$ and $\propto |\delta a(t)|^2$ are neglected as small perturbations $\delta(a,x) \ll (\bar{a},\bar{x})$ are assumed. In addition, $\bar{a}$ can be assumed as real without loss of generality, as this can always be achieved by adjustment of the phase of the incoming drive $\bar{s}$. These equations can be solved in a straightforward manner after performing a Fourier transformation. The results are given by,

$$-i\Omega\delta a(\Omega) = \left(+i\bar{\Delta} - \frac{\kappa}{2}\right)\delta a(\Omega) - iG\bar{a}\delta x(\Omega) \tag{2.3.14}$$

$$-i\Omega\delta a^*(\Omega) = \left(-i\bar{\Delta} - \frac{\kappa}{2}\right)\delta a^*(\Omega) + iG\bar{a}\delta x(\Omega) \tag{2.3.15}$$

$$m_{\mathrm{eff}}\left(-\Omega^2 - i\Gamma_{\mathrm{m}}\Omega + \Omega_{\mathrm{m}}^2\right)\delta x(\Omega) = -\hbar G\bar{a}\left(\delta a(\Omega) + \delta a^*(\Omega)\right) + \delta F(\Omega), \tag{2.3.16}$$

with the assumption that $\delta a^*(\Omega) = (\delta a(-\Omega))$. The first two equations again prove the presence of the induced anti-Stokes and Stokes sidebands for an oscillating displacement $\delta x(\Omega)$ at Fourier frequency Ω. Their amplitudes are given by,

$$\delta a(\Omega) = \frac{-iG\bar{a}}{-i(\bar{\Delta} + \Omega) + \kappa/2}\delta x(\Omega), \tag{2.3.17}$$

$$\delta a^*(\Omega) = \frac{+iG\bar{a}}{+i(\bar{\Delta} - \Omega) + \kappa/2}\delta x(\Omega). \tag{2.3.18}$$

As shown in eq. (2.3.5), in the presence of sidebands, the intracavity power oscillates with the frequency of the mechanical degree of freedom. Following the definition in eq. (2.3.6), the radiation pressure force $\delta F_{\mathrm{rp}}(\Omega)$ therefore likewise oscillates and is now expressed as,

$$\begin{aligned}\delta F_{\mathrm{rp}}(\Omega) &= -\hbar G\bar{a}\left(\delta a(\Omega)+\delta a^*(\Omega)\right)\\ &= -\hbar G^2\bar{a}^2\left(\frac{\bar{\Delta}+\Omega}{(\bar{\Delta}+\Omega)^2+(\kappa/2)^2}+\frac{\bar{\Delta}-\Omega}{(\bar{\Delta}-\Omega)^2+(\kappa/2)^2}\right)\delta x(\Omega)\\ &\quad + i\hbar G^2\bar{a}^2\left(\frac{\kappa/2}{(\bar{\Delta}+\Omega)^2+(\kappa/2)^2}-\frac{\kappa/2}{(\bar{\Delta}-\Omega)^2+(\kappa/2)^2}\right)\delta x(\Omega).\end{aligned} \tag{2.3.19}$$

The real and imaginary part in this representation of the radiation pressure force are caused by the in-phase and quadrature component of the modulated intracavity power. The presence of this force can cause a substantial change of the mechanical oscillator's dynamics, an effect that is referred to as the *dynamical back-action* (DBA). For example, blue-detuning leads to a ”stiffened" mechanical oscillator while a detuning on the red side of the resonance ”softens" it. The latter situation can be used to cool the thermal motion of the mechanics towards its ground state [72, 137]. The modified mechanical response to the external force is found by insertion of eq. (2.3.19) back into eq. (2.3.16) and eq. (2.2.6),

$$\delta x(\Omega) = \chi_{\mathrm{eff}}(\Omega)\delta F(\Omega). \tag{2.3.20}$$

In this expression, χ_{eff} denotes the effective mechanical susceptibility,

$$\chi_{\mathrm{eff}}^{-1}(\Omega) = m_{\mathrm{eff}}\left(\left(\Omega_{\mathrm{m}}^2+\frac{k_{\mathrm{dba}}(\Omega)}{m_{\mathrm{eff}}}\right)-\Omega^2-i\left(\Gamma_{\mathrm{m}}+\Gamma_{\mathrm{dba}}(\Omega)\right)\Omega\right), \tag{2.3.21}$$

where the DBA damping rate Γ_{dba} and spring constant k_{dba} are introduced as,

$$\Gamma_{\mathrm{dba}} = \frac{\hbar G^2\bar{a}^2}{m_{\mathrm{eff}}\Omega}\left(\frac{\kappa/2}{(\bar{\Delta}+\Omega)^2+(\kappa/2)^2}-\frac{\kappa/2}{(\bar{\Delta}-\Omega)^2+(\kappa/2)^2}\right), \tag{2.3.22}$$

$$k_{\mathrm{dba}} = \frac{\hbar G^2\bar{a}^2}{m_{\mathrm{eff}}}\left(\frac{\bar{\Delta}+\Omega}{(\bar{\Delta}+\Omega)^2+(\kappa/2)^2}+\frac{\bar{\Delta}-\Omega}{(\bar{\Delta}-\Omega)^2+(\kappa/2)^2}\right). \tag{2.3.23}$$

For small induced changes of the dynamics, the oscillator retains its damped harmonic behavior with an effective damping and resonance frequency given by [137],

$$\Gamma_{\mathrm{eff}} \approx \Gamma_{\mathrm{m}} + \frac{\hbar G^2\bar{a}^2}{m_{\mathrm{eff}}\Omega_{\mathrm{m}}}\left(\frac{\kappa/2}{(\bar{\Delta}+\Omega_{\mathrm{m}})^2+(\kappa/2)^2}-\frac{\kappa/2}{(\bar{\Delta}-\Omega_{\mathrm{m}})^2+(\kappa/2)^2}\right), \tag{2.3.24}$$

$$\Omega_{\mathrm{eff}} \approx \Omega_{\mathrm{m}} + \frac{\hbar G^2\bar{a}^2}{2m_{\mathrm{eff}}\Omega_{\mathrm{m}}}\left(\frac{\bar{\Delta}+\Omega_{\mathrm{m}}}{(\bar{\Delta}+\Omega_{\mathrm{m}})^2+(\kappa/2)^2}+\frac{\bar{\Delta}-\Omega_{\mathrm{m}}}{(\bar{\Delta}-\Omega_{\mathrm{m}})^2+(\kappa/2)^2}\right). \tag{2.3.25}$$

The change in resonance frequency due to dynamical back-action is referred to as the *optical spring* effect.

2.3.2 Quantum mechanical formulation

The quantum Langevin approach allows for the description of cavity optomechanics in a more general formalism than the simple classical formulation introduced above [106]. This formalism is especially powerful since it grants access to the quantum dynamics in an optomechanical system and provides the foundations to understand effects that are based on the quantum nature of light.

Optomechanical Hamiltonian

The first step towards a quantum mechanical description of a generic cavity optomechanical system is to obtain a Hamiltonian formulation by following the standard procedures of quantum mechanics [4, 138]. Accordingly, the first two contributions to the system Hamiltonian are the Hamiltonians of the optical cavity ($\hat{H}_{\mathrm{opt}}$) and mechanical oscillator ($\hat{H}_{\mathrm{mech}}$),

$$\hat{H}_{\mathrm{opt}} = \hbar\omega_{\mathrm{c}}\left(\hat{a}^{\dagger}\hat{a} + \frac{1}{2}\right) \tag{2.3.26}$$

$$\hat{H}_{\mathrm{mech}} = \frac{\hat{p}^2}{2m_{\mathrm{eff}}} + \frac{1}{2}m_{\mathrm{eff}}\Omega_{\mathrm{m}}^2\hat{x}^2. \tag{2.3.27}$$

Here, $\hat{a}^{\dagger}$ and $\hat{a}$ denote the creation and annihilation operators for the optical field while $\hat{x}$ and $\hat{p} = m_{\mathrm{eff}}\dot{\hat{x}}$ are the conjugated mechanical displacement and momentum operators. The occupation number operator of the optical mode in the system is defined as $\hat{n}_{\mathrm{c}} \equiv \hat{a}^{\dagger}\hat{a}$. The canonical commutation relation between the position and displacement operator of the mechanical mode, $\left[\hat{x}, \hat{p}\right] = i\hbar$, can be realized by defining the two operators $\hat{b}$ and $\hat{b}^{\dagger}$ for the quantized mechanical harmonic oscillator,

$$\hat{b} = \frac{1}{2}\left(\frac{\hat{x}}{\sqrt{\hbar/(2m_{\mathrm{eff}}\Omega_{\mathrm{m}})}} + i\frac{\hat{p}}{\sqrt{\hbar m_{\mathrm{eff}}\Omega_{\mathrm{m}}/2}}\right) \tag{2.3.28}$$

$$\hat{b}^{\dagger} = \frac{1}{2}\left(\frac{\hat{x}}{\sqrt{\hbar/(2m_{\mathrm{eff}}\Omega_{\mathrm{m}})}} - i\frac{\hat{p}}{\sqrt{\hbar m_{\mathrm{eff}}\Omega_{\mathrm{m}}/2}}\right). \tag{2.3.29}$$

With this, the free Hamiltonian of eq. (2.3.27) can be reformulated as,

$$\hat{H}_{\mathrm{mech}} = \hbar\Omega_{\mathrm{m}}\left(\hat{b}^{\dagger}\hat{b} + \frac{1}{2}\right), \tag{2.3.30}$$

where the additional $\frac{1}{2}$ arises from the commutation of $\hat{x}$ and $\hat{p}$ and describes the intrinsic vacuum fluctuations, analogous to the optical Hamiltonian. In equilibrium, the canonical thermal state is given by,

$$\hat{\rho}_{\mathrm{m}} = \frac{e^{-\beta\hat{H}_{\mathrm{mech}}}}{\mathrm{Tr}\left[e^{-\beta\hat{H}_{\mathrm{mech}}}\right]}, \tag{2.3.31}$$

with $\beta = (k_\mathrm{B} T)^{-1}$ and $\mathrm{Tr}\hat{\rho}_\mathrm{m} = 1$. The mean phonon occupation can then be obtained from,

$$n_\mathrm{th} := \mathrm{Tr}\left[\hat{b}^\dagger \hat{b} \hat{\rho}_\mathrm{m}\right] = \frac{1}{e^{\hbar\Omega_\mathrm{m}/(k_\mathrm{B}T)} - 1} \overset{k_\mathrm{B}T \gg \hbar\Omega_\mathrm{m}}{\approx} \frac{k_\mathrm{B}T}{\hbar\Omega_\mathrm{m}}. \tag{2.3.32}$$

where the approximation is referred to as the high-temperature limit.

Calculation of the variance in the oscillator position,

$$\mathrm{Var}\left[\hat{x}\right] = \mathrm{Tr}\left[\hat{x}^2 \hat{\rho}_\mathrm{m}\right] = (2n_\mathrm{th} + 1)x_\mathrm{ZPF}^2, \quad x_\mathrm{ZPF} := \sqrt{\frac{\hbar}{2m_\mathrm{eff}\Omega_\mathrm{m}}}, \tag{2.3.33}$$

reveals a contribution due to the zero-point fluctuations of magnitude x_ZPF.

The optomechanical interaction is attributed to the parametric coupling between the optical and mechanical modes, i.e. the resonance frequency of the cavity ω_c is modulated by the mechanical displacement x and is given by

$$\omega_\mathrm{c}(x) = \omega_\mathrm{c} + x\frac{\partial\omega_\mathrm{c}}{\partial x} + \ldots \tag{2.3.34}$$

For most experimental realizations, it is sufficient to only consider first-order terms and therefore define the optical frequency shift per displacement as the optomechanical coupling parameter $G = \frac{\partial\omega_\mathrm{c}}{\partial x}$. With this, an interaction Hamiltonian $\hat{H}_\mathrm{int}$ can be defined as,

$$\hat{H}_\mathrm{int} = \hbar G \hat{x} \hat{a}^\dagger \hat{a} = \hbar G x_\mathrm{ZPF} \hat{a}^\dagger \hat{a}\left(\hat{b} + \hat{b}^\dagger\right). \tag{2.3.35}$$

where $\hat{x} := x_\mathrm{ZPF}\left(\hat{b} + \hat{b}^\dagger\right)$ is the quantized displacement.

At this point it is useful to introduce the vacuum optomechanical coupling rate $g_0 = Gx_\mathrm{ZPF}$ characterizing the optical frequency shift for the displacement of a ground-state mechanical oscillator. This quantity allows for direct comparison of optomechanical systems, as often measurements relative to the vacuum fluctuations are of interest. Adding an external drive to the system expressed as

$$\hat{H}_\mathrm{drive} = i\hbar\sqrt{\eta_\mathrm{c}\kappa}\left(\bar{s}\hat{a}^\dagger e^{-i\omega_\mathrm{L}t} - \bar{s}^* \hat{a} e^{+i\omega_\mathrm{L}t}\right), \tag{2.3.36}$$

with the drive amplitude $\bar{s}$ normalized to the photon flux at input power P_in and drive frequency ω_L, such that $|\bar{s}|^2 = \frac{P_\mathrm{in}}{\hbar\omega_\mathrm{L}}$, the total Hamiltonian of a cavity optomechanical system can be expressed as,

$$\hat{H} = \hat{H}_\mathrm{opt} + \hat{H}_\mathrm{mech} + \hat{H}_\mathrm{int} + \hat{H}_\mathrm{drive} \tag{2.3.37}$$

$$= \hbar\omega_\mathrm{c}\left(\hat{a}^\dagger\hat{a} + \frac{1}{2}\right) + \hbar\Omega_\mathrm{m}\left(\hat{b}^\dagger\hat{b} + \frac{1}{2}\right) + \hbar g_0 \hat{a}^\dagger\hat{a}\left(\hat{b} + \hat{b}^\dagger\right) + i\hbar\sqrt{\eta_\mathrm{c}\kappa}\left(\bar{s}\hat{a}^\dagger e^{-i\omega_\mathrm{L}t} - \bar{s}^*\hat{a}e^{+i\omega_\mathrm{L}t}\right). \tag{2.3.38}$$

Note that often the zero-point energies $\frac{1}{2}\hbar\omega_\mathrm{c}$ and $\frac{1}{2}\hbar\Omega_\mathrm{c}$ in the optical and mechanical Hamiltonians are neglected as energy offsets often have no relevance to the dynamics.

The radiation pressure force $\hat{F}_{\mathrm{rp}}$ can be obtained from

$$\hat{F}_{\mathrm{rp}} = -\frac{\partial \hat{H}_{\mathrm{int}}}{\partial \hat{x}} = -\hbar G \hat{a}^{\dagger}\hat{a}. \tag{2.3.39}$$

Quantum Langevin equations

The time evolution of the individual operators can be derived from the Hamiltonian description. This leads to a set of quantum Langevin equations (QLEs) that also take into account mechanical and optical dissipation as well as the corresponding fluctuations [139]. The expressions are given by (in a frame rotating at ω_{L}),

$$\dot{\hat{a}} = \left(i\Delta - \frac{\kappa}{2}\right)\hat{a} - i g_0 \hat{a}(\hat{b} + \hat{b}^{\dagger}) + \sqrt{\kappa_{\mathrm{ex}}}\,(\bar{s}_{\mathrm{in}} + \delta\hat{s}_{\mathrm{in}}(t)) + \sqrt{\kappa_0}\,\delta\hat{s}_{\mathrm{vac}}(t), \tag{2.3.40}$$

$$\dot{\hat{x}} = \frac{\hat{p}}{m_{\mathrm{eff}}}, \tag{2.3.41}$$

$$\dot{\hat{p}} = -m_{\mathrm{eff}}\Omega_{\mathrm{m}}^2\hat{x} - \hbar G\hat{a}^{\dagger}\hat{a} - \Gamma_{\mathrm{m}}\hat{p} + \delta\hat{F}_{\mathrm{th}}(t), \tag{2.3.42}$$

with the noise terms $\delta\hat{s}_{\mathrm{in}}$, $\delta\hat{s}_{\mathrm{vac}}$ and $\delta\hat{F}_{\mathrm{th}}$. They fulfill the commutation relations [140],

$$\left[\delta\hat{s}_{\mathrm{in}}(t), \delta\hat{s}_{\mathrm{in}}^{\dagger}(t')\right] = \left[\delta\hat{s}_{\mathrm{vac}}(t), \delta\hat{s}_{\mathrm{vac}}^{\dagger}(t')\right] = \delta(t - t'), \tag{2.3.43}$$

and,

$$\left\langle \delta\hat{s}_{\mathrm{in}}(t)\delta\hat{s}_{\mathrm{in}}^{\dagger}(t')\right\rangle = \left\langle \delta\hat{s}_{\mathrm{vac}}(t)\delta\hat{s}_{\mathrm{vac}}^{\dagger}(t')\right\rangle = \delta(t - t') \tag{2.3.44}$$

as the only non-zero correlators. Here, $\delta\hat{s}_{\mathrm{in}}$ denotes vacuum noise entering the optical cavity through the pump port, while $\delta\hat{s}_{\mathrm{vac}}$ represents vacuum noise entering through the remaining loss channels, assuming no thermal excitation of the optical mode.

Similar as derived in the classical formalism, the QLEs are simplified in a first step by separating static and dynamic behavior. For this, the dynamics of the system are investigated by considering small fluctuations around the equilibrium positions by defining $\hat{a}(t) = \bar{a} + \delta\hat{a}(t)$ and $\hat{x}(t) = \bar{x} + \delta\hat{x}(t)$ with $\langle\delta\hat{a}(t)\rangle = \langle\delta\hat{x}(t)\rangle = 0$ and the steady-state solutions for the mode amplitude $\bar{a}$ and displacement $\bar{x}$. With this, the Heisenberg equations of motion for the fluctuations $\delta\hat{a}$, $\delta\hat{a}^{\dagger}$ and $\delta\hat{x}$ can be derived. Under the assumption of a strong coherent drive $\bar{a} \gg 1$, where the choice of the appropriate phase of $\bar{s}_{\mathrm{in}}$ ensures that $\bar{a}$ is positive and real, the linearized quantum Langevin equations can be derived by dropping terms $\propto \delta\hat{a}\delta\hat{x}, \delta\hat{a}^{\dagger}\delta\hat{x}$, or

$\delta\hat{a}^\dagger\delta\hat{a}$. They are then found as,

$$\frac{\mathrm{d}}{\mathrm{d}t}\delta\hat{a}(t) = \left(+i\bar{\Delta} - \frac{\kappa}{2}\right)\delta\hat{a}(t) - iG\bar{a}\delta\hat{x}(t) + \sqrt{\kappa_{\mathrm{ex}}}\delta\hat{s}_{\mathrm{in}} + \sqrt{\kappa_0}\delta\hat{s}_{\mathrm{vac}} \tag{2.3.45}$$

$$\frac{\mathrm{d}}{\mathrm{d}t}\delta\hat{a}^\dagger(t) = \left(-i\bar{\Delta} - \frac{\kappa}{2}\right)\delta\hat{a}^\dagger(t) + iG\bar{a}\delta\hat{x}(t) + \sqrt{\kappa_{\mathrm{ex}}}\delta\hat{s}_{\mathrm{in}}^\dagger + \sqrt{\kappa_0}\delta\hat{s}_{\mathrm{vac}}^\dagger \tag{2.3.46}$$

$$\frac{\mathrm{d}^2}{\mathrm{d}t^2}\delta\hat{x}(t) + \Gamma_{\mathrm{m}}\frac{\mathrm{d}}{\mathrm{d}t}\delta\hat{x}(t) + \Omega_{\mathrm{m}}^2\delta\hat{x}(t) = -\frac{\hbar G}{m_{\mathrm{eff}}}\bar{a}\left(\delta\hat{a}(t) + \delta\hat{a}^\dagger(t)\right) + \frac{\delta\hat{F}_{\mathrm{th}}(t)}{m_{\mathrm{eff}}}, \tag{2.3.47}$$

where the Hermitian property $\delta\hat{x}(t) = \delta\hat{x}^\dagger(t)$ was used. The solutions of these equations are again obtained by transformation to the Fourier domain and yield,

$$\left(-i(\bar{\Delta}+\Omega) + \frac{\kappa}{2}\right)\delta\hat{a}(\Omega) = -iG\bar{a}\delta\hat{x}(\Omega) + \sqrt{\kappa_{\mathrm{ex}}}\delta\hat{s}_{\mathrm{in}}(\Omega) + \sqrt{\kappa_0}\delta\hat{s}_{\mathrm{vac}}(\Omega) \tag{2.3.48}$$

$$\left(+i(\bar{\Delta}-\Omega) + \frac{\kappa}{2}\right)\delta\hat{a}^\dagger(\Omega) = +iG\bar{a}\delta\hat{x}(\Omega) + \sqrt{\kappa_{\mathrm{ex}}}\delta\hat{s}_{\mathrm{in}}^\dagger(\Omega) + \sqrt{\kappa_0}\delta\hat{s}_{\mathrm{vac}}^\dagger(\Omega) \tag{2.3.49}$$

$$m_{\mathrm{eff}}\left(\Omega_{\mathrm{m}}^2 - \Omega^2 - i\Gamma_{\mathrm{m}}\Omega\right)\delta\hat{x}(\Omega) = -\hbar G\bar{a}\left(\delta\hat{a}(\Omega) + \delta\hat{a}^\dagger(\Omega)\right) + \delta\hat{F}_{\mathrm{th}}(\Omega). \tag{2.3.50}$$

In the frequency domain, the only non-zero correlators are given as

$$\left\langle \delta\hat{s}_{\mathrm{in}}(\Omega)\delta\hat{s}_{\mathrm{in}}^\dagger(\Omega')\right\rangle = 2\pi\delta(\Omega-\Omega') \tag{2.3.51}$$

$$\left\langle \delta\hat{s}_{\mathrm{vac}}(\Omega)\delta\hat{s}_{\mathrm{vac}}^\dagger(\Omega')\right\rangle = 2\pi\delta(\Omega-\Omega') \tag{2.3.52}$$

$$\left\langle \delta\hat{F}_{\mathrm{th}}(\Omega)\delta\hat{F}_{\mathrm{th}}^\dagger(\Omega')\right\rangle = 2\pi\delta(\Omega-\Omega')\hbar m_{\mathrm{eff}}\Gamma_{\mathrm{m}}\Omega\left(\coth\left(\frac{\hbar\Omega}{2k_{\mathrm{B}}T}\right)+1\right). \tag{2.3.53}$$

The input-output relations for the fluctuations read

$$\delta\hat{s}_{\mathrm{out}}(\Omega) = \delta\hat{s}_{\mathrm{in}}(\Omega) - \sqrt{\eta_{\mathrm{c}}\kappa}\delta\hat{a}(\Omega) \tag{2.3.54}$$

$$\delta\hat{s}_{\mathrm{out}}^\dagger(\Omega) = \delta\hat{s}_{\mathrm{in}}^\dagger(\Omega) - \sqrt{\eta_{\mathrm{c}}\kappa}\delta\hat{a}^\dagger(\Omega), \tag{2.3.55}$$

which complete the formalism of the quantum Langevin equations that provides a powerful mean to understand relevant effects in cavity optomechanics.

Radiation-pressure cooling

One prominent example often investigated in optomechanics is the cavity-assisted sideband cooling of the mechanical motion. Under the assumption of the weak-coupling regime, $g \ll \kappa$, the effect of this radiation-pressure cooling can be described in the Raman picture via a perturbative approach in the linear approximation [25]. Here, $g = g_0\sqrt{n_{\mathrm{c}}}$ denotes the light-enhanced optomechanical coupling rate. As discussed earlier, photons that are red detuned from the cavity resonance will be preferentially anti-Stokes scattered (cf. fig. 2.9) and as a result undergo a blue-shift of Ω_{m}. This can be understood as the removal of one quantum of mechanical energy from the system. Assuming, these anti-Stokes processes occur at a rate A^-, the transition rate from the state of n to $n-1$ phonons is given by [72, 141],

$$\Gamma_{n\to n-1} = nA^-. \tag{2.3.56}$$

Accordingly, the suppressed Stokes scattered photons (at rate A^+) experience a red-shift and hence add a quantum of mechanical energy to the oscillator, with $\Gamma_{n\to n+1} = (n+1)A^+$. The net optomechanical damping rate can then be written as,

$$\Gamma_{\text{opt}} = A^- - A^+. \tag{2.3.57}$$

The change in the mean phonon occupation $\bar{n}$ follows from the rates $\Gamma_{n\to n\pm 1}$ and is calculated as,

$$\dot{\bar{n}} = (\bar{n}+1)(A^+ + A^+_{\text{th}}) - \bar{n}(A^- + A^-_{\text{th}}). \tag{2.3.58}$$

Here, also the coupling to the thermal bath at phonon occupation $\bar{n}_{\text{th}}$ is considered, occurring at rates $A^+_{\text{th}} = \bar{n}_{\text{th}}\Gamma_{\text{m}}$ and $A^-_{\text{th}} = (\bar{n}_{\text{th}}+1)\Gamma_{\text{m}}$. The resulting steady-state phonon occupation $\bar{n}_{\text{f}}$ is found from the above expression for $\dot{\bar{n}} = 0$:

$$\bar{n}_{\text{f}} = \frac{A^+ + \bar{n}_{\text{th}}\Gamma_{\text{m}}}{\Gamma_{\text{opt}} + \Gamma_{\text{m}}}. \tag{2.3.59}$$

In the absence of optomechanical coupling ($A^- = A^+ = 0$), the system thermalizes to the thermal environment as the steady-state solution becomes $\bar{n}_{\text{f}} = \bar{n}_{\text{th}}$. In the optimal case of no coupling to a thermal bath on the other hand ($\Gamma_{\text{m}} = 0$), the minimum achievable occupation number can be found as,

$$\bar{n}_{\text{min}} = \frac{A^+}{\Gamma_{\text{opt}}} = \frac{A^+}{A^- - A^+}. \tag{2.3.60}$$

The rates $A^\pm$ can be calculated from the known quantum noise spectrum of the force, $S_{FF}(\Omega)$ and are given by [142],

$$A^\pm = \frac{x^2_{\text{ZPF}}}{\hbar^2} S_{FF}(\Omega = \mp\Omega_{\text{m}}) = g_0^2 S_{NN}(\Omega = \mp\Omega_{\text{m}}), \tag{2.3.61}$$

where the photon number noise spectrum of a laser-driven cavity,

$$S_{NN}(\Omega) = n_{\text{c}} \frac{\kappa}{(\kappa/2)^2 + (\Delta+\Omega)^2}, \tag{2.3.62}$$

has been introduced [141]. Equations (2.3.57), (2.3.61) and (2.3.62) finally yield the expression for the optomechanical damping rate, reproducing the result of eq. (2.3.24). The minimum occupation number is then calculated as,

$$\bar{n}_{\text{min}} = \left(\frac{A^-}{A^+} - 1\right)^{-1} = \left(\frac{(\kappa/2)^2 + (\Delta - \Omega_{\text{m}})^2}{(\kappa/2)^2 + (\Delta + \Omega_{\text{m}})^2} - 1\right)^{-1}. \tag{2.3.63}$$

In the resolved sideband regime ($\Omega_{\text{m}} \gg \kappa$), this value is maximized at a detuning $\Delta = -\Omega_{\text{m}}$

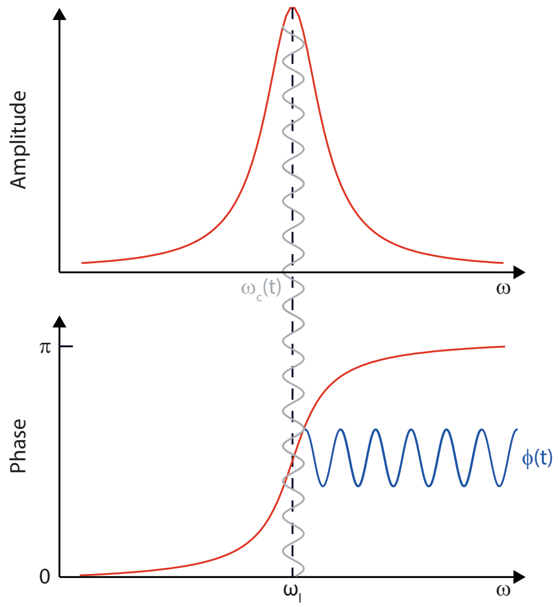

Figure 2.10 – **Cavity response in an optomechanical system:** The input field at frequency ω_L (black dashed line) acquires a phase shift depending on the mutual detuning between cavity resonance and laser. The oscillation of the mechanical degree of freedom $x(t)$ induces a modulation of the cavity resonance frequency $\omega_c(t)$ and phase $\phi(t)$ of the detected field s_{out}.

and becomes in this case,

$$\bar{n}_{\mathrm{min}} \approx \left(\frac{\kappa}{4\Omega_{\mathrm{m}}}\right)^2 < 1, \tag{2.3.64}$$

permitting ground-state cooling. In the for this thesis relevant case of the bad-cavity limit ($\Omega_{\mathrm{m}} \ll \kappa$), the minimal occupation at optimal detuning $\Delta = -\kappa/2$ becomes,

$$\bar{n}_{\mathrm{min}} \approx \frac{\kappa}{4\Omega_{\mathrm{m}}} \gg 1. \tag{2.3.65}$$

In general, the final occupation number (eq. (2.3.59)) in the presence of coupling to a thermal environment is given by,

$$\bar{n}_{\mathrm{f}} = \frac{\Gamma_{\mathrm{opt}}\bar{n}_{\mathrm{min}} + \Gamma_{\mathrm{m}}\bar{n}_{\mathrm{th}}}{\Gamma_{\mathrm{opt}} + \Gamma_{\mathrm{m}}}. \tag{2.3.66}$$

When operating blue detuned ($\Delta > 0$), the Stokes scattering process becomes dominant which results in an anti-damping $\Gamma_{\mathrm{opt}} < 0$ and the motion of the mechanical oscillator is hence amplified. When exceeding the threshold $\Gamma_{\mathrm{m}} + \Gamma_{\mathrm{opt}} = 0$, eventually the regime of optomechanical instability is reached [143].

2.4 Optomechanical readout of motion

Starting point for any cavity optomechanical experiment is the sensitive readout of the mechanical displacement fluctuations S_{xx} that have been introduced in section 2.2. The principle behind any such measurement is illustrated in fig. 2.10. Essentially, the motion of the oscillator causes the frequency of the cavity mode to shift, which changes the phase of the output light field corresponding to the motion of the oscillator. In particular, the phase noise spectral density is obtained by,

$$S_{\phi\phi} = \frac{1}{\Omega^2} S_{\omega\omega}(\Omega) = \frac{G^2}{\Omega^2} S_{xx}(\Omega), \tag{2.4.1}$$

which can be detected with standard detection techniques, such as the side-of-the-line method [144], the Pound-Drever-Hall technique [145–147] or a homodyne scheme [44]. Before describing the relevant detection schemes applied here (section 2.4.4), the fundamental limitations on displacement sensing are investigated in section 2.4.1, leading to the so-called standard quantum limit (SQL) (section 2.4.2). In addition, the influence of laser noise is discussed (section 2.4.3).

2.4.1 Quantum noise limitations in displacement sensing

The experimental results in this thesis were obtained by measurements with resonant probing ($\bar{\Delta} = 0$) where the dynamical properties of the mechanical oscillator are not affected by the measurement process, i.e. $\Gamma_{\text{dba}} = \Omega_{\text{dba}} = 0$. Because of this, extremely sensitive measurements of the mechanical mode can be achieved. To get an understanding about the fundamental quantum limits of such a displacement measurement, eqs. 2.3.48-2.3.55 are used to calculate the noise in the light field at the output of a system. This gives

$$\delta\hat{s}_{\text{out}}(\Omega) = \delta\hat{s}_{\text{in}}(\Omega) - \frac{\eta_c\kappa}{-i\Omega+\kappa/2}\left(-iG\bar{a}\delta\hat{x}(\Omega) + \sqrt{\kappa_{\text{ex}}}\delta\hat{s}_{\text{in}} + \sqrt{\kappa_0}\delta\hat{s}_{\text{vac}}\right) \tag{2.4.2}$$

$$\delta\hat{s}^\dagger_{\text{out}}(\Omega) = \delta\hat{s}_{\text{in}}(\Omega) - \frac{\eta_c\kappa}{+i\Omega+\kappa/2}\left(+iG\bar{a}\delta\hat{x}(\Omega) + \sqrt{\kappa_{\text{ex}}}\delta\hat{s}^\dagger_{\text{in}} + \sqrt{\kappa_0}\delta\hat{s}^\dagger_{\text{vac}}\right). \tag{2.4.3}$$

At this point, hermitian operators for the amplitude and phase quadratures may be introduced,

$$\delta\hat{q}_{\text{out}}(\Omega) := \frac{1}{\sqrt{2}}\left(\delta\hat{s}_{\text{out}}(\Omega) + \delta\hat{s}^\dagger_{\text{out}}(\Omega)\right) \tag{2.4.4}$$

$$\delta\hat{p}_{\text{out}}(\Omega) := \frac{1}{i\sqrt{2}}\left(\delta\hat{s}_{\text{out}}(\Omega) - \delta\hat{s}^\dagger_{\text{out}}(\Omega)\right). \tag{2.4.5}$$

The symmetrized (double-sided) spectral density of the phase quadrature can be found by,

$$\bar{S}^{\text{out}}_{pp}(\Omega) = \frac{1}{2}\left(S^{\text{out}}_{pp}(+\Omega) + S^{\text{out}}_{pp}(-\Omega)\right), \tag{2.4.6}$$

and

$$\left\langle \delta\hat{p}_{\text{out}}(\Omega)\delta\hat{p}^\dagger_{\text{out}}(\Omega')\right\rangle = 2\pi\delta(\Omega-\Omega')S^{\text{out}}_{pp}(\Omega), \tag{2.4.7}$$

and is given as,

$$\bar{S}^{\text{out}}_{pp}(\Omega) = 1 + \frac{4\bar{a}^2G^2\eta_c\kappa}{\Omega^2+(\kappa/2)^2}\bar{S}_{xx}(\Omega), \tag{2.4.8}$$

by application of the correlators defined earlier. It contains information about the displacement spectrum $\bar{S}_{xx}$ on top of a background which is here normalized to 1. This background term originates from the quantum fluctuations of the probing light and is referred to as the *measurement imprecision*. Its spectral density expressed as displacement noise is hence given as,

$$\bar{S}_{xx}^{\mathrm{imp}}(\Omega) = \frac{\Omega^2 + (\kappa/2)^2}{4\bar{a}^2 G^2 \eta_{\mathrm{c}} \kappa} = \frac{\kappa}{16 n_{\mathrm{c}} G^2 \eta_{\mathrm{c}}} \left(1 + 4\frac{\Omega^2}{\kappa^2}\right), \tag{2.4.9}$$

where quantum noise as the only noise source was assumed and the previously introduced normalization of the squared mode amplitude to the intracavity photon number $n_{\mathrm{c}} = \bar{a}^2$ was used. This imprecision represents an apparent displacement noise and hence defines the smallest possible displacement $\delta x_{\mathrm{min}}(\Omega)$ that can be measured in an experiment. Specifically,

$$\delta x_{\mathrm{min}}(\Omega) = \sqrt{\Delta f \bar{S}_{xx}^{\mathrm{imp}}(\Omega)} = \sqrt{\Delta f \frac{\kappa}{16 n_{\mathrm{c}} G^2 \eta_{\mathrm{c}}} \left(1 + 4\frac{\Omega^2}{\kappa^2}\right)}. \tag{2.4.10}$$

Here, Δf represents the measurement bandwidth. An important remark is that no assumption regarding the detection method was made here. In principle this minimum displacement can be achieved in any measurement scheme as long as it is quantum limited.

2.4.2 Standard quantum limit

As evident from eq. (2.4.9), by performing a stronger measurement with a larger photon number n_{c}, the imprecision decreases leading to an increased sensitivity. However, this comes at the cost of an increased measurement back-action as any measurement of a mechanical oscillator's position produces a disturbance on its momentum [21]. In an optomechanical system, the measurement back-action is induced by the radiation-pressure force [22]. Following eq. (2.3.13), it takes the form,

$$\delta \hat{F}_{\mathrm{rp}}(\Omega) = -\hbar G \bar{a} \left(\delta \hat{a}(\Omega) + \delta \hat{a}^\dagger(\Omega)\right), \tag{2.4.11}$$

from which we can obtain the spectral density of the back-action noise force,

$$\bar{S}_{FF}^{\mathrm{ba}}(\Omega) = \frac{\bar{a}^2 G^2 \kappa \hbar^2}{\Omega^2 + (\kappa/2)^2} = \frac{4\hbar^2 n_{\mathrm{c}} G^2}{\kappa} \left(1 + 4\frac{\Omega^2}{\kappa^2}\right)^{-1}. \tag{2.4.12}$$

In case of pure quantum noise, as assumed again in above expression, the force noise is referred to as *quantum back-action* (QBA) or *radiation-pressure shot noise* (RPSN). Together, the imprecision and back-action noise spectra from eqs. (2.4.9) and (2.4.12) fulfill a fundamental quantum mechanical inequality derived from Heisenberg's uncertainty principle [21, 142]. The imprecision-back-action product reads,

$$\bar{S}_{xx}^{\mathrm{imp}}(\Omega) \bar{S}_{FF}^{\mathrm{ba}}(\Omega) = \frac{\hbar^2}{4\eta_{\mathrm{c}}} \geq \frac{\hbar^2}{4}, \tag{2.4.13}$$

where the equality is fulfilled for a strongly overcoupled cavity with $\kappa = \kappa_0 + \kappa_{\mathrm{ex}} \approx \kappa_{\mathrm{ex}}$. The total displacement noise at the detector is composed of intrinsic thermal fluctuations, imprecision noise and noise induced by the back-action force mediated by the mechanical susceptibility χ_x,

$$\bar{S}^{\mathrm{tot}}_{xx}(\Omega) = \bar{S}^{\mathrm{th}}_{xx}(\Omega) + \bar{S}^{\mathrm{imp}}_{xx}(\Omega) + \bar{S}^{\mathrm{ba}}_{FF}(\Omega)|\chi_x(\Omega)|^2. \tag{2.4.14}$$

Defining the sum of the last two terms as the added noise and making it a function of the measurement strength,

$$\bar{S}^{\mathrm{add}}_{xx}(\Omega, n_{\mathrm{c}}) = \bar{S}^{\mathrm{imp}}_{xx}(\Omega, n_{\mathrm{c}}) + \bar{S}^{\mathrm{ba}}_{FF}(\Omega, n_{\mathrm{c}})|\chi_x(\Omega)|^2 = \frac{\kappa}{16 n_{\mathrm{c}} G^2 \eta_{\mathrm{c}}}\left(1 + 4\frac{\Omega^2}{\kappa^2}\right) + \frac{4\hbar^2 n_{\mathrm{c}} G^2}{\kappa}\left(1 + 4\frac{\Omega^2}{\kappa^2}\right)^{-1}, \tag{2.4.15}$$

from eq. (2.4.13) it becomes evident that in a measurement a trade-off between imprecision and measurement back-action has to be made in order to achieve the optimal sensitivity. Considering a measurement at the mechanical resonance frequency, the optimal power for a minimum displacement uncertainty is given as,

$$P^{\mathrm{SQL}}_{\mathrm{in}} = \hbar\omega_{\mathrm{c}}\Gamma_{\mathrm{m}}\frac{\kappa^2}{64 g_0^2 \eta_{\mathrm{c}}^{3/2}}\left(1 + 4\frac{\Omega_{\mathrm{m}}^2}{\kappa^2}\right), \tag{2.4.16}$$

which defines the *standard quantum limit* (SQL). Into the above expression, the mechanical susceptibility on mechanical resonance $\chi_x(\Omega_{\mathrm{m}})$ (eq. (2.2.7)) and the intracavity photon number for zero detuning $n_{\mathrm{c}}(\Delta = 0) = \frac{4}{\kappa}\frac{P_{\mathrm{in}}}{\hbar\omega_{\mathrm{c}}}$ (eq. (2.1.14)) were inserted. Figure 2.11a illustrates the contributions from eq. (2.4.14) to the total noise spectrum while fig. 2.11b shows the noise sources as a function of measurement power. For this, the spectra are normalized to two times the zero-point displacement spectrum $2S^{\mathrm{ZPF}}_{xx} = \frac{4x^2_{\mathrm{ZPF}}}{\Gamma_{\mathrm{m}}}$, using eq. (2.2.14), such that $\frac{S^{\mathrm{th}}_{xx}}{2S^{\mathrm{ZPF}}_{xx}} = n_{\mathrm{th}}$. In this normalization, it is obvious that any measurement will add at least half a quantum of noise which equals the zero-point motion. This results in a total phonon-equivalent noise at the detector output of 1 quanta for optimal detection and a ground-state mechanical oscillator. At the SQL, both the imprecision and back-action contribute equally to the added noise, however only the latter causes a physical heating of the oscillator by a temperature corresponding to a quarter quantum.

To estimate the impact of quantum back-action in an experiment, the ratio of it to the thermal force noise can be found from eqs. (2.2.13) and (2.4.12) to be,

$$\frac{\bar{S}^{\mathrm{ba}}_{FF}(\Omega_{\mathrm{m}})}{S^{\mathrm{th}}_{FF}} = \frac{2\hbar n_{\mathrm{c}} G^2}{m_{\mathrm{eff}} n_{\mathrm{th}} \kappa \Gamma_{\mathrm{m}} \Omega_{\mathrm{m}}}\frac{1}{1 + 4\Omega_{\mathrm{m}}^2/\kappa^2} \approx C_0 \frac{n_{\mathrm{c}}}{n_{\mathrm{th}}}. \tag{2.4.17}$$

Here, the single-photon cooperativity $C_0 = \frac{4g_0^2}{\kappa\Gamma_{\mathrm{m}}}$ was introduced, an important figure of merit characterizing the coupling strength between photons and phonons in a cavity optomechanical system. The term $(1 + 4\Omega_{\mathrm{m}}^2/\kappa^2)^{-1}$ can be understood as an additional efficiency factor attributed to the cavity acting as a low-pass filter due to the limited bandwidth. For operation deep in the bad-cavity limit ($\Omega_{\mathrm{m}} \ll \kappa$), the aforementioned factor equals unity and is there-

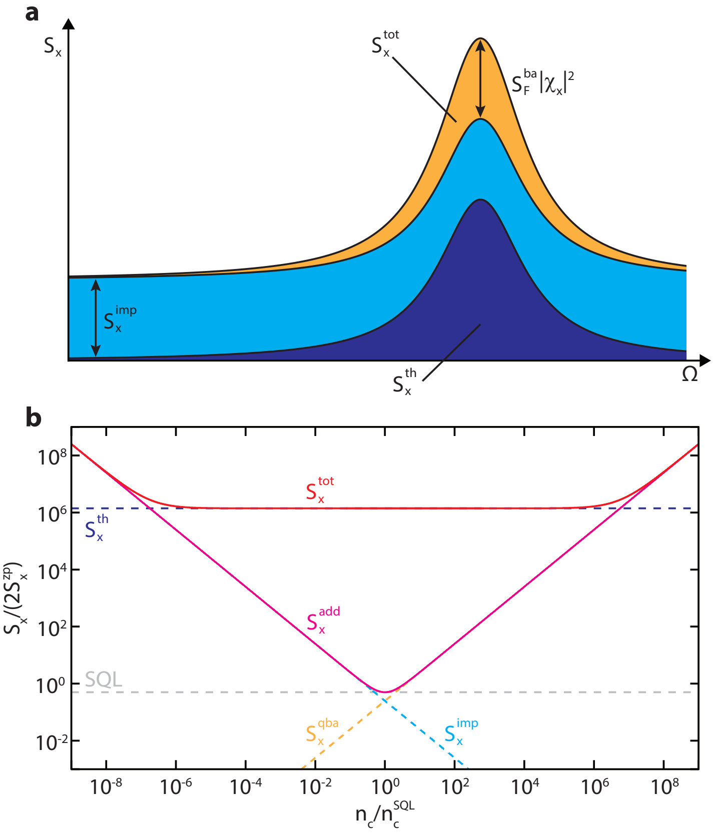

Figure 2.11 – **Quantum noise contributions and the SQL:** (a) The total measured noise is the sum of the intrinsic fluctuations of the mechanical oscillator S_x^{th}, the measurement imprecision S_x^{imp} and the heating due to the quantum back-action $S_F^{\mathrm{ba}}|\chi_x|^2$. (b) The added quantum noise at detection (magenta trace) versus input power, normalized to that at the SQL. At low powers, the measurement is dominated by imprecision noise (light blue dashed trace), while the back-action heating increases with measurement strength and dominates at powers above the SQL (orange dashed trace). The dark blue dashed trace shows the intrinsic thermal motion for an oscillator in a thermal state. In this case, the total noise is given as the red trace.

fore neglected in the last equality. With this, the imprecision and back-action noise can be expressed in terms of phonon-equivalent quantities,

$$n_{\mathrm{imp}} = \frac{1}{16\eta_{\mathrm{c}} C_0 n_{\mathrm{c}}} \tag{2.4.18}$$

$$n_{\mathrm{qba}} = C_0 n_{\mathrm{c}}, \tag{2.4.19}$$

with the imprecision-back-action product taking the form,

$$n_{\mathrm{imp}}\left(n_{\mathrm{qba}} + n_{\mathrm{th}}\right) \geq n_{\mathrm{imp}} n_{\mathrm{qba}} = \frac{1}{16\eta_{\mathrm{c}}} \geq \frac{1}{16}. \tag{2.4.20}$$

From the equation above, it becomes evident that in order to achieve such a quantum-limited measurement, two requirements must be met. First, a quantum-limited meter in a strongly overcoupled cavity is required, such that $n_{\mathrm{imp}} n_{\mathrm{qba}} \rightarrow 1/16$ is achieved. Due to the nature of the optical field performing this measurement, this condition can be assumed to be fulfilled. Secondly, a large ratio $n_{\mathrm{qba}}/n_{\mathrm{th}}$ is required, demanding that the mechanical oscillator is predominantly coupled to the meter rather than to the thermal reservoir.

In actual experiments, the observation of the effects of quantum back-action remained an elusive goal for a long time. The first successful demonstration was achieved in cold-atom experiments [56, 148] and in a membrane-in-the-middle setup at cryogenic temperatures [74]. The main result of this thesis is the observation of radiation-pressure shot noise effects on a mechanical oscillator under room temperature conditions (see chapter 4). To this end, we developed an optomechanical device with single-photon cooperativity approaching unity and the capability of supporting a large photon number without reaching instabilities (see chapter 3).

2.4.3 Laser noise

An optomechanical system is usually probed using a resonant laser at frequency $\omega_{\mathrm{L}} = \omega_{\mathrm{c}}$. Following eq. (2.3.40), the photon flux amplitude operator is assumed to be given by,

$$\hat{s}_{\mathrm{in}}(t) = e^{-i\omega_{\mathrm{L}} t} \left(\bar{s}_{\mathrm{in}} + \delta\hat{s}_{\mathrm{in}}(t)\right), \tag{2.4.21}$$

with the normalization $\bar{s}_{\mathrm{in}} = \sqrt{\frac{P_{\mathrm{in}}}{\hbar\omega_{\mathrm{L}}}}$. The commutator of these fluctuations satisfies [149],

$$\left[\delta\hat{s}_{\mathrm{in}}(t), \delta\hat{s}_{\mathrm{in}}^{\dagger}(t')\right] = \delta(t-t'). \tag{2.4.22}$$

At this point, hermitian quadrature operators for amplitude and phase of these fluctuations can be introduced as,

$$\delta\hat{q}_{\mathrm{in}}(t) \equiv \frac{1}{\sqrt{2}}\left(\delta\hat{s}_{\mathrm{in}}(t) + \delta\hat{s}_{\mathrm{in}}^{\dagger}(t)\right) \tag{2.4.23}$$

$$\delta\hat{p}_{\mathrm{in}}(t) \equiv \frac{1}{i\sqrt{2}}\left(\delta\hat{s}_{\mathrm{in}}(t) - \delta\hat{s}_{\mathrm{in}}^{\dagger}(t)\right), \tag{2.4.24}$$

such that,

$$\left[\delta\hat{q}_{\mathrm{in}}(t), \delta\hat{p}_{\mathrm{in}}(t')\right] = \frac{i}{2}\delta(t-t'). \tag{2.4.25}$$

With this, eq. (2.4.21) takes the form,

$$\hat{s}_{\mathrm{in}}(t) = e^{-i\omega_{\mathrm{L}} t}\left(\bar{s}_{\mathrm{in}} + \frac{\delta\hat{q}_{\mathrm{in}}(t)}{\sqrt{2}} + i\frac{\delta\hat{p}_{\mathrm{in}}(t)}{\sqrt{2}}\right). \tag{2.4.26}$$

Under real conditions, $\delta\hat{s}_{\mathrm{in}}(t)$ (and equivalently $\delta\hat{q}_{\mathrm{in}}(t)$, $\delta\hat{p}_{\mathrm{in}}(t)$) may contain classical fluctuations in addition to the intrinsic vacuum. This classical noise, e.g. excess noise in the laser, can be arbitrarily distributed among the quadratures. The detection techniques applied in this thesis (section 2.4.4) allow for the measurement of an arbitrary quadrature of the optical field.

However, because of the large coherent amplitude of the light states, the two-time correlators of the quadratures contain already almost all of the information carried by the state. Therefore, the focus is limited to [150],

$$\begin{pmatrix} S_{qq}(t) & S_{qp}(t) \\ S_{pq}(t) & S_{pp}(t) \end{pmatrix} := \begin{pmatrix} \left\langle \delta \hat{q}_{\text{in}}(t) \delta \hat{q}_{\text{in}}(0) \right\rangle & \left\langle \delta \hat{q}_{\text{in}}(t) \delta \hat{p}_{\text{in}}(0) \right\rangle \\ \left\langle \delta \hat{p}_{\text{in}}(t) \delta \hat{q}_{\text{in}}(0) \right\rangle & \left\langle \delta \hat{p}_{\text{in}}(t) \delta \hat{q}_{\text{in}}(0) \right\rangle \end{pmatrix}, \tag{2.4.27}$$

with real S_{qq} and S_{pp} due to the hermitian property of the quadratures. Here, the contributions that are purely due to quantum mechanical origin can be separated out from these correlators. From eq. (2.4.25) follows,

$$S_{qp}(t) - S_{pq}(t) = i\delta(t), \tag{2.4.28}$$

which can be satisfied by the appropriate choices for S_{qp} and S_{pq},

$$S_{qp}(t) = +\frac{i}{2}\delta(t) + C_{qp}(t), \tag{2.4.29}$$

$$S_{pq}(t) = -\frac{i}{2}\delta(t) + C_{qp}(t), \tag{2.4.30}$$

with $C_{qp}(t) = \bar{S}_{qp}(t)$, following from the calculation of the symmetrized correlation. Analogously, the coherent state has the property $S_{qq}(t) = S_{pp}(t) = \frac{1}{2}\delta(t)$, and a similar separation of the quantum mechanical contribution can be found as,

$$S_{qq}(t) = \frac{1}{2}\delta(t) + C_{qq}(t), \tag{2.4.31}$$

$$S_{pp}(t) = \frac{1}{2}\delta(t) + C_{pp}(t). \tag{2.4.32}$$

Equation (2.4.27) hence becomes,

$$\begin{pmatrix} \left\langle \delta \hat{q}_{\text{in}}(t) \delta \hat{q}_{\text{in}}(0) \right\rangle & \left\langle \delta \hat{q}_{\text{in}}(t) \delta \hat{p}_{\text{in}}(0) \right\rangle \\ \left\langle \delta \hat{p}_{\text{in}}(t) \delta \hat{q}_{\text{in}}(0) \right\rangle & \left\langle \delta \hat{p}_{\text{in}}(t) \delta \hat{q}_{\text{in}}(0) \right\rangle \end{pmatrix} = \begin{pmatrix} \frac{1}{2} & \frac{i}{2} \\ -\frac{i}{2} & \frac{1}{2} \end{pmatrix} \delta(t) + \begin{pmatrix} C_{qq}(t) & C_{qp}(t) \\ C_{pq}(t) & C_{pp}(t) \end{pmatrix}. \tag{2.4.33}$$

With this, the symmetrized correlations are found as,

$$\bar{S}_{qq}(\Omega) = \frac{1}{2} + C_{qq}(\Omega), \tag{2.4.34}$$

$$\bar{S}_{pp}(\Omega) = \frac{1}{2} + C_{pp}(\Omega), \tag{2.4.35}$$

$$\bar{S}_{qp}(\Omega) = C_{qp}(\Omega). \tag{2.4.36}$$

2.4.4 Photodetection of noise spectra

As the measurements presented here are carried out in the optical domain ($\omega_{\text{L}} \sim 2\pi \frac{c}{780\,\text{nm}} \sim 2\pi \cdot 380$ THz), this subsection will detail the principles of photodetection and the relevant detection techniques.

The optical detection of the outcoupled light is realized by guiding the output field, described by its amplitude flux $\hat{s}_{\text{out}}$, onto a detector that performs a linear measurement on the amplitude quadrature of the incident field. Following the principles of the photoelectric effect, the absorbed photons are subsequently converted into electrons with a quantum efficiency $\eta \leq 1$. Typical detectors at these wavelengths are based on a silicon (Si) diode and possess an efficiency of $\eta \sim 0.8$. This imperfection in detecting an optical signal can be interpreted as an additional loss channel that is described by the injection of the light into a beam splitter with transmissivity η followed by a flawless detector receiving the transmitted field $\hat{a}_\eta(t)$ [151],

$$\hat{a}_\eta(t) = \sqrt{\eta}\hat{s}_{\text{out}} + i\sqrt{1-\eta}\delta\hat{s}_{\text{vac}}(t). \tag{2.4.37}$$

Here, the incident light on the detector is composed of part of the outcoupled light from the optomechanical system $\hat{s}_{\text{out}} = (\bar{s} + \delta\hat{s}(t))e^{-i\omega_{\text{L}}t}$ as defined earlier, and vacuum noise $\delta\hat{s}_{\text{vac}}$ entering the beam splitter from its second input. The photocurrent operator of the detector can be defined as,

$$\hat{I}(t) = q_e\hat{a}^\dagger_\eta(t)\hat{a}_\eta(t) \equiv q_e\hat{n}_\eta(t), \tag{2.4.38}$$

with the electron charge q_e and the photon flux,

$$\hat{n}_\eta(t) = \hat{a}^\dagger_\eta(t)\hat{a}_\eta(t) \approx \eta|\bar{s}|^2 + \sqrt{2}\eta|\bar{s}|\delta\hat{q}(t) + \sqrt{2\eta(1-\eta)}|\bar{s}|\delta\hat{p}_0, \tag{2.4.39}$$

where the approximation indicates the omission of second-order terms in fluctuation, and $\delta\hat{q}$ and $\delta\hat{p}_0$ denote the signal amplitude and vacuum phase quadrature fluctuations. From the above expression, the mean of the photon flux as well as its fluctuations can be derived as,

$$\langle\hat{n}_\eta(t)\rangle = \eta|\bar{s}|^2 \tag{2.4.40}$$

$$\delta\hat{n}_\eta(t) = \hat{n}_\eta(t) - \langle\hat{n}_\eta(t)\rangle = \sqrt{2}\eta|\bar{s}|\delta\hat{q}(t) + \sqrt{2\eta(1-\eta)}|\bar{s}|\delta\hat{p}_0. \tag{2.4.41}$$

Since the photocurrent is the actual observable in photodetection, with eq. (2.4.38) its mean and the fluctuations due to the incident field are found as,

$$\langle\hat{I}(t)\rangle = q_e\langle\hat{n}_\eta(t)\rangle = q_e\eta|\bar{s}|^2 = \eta RP \tag{2.4.42}$$

$$\delta\hat{I}(t) = q_e\delta\hat{n}_\eta(t) = \sqrt{2}q_e|\bar{s}|\left(\eta\delta\hat{q}(t) + \sqrt{\eta(1-\eta)}\delta\hat{p}_0\right), \tag{2.4.43}$$

where the responsivity of the detector $R = \frac{q_e}{\hbar\omega_{\text{L}}}$ and the incident power $P = \hbar\omega_{\text{L}}|\bar{s}|^2$ were introduced. The symmetrized (double-sided) corresponding photocurrent spectrum is obtained from the photocurrent fluctuations as,

$$\bar{S}_{II}(\Omega) = 2q_e^2|\bar{s}|^2\left(\eta^2\bar{S}_{qq}(\Omega) + \eta(1-\eta)\bar{S}^0_{pp}(\Omega)\right). \tag{2.4.44}$$

For a quantum-noise limited measurement, following eqs. (2.4.4) and (2.4.5), any detection of the amplitude quadrature will be composed of the signal and a contribution due to vacuum fluctuations, leading to $\delta\hat{q}(t) = \delta\hat{q}_{\mathrm{sig}}(t) + \delta\hat{q}_{\mathrm{vac}}(t)$, which can in general be assumed not to be correlated. Under these conditions, $\bar{S}_{qq}(\Omega) = \bar{S}_{qq}(\Omega)^{\mathrm{sig}} + \bar{S}^{\mathrm{vac}}_{qq}(\Omega)$ and $\bar{S}^{\mathrm{vac}}_{qq}(\Omega) = \bar{S}^{0}_{pp}(\Omega) = \frac{1}{2}$ with the resulting single-sided photocurrent spectrum,

$$S_I(\Omega) = 2\eta q_e^2 |\bar{s}|^2 \left(\eta S_q^{\mathrm{sig}}(\Omega) + 1\right). \tag{2.4.45}$$

Here, the single-sided spectrum is used since photodiodes convert negative to positive frequencies such that $S_a(\Omega) = 2\bar{S}_{aa}(\Omega)$ for $\Omega > 0$. The constant background in this expression is caused by the amplified vacuum fluctuations and is referred to as the shot noise,

$$S_I^{\mathrm{shot}}(\Omega) = 2\eta q_e^2 |\bar{s}|^2 = 2q_e \left\langle \hat{I}(t) \right\rangle = 2q_e \eta R P. \tag{2.4.46}$$

The signal-to-noise ratio of a measurement is hence determined by the detection efficiency η.

In reality, the measured photocurrent is subject to one additional noise source – the thermal noise in the electronics of the detector. This is commonly characterized by the noise-equivalent power (NEP) spectrum $S_P^{\mathrm{NE}}(\Omega)$ in the specifications of the photodetector. Converting this to a photocurrent spectrum using the responsivity,

$$S_I^{\mathrm{det}}(\Omega) = R^2 S_P^{\mathrm{NE}}(\Omega), \tag{2.4.47}$$

results in the expression of the total detected photocurrent (eqs. (2.4.45) to (2.4.47)),

$$S_I(\Omega) = \underbrace{R^2 S_P^{\mathrm{NE}}(\Omega)}_{S_I^{\mathrm{det}}} + \underbrace{2q_e \eta R P}_{S_I^{\mathrm{shot}}} + \underbrace{2q_e \eta^2 R P S_q^{\mathrm{sig}}(\Omega)}_{S_I^{\mathrm{sig}}}. \tag{2.4.48}$$

To overcome the detector noise, the measurement has to be performed with sufficient optical power such that the detector noise is dominated by shot noise, specifically,

$$S_I^{\mathrm{shot}} \geq S_I^{\mathrm{det}} \Leftrightarrow P \geq \frac{R}{2q_e \eta} S_P^{\mathrm{NE}}(\Omega). \tag{2.4.49}$$

Once the detector noise is overwhelmed by shot noise, the maximum possible signal-to-noise ratio for a given optical power is achieved. Beyond this, the SNR scales with $\sqrt{P}$ up to the saturation of the detector. Figure 2.12 shows a measurement of a spectrum consisting of the electronic noise S_I^{det} (grey trace), the added shot noise S_I^{shot} (blue trace) and the total signal due to a mechanical resonance S_I^{sig} (red trace).

Side-of-line detection

As mentioned in the introduction of this section, the aim is to measure the phase fluctuations imparted by the motion of the mechanical oscillator. Applying the method of direct detection by simply directing the outcoupled light onto a photodiode, only amplitude fluctuations of the light field, i.e. the amplitude quadrature fluctuations $\delta\hat{q}$, can be detected, as the

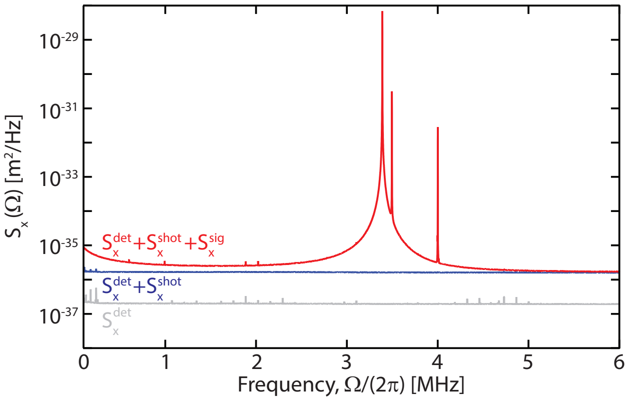

Figure 2.12 – **Example of a detected spectrum:** The total measured signal (red trace) consists of the detector noise S_x^{det} (gray trace), the shot noise S_x^{shot} (blue trace) and the actual signal due to a mechanical resonance S_x^{sig}. The measurement was taken with sample AE/L2/B2/34.

induced photocurrent carries no phase information. Therefore, it becomes obvious that a measurement at the cavity resonance is in this scheme impossible for two reasons: (1) at cavity resonance, the slope of the transmission dip is zero (see fig. 2.10) such that the small frequency fluctuations caused by the mechanical motion cause almost no amplitude modulation. (2) Measurements are often carried out close to the critically coupled regime ($\eta_c \sim 0.5$) as mentioned in section 2.1.3, resulting in almost zero transmission at the output.

One way to circumvent these two problems at once is to operate detuned from the cavity resonance where the cavity can convert the frequency fluctuations to an amplitude modulation of the outcoupled light. In practice, a detuning of $\Delta = \kappa/2$ is chosen where the slope of the cavity is the largest. This technique is the so-called *side-of-line* detection. This technique however has the significant disadvantage of changing the mechanical susceptibility due to dynamical back-action effects (see section 2.3.1), especially at optical powers necessary to overcome the detector noise for a shot-noise limited measurement as discussed above. Typically, the required powers range from around 100 μW for a trans-impedance amplified silicon photodiodes to as low as a few microwatts for an avalanche photodiode (APD). APDs however possess the caveat that they already saturate at very low powers.

In this work, the side-of-line method is used to characterize the optomechanical devices, i.e. accessing the intrinsic optical and mechanical linewidth as well as the optomechanical coupling rate. To this end, we work in the far undercoupled regime at very low optical powers of only a few nW to avoid any back-action and use an APD for detection (see chapter 3).

For the reasons discussed above, most experiments in cavity optomechanics utilize interferometric readout schemes as they allow a phase-sensitive measurement at the optical resonance where dynamic back-action is completely suppressed. This in turn allows for higher optical powers to be used such that the shot noise limit can be easily reached. Now, the scheme used in this work, balanced homodyne detection, will be detailed.

Balanced homodyne spectroscopy

The balanced homodyne technique [152] was used to achieve the main results of this thesis. This method allows for shot-noise limited operation on resonance ($\Delta = 0$) where dynamic back-action effects are absent (see section 2.3.1). Another important difference is that with a homodyne interferometer, an arbitrary superposition of amplitude and phase quadrature can be measured by an appropriate choice of the phase angle θ:

$$\delta \hat{q}^{\theta}(t) := \delta \hat{q}(t) \cos\theta + \delta \hat{p}(t) \sin\theta = \frac{1}{\sqrt{2}} \left(\delta \hat{a}(t) e^{-i\theta} + \delta \hat{a}^{\dagger}(t) e^{i\theta} \right). \tag{2.4.50}$$

The principle of the homodyne scheme is illustrated in fig. 2.13. The signal field $\hat{a}_{\mathrm{sig}}$ in question is superimposed with a local oscillator (LO) field $\hat{a}_{\mathrm{LO}}$ on a beam splitter (ideally balanced with transmissivity $\eta_{\mathrm{t}} = 0.5$) such that the transverse mode profiles in each output arm of the interferometer overlap. The output fields $\hat{a}_{\pm}$ of the beam splitter are then given by [151],

$$\hat{a}_{+} = \sqrt{\eta_{\mathrm{t}}}\, \hat{a}_{\mathrm{sig}} + i \sqrt{1-\eta_{\mathrm{t}}}\, \hat{a}_{\mathrm{LO}} \tag{2.4.51}$$

$$\hat{a}_{-} = i \sqrt{1-\eta_{\mathrm{t}}}\, \hat{a}_{\mathrm{sig}} + \sqrt{\eta_{\mathrm{t}}}\, \hat{a}_{\mathrm{LO}}, \tag{2.4.52}$$

and are each directed into independent but identical photodiodes inducing the respective photocurrents $\hat{I}_{\pm}(t) = q_e \hat{a}^{\dagger}_{\pm}(t) \hat{a}_{\pm}(t)$ that are then subtracted from each other to obtain the homodyne signal,

$$\begin{aligned} \hat{I}_{\mathrm{hom}}(t) = \hat{I}_{+}(t) - \hat{I}_{-}(t) = & q_e \left(1 - 2\eta_{\mathrm{t}}\right) \left(\hat{n}_{\mathrm{LO}}(t) - \hat{n}_{\mathrm{sig}}(t)\right) \\ & + 2 i q_e \sqrt{\eta_{\mathrm{t}}(1-\eta_{\mathrm{t}})} \left(\hat{a}^{\dagger}_{\mathrm{sig}}(t) \hat{a}_{\mathrm{LO}}(t) - \hat{a}^{\dagger}_{\mathrm{LO}}(t) \hat{a}_{\mathrm{sig}}(t) \right), \end{aligned} \tag{2.4.53}$$

with the signal (LO) photon flux $\hat{n}_{\mathrm{sig(LO)}}(t) = \hat{a}^{\dagger}_{\mathrm{sig(LO)}}(t) \hat{a}_{\mathrm{sig(LO)}}(t)$. If the signal and LO fields are both coherent, their amplitudes can be expressed as,

$$\hat{a}_{\mathrm{sig(LO)}} = \left(\sqrt{\langle \hat{n}_{\mathrm{sig(LO)}} \rangle} + \delta \hat{a}_{\mathrm{sig(LO)}}(t) \right) e^{-i(\omega_{\mathrm{L}} t + \theta_{\mathrm{sig(LO)}})}, \tag{2.4.54}$$

with the mean amplitude expressed in terms of the mean photon flux $\sqrt{\langle \hat{n}_{\mathrm{sig(LO)}} \rangle}$. The quantity $\theta_{\mathrm{sig(LO)}}$ denotes the phase of the signal (LO) field. With this, the mean value of the homodyne photocurrent can be approximated as,

$$\langle \hat{I}_{\mathrm{hom}}(t) \rangle \approx q_e \left(1 - 2\eta_{\mathrm{t}}\right) \left(\langle \hat{n}_{\mathrm{(LO)}} \rangle - \langle \hat{n}_{\mathrm{(sig)}} \rangle \right) - 4 q_e \sqrt{\eta_{\mathrm{t}} \left(1 - \eta_{\mathrm{t}}\right)} \sqrt{\langle \hat{n}_{\mathrm{(LO)}} \rangle \langle \hat{n}_{\mathrm{(sig)}} \rangle} \sin\theta_{\mathrm{hom}}, \tag{2.4.55}$$

while the fluctuations take the form,

$$\begin{aligned} \delta \hat{I}_{\mathrm{hom}}(t) \approx & q_e \left(1 - 2\eta_{\mathrm{t}}\right) \left(\sqrt{2 \langle \hat{n}_{\mathrm{(LO)}} \rangle} \delta \hat{q}^{0}_{\mathrm{LO}} - \sqrt{2 \langle \hat{n}_{\mathrm{(sig)}} \rangle} \delta \hat{q}^{0}_{\mathrm{sig}} \right) \\ & - q_e \sqrt{2\eta_{\mathrm{t}} \left(1 - \eta_{\mathrm{t}}\right)} \left(\sqrt{2 \langle \hat{n}_{\mathrm{(LO)}} \rangle} \delta \hat{q}^{\theta_{\mathrm{hom}} + \pi/2}_{\mathrm{sig}} - \sqrt{2 \langle \hat{n}_{\mathrm{(sig)}} \rangle} \delta \hat{q}^{-\theta_{\mathrm{hom}} - \pi/2}_{\mathrm{LO}} \right), \end{aligned} \tag{2.4.56}$$

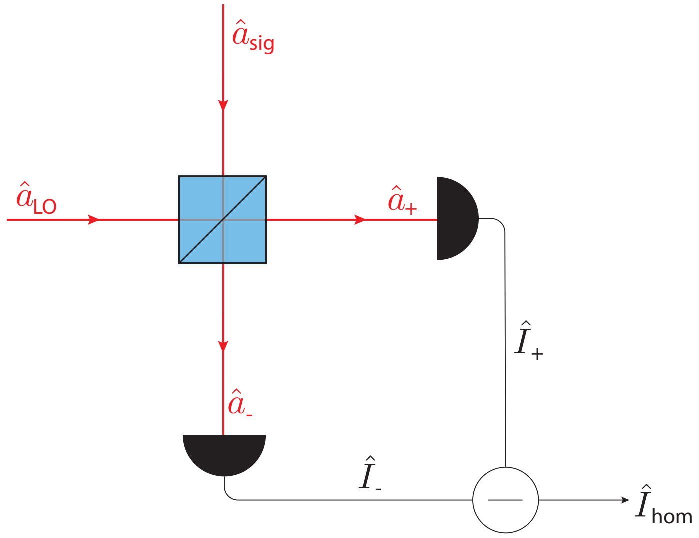

Figure 2.13 – **Homodyne detection principle:** At a beam splitter, the signal beam is combined with a local oscillator from the same laser source such that the output beams are both spatially overlapped. Both outputs are then sent to independent but identical photodiodes where the induced photocurrents are subtracted from each other. For details, refer to the text.

with the mean phase difference between signal and LO fields $\theta_{\text{hom}} := \theta_{\text{sig}} - \theta_{\text{LO}}$ at the beam splitter. Second-order fluctuation terms were omitted. The expression for the fluctuations can be interpreted as the homodyne measuring a combination of the signal and LO quadratures $\delta\hat{q}_{\text{sig(LO)}}^{\pm\theta_{\text{hom}}\mp\pi/2}$ at different angles. In order to isolate the signal quadrature in a measurement, a homodyne interferometer is usually operated with a very strong local oscillator compared to the signal beam ($\langle\hat{n}_{\text{(LO)}}\rangle \gg \langle\hat{n}_{\text{(sig)}}\rangle$) in addition to an ideal beam splitter ($\eta_{\text{t}} = \frac{1}{2}$). According to the first term in eq. (2.4.56), the latter has the additional advantage of canceling out any classical noise present in the strong LO [153]. Under these conditions, eqs. (2.4.55) and (2.4.56) simplify to,

$$\langle\hat{I}_{\text{hom}}(t)\rangle \approx -q_e\sqrt{\langle\hat{n}_{\text{(LO)}}\rangle\langle\hat{n}_{\text{(sig)}}\rangle}\sin\theta_{\text{hom}} \tag{2.4.57}$$

$$\delta\hat{I}_{\text{hom}}(t) \approx q_e\sqrt{2\langle\hat{n}_{\text{(LO)}}\rangle}\delta\hat{q}_{\text{sig}}^{\theta_{\text{hom}}+\pi/2}(t), \tag{2.4.58}$$

such that the fluctuating part of the detected photocurrent renders a linear measurement of purely the signal quadrature $\delta\hat{q}_{\text{sig}}^{\theta_{\text{hom}}+\pi/2}(t)$.

The total detected photocurrent consists, similarly to eq. (2.4.48), of the three contributions,

$$S_I^{\text{hom}}(\Omega) = \underbrace{R^2 S_P^{\text{NE}}(\Omega)}_{S_I^{\text{hom,det}}} + \underbrace{2q_e\eta R P_{\text{LO}}}_{S_I^{\text{hom,shot}}} + \underbrace{2q_e\eta^2 R P_{\text{LO}} S_{q_{\theta_{\text{hom}}+\pi/2}}^{\text{sig}}(\Omega)}_{S_I^{\text{hom,sig}}}. \tag{2.4.59}$$

In contrast to direct detection methods where only the amplitude quadrature can be detected, homodyne interferometers usually operate at the phase quadrature where $\theta_{\text{hom}} = 0$ where the measurement record can be interpreted as a measurement of the phase fluctuations between the signal and the local oscillator, as the relation between phase quadrature and phase fluctuations is given as $\delta\hat{p} = \sqrt{2\langle\hat{n}\rangle}\delta\hat{\phi}$ [142]. Operating with a strong LO such that the measurement is shot-noise limited and therefore omitting the detector noise contribution, the photocurrent now takes the form,

$$S_I^{\text{hom}}(\Omega)\Big|_{\theta_{\text{hom}}=0} = 2q_e\eta R P_{\text{LO}} + 4\eta^2 R^2 P_{\text{sig}} P_{\text{LO}} S_\phi^{\text{sig}}(\Omega) = 4\eta^2 R^2 P_{\text{sig}} P_{\text{LO}} \left(S_\phi^{\text{sig}}(\Omega) + \frac{q_e}{2\eta R P_{\text{sig}}} \right), \tag{2.4.60}$$

where again the constant background defines the shot noise level and can be taken as the measurement imprecision of the homodyne detected signal,

$$S_\phi^{\text{hom,imp}}(\Omega) = \frac{1}{2\eta}\frac{\hbar\omega_{\text{L}}}{P_{\text{sig}}}. \tag{2.4.61}$$

Note that once the LO shot noise overwhelms the detector noise, the signal-to-noise ratio is again maximized and weakly dependent of a further increase in P_{LO}.

For the main experimental results in this work, the technique of variational measurements [79] was applied in which homodyne spectra $S_I^\theta(\Omega)$ are acquired for a sweep of the quadrature angle through the amplitude quadrature (see chapter 4). An additional section about the experimental details and challenges in the setup and operation of a homodyne interferometer can be found in appendix D.

3 High-cooperativity near-field optomechanical transducer

A particularly promising platform for optomechanical transduction, as described in the previous chapter, turns out to be a (dielectric) mechanical substrate placed next to the surface of a WGM microcavity, so that it samples its evanescent field. Since the evanescent decay length is $\sim \lambda/10$, this topology offers the opportunity for strong gradient force coupling to nanoscale mechanical devices. It also has the virtue of naturally accommodating optical and mechanical substrates of dissimilar material and geometry, enabling separate optimization of $Q/(\text{mode volume})$. Moreover, WGMs can be input/output coupled with high ideality using tapered optical fibers [154], making them well-suited to interferometric displacement sensing. Recent work has focused on coupling of nanobeams [135], -cantilevers [155], and -membranes [156] to the evanescence of WGM microtoroids [135], -spheres [156, 157], and -disks [155, 158], with mechanical materials ranging from (ultra low loss) high-stress Si_3N_4 [135] to (ultra low mass) single-layer graphene [156], typically using SiO_2 as the optical material. Gradient force coupling as high as $G \sim 2\pi \cdot 100$ MHz/nm has been achieved [135]. Combined with the high power handling capacity of SiO_2 and low extraneous displacement noise (typically thermorefractive noise (TRN) in the cavity substrate [159]), optimized systems have achieved room temperature displacement imprecisions as low as $10^{-16}\,\mathrm{m}/\sqrt{\mathrm{Hz}}$, sufficient to in principle resolve the zero-point motion in several cases [135, 159].

Despite these advances, the full potential of evanescent cavity optomechanics has been inhibited by the difficulty of positioning the nanomechanical element within $\lambda/10 \sim 100$ nm of the cavity substrate. Early systems made use of nanopositioning stages and suffered from vibrational instability [135]. In a first version of the here presented architecture, this challenge was addressed by integrating a Si_3N_4 nanobeam and a SiO_2 microdisk on a chip; however, due to fabrication constraints, the beam-disk separation was limited to 250 nm and the optical Q was reduced by a factor of 10 [158].

This chapter presents a novel device design that features the integration of a high-stress Si_3N_4 thin film resonator and a SiO_2 microdisk cavity *within the evanescent near-field*, without deteriorating the intrinsic Q of either element [160]. Responsible for the vast improvement in performance of the optomechanical system hereby is a refined fabrication process that allows the suspension of a nanobeam as little as 25 nm above a SiO_2 microdisk – a factor of three smaller than the evanescent decay length of its WGMs – while maintaining mechanical and optical mode qualities in excess of 10^5 and 10^6, respectively. The chapter covers the design of the device (section 3.1), an outline of the fabrication process (section 3.2), a description of characterization measurements (section 3.3), and a demonstration of the exceptionally high displacement sensitivity (section 3.4), the key ingredient for the main results of this thesis that are discussed in chapter 4.

3.1 Device design

The following section presents a description of the design of the optomechanical system used in the experiments. To begin with, the first two subsections detail the design and properties of the mechanical oscillator (section 3.1.1) and the optical cavity (section 3.1.2), before the final part combines them to explain the optomechanical coupling between the two elements (section 3.1.3).

3.1.1 Nanomechanical beam

The mechanical oscillator in our optomechanical system is a silicon nitride (SI_3N_4) doubly-clamped nanobeam. It is released from a high-stress (~ 1 GPa) thin film as this grants an exceptionally high Q/m ratio for the string-like flexural modes. Typical beams used in our experiments have dimensions $\{\text{length}\,(l), \text{width}\,(w), \text{thickness}\,(t)\} \sim \{60, 0.5, 0.05\}\ \mu$m, leading to an effective mass, $m \sim 10$ pg. The frequency of the fundamental mechanical mode is about $\Omega_m \sim 2\pi \cdot 4$ MHz with a quality factor, $Q_m > 10^5$. This exceptionally high value can be mainly attributed to two effects; the first is the realization of a large impedance mismatch from the anchoring body which reduces extrinsic losses at the clamping points [161]. The second origin of the high quality factor is the so-called *stress-related dilution* of intrinsic loss, an effect first discussed in the context of pendulum supports for the mirrors in gravitational wave interferometers [162]. Here, the high tensile stress leads to an increase of the stored elastic energy inside the material without altering its loss tangent [129, 163, 164].

From the standpoint of quantum-limited measurements, an important consequence of the high Q/m ratio is that high-stress nanobeams exhibit large zero-point fluctuations. Expressed as a single-sided spectral density evaluated at the mechanical frequency, the above parameters correspond to a peak zero-point displacement noise density of $S_x^{\mathrm{zp}}(\Omega_\mathrm{m}) = 2\hbar Q_\mathrm{m}/m\Omega_m^2 \sim 10\ \mathrm{fm}/\sqrt{\mathrm{Hz}}$. This value occurs in a radio frequency window, 1-10 MHz, where low noise electronics and laser sources are readily available. As such, nanobeams were the first solid-state mechanical resonators to be electrically [165] and optically [159] read out with an imprecision lower than $S_x^{\mathrm{zp}}(\Omega_\mathrm{m})$.

Figure 3.1 shows measurements of quality factors and $Q \times$ frequency products for odd-ordered, out-of-plane flexural modes of a typical nanobeam with dimensions $\{l, w, t\} = \{60, 0.6, 0.05\}\ \mu$m.

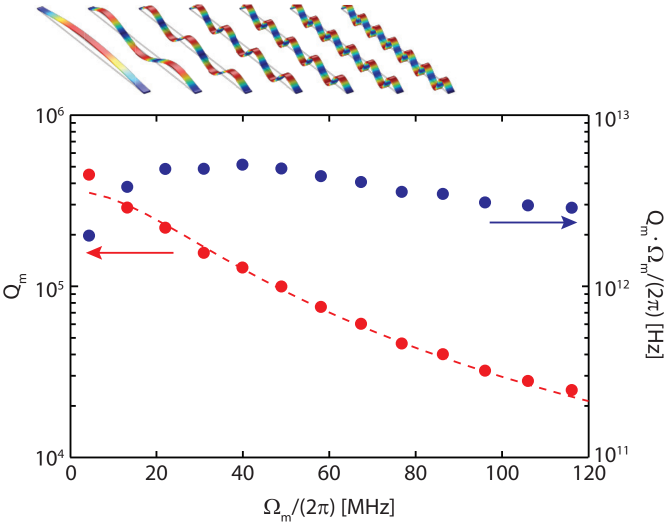

Figure 3.1 – **Measurement of odd-ordered, out-of-plane flexural modes of a nanobeam.** Measured Q-factors (red) and $Q \cdot$ frequency products (blue) of a nanobeam with dimensions $\{l, w, t\} = \{60, 0.6, 0.05\}$ μm (sample M2/CU/T/+1) are plotted versus the mode frequency. The dashed red curve is a fit to the Q-dilution model in [164], implying a limiting contribution from surface-related intrinsic loss. Above the plot is an FEM simulation illustrating the first seven measured beam modes.

The achieved values go as high as $4 \cdot 10^{12}$ for the $Q \times f$ products and are on par with the state-of-the-art for high-stress Si_3N_4 nanobeams of similar dimensions [164, 166]. From the near-linear eigenfrequency spectrum $\Omega_m^{(n)} \approx 2\pi n \cdot 4.3$ MHz, we can access the tensile stress of $\sigma \approx (\rho l \Omega_m^{(0)}/\pi)^2 \approx 800$ MPa of our film, assuming a density of $\rho = 2700$ kg/m^3 [129]. The mechanical-Q spectrum is consistent with the intrinsic loss model of [163, 164],

$$Q_\mathrm{m}^{(n)} = \frac{Q_\mathrm{int}}{\lambda + n^2\pi^2\lambda^2}, \tag{3.1.1}$$

and is fit using $Q_\mathrm{m}^{(n)} \approx 3.6 \cdot 10^5/(1 + 0.023 \cdot n^2)$ (dashed red line in fig. 3.1). Here, $\lambda = \frac{t}{l}\sqrt{E/(12\sigma)}$, E is the elastic modulus of the film, and Q_int is the intrinsic quality factor of the film when unstressed. The inferred value of $Q_\mathrm{int} \approx 6700$ (using $E = 200$ GPa), is roughly an order of magnitude lower than that for bulk Si_3N_4. Interpreted as surface loss, however, the inferred coefficient of $Q_\mathrm{int}/t \approx 1.1 \cdot 10^5$ μm^{-1} is within a factor of two of the typical value for LPCVD SiN thin films [164].

In addition to its favorable mechanical properties when stressed, Si_3N_4 is an attractive optical material. It has a relatively large index of refraction, $n \approx 2$, and, owing to its ~ 3 eV bandgap, respectably low optical absorption at near infrared wavelengths, characterized by an imaginary index of $n_\mathrm{im} \sim 10^{-5} - 10^{-6}$ [167].

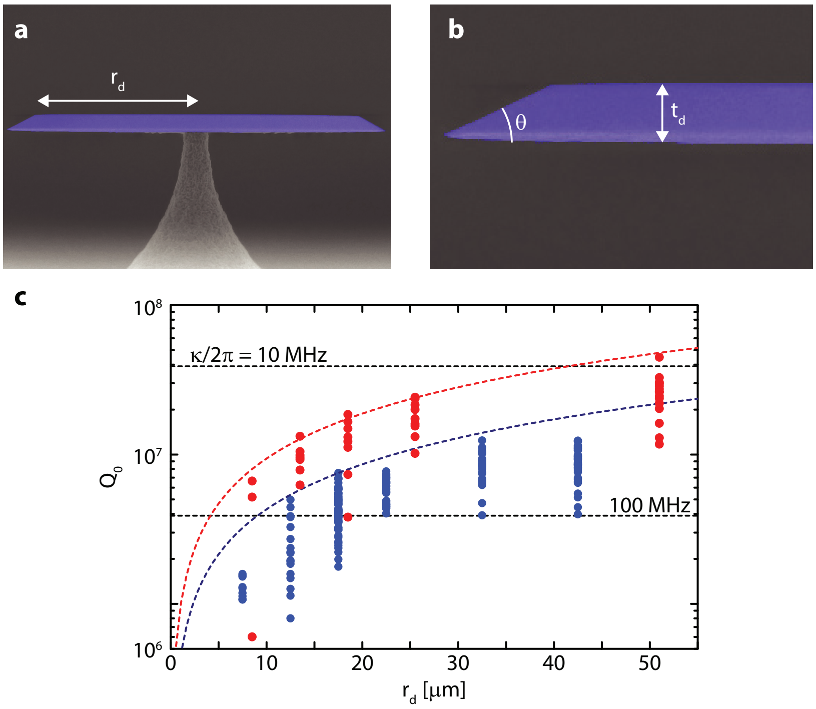

Figure 3.2 – **Measurement results of optical quality factors.** (a,b) SEM of a wedged microdisk; blue and gray indicate SiO_2 and Si, respectively. (c) Intrinsic WGM quality factor Q_0 as a function of disk radius r_d for stand-alone SiO_2 microdisks of thickness $t_d \approx 700\,\text{nm}$. TE and TM modes are not distinguished. Blue (red) points correspond to disks prepared with photo lithography (e-beam lithography), which produce wedge angles of $\theta \approx 30(11)^\circ$. Horizontal lines represent constant cavity linewidth, $\kappa = 2\pi c/(\lambda Q_o)$, with $\lambda = 780$ nm. Blue (red) dashed line is a guide-to-the-eye for $Q \propto r_d$, corresponding to a fixed finesse of $\mathscr{F} = 0.6\,(1.2) \cdot 10^5$.

3.1.2 Optical microdisk

The optical resonator used in our system is a silicon dioxide (SiO_2) microdisk that supports whispering-gallery modes (WGMs) along its periphery. SiO_2 microdisks possess several advantages for evanescent sensing. The first advantage is that the material exhibits a wide transparency window and a large power handling capacity, enabling large intracavity photon numbers n_c. The practically achievable photon number is typically limited by Kerr and Raman nonlinearities. At visible and telecommunication wavelengths, as of relevance for the experiments carried out in this work, other effects such as multi-photon absorption do not play a significant role in SiO_2, in contrast to Si and other semiconductors. A second advantage is that standard lithographic techniques, in conjunction with wet-etching, can produce SiO_2 microdisks with exceptionally high Q (recently exceeding 10^7 in the telecommunication band [168, 169]). This feature is related to the wedged rim of the disk, which supports WGMs that are spatially isolated from the surface, and thereby experience very low surface scattering/absorption loss. Finally, a third advantage is that microdisk WGMs can be evanescently coupled to tapered optical fibers with high ideality [154]. This feature is critical for sensing applications, as optical loss of the outcoupled light field would produce elevated shot-noise imprecision

[44].

Microdisk resonators for the in this thesis presented results were studied at $\lambda \approx 750-850$ nm (outside of the telecommunications window), to allow for smaller optical mode volumes. As discussed in the following section 3.1.3, reducing the disk radius (r_d) and thickness ($t_\mathrm{d} \sim \lambda/n$) results in smaller mode volumes with fractionally larger evanescent components, thereby increasing the optomechanical coupling strength. Figure 3.2 shows measurement results of intrinsic optical Q_0 versus disk radius (r_d) for microdisk samples of thickness $t_\mathrm{d} = 0.7\ \mu$m. Two sets of devices are considered. The first set was prepared with photo lithography, the second with electron-beam lithography. The sets differ by their corresponding wedge angle, which is 30 (11) degrees for photo (e-beam) lithography. For both disk preparation methods, intrinsic $Q_0 > 10^6$ was measured for radii as low as 10 μm, corresponding to loss rates of $\kappa_0 \sim 2\pi \cdot 100$ MHz. For shallower wedge angles, Q_0 as high as $4 \cdot 10^7$ ($\kappa_0 \sim 2\pi \cdot 10$ MHz) was obtained – notably similar to those measured at telecommunications wavelengths, where scattering losses are significantly lower [168, 169]. Numerical simulations [170] reveal that radiation contributes negligibly to the measured loss. Dotted blue (red) lines in fig. 3.2 are guide-to-the-eye models for $Q_0 \propto r_\mathrm{d}$, consistent with loss due to surface absorption/scattering [171], and corresponding to a fixed finesse of $\mathscr{F} \equiv \Delta\omega_\mathrm{FSR}/\kappa_0 \approx c/(r_\mathrm{d}\kappa_0) = 0.6\ (1.2) \cdot 10^5$, with the free spectral range, $\Delta\omega_\mathrm{FSR}$. As discussed in section 3.3.5, the intrinsic optical Q_0 is ultimately reduced by loss introduced by the nanobeam, for beam-disk separations of less than 100 nm.

3.1.3 Evanescent optomechanical coupling

Optomechanical coupling in our system is achieved by placing the nanobeam near the surface of the microdisk, such that the beam's center is located in the evanescent volume of the optical resonance. When the WGM is excited, the beam experiences a gradient force, F_opt. The magnitude of this force, and likewise the optomechanical coupling factor $G = \partial\omega_\mathrm{c}/\partial x$, can be derived by computing the work done on the WGM, $-\delta U_\mathrm{cav}$, by a small displacement of the beam, δx: that is, $F_\mathrm{opt} = -\partial U_\mathrm{cav}/\partial x \approx -G U_\mathrm{cav}/\omega_\mathrm{c}$, where U_cav is the potential energy stored in the cavity field [78, 172]. To first order, it can be shown that [135]

$$G \approx \frac{\omega_\mathrm{c}^{(0)}}{2}\frac{\partial}{\partial x}\left(\frac{\int_\mathrm{beam}(\epsilon(\vec{r})-1)|\vec{E}^{(0)}(\vec{r})|^2 d^3r}{\int_\mathrm{disk}\epsilon(\vec{r})|\vec{E}^{(0)}(\vec{r})|^2 d^3r}\right) \approx \frac{\omega_\mathrm{c}^{(0)}}{2}\frac{\partial}{\partial x}\left(\frac{n_\mathrm{SiN}^2-1}{n_\mathrm{SiO_2}}\frac{|E_\mathrm{max}^{(0,\mathrm{beam})}|^2}{|E_\mathrm{max}^{(0,\mathrm{disk})}|^2}\frac{V_\mathrm{beam}}{V_\mathrm{disk}}\right) \qquad (3.1.2)$$

where $\epsilon(\vec{r})$ is the local relative permittivity, $\vec{E}^{(0)}(\vec{r})$ is the unperturbed cavity field amplitude, and $\int_\mathrm{beam(disk)}$ indicates an integral over the volume occupied by the beam (disk). The simplified expression in (3.1.2) replaces ϵ with an index of refraction n and parameterizes each integral in terms of the intensity-weighted volume of the beam (disk), $V_\mathrm{beam(disk)} \equiv \int_\mathrm{beam(disk)}|E_0|^2 d^3r/|E_\mathrm{max}^{(0,\mathrm{beam(disk)})}|^2$, where $E_\mathrm{max}^{(0,\mathrm{beam(disk)})}$ is the maximum of the unperturbed field within the beam (disk).

To gain physical insight into eq. (3.1.2), we consider the configuration shown in fig. 3.3. Here, the beam is placed above the disk, so that it samples the vertical evanescence of a WGM.

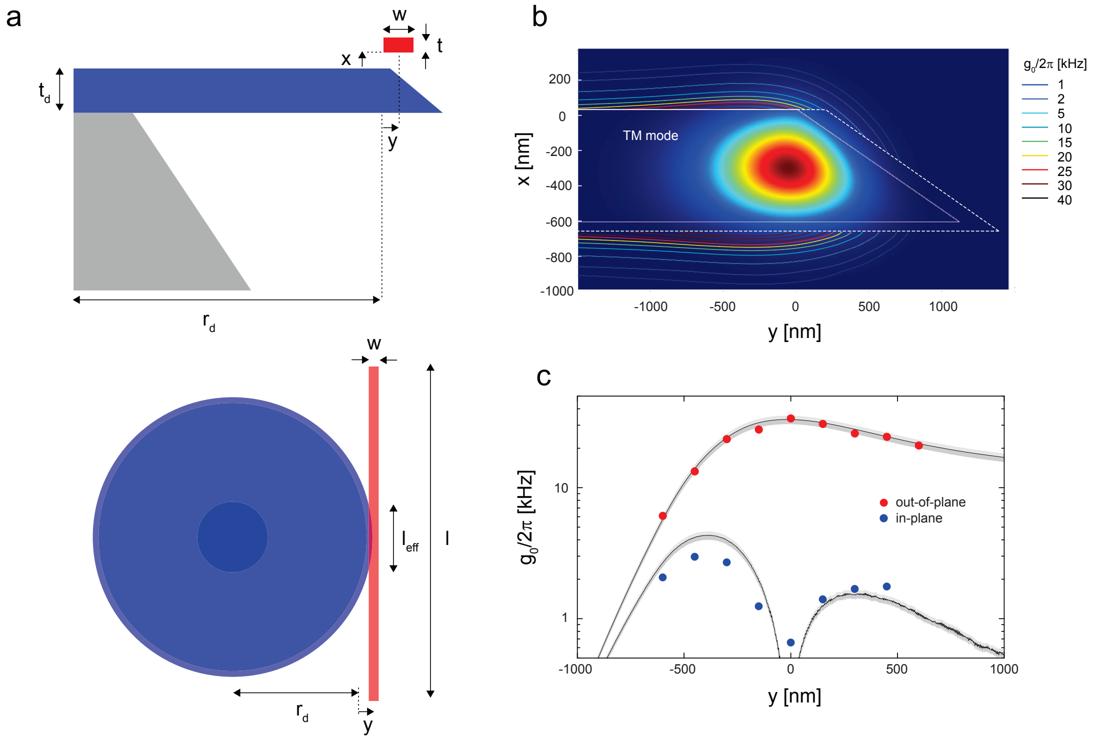

Figure 3.3 – **Simulation of the evanescent optomechanical coupling.** (a) Geometry of the nanobeam-microdisk system: x, y represent the vertical (out-of-plane) and lateral (in-plane) position of the beam, respectively, with respect to the inner rim of the disk (thickness t_d, radius r_d). (b) Simulated optomechanical coupling versus beam position for the device shown in fig. 3.4. The intensity profile of a TM-like WGM (computed using finite element analysis) is shown in the background. Solid and dashed white lines denote the disk surface and the boundary within which the beam touches the disk surface, for the coordinate system defined in (a). Contours indicate lines of constant g_0 for the 4.3 MHz fundamental out-of-plane mode. (c) Measured and simulated g_0 versus y for the beam shown in fig. 3.4 (samples on chip M2/BD/T). Black and blue data are for fundamental out-of-plane and in-plane vibrational modes, respectively (for details, see section 3.3.5). Black lines correspond to numerical solutions to eq. (3.1.2) with a vertical offset of $x = 25$ nm. Gray shading shows the solution space for $x = 20$ to 30 nm.

For simplicity, the transverse dimensions of the beam are assumed to be much smaller than that of the evanescent field; that is, $w \ll \sqrt{A_\mathrm{WGM}}$ and $w \ll x_\mathrm{ev}$, where A_WGM is the effective cross-sectional area of the WGM and x_ev is the exponential decay length of the evanescent field. In this case V_beam can be approximated as twl_eff, where $l_\mathrm{eff} < l$ is the intensity-weighted "sampling length" of the beam. Likewise V_disk can be parameterized as $V_\mathrm{disk} \approx 2\pi r_\mathrm{d} A_\mathrm{WGM}$, where r_d is the physical disk radius. Assuming the form $|E_\mathrm{max}^{(0,\mathrm{beam})}|/|E_\mathrm{max}^{(0,\mathrm{disk})}| = \xi e^{-\frac{x+t/2}{x_\mathrm{ev}}}$, neglecting the weak position dependence of V_beam, and assuming the effective mass of a point probe, $m = \rho twl/2$, the vacuum optomechanical coupling rate can be approximated as

$$g_0 \approx \frac{1}{2}\frac{\omega_\mathrm{c}^{(0)}}{x_\mathrm{ev}}\frac{n_\mathrm{SiN}^2 - 1}{n_\mathrm{SiO_2}}\frac{twl_\mathrm{eff}}{2\pi r_\mathrm{d} A_\mathrm{WGM}}\xi^2 e^{-\frac{x+t/2}{x_\mathrm{ev}}} \cdot \sqrt{\frac{\hbar}{\rho twl\Omega_\mathrm{m}}} \tag{3.1.3}$$

where ρ is the mass density of the beam. In practice x_ev, A_WGM, and ξ must be determined numerically for a wedged microdisk. An estimate can be made, however, by assuming the mode shape of a microtoroid WGM with a minor radius of $t_\mathrm{d}/2$ [135]. In this case, using $n_\mathrm{SiO_2} \approx$

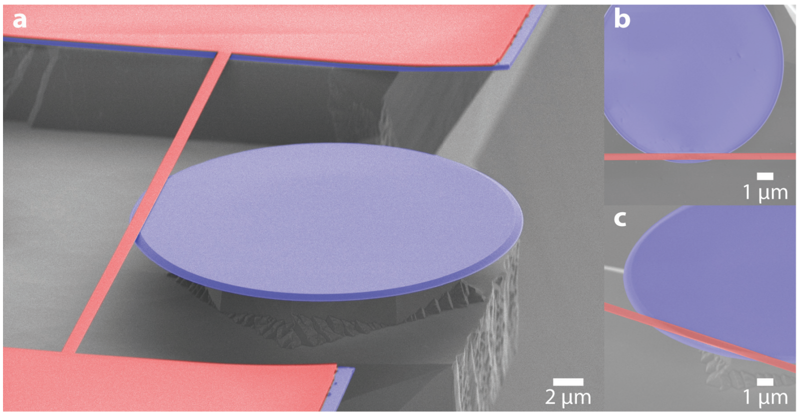

Figure 3.4 – **False-colored scanning electron micrograph of the device:** a high-stress Si_3N_4 (red) nanomechanical beam integrated into the evanescent mode volume of a SiO_2 (blue) microdisk. Disk and beam are integrated on a Si (gray) microchip. Subpanel b (c) highlights the lateral (vertical) positioning of the beam.

1.4, one has $x_{\mathrm{ev}} \approx \lambda/(2\pi\sqrt{n^2_{\mathrm{SiO_2}}-1}) \approx \lambda/12$, $A_{\mathrm{WGM}} \approx 0.15 r_{\mathrm{d}}^{7/12} t_{\mathrm{d}}^{1/4} \lambda^{7/6}$ and $\xi \approx 1.1(\lambda/r_d)^{1/3}$ [173]. Using these formulas, the device geometry in fig. 3.4 ($\{t, w, l\} = \{0.06, 0.4, 60\}$ μm, $x = 25$ nm, $r_{\mathrm{d}} = 14.2$ μm, $t = 0.65$ μm) and assuming $\lambda = 780$ nm, $n_{\mathrm{SiN}} = 2.0$, $\rho = 2700$ kg/m^3, $\Omega_{\mathrm{m}} = 2\pi \cdot 4.3$ MHz, and $l_{\mathrm{eff}} = 10$ μm (see section 3.3.7), eq. (3.1.3) predicts that $G \approx 2\pi \cdot 1.0$ GHz/nm, $x_{\mathrm{zp}} \approx 33$ fm, and $g_0 = G \cdot x_{\mathrm{zp}} = 2\pi \cdot 33$ kHz. As shown in fig. 3.3d, this estimate agrees well with numerically and experimentally determined values. Notably, (3.1.3) implies that to achieve large g_0, it is necessary to reduce the vertical gap to $x < x_{\mathrm{ev}} \approx 100$ nm, and to maximize l_{eff} by laterally positioning the beam *above* the disk.

A numerical model for $g_0(x, y)$ is shown in fig. 3.3b. Intrinsic WGM mode shapes, $\vec{E}^{0)}(\vec{r})$, were computed using an axially-symmetric finite element model (COMSOL FEM axial symmetric package [170]). The energy stored in the WGM,

$$U_{\mathrm{cav}}^{(0)} \approx \tfrac{1}{2} \int_{\mathrm{disk}} \epsilon(\vec{r}) |\vec{E}^{(0)}(\vec{r})|^2 d^3 r, \tag{3.1.4}$$

and the energy shift due to the beam,

$$\Delta U_{\mathrm{cav}}(x, y) \approx \tfrac{1}{4} \int_{\mathrm{beam}} (\epsilon(\vec{r}) - 1) |\vec{E}^{(0)}(\vec{r})|^2 d^3 r, \tag{3.1.5}$$

were computed by numerical integration in Matlab. Differentiating the 2D energy landscape gives $G(x, y) = \omega_{\mathrm{c}} \frac{\partial}{\partial x} (\Delta U_{\mathrm{cav}}(x, y)/U_{\mathrm{cav}}^{(0)})$ for out-of-plane motion. Figure 3.3b shows $g_0(x, y) = G(x, y) \cdot x_{\mathrm{zp}}$ for a beam and disk with the dimensions given above, for a TM-like WGM mode. Contours indicate that the optimal position of the beam is above and inside the inner rim of the disk, and that the magnitude of g_0 scales exponentially with vertical displacement from the disk surface, with a decay length of ~ 100 nm. A horizontal cut through the contours for $x = 25$ nm is shown in fig. 3.3c. Upper and lower curves show models for fundamental in-plane (IP) and out-of-plane (OP) flexural modes. Significantly, maximizing $g_0^{(\mathrm{OP})}$ also minimizes

$g_0^{(\mathrm{IP})}$; this opens a wide spectral window, $\Delta\Omega \sim \Omega_\mathrm{m}$, for measurement of the out-of-plane mode. Experimental measurements (see section 3.3.2) of $g_0(25\ \mathrm{nm}, y)$ are also shown in fig. 3.3c. The model agrees well with experiment assuming a vertical offset of 25 ± 5 nm.

3.2 Fabrication details

The fabrication process is outlined in fig. 3.5. Four key elements of the process, detailed in the following subsections, are: (A) fabrication of the SiO_2 microdisk, (B) formation of a planarized sacrificial layer, (C) fabrication of the Si_3N_4 nanobeam, and (D) release of the sacrificial layer. Of particular importance is the sacrificial layer, which allows the mechanical (Si_3N_4) and optical (SiO_2) elements to be designed independently while maintaining the high optical quality and achieving a vertical beam-disk separation of less than 100 nm. Also important is the use of e-beam lithography to pattern the Si_3N_4, as this enables fine tuning of the lateral beam position.

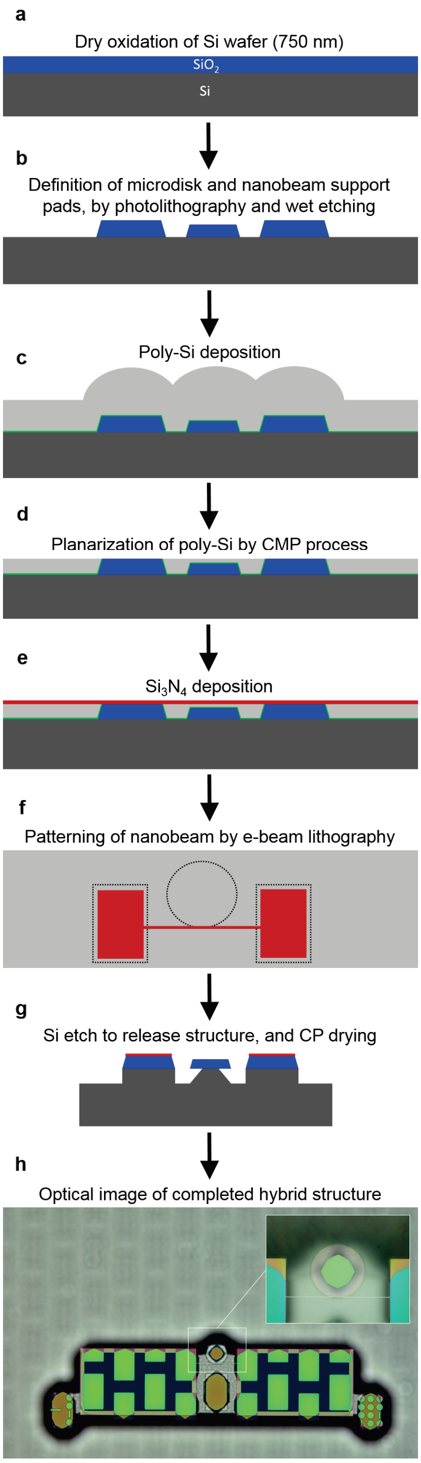
a
Dry oxidation of Si wafer (750 nm)
SiO2
Si
b
Definition of microdisk and nanobeam support pads, by photolithography and wet etching
c
Poly-Si deposition
d
Planarization of poly-Si by CMP process
e
Si3N4 deposition
f
Patterning of nanobeam by e-beam lithography
g
Si etch to release structure, and CP drying
h
Optical image of completed hybrid structure

Figure 3.5 – **Fabrication process flow:** blue, red, green, and (light) gray indicate SiO_2, Si_3N_4, Al_2O_3, and (poly-)Si, respectively.

3.2.1 Microdisk fabrication

The process begins with an undoped, float-zone silicon (Si) wafer, on which a 750 nm film of SiO_2 is grown by dry oxidation (fig. 3.5a). Three structures are patterned into the dioxide film: the microdisk, rectangular pads that later serve as a platform for the nanobeam and a reference plane for CMP polishing, and markers that are later used for e-beam alignment. As illustrated in fig. 3.6, the SiO_2 pattern is processed in two stages. In the first stage all structures are defined. In the second stage the microdisk is etched preferentially, recessing it from the pads and defining the vertical gap between disk and the beam.

Details of the SiO_2 patterning process are as follows: The first mask, containing all structures, is exposed in 1.1 μm of Microchemicals AZ 1512 photoresist using a Karl Süss MA 150 mask aligner and a broadband Hg lamp. A subsequent reflow step is used to smoothen the pattern boundaries and minimize standing wave patterns. Afterwards, the pattern is transferred to SiO_2 by etching in a room-temperature bath of BHF. The pho-

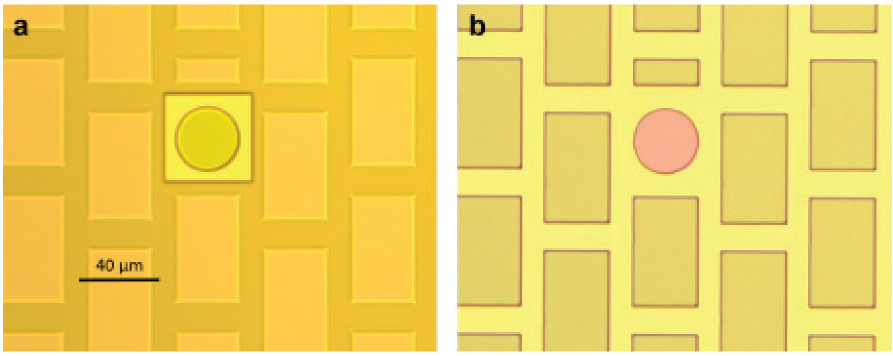

Figure 3.6 – **Defining the vertical gap between the disk and the nanobeam:** (a) Top view of patterned SiO_2 prior to selective etch of the microdisk. Photoresist protects the sacrificial structures, while a window is exposed around the microdisk. (b) Top view after selective etch of the microdisk and removal of the photoresist. The altered color of the microdisk indicates thinning.

toresist is then stripped and a second mask is applied. The second mask covers all structures on the wafer except for the microdisk, leaving it exposed for etching (fig. 3.6a). Subsequently, the microdisk is preferentially etched in BHF until it is 10-100 nm thinner than the surrounding pads (later defining the beam-disk gap). The result, after the photoresist is stripped, is shown in fig. 3.6b. Note that the microdisk reflects a different color than the surrounding pads due to its reduced thickness. Also seen in fig. 3.6 is a matrix of sacrificial pads surrounding the disk. This matrix extends across the entire wafer and is only broken where microdisks or alignment marks are placed. As discussed in section 3.2.2, a uniform matrix of pads is necessary to achieve a flat surface when performing chemical mechanical polishing of the sacrificial layer.

The final result of microdisk fabrication is illustrated in fig. 3.5b. Blue indicates (in profile) the patterned SiO_2 film, with the microdisk in the center and nanobeam support pads on either side. The offset between the microdisk and the pads is highlighted with a dashed line. Not shown are sacrificial pillars and alignment marks. In the next processing step, all structures are buried in a sacrificial layer, onto which a silicon nitride (Si_3N_4) film will be grown.

3.2.2 Planarized sacrificial layer

After patterning, the SiO_2 film is covered with a layer of sacrificial material. The sacrificial layer is used as a substrate for deposition and patterning of the Si_3N_4 film, meanwhile protecting the underlying microdisk. A crucial consideration is the thickness and flatness of the sacrificial layer, which is initially uneven because of its conformity to the underlying SiO_2 pattern. Poly-Si is chosen as sacrifical material because it can be isotropically etched with high selectivity to SiO_2 and Si_3N_4, and is well-suited to CMP. In addition, it can withstand the high temperatures of up to > 800°C required for LPCVD Si_3N_4 (see section 3.2.3), and can be used to undercut the nanobeam and the microdisk in a single step (see section 3.2.4). A 1.5 μm thick layer is deposited by LPCVD at 800°C using silane and disilane as reactants. In addition, immediately before poly-Si deposition, a 5 nm aluminum oxide (Al_2O_3) film is deposited atop the SiO_2

using atomic layer deposition[1]. This film later serves as an etch-stop to protect the microdisk when releasing the Si_3N_4 nanobeam, as Al_2O_3 etches over 100× slower than Si_3N_4 in fluorine-based RIE, and thus a few nanometers is sufficient to protect the microdisk. A profile of the pre-polished sacrificial layer is sketched in fig. 3.5c. The Al_2O_3 etch-stop film is indicated by green. Immediately above the etch-stop is the layer of poly-Si (gray). Because of the underlying SiO_2 structures, the surface of the poly-Si is uneven. This surface is planarized by chemical-mechanical planarization (CMP) before Si_3N_4 is deposited.

The objective of the CMP process is to remove poly-Si until the pads are exposed, while maintaining a thin layer above the recessed microdisk (fig. 3.5d). CMP involves pressing the wafer against a rotating polishing pad in the presence of an abrasive and corrosive chemical slurry. Abrasion is provided by SiO_2 particles 30-50 nm in diameter. The slurry pH is adjusted to achieve the desired polishing rate. In practice, the polishing rate is also a function of applied force, rotation speed, and wafer topography. In order to reduce the poly-Si thickness to less than 100 nm over the entire 100 mm wafer, a uniform polishing rate is critical. This is the reason for patterning a matrix of sacrificial pads as discussed in the previous subsection. The entire procedure is complicated by the fact that the polishing rate varies across the wafer and, more importantly, that the polishing rate above the microdisk is faster than the rate above the adjacent nanobeam support pads. The latter results in a poly-Si layer which is thinner above the microdisk than at the nanobeam supports. To reduce this "dishing" effect, the support pads are brought as close to the microdisk as possible (limited to 7 μm by photo lithography and BHF biasing). To further reduce dishing, a two-step polishing technique is used. First, a slurry designed to etch poly-Si is used to remove the bulk of the material, leaving approximately 100 nm above the pads. The remaining material is removed with a different slurry that is designed to etch SiO_2 faster than poly-Si. When the surface of the SiO_2 pads is reached, the dishing effect therefore begins to reverse, resulting in an overall flat surface.

The gap between the microdisk and nanobeam is not determined by the thickness of the sacrificial layer, but rather by the pre-defined difference in thickness between the microdisk and the pads (fig. 3.5b). During the final steps of CMP, however, the support pads are etched. The final gap is therefore smaller than originally defined by thinning of the microdisk. In order to precisely tune the gap, the thickness of the clamping pads is iteratively measured by reflectometry until a desired value is reached. The sample is then ready for the deposition of Si_3N_4.

3.2.3 Nanobeam fabrication

To form the nanobeam, a 50-100 nm thick film of high-stress Si_3N_4 is deposited onto the planarized poly-Si layer (fig. 3.5e). Low pressure chemical vapor deposition (LPCVD) is performed

---

[1] ALD achieves atomic layer control of film growth by separating the reactants into 2 precursors that are introduced to the chamber sequentially and cyclically, allowing growth of one molecular layer at a time. This process is used to produce very thin continuous films with high conformity - both of which are critically important here.

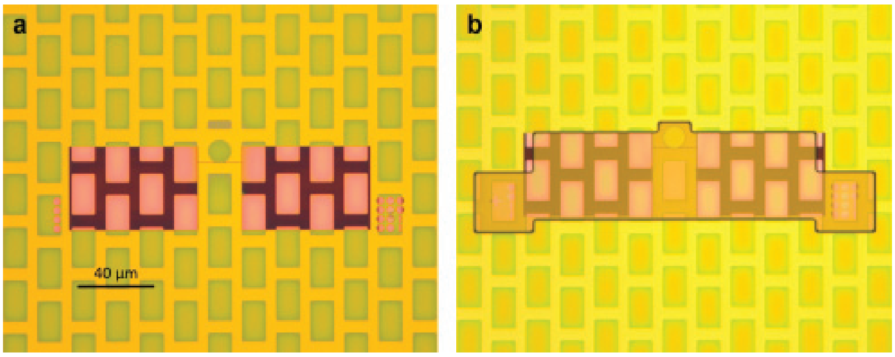

Figure 3.7 – **Definition of the nanobeam and the "mesa":** (a) Top view of sample after etching of Si_3N_4 (pink and purple). Surrounding SiO_2 structures, including microdisk, appear green. (b) Image of the “mesa" photomask.

at 800°C using dichlorosilane and ammonia, producing a nearly stoichiometric Si_3N_4. High stoichiometry is important for reducing absorption caused by hydrogen and oxygen impurities [167]. The high stress (800 MPa) on the other hand, resulting from the high temperature deposition, is important for achieving high mechanical quality factors [129].

To maximize optomechanical coupling, it is necessary to fine-tune the lateral beam-disk separation with 100 nm precision (fig. 3.3c), as the coupling strength strongly depends on the exact beam position (see section 3.3.5). This is accomplished using e-beam lithography to define the beams, in conjunction with the alignment markers defined during SiO_2 patterning (fig. 3.5f). Importantly, after the nitride deposition, the markers are buried under Si_3N_4 and poly-Si, and cannot be seen by the electron-beam. A series of etch steps are used to locally uncover the markers; in addition, to improve contrast, the exposed markers are used as a hard mask to etch 2 μm into the underlying Si, using a highly selective fluorine-based etch. The resulting high-contrast markers permit alignment of the Si_3N_4 mask with sub-100 nm precision.

The nanobeams, support pads, and sample labels are patterned in a 180 nm-thick hydrogen silsesquioxane (HSQ) negative photoresist[2]. To reduce the writing time, the pattern is separated into two parts, one containing the nanobeams and one containing the pads and labels. The former is written with a high resolution of 5 nm, while the latter is written with a 50 nm resolution. Proximity effect correction is used to ensure a high fidelity pattern[3]. The e-beam pattern is transferred to Si_3N_4 using an SF_6 RIE etch. The resulting structure is shown in fig. 3.7a.

---

[2] After development in tetramethylammonium hydroxide, HSQ is chemically similar to SiO_2.

[3] Proximity effect correction software calculates the dose from this backscattering at each grid point and adjusts the writing dose to ensure the correct *effective dose* is achieved.

3.2.4 Structural release

Mesa and sample chip

Before the nanobeam and microdisk are released, they are elevated from the surrounding wafer on a rectangular "mesa". This later facilitates alignment of a straight tapered optical fiber to the microdisk [174]. Figure 3.7b shows the mesa defined in a 5 μm mask of MicroChemicals AZ 9260 photoresist. Fluorine-based RIE is used to remove the surrounding poly-Si. The underlying sacrificial SiO_2 pads are removed by a subsequent BHF etch, exposing the Si substrate. To create the elevated mesa, exposed Si is recessed an additional 50 μm by RIE (fig. 3.3g).

After releasing the mesa, the sample chips are defined. To define the sample chips, the wafer is coated with a protective photoresist layer and partially diced (300 μm deep) with a high precision Si dicing saw. Partial dicing is important as it leaves the wafer intact, enabling further processing using wafer-scale equipment. After partial dicing the photoresist is stripped, so that final release steps can be carried out.

Nanobeam and microdisk

To release the nanobeam and undercut the microdisk, the partially diced wafer is immersed in 40% KOH at 45°C, selectively removing poly-Si but also etching Si. The etch time is fine-tuned with two opposing criteria in mind: first, to ensure that the microdisk is undercut sufficiently far from its rim to avoid optical losses, and second, to ensure that Si underneath the nanobeam clamping point is not etched away. After KOH etching, the wafer is rinsed in water and any remaining potassium is neutralized in a bath of hydrochloric acid. Organic cleaning is then performed using an exothermic mixture of three parts sulfuric acid to one part 30% hydrogen peroxide (a "piranha etch"). After rinsing again, the wafer is transferred directly to the ethanol bath of a critical-point-drying (CPD) machine[4]. After CPD, the wafer is broken into sample chips along the partially diced lines, concluding the fabrication process. An optical image of the finalized samples is shown in fig. 3.5h.

3.3 Characterization measurements

This section presents the characterization measurements and their results and is divided into six subsections. First, a brief description of the experimental setup is given in section 3.3.1. The second subsection presents the thermal noise measurement to determine the mechanical properties (resonance frequency, Ω_m, and linewidth, Γ_m) as well as the optomechanical

---

[4] CPD is a technique used to dry suspended parts that would otherwise stick together under the tension of evaporative drying. This is accomplished through avoiding the liquid to gas phase transition and instead passing through the supercritical regime. CPD does this by replacing EtOH with carbon dioxide (CO_2), and then controlling the pressure and temperature of the CO_2, such that the transition from liquid to gas is circumvented via the supercritical regime.

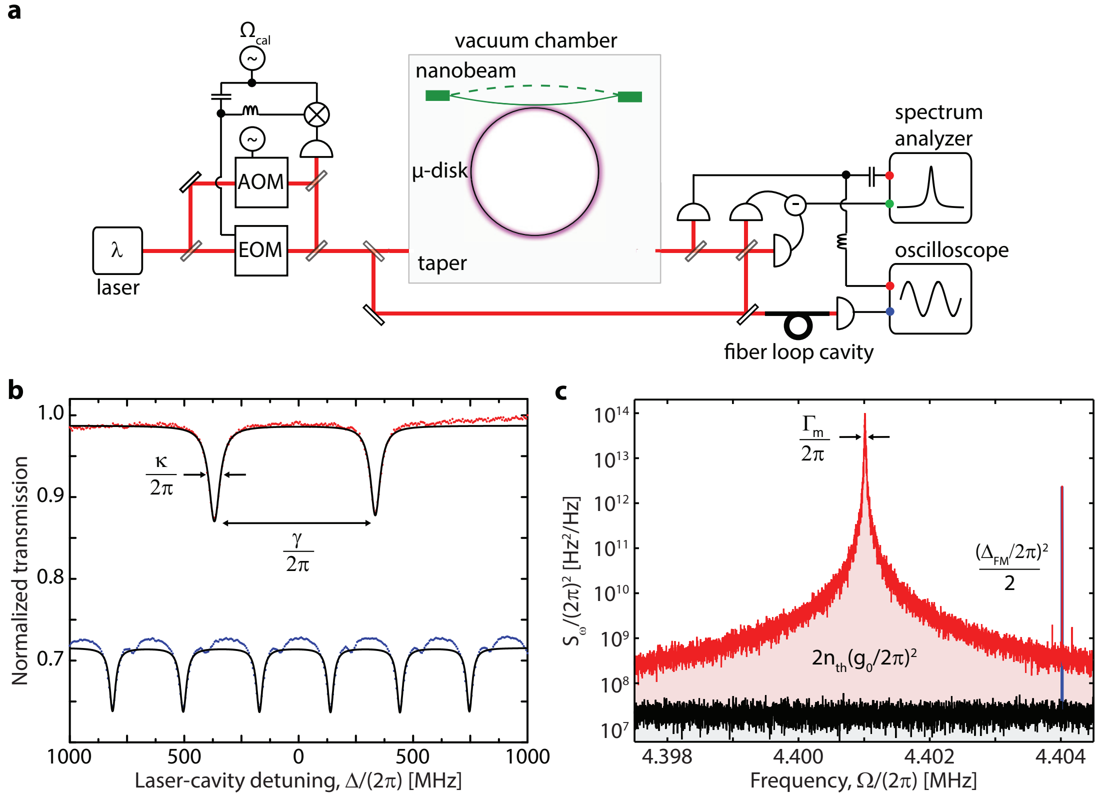

Figure 3.8 – **Characterization setup and measurements.** (a) Overview of the experimental apparatus, described in section 3.3.1. (b) Representative optical Q measurement. WGM loss rates (κ) and mode splitting (γ) are inferred from the cavity transmission profile (red), generated by sweeping the diode laser frequency while monitoring the transmitted power. The sweep is calibrated by simultaneously monitoring transmission through a fiber loop cavity (blue). (c) Representative thermomechanical noise measurement. Ω_m, Γ_{th}, and g_0 are inferred from the center frequency, linewidth, and area beneath the thermal noise peak (pink), respectively. The latter is calibrated by normalizing to the area beneath a FM tone (blue).

coupling strength, g_0 (section 3.3.2). This is followed by a subsection demonstrating the optical spring effect, an alternative way of calibrating g_0 (section 3.3.4). Sections 3.3.5 and 3.3.6 show the behavior of g_0 for swept sample parameters, such as the lateral beam position, beam width and disk thickness. The final section investigates the optomechanical coupling strength for higher-order mechanical modes from which a effective sampling length can be derived (section 3.3.7).

3.3.1 Experimental setup

Samples are characterized using the experimental setup shown in fig. 3.8a. Light from a 765 – 785 nm tunable diode laser (New Focus Velocity 6312) is coupled into the microdisk using a tapered optical fiber (780 HP) [154]. The forward-scattered ("transmitted") field is monitored using one of two techniques: direct detection with an avalanche photo diode (Thorlabs APD110) and balanced homodyne detection with a pair of fast Si photo diodes

(FEMTO HCA-S-100). DC- and AC-filtered photosignals are split between an oscilloscope (Tektronix DPO4034) and a spectrum analyzer (Tektronix RSA5106A). Optical decay rates are inferred from measurements of transmitted power versus laser detuning (fig. 3.8b). To calibrate laser-cavity detuning, a fraction of the input field is simultaneously passed through a 20-cm-long (FSR ~ 350 MHz) fiber loop cavity. Mechanical properties, including the optomechanical coupling rates, are inferred from measurements of thermomechanical cavity frequency noise [175] (fig. 3.8c). To calibrate this noise, the input field is frequency modulated using an electro-optic modulator (iXBlue). Residual amplitude modulation – an important source of calibration error – is suppressed by temperature stabilizing the EOM and supplying it with a DC voltage in addition to the RF drive in order to match the polarization direction to the input field [176]. To eliminate gas damping of the nanobeam (section 3.3.3), the sample chip and the fiber coupling setup (based on an Attocube stack) are embedded in a vacuum chamber operating at $< 10^{-5}$ mbar.

3.3.2 Calibrated thermal noise measurement

The mechanical mode frequencies Ω_m, intrinsic damping rates Γ_m, and optomechanical coupling rates g_0, are determined by analyzing the cavity resonance frequency noise produced by thermal motion of the nanobeam. Thermal motion of the nanobeam $x(t)$ is written onto the cavity resonance frequency $\omega_c(t)$ via the optomechanical coupling $G = d\omega_c/dx$. To measure $\omega_c(t)$, we monitor the power of the transmitted field while operating at a fixed detuning of $|\Delta| \approx \kappa/2$. Referred to the output voltage (V) of the photodetector trans-impedance amplifier, the uncalibrated noise spectrum can be expressed as (neglecting detector noise),

$$S_V(\Omega) = |G_{V\omega}(\Omega)|^2 \left(S_\omega^\mathrm{imp}(\Omega) + S_\omega^\mathrm{cav}(\Omega)\right) = S_V^\mathrm{imp}(\Omega) + \underbrace{|G_{V\omega}(\Omega)|^2 S_\omega^\mathrm{cav}(\Omega)}_{S_V^\mathrm{cav}(\Omega)}, \tag{3.3.1}$$

where $G_{V\omega}(\Omega)$ is the measurement transfer function, $S_\omega^\mathrm{imp}(\Omega)$ is the imprecision frequency noise and $S_\omega^\mathrm{cav}(\Omega)$ are the cavity frequency fluctuations. For both direct and homodyne detection schemes, laser frequency fluctuations imparted on the probing beam before entering the cavity are transduced in the same way as cavity frequency fluctuations [175]. To calibrate the measurement transfer function, we can hence use an EOM to frequency modulate the input laser light with a known modulation depth β at frequency Ω_cal. This adds a third contribution to the detected voltage noise spectrum which can be used as a calibration tone,

$$S_V(\Omega) = S_V^\mathrm{imp}(\Omega) + |G_{V\omega}(\Omega)|^2 \left(S_\omega^\mathrm{cav}(\Omega) + S_\omega^\mathrm{cal}(\Omega_\mathrm{cal})\right), \tag{3.3.2}$$

where the frequency noise spectrum of the injected modulation is given by,

$$S_\omega^\mathrm{cal}(\Omega_\mathrm{cal}) = \frac{\beta^2\Omega_\mathrm{cal}^2}{2}\delta\left[\Omega - \Omega_\mathrm{cal}\right]. \tag{3.3.3}$$

The cavity frequency noise fluctuations in the presented experiments arise from the motion of a high-Q mechanical oscillator with resonance frequency Ω_m and can therefore be expressed as, $S_\omega^\mathrm{cav}(\Omega) = G^2 S_x(\Omega) = g_0^2 S_x(\Omega)/x_\mathrm{ZPF}^2$ (cf. section 2.4), and lead to the total detected signal,

$$S_V(\Omega) \approx S_V^\mathrm{imp}(\Omega) + |G_{V\omega}(\Omega_\mathrm{cal})|^2 \frac{\beta^2\Omega_\mathrm{cal}^2}{2} \delta\left[\Omega - \Omega_\mathrm{cal}\right] + |G_{V\omega}(\Omega_\mathrm{m})|^2 \frac{g_0^2}{x_\mathrm{ZPF}^2} S_x(\Omega). \tag{3.3.4}$$

Under the assumption that the mechanical oscillator is in equilibrium at a certain temperature T we can apply the equipartition identity $\mathrm{Var}\left[\hat{x}\right] = 2x_\mathrm{ZPF}^2 \frac{k_\mathrm{B}T}{\hbar\Omega_\mathrm{m}} = 2x_\mathrm{ZPF}^2 n_\mathrm{th}$ (eq. (2.2.15)) and hence calibrate the spectrum by considering the ratio,

$$\frac{\mathrm{Var}\left[V_\mathrm{mech}\right]}{\mathrm{Var}\left[V_\mathrm{cal}\right]} \approx \frac{|G_{V\omega}(\Omega_\mathrm{m})|^2}{|G_{V\omega}(\Omega_\mathrm{cal})|^2} \frac{4g_0^2 n_\mathrm{th}}{\beta^2\Omega_\mathrm{cal}^2}. \tag{3.3.5}$$

By choosing a modulation frequency close to the mechanical resonance frequency, it can be safely assumed that $|G_{V\omega}(\Omega_\mathrm{m})| \approx |G_{V\omega}(\Omega_\mathrm{cal})|$, the known phonon occupation (temperature) of the oscillator can be used to extract g_0 or vice versa and to calibrate the spectrum in frequency or displacement noise units.

A representative measurement of a spectrum with present calibration tone is shown in fig. 3.8c. Red, blue, and grey components correspond to thermal noise, $S_\omega^\mathrm{th}(\Omega)$, the calibration tone, $S_\omega^\mathrm{cal}(\Omega)$, and measurement imprecision, $S_\omega^\mathrm{imp}(\Omega)$, respectively. The full signal can be modeled as

$$\begin{aligned} S_\omega(\Omega) &= S_\omega^\mathrm{th}(\Omega) + S_\omega^\mathrm{cal}(\Omega) + S_\omega^\mathrm{imp}(\Omega) \\ &\approx 2g_0^2 n_\mathrm{th} \cdot \mathscr{L}(\Omega - \Omega_\mathrm{m}) + \frac{\beta^2\Omega_\mathrm{cal}^2}{2} \cdot \mathscr{G}(\Omega - \Omega_\mathrm{cal}) + S_\omega^\mathrm{imp}(\Omega), \end{aligned} \tag{3.3.6}$$

where $\mathscr{L}(\Omega) = 4\Gamma_\mathrm{m}/(\Gamma_\mathrm{m}^2 + 4\Omega^2)$ is a normalized Lorentzian (characterizing the mechanical susceptibility) and $\mathscr{G}(\Omega) = e^{-\Omega^2/(2B^2)}/\sqrt{2\pi B^2}$ is a normalized Gaussian (characterizing the window function of the spectrum analyzer, which is assumed to have a resolution bandwidth $B \ll \Gamma_\mathrm{m}$). Fitting the calibrated spectrum to eq. (3.3.6) gives Ω_m, Γ_m, and g_0. As mentioned above, the last inference requires knowledge of n_th, which by using input powers low enough to neglect photothermal/radiation pressure damping (< 10 nW), we assume to be $n_\mathrm{th} \approx k_\mathrm{B} \cdot 295\,\mathrm{K}/(\hbar\Omega_\mathrm{m}) \approx 10^6$.

To calibrate the modulation index β, we perform a separate heterodyne measurement of the modulated light before it enters the optomechanical system. The heterodyne setup is shown in fig. 3.8a and consists of a local oscillator that is frequency shifted by $\Omega_\mathrm{AOM} = 2\pi \cdot 238\,\mathrm{MHz}$ using an acousto-optical modulator (AOM) and afterwards recombined with the frequency-modulated light for detection. The EOM is driven by a tone with fixed amplitude and frequency close to the mechanical resonance, both left unchanged during the characterization experiment. Figure 3.9a presents the measured heterodyne spectrum showing the carrier at Ω_AOM and generated sidebands up to third order (here, $\Omega_\mathrm{cal} = 2\pi \cdot 3.4\,\mathrm{MHz}$). The amplitude of

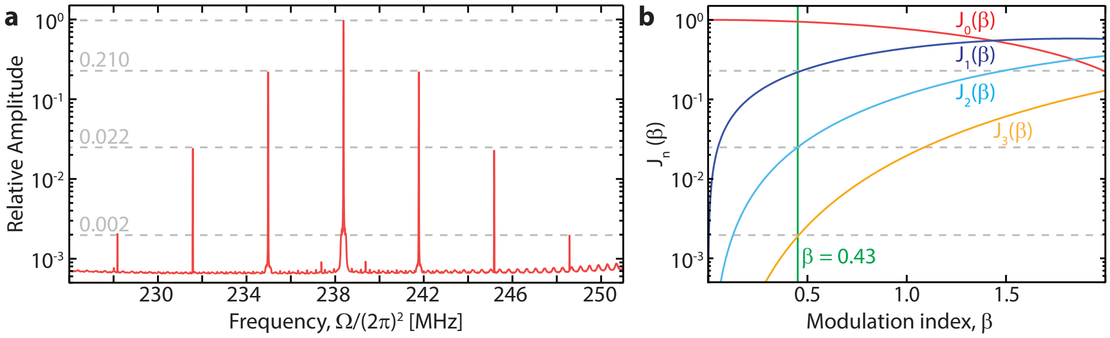

Figure 3.9 – **Calibration of modulation index.** (a) Measured heterodyne spectrum for a modulation drive at $\Omega_{\mathrm{cal}} = 2\pi \cdot 3.4$ MHz with given signal strength. The amplitude of the generated sidebands is normalized to the carrier tone in the absence of modulation. Grey dashed lines mark the amplitudes of the generated sidebands. (b) Bessel functions of the first kind, $J_n(\beta)$ versus modulation index β. The measured relative amplitudes of the n-th sideband pair in the heterodyne measurement correspond to $J_n(\beta)$ from which the modulation index $\beta = 0.43$ for this measurement is extracted.

the measured signal $\sqrt{S_V^{\mathrm{het}}(\Omega)}$ is normalized to the carrier amplitude in the absence of any modulation, $\sqrt{S_V^{\mathrm{het},0}(\Omega_{\mathrm{AOM}})}$. In these relative units, the amplitudes of the n-th modulation sideband pair correspond to the Bessel function $J_n(\beta)$ evaluated at the modulation index of the EOM, as shown in fig. 3.9b) [177]. All generated sidebands show very good agreement to a modulation index $\beta = 0.43$ in this measurement, as indicated by the grey dashed lines. With the now known modulation index, a measured thermal noise spectrum can subsequently be calibrated in frequency noise units and used for determination of the vacuum optomechanical coupling strength g_0. Note that in general, the modulation index of an EOM can be frequency-dependent. For this reason, to avoid systematic errors, recalibration when changing the modulation frequency is necessary.

3.3.3 Gas damping

To investigate the influence of residual gas molecules, we measure the pressure dependence of the mechanical quality factor $Q_{\mathrm{m}}(p)$, where p denotes the pressure inside the vacuum chamber. For this experiment, we continuously measure the mechanical noise spectrum as before while varying the pressure. An example of a measured spectrum is shown in fig. 3.10a with a lorentzian fit to extract the exact resonance frequency and mechanical linewidth. Starting from high vacuum ($p < 10^{-6}$ mbar), we now gradually close the gate valve to the ion pump, slowly isolating the pump from any pumping. Further increase of the pressure is achieved by slowly opening the valve to a regulator valve that injects dry nitrogen gas at a low enough flow rate to slowly increase the pressure. The measured quality factor is shown in fig. 3.10b. No change in the mechanical quality factor is observable for pressures $p < 10^{-4}$ mbar, indicating that the limiting factor in this regime is rather defined by intrinsic loss channels, such as clamping losses. Above these pressures, a loss increase is noticeable which can be accounted for by a modified mechanical linewidth $\Gamma = \Gamma_{\mathrm{m}} + \Gamma_{\mathrm{gas}}(p)$ and follows

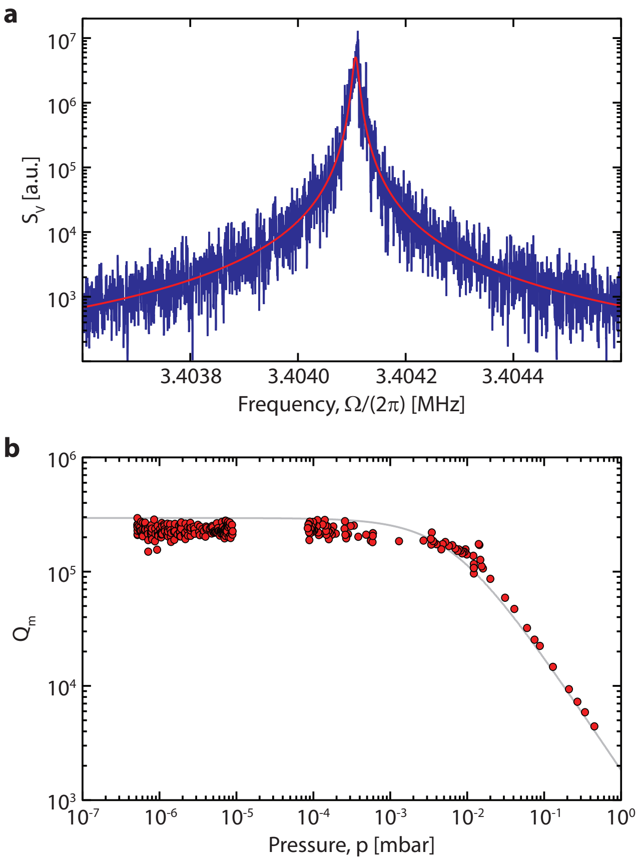

Figure 3.10 – **Gas damping measurement.** (a) Measured noise spectrum (blue) and fit (red for a gas damped mechanical resonance. (b) Plot of mechanical quality factor Q_m versus pressure. The grey line is a simple model introducing the gas damping as additional loss channel with proportionality constant, $D = 2.4\,\mathrm{kHz\,mbar}^{-1}$. The measurements were taken from sample AE/L2/B1/34. For details, refer to the text.

the simple model,

$$Q_\mathrm{m}(p) = \frac{\Omega_\mathrm{m}}{\Gamma_\mathrm{m} + \Gamma_\mathrm{gas}(p)} = \frac{\Omega_\mathrm{m}}{\Gamma_\mathrm{m} + D \cdot p}, \tag{3.3.7}$$

with the damping constant $D = \frac{\mathrm{d}\Gamma_\mathrm{gas}}{\mathrm{d}p} = 2.4\,\mathrm{kHz\,mbar}^{-1}$ in this case. We conclude that under normal experimental conditions ($p < 10^{-6}$ mbar), we are far below the gas damping limited regime and mainly susceptible to intrinsic loss channels.

3.3.4 Optical spring effect

As a cross-check of the thermal noise measurement, g_0 can be independently estimated from the optical spring effect [25]. In the experimentally relevant bad cavity limit ($\Omega_\mathrm{m} \ll \kappa$), the mechanical frequency shift produced by a radiation pressure optical spring is (see eq. (2.3.25)),

$$\Delta\Omega_\mathrm{m}(\Delta) \approx \frac{8g_0^2}{\kappa} \cdot n_\mathrm{c}(\Delta) \cdot \frac{\Delta/\kappa}{1 + 4(\Delta/\kappa)^2} \tag{3.3.8}$$

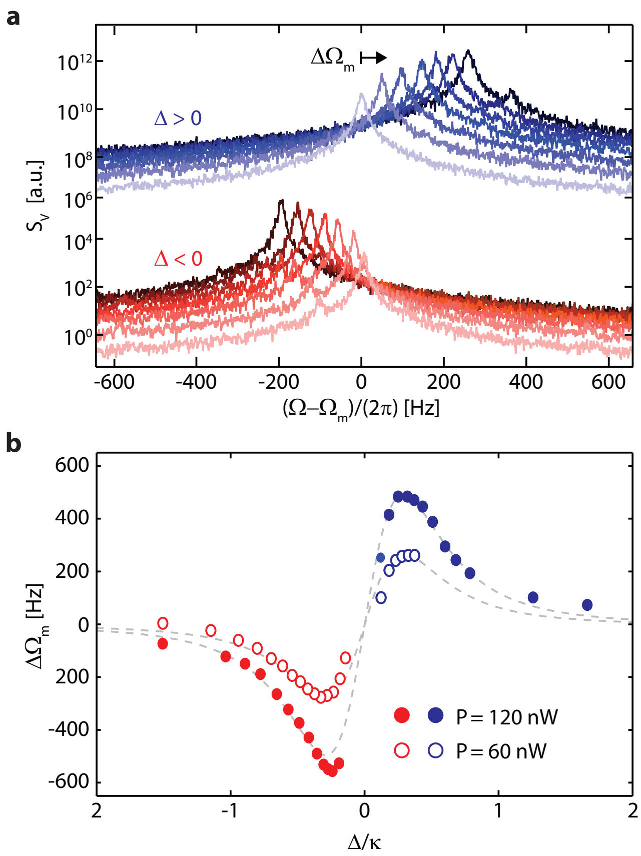

Figure 3.11 – **Optical spring measurement.** (a) Thermal noise spectrum of the fundamental beam mode as a function of laser detuning. Blue and red spectra indicated blue ($\Delta > 0$) and red ($\Delta < 0$) detuning, respectively. Lighter shades indicate smaller detuning. Blue spectra are vertically offset. (b) Plot of optical spring shift, $\Delta\Omega_m$, versus normalized detuning, Δ/κ. Dashed gray lines are a fit to eq. (3.3.8) using g_0 as a free parameter. The measurements were taken with sample M2/CU/T/-1.

where Δ is the laser-cavity detuning, $n_c(\Delta) = (4P_{in}/(\hbar\omega_0\kappa))(\kappa_{ex}/\kappa)/(1+4(\Delta/\kappa)^2)$ is the intracavity photon number, and P_{in} is the power injected into the cavity. Radiation pressure damping also occurs for a detuned input field; however, in the devices studied, for which $\Omega_m/\kappa \sim 0.01$, this effect was found to be overwhelmed by photothermal damping [178].

A measurement of the optical spring effect is shown in fig. 3.11, corresponding to the sample also characterized in fig. 3.8c. The injected powers used – $P_{in} = 60, 120$ nW – were chosen to avoid instabilities due to photothermal/radiation pressure damping. The cavity was critically coupled ($\kappa_{ex} \approx \kappa_0 \approx \kappa/2 \approx 2\pi \cdot 550$ MHz) and laser detuning was estimated from the mean transmitted power. Overlaid models correspond to eq. (3.3.8) with the value $g_0 = 2\pi \cdot 60$ kHz, inferred from a least-squared fit to the low power measurement. This value is within 10% of that inferred from thermal noise in fig. 3.8c.

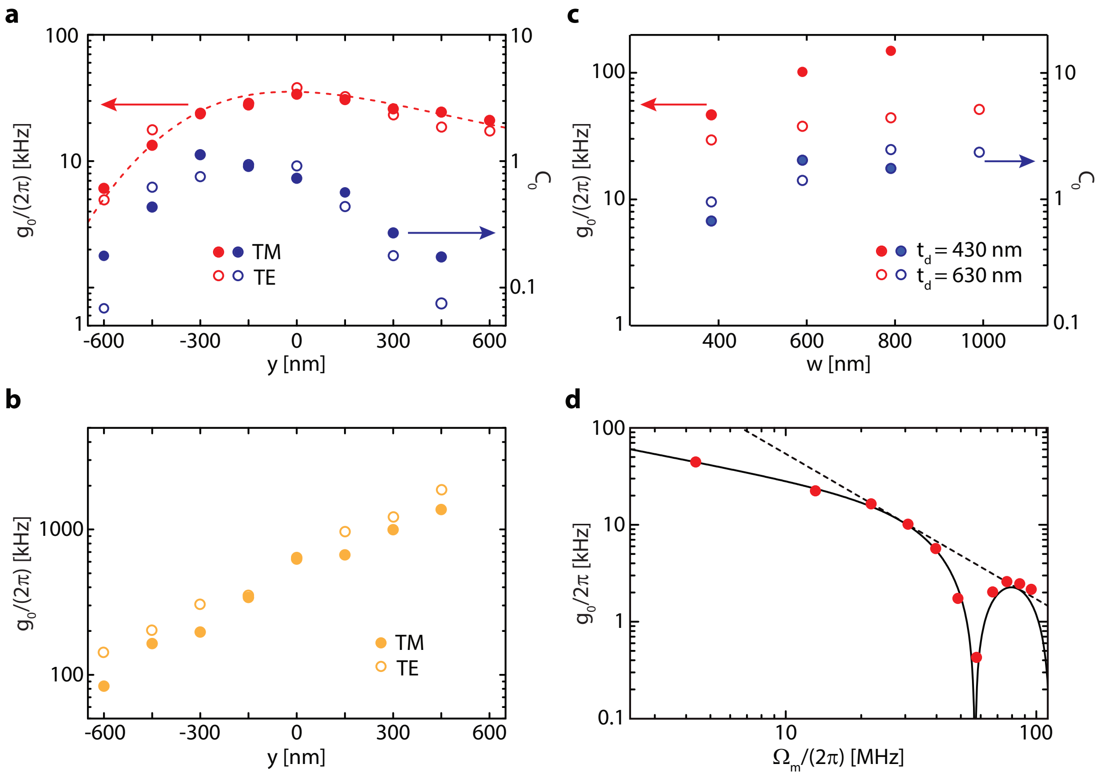

Figure 3.12 – **Characterization measurements for swept sample parameters.** (a) Measured vacuum optomechanical coupling rate (g_0) and cooperativity (C_0, assuming $\Gamma_\mathrm{m} = 2\pi\cdot 20$ Hz) versus lateral beam position (y) for TM (solid circles) and TE (open circles) cavity modes. (b) Corresponding intrinsic cavity decay rate (κ_0). (c) Measured g_0 versus beam width (w) for two disk thicknesses (t_d). (d) Measured g_0 versus mode frequency, $\Omega_\mathrm{m}^{(n)} \approx n\Omega_\mathrm{m}^{(0)}$. Red dots correspond to odd harmonics ($n = 1,3,5...$). Solid and dashed lines are model curves (Eq. 3.3.9) for a sampling length of $l_\mathrm{eff} = 9.6$ and $l_\mathrm{eff} = 0$, respectively.

3.3.5 g_0 and C_0 versus lateral beam position

As discussed in section 3.1.3, the vacuum optomechanical coupling rate g_0 depends sensitively on the lateral positioning of the nanobeam, and assumes a maximum (minimum) value for out-of-plane (in-plane) flexural modes when centered above the WGM. This behavior was studied by sweeping the lateral position of the beam and measure g_0 for each of these positions. The results are shown in fig. 3.12a for beam and disk dimensions of $\{l, w, t\} = \{60, 0.4, 0.06\}\,\mu$m and $\{r, t_\mathrm{d}, \theta\} = \{15\,\mu\mathrm{m}, 0.60\,\mu\mathrm{m}, 30°\}$, respectively, and for a vertical gap of 25 nm. The in-plane modes exhibit typically an order of magnitude lower g_0 for geometrical reasons, and are not considered. In agreement with numerical modeling (dashed line), g_0 assumes a maximum of $2\pi\cdot 40$ kHz as the outer edge of the beam eclipses the rim of the disk. Notably, the observed $g_0 > 2\pi\cdot 10$ kHz is 20 dB larger than previous chip-scale devices [158], owing to the small vertical gap and optimal lateral placement of the beam.

Also shown in fig. 3.12b are measurements of κ versus lateral beam position (y). When the beam is displaced far from the disk, κ converges to the intrinsic value of $\sim 2\pi\cdot 100$ MHz observed in fig. 3.2, suggesting that the additional fabrication steps to implement the beam did not significantly affect microdisk surface quality. As the beam is brought within 100 nm of the disk, κ is observed to increase sharply. The observed exponential dependence κ on y is independent of mode polarization and similar to the scaling observed in [159] with a beam coupled to a microtoroid. The absolute magnitude of the loss is also inconsistent with bulk Si_3N_4 optical absorption – specifically, accounting for the relatively small fraction of energy stored in the beam, the observed loss would require an imaginary index of $\sim 10^{-4}$, which is 1-2 orders of magnitude larger than conventionally observed for Si_3N_4 at NIR wavelengths [37, 167]. We thus conjecture that this loss is due to scattering from the beam and/or waveguide coupling into the beam.

Combining measurements of g_0 and κ with the room temperature mechanical damping rate of $\Gamma_\mathrm{m} = 2\pi \cdot 15$ Hz (we observed no change in Γ_m for small beam-disk separation, suggesting that squeeze-film gas damping [166] was not a factor), the single-photon cooperativity is observed to approach $C_0 \sim 1$. This value is limited by the unfavorable scaling of g_0^2/κ as g_0 begins to saturate. Despite this limitation, the inferred C_0 represents a nearly 50 dB increase over prior chip-scale implementations [158], owing to the combined 100-fold increase of g_0 and 10-fold reduction in κ due to a more sophisticated fabrication process. Figure 3.12b suggests that the optical linewidth, κ, is ultimately dominated by beam-induced scattering/absorption loss, rather than deterioration of intrinsic disk loss (fig. 3.2), implying that an additional 10-fold reduction in κ may yet be realized with appropriate beam shaping/positioning.

3.3.6 g_0 and C_0 versus beam width and disk thickness

Wider beams ($w \sim \lambda$) and thinner disks ($t_\mathrm{d} < \lambda$) were fabricated in an attempt to increase g_0 and C_0 (see eq. (3.1.3)). Measurements of $\{g_0, C_0\}$ for different beam widths, w, and for two microdisk thicknesses, $t_\mathrm{d} \approx 0.43$ and 0.63 μm, are shown in fig. 3.12c. Fixed dimensions of the nanobeam and microdisk are $\{t, l\} \approx \{0.06, 60\}$ μm and $\{r_\mathrm{d}, \theta\} \approx \{15\ \mu\mathrm{m}, 30\ \mathrm{deg.}\}$, respectively. The lateral beam position was chosen to maximize g_0 for the 0.4 μm-wide beam (see fig. 3.12). For the TE optical modes studied, a roughly 2× increase in g_0 was observed for the 30% thinner disk. In both cases, g_0 scaled roughly linearly for widths $w \in [0.4, 1]$ μm. C_0 also increased with w, roughly in proportion to g_0^2, for both t_d. This is due to the fact that κ (not shown) was roughly independent of w for both disk thicknesses and a factor of four larger for the thinner disk. The highest optomechanical coupling rate we have measured, $g_0 \approx 2\pi \cdot 150$ kHz, was for a 1 μm wide beam coupled to a 0.43 μm thick disk. The highest cooperativities observed, $C_0 > 2.5$, were for 1 μm wide beams coupled to disks of both thicknesses.

3.3.7 g_0 versus mechanical mode order

The vacuum optomechanical coupling rate, g_0, was also studied for higher order mechanical modes. As shown in fig. 3.12d, g_0 decreases as the vibrational node spacing approaches the dimensions of the effective sampling length l_eff. In this case the model in section 3.1.3 – which assumes rigid displacement of a beam with effective mass $m = \rho t w l/2$ – breaks down. A simple extension of the model is shown as a red line in fig. 3.12d. Here, m is computed with respect to optical-intensity-weighted displacement of the mechanical mode:

$$m = \frac{\int_{\text{beam}} \rho |u(r)|^2 d^3 r}{|\int_{\text{beam}} |E(r)|^2 u(r) d^3 r / \int_{\text{beam}} |E(r)|^2 d^3 r|^2} \approx \frac{\rho t w l}{1-(-1)^n} \frac{1}{\text{sinc}^2\left(\frac{n\pi}{2}\frac{l_{\text{eff}}}{l}\right)} \tag{3.3.9}$$

where $\vec{u}(x,y,z) \approx \sin(n\pi x/l)\hat{z}$ is the displacement profile of the nth-order out-of-plane flexural mode. The latter expression is appropriate when the transverse dimensions of the beam are much smaller than that of the WGM, and assumes that the intensity distribution sampled by the beam is uniform along the beam axis with an effective sampling length l_{eff}. Using $\Omega_{\text{m}} \propto n$ gives $g_0^{(n)}/g_0^{(0)} \approx |\text{sinc}\left(\frac{n\pi}{2}\frac{l_{\text{eff}}}{l}\right)|/\sqrt{n}$ for odd n and 0 for even n. The model shown in fig. 3.12d agrees quantitatively with experiment assuming an effective length of $l_{\text{eff}} = 9.6\ \mu$m as the only free parameter. A simple route to increasing g_0 is to remove mass from the beam outside of the effective sampling length, to either produce a double-tethered (shown in fig. 3.15), or a single-tethered nanobeam, as it is used for the main results of this thesis (see section 4.3.1).

3.4 Displacement sensitivity

As an illustration of the device performance, we use the microdisk to perform a cavity-enhanced interferometric measurement of the beam's displacement. For this purpose, the fiber taper and microdisk are embedded in one arm of a length- and power-balanced homodyne interferometer (fig. 3.8). The cavity is driven on resonance using the Pound-Drever-Hall technique [146]. A piezoelectric mirror is use to stabilize the interferometer path length difference so that the homodyne photocurrent is proportional to the phase of the transmitted cavity field. The operation of a homodyne interferometer is detailed in appendix D.

The measured displacement noise spectra are shown in fig. 3.13 for a $\{l, w, t\} = \{60, 0.4, 0.06\}\ \mu$m beam with a vertical beam-disk separation of approximately 35 nm and optomechanical parameters $\{\Omega_{\text{m}}, \Gamma_{\text{m}}, \kappa, g_0, C_0\} \approx \{2\pi \cdot 4.4\,\text{MHz}, 2\pi \cdot 10\,\text{Hz}, 2\pi \cdot 700\,\text{MHz}, 2\pi \cdot 28\,\text{kHz}, 0.45\}$. Here κ corresponds to the critically-coupled cavity linewidth while the mechanical parameters correspond to the fundamental out-of-plane mechanical mode. For the measurements shown, the cavity was critically coupled and the power of the input field was swept from $0.01 - 20\ \mu$W. The homodyne photocurrent noise spectrum is plotted in units relative to the signal produced by a phonon of displacement $2S_\omega^{\text{zp}}(\Omega_{\text{m}}) \approx (2\pi \cdot 10\,\text{kHz}/\sqrt{\text{Hz}})^2$ (equivalent to $2S_x^{\text{zp}}(\Omega_{\text{m}}) \approx (2\pi \cdot 8.9\,\text{fm}/\sqrt{\text{Hz}})^2$ assuming $x_{\text{zp}} = 25$ fm). In these units, the magnitude of the fundamental thermal noise peak (neglecting photothermal or dynamical back-action) is equal to the effective thermal occupation $n_{\text{tot}} \equiv S_\omega(\Omega_{\text{m}})/(2S_\omega^{\text{zp}}(\Omega_{\text{m}}) = n_{\text{th}} + n_{\text{ba}} + n_{\text{imp}}$, where $n_{\text{th}} \equiv S_\omega^{\text{th}}(\Omega_{\text{m}})/2S_\omega^{\text{zp}}(\Omega_{\text{m}})$ is the ambient bath occupation, n_{ba} is the effective thermal bath occupation associated with classical and quantum measurement back-action (radiation pressure shot noise), and $n_{\text{imp}} \equiv S_\omega^{\text{imp}}(\Omega_{\text{m}})/2S_\omega^{\text{zp}}(\Omega_{\text{m}})$ is the apparent thermal occupation associated with the measurement imprecision. The noise spectra are calibrated by bootstrapping a low

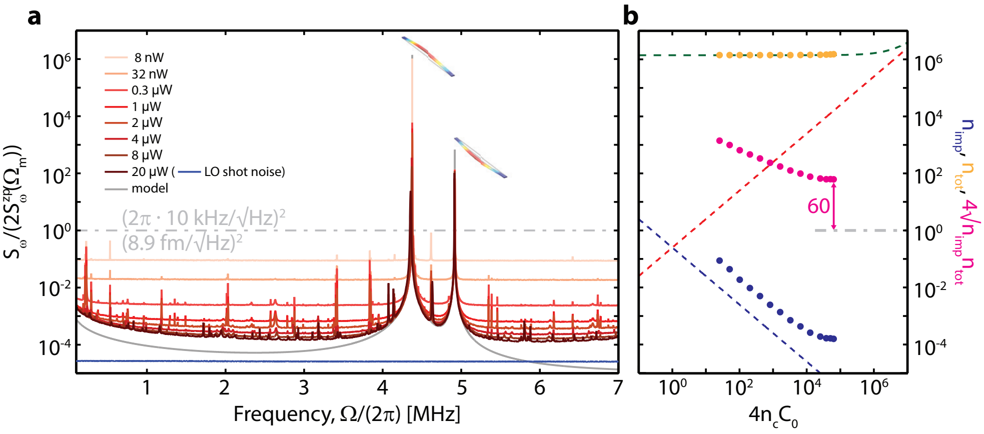

Figure 3.13 – **Displacement sensitivity measurement.** (a) Nanobeam displacement noise, measured by balanced homodyne detection of the microdisk output field, for various input powers. The measurements were taken with sample M2/CU/T/-1. Noise spectra are expressed in units relative to the cavity frequency noise produced by one phonon of fundamental out-of-plane vibration, $2S_\omega^{\mathrm{zp}}(\Omega_\mathrm{m}) = (2\pi\cdot 10\,\mathrm{kHz}/\sqrt{\mathrm{Hz}})^2$, where $\Omega_\mathrm{m} = 2\pi\cdot 4.4$ MHz. At large powers, the fundamental noise peak is shifted and broadened by optical spring softening and damping, respectively. The peak at 4.9 MHz is due to thermal motion of the fundamental in-plane mode. The gray curve is a model for the intrinsic thermal motion of the fundamental out-of-plane and in-plane modes (eq. (3.4.1)). (b) Measured phonon equivalent displacement, $n_\mathrm{tot} = S_\omega(\Omega_\mathrm{m})/2S_\omega^{\mathrm{zp}}(\Omega_\mathrm{m})$, displacement imprecision, $n_\mathrm{imp} \equiv S_\omega^{\mathrm{imp}}(\Omega_\mathrm{m})/2S_\omega^{\mathrm{zp}}(\Omega_\mathrm{m})$, and their geometric mean versus intracavity photon number n_c weighted by single-photon cooperativity C_0. Dashed lines denote ideal values for $n_\mathrm{tot} = n_\mathrm{th} + n_\mathrm{ba} + n_\mathrm{imp}$ (green), $n_\mathrm{ba} = C_0 n_\mathrm{c}$ (red), and $n_\mathrm{imp} = 1/16C_0 n_\mathrm{c}$ (blue), using $n_\mathrm{th} \approx 1.4\cdot 10^6$ and $C_0 = 0.45$. Magenta arrow indicates proximity to the uncertainty limit, $4\sqrt{n_\mathrm{imp} n_\mathrm{tot}} \geq 1$.

power measurement to $n_\mathrm{tot} \approx n_\mathrm{th} \approx k_\mathrm{B}T/\hbar\Omega_\mathrm{m} \approx 1.4\cdot 10^6$ (for larger optical powers, dynamic spring/damping forces modify the peak value, $S_\omega(\Omega_\mathrm{m})$). At the highest optical powers, the displacement imprecision in the vicinity of Ω_m is estimated (from the saddle at 2.5 MHz) to be $n_\mathrm{imp} \approx 1.5\cdot 10^{-4}$, while the shot-noise imprecision (blue curve, obtained by blocking the signal interferometer arm) is $n_\mathrm{imp}^{(\mathrm{shot})} \approx 2.6\cdot 10^{-5}$. These correspond to imprecisions 32 and 40 dB below that at the SQL ($n_\mathrm{imp} = 0.25$), respectively. The magnitude of the extraneous imprecision, $2S_\omega^{\mathrm{zp}}(\Omega_\mathrm{m})\cdot(n_\mathrm{imp} - n_\mathrm{imp}^{(\mathrm{shot})}) \approx (2\pi\cdot 110\,\mathrm{Hz}/\sqrt{\mathrm{Hz}})^2$, is independent of optical power and gives rise to the saturation of the blue points in 3.13b. This extraneous noise is consistent with a mixture of diode laser frequency noise ($\sim 30\,\mathrm{Hz}/\sqrt{\mathrm{Hz}}$ [73]), thermorefractive noise ($\sim 10\,\mathrm{Hz}/\sqrt{\mathrm{Hz}}$ [135]), and off-resonant thermal noise ($\sim 70\,\mathrm{Hz}/\sqrt{\mathrm{Hz}}$). The latter is estimated using the ‘structural damping’ model of Saulson [121],

$$\frac{S_\omega(\Omega)}{2S_\omega^{\mathrm{zp}}(\Omega_\mathrm{m})} \approx n_\mathrm{th}\frac{\Omega_\mathrm{m}}{\Omega}\frac{\Gamma_\mathrm{m}^2\Omega_\mathrm{m}^2}{(\Omega^2-\Omega_\mathrm{m}^2)^2+\Gamma_\mathrm{m}^2\Omega_\mathrm{m}^2} \gtrsim \frac{7n_\mathrm{th}}{Q_\mathrm{m}^2}, \tag{3.4.1}$$

shown in gray in fig. 3.13, for $Q_\mathrm{m} = \Omega_\mathrm{m}/\Gamma_\mathrm{m} = 4.4\cdot 10^5$.

The total efficiency of the measurement is estimated by comparing the power dependence of the imprecision (n_imp), the effective thermal bath occupation (n_tot), and their geometric mean $\sqrt{n_\mathrm{imp} n_\mathrm{tot}}$ to the ideal values $1/(16C_0 n_\mathrm{c})$, $C_0 n_\mathrm{c}$, and $1/4$, respectively, where the last case represents the Heisenberg uncertainty limit. As shown on the right hand side of fig. 3.13, the imprecision is a factor of 7.5 larger than ideal, due to a combination of cavity loss (50%, corresponding to critical coupling), taper loss (~ 10%), homodyne detector loss/misalignment, and optical mode splitting [73]. The effective thermal bath occupation is inferred by fitting to the off-resonant tail of the fundamental noise peak (to avoid the systematic error due to optical damping). From these fits we infer a heating of $C_0^{\mathrm{ext}} \equiv (n_{\mathrm{tot}} - n_{\mathrm{th}})/n_{\mathrm{c}} = 1.4$, two times larger than expected due to quantum measurement back-action. The imprecision-back-action product is constrained, at high powers, to $4\sqrt{n_{\mathrm{imp}} n_{\mathrm{tot}}} \approx 60$, due to the saturation of the measurement imprecision. To the best of our knowledge, this represents the closest approach to the uncertainty limit for a room temperature mechanical oscillator.

3.5 Structural damping

In a recent experiment [179], we resolved and investigated the thermal motion of a nanobeam far below its mechanical resonance frequency and gained evidence that the mechanical oscillator is driven by a $1/f$ thermal force, which is in contrast to the generally assumed model of a white (frequency-independent) thermal noise that drives the oscillator. This observation suggests that the loss angle ϕ_0 (defined in eq. (2.2.7)) of the system is frequency-independent.

As discussed in the section about the fundamentals of mechanical motion (section 2.2.1), the thermal force driving a nanomechanical oscillator is commonly assumed to be a Langevin force with a white (frequency-independent) spectrum [121]. To recall, the (single-sided) force spectrum of the thermal force is given as,

$$S_F^{\mathrm{th}}(\Omega) = -\frac{4k_{\mathrm{B}}T}{\Omega}\mathrm{Im}\left(\chi_x(\Omega)^{-1}\right), \tag{3.5.1}$$

with the mechanical susceptibility,

$$\chi_x(\Omega) = \frac{m^{-1}}{\Omega_m^2(1 - i\phi(\Omega)) - \Omega^2}, \tag{3.5.2}$$

and the loss angle of the beam material $\phi(\Omega)$. So far, this loss angle has been assumed to be frequency dependent, in particular $\phi(\Omega) = Q_{\mathrm{m}}^{-1}\frac{\Omega}{\Omega_{\mathrm{m}}}$, in order to achieve a white thermal force spectrum which arises for viscous (velocity-proportional) damping mechanisms, such as gas damping [166].

In the absence of external losses, the modes of the silicon nitride nanobeam would exhibit a frequency-independent loss angle, $\phi(\Omega) = \phi = Q_{\mathrm{m}}^{-1}$. This scenario is the so-called ”structural damping" which results in a ”pink" ($1/f$, with $f = \Omega/(2\pi)$) thermal force spectrum,

$$S_F^{\mathrm{th}}(\Omega) = 4k_{\mathrm{B}}Tm_{\mathrm{eff}}\Gamma_{\mathrm{m}}\frac{\Omega_{\mathrm{m}}}{\Omega}. \tag{3.5.3}$$

Structural damping has been studied for precision macroscopic oscillators, such as pendulums [180, 181] and gram-scale mirror oscillators [182]. In terms of nanomechanical oscillators, structural damping had not been verified yet due to the difficulties (a) of fabricating samples

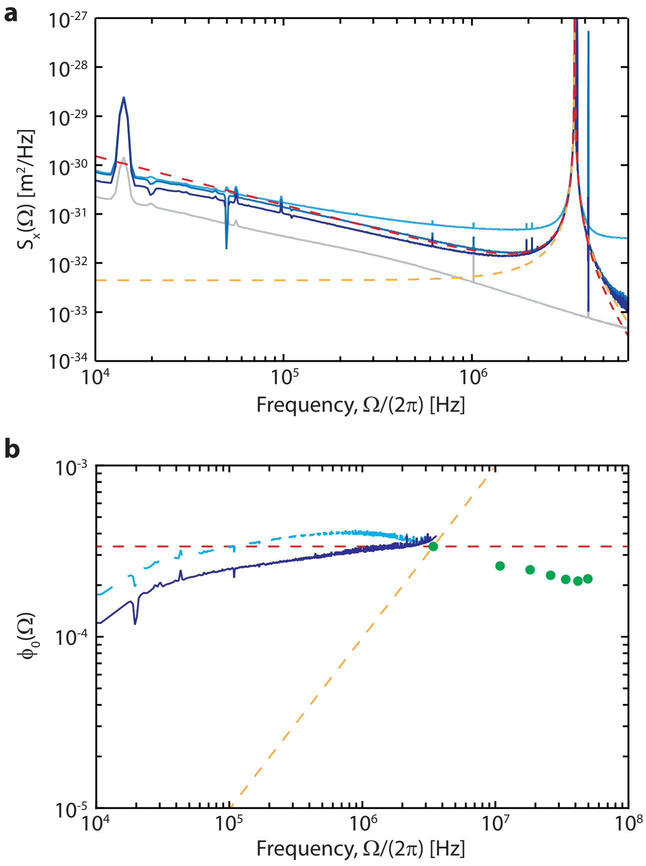

Figure 3.14 – **Structural damping measurement:** (a) Broadband thermal motion of a Si_3N_4 nanobeam with resonance frequency at $\Omega_m = 2\pi \cdot 3.4$ MHz as displacement noise $S_x(\Omega)$. Shown are the unprocessed homodyne spectrum (light blue trace), the shot noise subtracted signal (blue trace) and in dark blue a trace where also the extraneous cavity noise (shown as the grey trace) has been subtracted. The data clearly shows better agreement to a pink $1/f$ thermal noise model (red dashed trace) representing structural damping compared to a white viscous damping model (orange dashed trace). (b) Intrinsic loss angle versus frequency inferred from the the low-frequency displacement spectrum (blue trace), spectrum without extraneous noise subtraction (light blue dashed trace) and quality factor measurements of higher-order flexural modes (green data points). Also shown are the predictions for the loss angle from the viscous (orange) and structural damping model (red). All measurements were taken with sample AE/L2/B1/34.

that are limited by internal losses and (b) of being capable of resolving the thermal motion far below resonance.

Our recent results indeed indicate that the viscous damping model does not seem to agree with the measurement, as seen in the low-frequency part of fig. 3.13 which was fitted using a structural damping model (eq. (3.4.1)). This suggests that the nanomechanical oscillator in our system is in fact limited by internal losses, characterized by the actual material loss angle for the nanobeams $\phi(\Omega) = \phi = Q_m^{-1}$ which is frequency-independent.

The results of our measurements are shown in fig. 3.14a. For this measurement, we utilized a nanobeam with mechanical resonance frequency at $\Omega_m = 2\pi \cdot 3.4$ MHz and intrinsic dissipation rate $\Gamma_\mathrm{m} = 2\pi \cdot 15\,\mathrm{Hz}$. When attempting to fit both, a viscous damping model (indicating a dominating extrinsic damping) and a structural damping model (dissipation purely intrinsic) to the measured spectrum, especially the low frequency part, down to two decades below the resonance frequency of the fundamental mode, appears in better agreement to the structural damping model. The extraneous noise from the disk (thermorefractive noise [183, 184]) was estimated by measuring the frequency noise spectrum of a bare microdisk resonator without mechanical oscillator in its evanescent field.

From the fit to the measured data, we infer the material loss angle $\phi \approx 4.5 \cdot 10^{-6}$, almost two orders of magnitude lower than values for bulk silicon [164]. We attribute this to "loss dilution" due to the high stress in our nanobeam samples. Taking this into account, we infer an intrinsic loss angle in the absence of stress of $\phi_0 \approx 3 \cdot 10^{-4}$. This value is remarkably stable between frequencies of 50 kHz and 50 MHz and changes by less then a factor of two, as shown in fig. 3.14b. Our inferred value for ϕ_0 is in good agreement with a recent survey of stressed $\mathrm{Si_3N_4}$ films [164].

Our result shows that white thermal noise is not applicable to silicon nitride nanobeam resonators in case they are limited by internal losses. The viscous damping model underestimates the low-frequency part of the displacement spectrum which can have significant impact on broadband measurements in the quantum regime as the increased noise at low frequencies constitutes an even higher hurdle when attempting to perform quantum-enhanced force sensing [79] or squeezed light generation [185, 186] with an optomechanical system.

3.6 Conclusion

Building on earlier strategies of integrating a high-stress, $\mathrm{Si_3N_4}$ nanobeam within the evanescent near-field of a $\mathrm{SiO_2}$ microdisk [135, 158], a refined fabrication technique now preserves the high $Q/(\text{mode volume})$ ratio of the optical resonator while enabling the beam and the disk to be separated by a vacuum gap of as small as 10-100 nm – significantly smaller than the evanescent decay length of the optical mode. Samples of various dimensions were fabricated and characterized. Simultaneously low mechanical loss, $\Gamma_\mathrm{m} = 2\pi \cdot (10-100)$ Hz, low optical loss, $\kappa = 2\pi \cdot (100-1000)$ MHz, and large optomechanical coupling rates, $g_0 = 2\pi \cdot (10-100)$ kHz, were measured, corresponding to room temperature single-photon cooperativities as high as $C_0 \equiv 4g_0^2/\Gamma_\mathrm{m}\kappa = 2$.

The engineered system holds particular promise as a quantum-limited displacement sensor even at room temperature, owing to the large vacuum displacement of the nanobeam and the high power handling capacity of the microdisk. For a typical device, possessing $\{\Omega_\mathrm{m}, \Gamma_\mathrm{m}, \kappa_0, g_0\} \approx 2\pi \cdot \{4.5\,\mathrm{MHz}, 15\,\mathrm{Hz}, 500\,\mathrm{MHz}, 50\,\mathrm{kHz}\}$, the resonant vacuum displacement noise, $S_\omega^\mathrm{zp}(\Omega_\mathrm{m}) = 4g_0^2/\Gamma_\mathrm{m} \approx (2\pi \cdot 26\ \mathrm{kHz}/\sqrt{\mathrm{Hz}})^2$, is orders of magnitude larger than major sources of imprecision, such as laser frequency and thermorefractive noise [159], and commensurate with shot noise for an ultra-low intracavity photon number of $n_\mathrm{c} = 1/(16C_0) = 0.05$. Operating a similar device at 4 K with $n_\mathrm{c} \sim 10^5$ (corresponding to $P_\mathrm{in} \sim 100\,\mu\mathrm{W}$ when critically

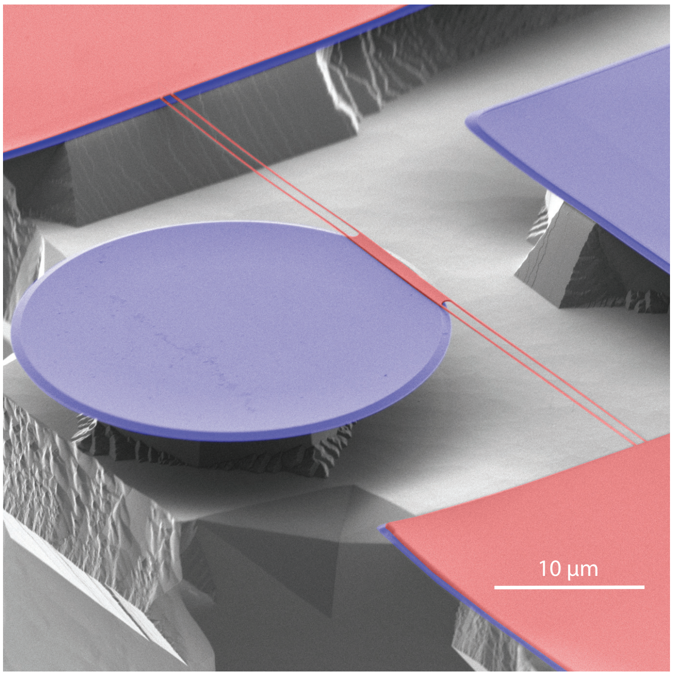

Figure 3.15 – **Tethered beam design.** Suspending the nanobeam from tethers enables higher g_0 by reducing the mass without changing optomechanical mode overlap. In this example, the central beam coincides with the effective sampling length of the optical mode.

coupled to the fiber waveguide), a displacement imprecision 43 dB below S_ω^{zp} was recently demonstrated, while maintaining an imprecision-back-action product within a factor of 5 of the uncertainty limit [73].

An intriguing question is whether the reported device may be used to realize Heisenberg-limited displacement measurements at room temperature – namely, an apparent imprecision-back-action product $\sqrt{(n_{\mathrm{ba}}+n_{\mathrm{th}})\cdot n_{\mathrm{imp}}} \to 1/4$ (see section 3.4). For the radio frequency oscillators under study ($n_{\mathrm{th}} \sim 10^6$), the main challenges are (1) pumping the cavity with $n_{\mathrm{c}} \geq n_{\mathrm{th}}/C_0 \sim 10^6$ photons in order to achieve the necessary measurement strength (characterized by a phonon-equivalent RPSN of $n_{\mathrm{ba}} = C_0 n_{\mathrm{c}} \geq n_{\mathrm{th}}$), (2) reducing extraneous sources of measurement imprecision to $S_\omega^{\mathrm{zp}}/n_{\mathrm{th}} < (2\pi \cdot 10\,\mathrm{Hz}/\sqrt{\mathrm{Hz}})^2$, and (3) reducing extraneous heating to ensure that n_{ba} is dominated by RPSN. Because of the (blue-stable) thermal self-locking effect in room temperature $\mathrm{SiO_2}$ microresonators [187], the first requirement (corresponding to an input power of $P_{\mathrm{in}} \sim 1$ mW for critically coupling with $\kappa \sim 1$ GHz) is expected to be limited by parametric radiation pressure instabilities, requiring active feedback damping. Taking a different approach, cross-correlation techniques may be employed to detect radiation pressure shot noise at the few-% level [58], significantly relaxing associated demands on input power and active stabilization (see main results presented in chapter 4). The second requirement – for microdisks with dimensions studied here – is expected to be limited by thermorefractive noise at the level of $S_\omega^{\mathrm{trn}} \sim (2\pi \cdot 10\,\mathrm{Hz}/\sqrt{\mathrm{Hz}})^2$ [159], an impressive 60 dB lower than S_ω^{zp}. Reaching $S_\omega^{\mathrm{trn}} < S_\omega^{\mathrm{zp}}/n_{\mathrm{th}}$ would require a moderate increase in $g_0^2 \cdot Q_{\mathrm{m}}$ (for instance, by using lower-mass, “tethered" beams [59]; see fig. 3.15). The third requirement depends on the details of the nanoscale heat transfer process. At 4 K, we have observed photothermal heating consistent with an extraneous cooperativity of $C_0^{\mathrm{ext}} \equiv n_{\mathrm{ba}}^{\mathrm{ext}}/n_{\mathrm{c}} \sim 1$ [73]; we anticipate this heating to reduce to tenable levels ($C_0^{\mathrm{ext}} < C_0$) at room temperature, provided that the underlying process is related to the temperature-dependent thermal conductivity of amorphous glass [188]. Preliminary room temperature measurements, discussed in section 3.4, suggest that $C_0^{\mathrm{ext}} \sim C_0$ can be met for a moderate $C_0 \sim 0.8$.

Furthermore, while the engineering of the device has been focused on achieving a quantum noise limited displacement sensor, possible applications of the presented architecture would be their utilization as mass/force/charge sensors [189]. To this end, the practical utility of the reported high-cooperativity evanescent sensing platform lies in the ability to resolve thermal motion with high signal-to-noise and a large bandwidth, which is in contrast to MEMS sensors where the thermal motion is typically masked by Johnson noise. For the nanobeam displacement measurements shown in fig. 3.13, thermal noise is resolved over a bandwidth of ~ MHz at the level of $4k_{\mathrm{B}}T\Gamma_{\mathrm{m}}m \sim (100\,\mathrm{aN}/\sqrt{\mathrm{Hz}})^2$ employing $\sim 10\,\mu\mathrm{W}$ of injected optical power. Notably, a moderate reduction in extraneous imprecision would enable thermal noise to be resolved over a full octave, a difficult challenge for high-Q resonators as it requires resolving the thermal peak with a signal-to-noise of $\sim Q^2$ (eq. (3.4.1)).

4 Quantum correlations of light at room temperature

The radiation pressure interaction of light with mechanical oscillators has been the subject of intense theoretical research in the gravitational wave community [18, 22, 190], leading, for example, to an understanding of the quantum limits of interferometric position measurements. An important insight that could potentially help evade this limit is that the two noise sources that enforce it – quantum (measurement) back-action and imprecision – are in general correlated [191]. From the perspective of the light in the interferometer, quantum fluctuations in its amplitude quadrature drive the oscillator leading to quantum back-action, and the driven motion is imprinted onto the phase quadrature. Ultimately, this leads to correlations between the quantum fluctuations of the amplitude and phase quadratures, i.e. quantum correlations. Correlations thus established form a valuable resource: the optomechanical system may be viewed as an effective Kerr medium generating squeezed states of the optical field [185, 186], or the correlations can be directly employed for back-action cancellation [79, 83, 192, 193]. Indeed, the ability to utilize quantum correlations generated *in-situ* is conceptually identical to injection of squeezed light [83], while circumventing the challenge of realizing a near-unity coupling efficiency between the squeezed light source and the interferometer [81]. The burden of quantum efficiency in this case is shifted to the detector, a problem that is largely solved [194]. Thus, a room-temperature interferometer capable of harnessing in-situ correlations is a platform that may help extend the practical reach of quantum optics, with applications ranging from gravitational wave detection to chip-scale accelerometry.

In practice, owing to the weakness of the radiation pressure force, optomechanical quantum correlations are typically obscured by thermal motion. Only in recent years has this challenge been broached, by the development of cavity optomechanical systems [25], which combine an engineered high Q, *cryogenically-cooled* micromechanical oscillator with a high finesse optical (or microwave) cavity. In such systems, it is possible to realize a regime in which the motion of the oscillator is dominated – or nearly so – by quantum back-action [73–75]. This has enabled studies of various effects related to optomechanical quantum correlations, such as ponderomotive squeezing [60, 61, 148, 150, 195] and motional sideband asymmetry (using autonomous [196–199] or measurement-based [150] feedback to cool the mechanical oscillator). Accessing this regime at *room-temperature* is difficult as the optical powers necessary to overwhelm thermal forces with back-action are typically accompanied by dynamic instabilities [200]. Various cross-correlation techniques have been proposed to relax these requirements and allow observation of quantum correlations near mechanical resonance [201, 202]. In a recent demonstration [67], such a technique was used in the regime of large measurement imprecision to unearth quantum correlations from beneath 60 dB of thermal noise. However, the generation of broadband quantum-noise-induced optomechanical correlations, that could simultaneously ameliorate the limits posed by imprecision and back-action on room-temperature interferometers [79, 83, 192, 203, 204], remains an outstanding challenge.

This chapter presents the first observation of broadband quantum correlations at room temperature, developed in an optical field after interacting with a nanomechanical oscillator [205]. To this end, we utilize an optomechanical system specifically engineered to demonstrate the effects of quantum back-action as described in the previous part of this thesis, and take advantage of its high-cooperativity near-field coupling to an optical microcavity [160].

4.1 Theoretical background

The following section presents the theoretical calculation of quantum correlations of light caused by a mechanical oscillator (section 4.1.1). Section 4.1.2 defines the asymmetry ratio, a useful quantity to evaluate the magnitude of the generated correlations. Finally, section 4.1.3 describes how these correlations can be taken advantage of in order to achieve quantum-enhanced force sensitivity.

4.1.1 Theoretical model for optomechanically induced quantum correlations

We start by considering an optomechanical system consisting of an optical cavity, whose intracavity field is described by the amplitude $a(t)$, dispersively coupled to a mechanical oscillator of effective mass m, whose position is described by $x(t)$. Following standard linearization procedure [25], as already covered in chapter 2, the fluctuations in either variable, denoted δa and δx respectively, satisfy the equations of motion,

$$\delta\dot{a} = \left(i\Delta - \frac{\kappa}{2}\right)\delta a + iG\bar{a}\delta x + \sqrt{\eta_\mathrm{c}\kappa}\,\delta s_\mathrm{in} + \sqrt{(1-\eta_\mathrm{c})\kappa}\,\delta s_\mathrm{vac} \tag{4.1.1}$$

$$m\left(\delta\ddot{x} + \Gamma_\mathrm{m}\delta\dot{x} + \Omega_\mathrm{m}^2\delta x\right) = \delta F_\mathrm{th} + \hbar G\bar{a}(\delta a + \delta a^\dagger). \tag{4.1.2}$$

Following the notations already established earlier, δF_th is the thermal force noise with spectral density, $\bar{S}_{FF}^\mathrm{th} \approx 2m\Gamma_\mathrm{m}k_BT$, and G is the cavity frequency pull parameter (the dispersive optomechanical coupling strength). The noise variables δa_in and δa_0 describe the fluctuations in the cavity input at the coupling port and the port modeling internal losses. The cavity coupling efficiency, $\eta_\mathrm{c} = \kappa_\mathrm{ex}/\kappa$, describes the relative strength of the external coupling port.

The steady state intracavity photon number, $n_c = \bar{a}^2$ is given by,

$$n_c = \frac{4\eta_c}{\kappa}\frac{P_{in}/\hbar\omega_L}{1+4\Delta^2/\kappa^2}, \tag{4.1.3}$$

where P_{in} is the injected probe power at optical frequency ω_L.

In the frequency domain, mechanical motion is described by susceptibility to the applied force $F[\Omega]$,

$$\delta x[\Omega] = \chi_x[\Omega]F[\Omega] = \frac{1}{m(\Omega_m^2 - \Omega^2 - i\Omega\Gamma_m[\Omega])}F[\Omega], \tag{4.1.4}$$

where $\Gamma_m[\Omega]$ is the frequency-dependent damping rate generalizing the velocity-proportional dissipation model in eq. (4.1.1). For the out-of-plane flexural modes of a Si_3N_4 nanostring, this rate is given as, $\Gamma_m[\Omega] \approx \Omega_m\Gamma_m/\Omega$ [179], where Γ_m without argument denotes the intrinsic linewidth of the oscillator's mechanical resonance.

For the following it is convenient to introduce the normalized position, $\delta z := \delta x/x_{ZPF}$, the single- and multi-photon optomechanical coupling rates, $g_0 := Gx_{ZPF}$ and $g := g_0\sqrt{n_c}$, as well as the single- and multi-photon cooperativities, $C_0 := 4g_0^2/\kappa\Gamma_m$ and $C := C_0 n_c$ into the formalism (cf. chapter 2). $x_{ZPF} = \sqrt{\hbar/2m\Omega_m}$ is the zero-point variance in the position of the mechanical oscillator.

In the experimentally relevant situation of resonant probing ($\Delta \approx 0$) and bad cavity limit ($\Omega_m \gg \kappa$), the equation of motion for the cavity field in eq. (4.1.1) assumes the form,

$$\delta a[\Omega] \approx \frac{2ig}{\kappa}\delta z[\Omega] + \frac{2}{\sqrt{\kappa}}\left(\sqrt{\eta_c}\delta s_{in}[\Omega] + \sqrt{1-\eta_c}\delta s_{vac}[\Omega]\right).$$

Using the input-output relation [106], $\delta s_{out} = \delta s_{in} - \sqrt{\eta_c\kappa}\delta a$, the transmitted fluctuations,

$$\delta s_{out}[\Omega] = (1-2\eta_c)\delta s_{in}[\Omega] - 2\sqrt{\eta_c(1-\eta_c)}\,\delta s_{vac}[\Omega] - i\sqrt{\eta_c C\Gamma_m}\,\delta z[\Omega], \tag{4.1.5}$$

carry information regarding the total mechanical motion δz, consisting of the thermal motion and the quantum back-action driven motion, i.e.,

$$\delta z[\Omega] = \delta z_{th}[\Omega] + \delta z_{BA}[\Omega].$$

Here and henceforth, we define the quadratures of the optical field δa,

$$\delta q(t) = \frac{1}{\sqrt{2}}\left(\delta a(t) + \delta a^\dagger(t)\right), \qquad \delta p(t) = \frac{1}{i\sqrt{2}}\left(\delta a(t) - \delta a^\dagger(t)\right). \tag{4.1.6}$$

The back-action motion is given by,

$$\delta z_{BA}[\Omega] = \sqrt{2C\Gamma_m}\chi_z[\Omega]\left(\sqrt{\eta_c}\delta q_{in}[\Omega] + \sqrt{1-\eta_c}\,\delta q_{vac}[\Omega]\right), \tag{4.1.7}$$

where δq_{in} and δq_0 are the amplitude quadrature fluctuations from the two cavity input ports and $\chi_z[\Omega] = \hbar\chi_x[\Omega]/x_{\mathrm{ZPF}}^2$ is the oscillator susceptibility in new units,

$$\chi_z[\Omega] = \frac{2\Omega_{\mathrm{m}}}{\Omega_{\mathrm{m}}^2 - \Omega^2 - i\Omega\Gamma_{\mathrm{m}}[\Omega]} \approx \frac{1}{(\Omega_{\mathrm{m}} - \Omega) - i\Gamma_{\mathrm{m}}/2}, \tag{4.1.8}$$

where the approximation is valid close to the mechanical resonance, i.e. for $|\Omega_{\mathrm{m}} - \Omega| \ll \Omega_{\mathrm{m}}$.

Inserting eq. (4.1.7) in eq. (4.1.5), the two quadratures of the cavity transmission are,

$$\begin{aligned}\delta q_{\mathrm{out}}[\Omega] =&(1-2\eta_{\mathrm{c}})\delta q_{\mathrm{in}}[\Omega] - 2\sqrt{\eta_{\mathrm{c}}(1-\eta_{\mathrm{c}})}\,\delta q_0[\Omega]\\ \delta p_{\mathrm{out}}[\Omega] =&(1-2\eta_{\mathrm{c}})\delta p_{\mathrm{in}}[\Omega] - 2\sqrt{\eta_{\mathrm{c}}(1-\eta_{\mathrm{c}})}\,\delta p_0[\Omega]\\ &- \sqrt{2\eta_{\mathrm{c}}C\Gamma_{\mathrm{m}}}\left[\delta z_{\mathrm{th}}[\Omega] + \sqrt{2C\Gamma_{\mathrm{m}}}\chi_z[\Omega]\left(\sqrt{2\eta_{\mathrm{c}}}\delta q_{\mathrm{in}}[\Omega] + \sqrt{2(1-\eta_{\mathrm{c}})}\delta q_0[\Omega]\right)\right].\end{aligned} \tag{4.1.9}$$

For a general quadrature at angle θ, defined by,

$$\delta q_{\mathrm{out}}^{\theta}[\Omega] \equiv \delta q_{\mathrm{out}}[\Omega]\cos\theta + \delta p_{\mathrm{out}}[\Omega]\sin\theta, \tag{4.1.10}$$

it follows that,

$$\begin{aligned}\left\langle \delta q_{\mathrm{out}}^{\theta}[\Omega]\delta q_{\mathrm{out}}^{\theta}[-\Omega]\right\rangle =&\cos^2\theta\,\langle\delta q_{\mathrm{out}}[\Omega]\delta q_{\mathrm{out}}[-\Omega]\rangle\\ &+\sin^2\theta\,\langle\delta p_{\mathrm{out}}[\Omega]\delta p_{\mathrm{out}}[-\Omega]\rangle\\ &+\sin(2\theta)\,\mathrm{Re}\,\langle\delta q_{\mathrm{out}}[\Omega]\delta p_{\mathrm{out}}[-\Omega]\rangle.\end{aligned} \tag{4.1.11}$$

The homodyne photocurrent spectrum is related to this correlator via,

$$\begin{aligned}&\bar{S}_{II}^{\theta}[\Omega]\cdot 2\pi\delta[0] \propto \bar{S}_{qq}^{\theta,\mathrm{out}}[\Omega]\cdot 2\pi\delta[0] = \frac{1}{2}\left\langle\{\delta q_{\mathrm{out}}^{\theta}[\Omega], \delta q_{\mathrm{out}}^{\theta}[-\Omega]\}\right\rangle,\\ \text{i.e.,}\quad &\bar{S}_{II}^{\theta}[\Omega] = \cos^2\theta\,\bar{S}_{qq}^{\mathrm{out}}[\Omega] + \sin^2\theta\,\bar{S}_{pp}^{\mathrm{out}}[\Omega] + \sin(2\theta)\,\bar{S}_{pq}^{\mathrm{out}}[\Omega].\end{aligned} \tag{4.1.12}$$

The relevant spectra of the output field quadratures is explicitly given by,

$$\bar{S}_{qq}^{\mathrm{out}}[\Omega] = \tfrac{1}{2}, \tag{4.1.13}$$

$$\bar{S}_{pp}^{\mathrm{out}}[\Omega] = \tfrac{1}{2} + 2\eta_{\mathrm{c}}C\Gamma_{\mathrm{m}}\left(\bar{S}_{zz}^{\mathrm{th}}[\Omega] + \bar{S}_{zz}^{\mathrm{BA}}[\Omega]\right), \tag{4.1.14}$$

$$\bar{S}_{pq}^{\mathrm{out}}[\Omega] = \eta_{\mathrm{c}}C\Gamma_{\mathrm{m}}\mathrm{Re}\,\chi_z[\Omega]. \tag{4.1.15}$$

For a detection near the amplitude quadrature ($\theta \approx 0$) where the signal due to the thermal motion is strongly suppressed, the asymmetric contribution (third term in eq. (4.1.12)) becomes significant. Figure 4.1 shows the total expected signal leading to a distorted Lorentzian line shape. The correlations can in principle even cause a back-action cancellation of the total signal below the shot noise level, a phenomenon called *ponderomotive squeezing* [185].

Inserting the above expressions in eq. (4.1.12), we arrive at the homodyne photocurrent spectrum (normalized to electronic shot noise and omitting the negligible contribution from

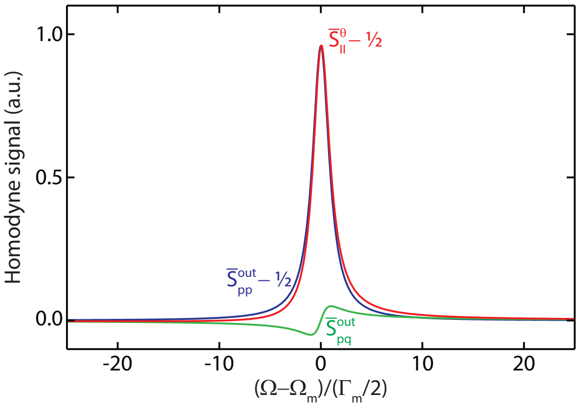

Figure 4.1 – **Model of the homodyne photocurrent spectrum.** For detection near the amplitude quadrature ($\theta \approx 0$), the measured signal $\bar{S}^{\theta}_{II}[\Omega]$ (red trace) has a symmetric part $\bar{S}^{\mathrm{out}}_{pp}[\Omega]$ (blue trace) due to physical motion, composed of thermal ($\bar{S}^{\mathrm{th}}_{zz}[\Omega]$) and back-action motion ($\bar{S}^{\mathrm{BA}}_{zz}[\Omega]$), and an asymmetric part $\bar{S}^{\mathrm{out}}_{pq}[\Omega]$ (green) due to quantum correlations (see eq. (4.1.12)). Note that the zero-point motion (contribution 1/2) is subtracted for $\bar{S}^{\mathrm{out}}_{pp}[\Omega]$.

detector electronic noise),

$$\bar{S}^{\theta}_{II}[\Omega] = 1 + 4\eta C\Gamma_{\mathrm{m}}\left(\bar{S}_{zz}[\Omega]\sin^2\theta + \frac{1}{2}\sin(2\theta)\,\mathrm{Re}\,\chi_z[\Omega]\right), \tag{4.1.16}$$

with the detection efficiency η. Note that henceforth, photocurrent spectra are implicitly normalized to shot noise. Using the fluctuation-dissipation theorem [142] to relate the thermal and back-action force noise to mean phonon occupations n_{th} and n_{QBA} respectively, the spectral density of the total motion,

$$\bar{S}_{zz}[\Omega] = \left|\chi_z[\Omega]\right|^2\left(\Gamma_{\mathrm{m}}[\Omega]\,n_{\mathrm{th}} + \Gamma_{\mathrm{m}}\,n_{\mathrm{QBA}}\right), \tag{4.1.17}$$

where, $n_{\mathrm{th}} = k_B T/\hbar\Omega_{\mathrm{m}} \gg 1$ is the average thermal occupation, and, $n_{\mathrm{QBA}} = C = C_0 n_{\mathrm{c}}$ is the average occupation due to (quantum) back-action arising from vacuum fluctuations in the input amplitude quadrature.

4.1.2 Analysis of the correlation magnitude

In the regime when $n_{\mathrm{QBA}} \ll n_{\mathrm{th}}$, as it is the case at ambient temperature, the correlation term in the eq. (4.1.16) is small compared to shot noise and thermomechanical noise $4\eta C\Gamma_{\mathrm{m}}\bar{S}_{zz}$. Therefore, in order to visualize the correlations we consider $R(\theta,\delta)$, the ratio of the homodyne spectral densities symmetrically detuned to the high and low frequencies from the mechanical resonance,

$$R(\theta,\delta) = \frac{\bar{S}^{\theta}_{II}[\Omega_{\mathrm{m}}+\delta]}{\bar{S}^{\theta}_{II}[\Omega_{\mathrm{m}}-\delta]}. \tag{4.1.18}$$

In the limit of $\delta \ll \Omega_\mathrm{m}$, the thermomechanical motion spectrum $\bar{S}_{zz}[\Omega]$ is symmetric about Ω_m and $\mathrm{Re}\,\chi_z[\Omega]$ is antisymmetric, so $R(\theta,\delta)$ only deviates from 1 due to the correlation term,

$$R(\theta,\delta)|_{\delta\ll\Omega_\mathrm{m}} \approx 1 + \frac{4\eta C\Gamma_\mathrm{m}\sin(2\theta)}{1+4\eta C\Gamma_\mathrm{m}\bar{S}_{zz}[\Omega_\mathrm{m}+\delta]\sin^2\theta}\mathrm{Re}\,\chi_z[\Omega_\mathrm{m}+\delta]. \tag{4.1.19}$$

Maximization/minimization of R given by the eq. (4.1.19) over θ yields

$$\begin{aligned}\Delta R(\delta) &= \max_\theta R(\theta,\delta) - \min_\theta R(\theta,\delta)\\ &= 2\frac{4\eta C\Gamma_\mathrm{m}\mathrm{Re}\,\chi_z[\Omega_\mathrm{m}+\delta]}{\sqrt{1+4\eta C\Gamma_\mathrm{m}\bar{S}_{zz}[\Omega_\mathrm{m}+\delta]}}\\ &\approx 4\frac{\eta C/n_\mathrm{th}}{\sqrt{(\delta/2\Gamma_\mathrm{m}n_\mathrm{th})^2+\eta C/n_\mathrm{th}}}\\ &\approx 4\sqrt{\frac{\eta C}{n_\mathrm{th}}} = 4\sqrt{\eta\frac{n_\mathrm{QBA}}{n_\mathrm{th}}} \quad \text{if} \quad \Gamma_\mathrm{m} \ll \delta \ll 2\Gamma_\mathrm{m}\sqrt{\eta C n_\mathrm{th}}.\end{aligned} \tag{4.1.20}$$

Considering broad frequency ranges, however, one has to account for the deviation of χ_x (and therefore also of χ_z) from a single-pole Lorentzian and for the thermal force noise not being perfectly white. Up to the 1-st order in $(\bar{S}_{zz}[\Omega_\mathrm{m}+\delta]-\bar{S}_{zz}[\Omega_\mathrm{m}-\delta])$ the approximation in this case is given as,

$$\begin{aligned}R(\theta,\delta) \approx 1 + \frac{4\eta C\Gamma_\mathrm{m}}{1+4\eta C\Gamma_\mathrm{m}\bar{S}_{zz}[\Omega_\mathrm{m}+\delta]\sin^2\theta}\Big(&\sin(2\theta)\mathrm{Re}\,\chi_z[\Omega_\mathrm{m}+\delta]\\ &+\frac{1}{2}\sin^2\theta(\bar{S}_{zz}[\Omega_\mathrm{m}+\delta]-\bar{S}_{zz}[\Omega_\mathrm{m}-\delta])\Big).\end{aligned} \tag{4.1.21}$$

In the approximation of eq. (4.1.19), $R_\theta - 1$ is antisymmetric in the quadrature angle θ, with its magnitude being proportional to $\sqrt{\eta\, n_\mathrm{QBA}/n_\mathrm{th}}$. For δ further from the mechanical resonance, the antisymmetric part of $R_\theta - 1$ still has the same meaning, but it becomes superimposed with a classical contribution symmetric in θ.

4.1.3 Quantum-enhanced force sensitivity

We consider now the problem of estimating an arbitrary force, δF, acting on the mechanical oscillator. The homodyne photocurrent spectrum carries information about the force. From eq. (4.1.12) follows,

$$\bar{S}^\theta_{II}[\Omega] = 1 + 4\eta C\Gamma_\mathrm{m}\left[\left|\chi_x[\Omega]\right|^2\left(\bar{S}_{FF}[\Omega]+\bar{S}^\mathrm{QBA}_{FF}[\Omega]\right)\sin^2\theta + \frac{1}{2}\sin(2\theta)\mathrm{Re}\chi_x[\Omega]\right]. \tag{4.1.22}$$

The spectrum of the force, $\bar{S}_{FF}[\Omega]$, can be estimated from the photocurrent spectrum via,

$$\bar{S}^{\mathrm{est},\theta}_{FF}[\Omega] \equiv \frac{\bar{S}^\theta_{II}[\Omega]}{4\eta C\Gamma_\mathrm{m}\left|\chi_x[\Omega]\right|^2\sin^2\theta}. \tag{4.1.23}$$

The spectrum of this force estimator takes the form,

$$\bar{S}_{FF}^{\mathrm{est},\theta}[\Omega] = \bar{S}_{FF}[\Omega] + \bar{S}_{FF}^{\mathrm{QBA}}[\Omega] + \underbrace{\frac{1}{4\eta C\Gamma_{\mathrm{m}}\left|\chi_x[\Omega]\right|^2 \sin^2\theta}}_{\bar{S}_{FF}^{\mathrm{imp},\theta}} + \cot\theta\,\frac{\mathrm{Re}\,\chi_x[\Omega]}{\left|\chi_x[\Omega]\right|^2}. \tag{4.1.24}$$

Here, the first term represents the spectral density to be estimated. The second term, positive at all frequencies, is the contamination in the measurement record due to quantum back-action. The third term, also positive, is the imprecision due to shot-noise in the detection. The last term is due to quantum correlations between the back-action and imprecision in homodyne measurement record that can be negative at some frequencies, providing for reduced uncertainty in the ability to estimate the force.

Note that precisely on resonance ($\Omega = \Omega_{\mathrm{m}}$), and/or, for phase quadrature homodyne measurement ($\theta = \pi/2$), correlations do not contribute to the estimator; so any reduction in uncertainty can only be expected away from resonance for quadrature-detuned homodyne measurement.

For a fixed probe strength, i.e. fixed cooperativity C, there exists a frequency dependent homodyne phase at which the correlation and the imprecision $\bar{S}_{FF}^{\mathrm{imp},\theta}$ achieve an optimal trade-off. This optimal angle $\theta_{\mathrm{opt}}[\Omega]$ is determined by,

$$\begin{aligned}\cot\theta_{\mathrm{opt}}[\Omega] &= -2\eta C\Gamma_{\mathrm{m}}\mathrm{Re}\,\chi_x[\Omega] \\ &= 4\eta C\frac{\Omega_{\mathrm{m}}\Gamma_{\mathrm{m}}(\Omega^2-\Omega_{\mathrm{m}}^2)}{(\Omega^2-\Omega_{\mathrm{m}}^2)^2+(\Omega\Gamma_{\mathrm{m}}[\Omega])^2}.\end{aligned} \tag{4.1.25}$$

At this optimal angle, the spectrum of the force estimator takes the form,

$$\bar{S}_{FF}^{\mathrm{est},\theta_{\mathrm{opt}}}[\Omega] = \bar{S}_{FF}[\Omega] + \bar{S}_{FF}^{\mathrm{QBA}}[\Omega] + \frac{1}{4\eta C\Gamma_{\mathrm{m}}\left|\chi_x[\Omega]\right|^2} - \eta C\Gamma_{\mathrm{m}}\left(\frac{\mathrm{Re}\,\chi_x[\Omega]}{\left|\chi_x[\Omega]\right|}\right)^2. \tag{4.1.26}$$

Noting that the third term is simply $\bar{S}_{FF}^{\mathrm{imp},\pi/2}$, and that $\bar{S}_{FF}^{\mathrm{QBA}}[\Omega] = C\Gamma_{\mathrm{m}}$, this equation can be re-expressed in the suggestive form,

$$\bar{S}_{FF}^{\mathrm{est},\theta_{\mathrm{opt}}}[\Omega] = \bar{S}_{FF}[\Omega] + \bar{S}_{FF}^{\mathrm{imp},\pi/2}[\Omega] + \bar{S}_{FF}^{\mathrm{QBA}}[\Omega]\left[1-\eta\left(\frac{\mathrm{Re}\,\chi_x[\Omega]}{\left|\chi_x[\Omega]\right|}\right)^2\right]. \tag{4.1.27}$$

Thus, at the optimal detection angle, *quantum correlations conspire to cancel quantum back-action (in the measurement record) and reduce the error in the force estimation* compared to the conventional choice $\theta = \pi/2$, for which correlations are absent and

$$\bar{S}_{FF}^{\mathrm{est},\pi/2}[\Omega] = \bar{S}_{FF} + \bar{S}_{FF}^{\mathrm{imp},\pi/2}[\Omega] + \bar{S}_{FF}^{\mathrm{QBA}}[\Omega]. \tag{4.1.28}$$

Correlation enhanced thermal force sensing

In the case of an oscillator in thermal equilibrium quantum correlations can yield improved sensitivity in the detection of the thermal force. In such a case the signal is the thermal force noise, i.e. $\bar{S}_{FF} = \bar{S}_{FF}^{\mathrm{th}}$. Assuming that the recorded periodogram of the photocurrent has converged to the theoretical power spectrum, the homodyne angle dependent uncertainty in the spectral estimation of the thermal force may be defined by,

$$\epsilon_\theta[\Omega] \equiv \bar{S}_{FF}^{\mathrm{est},\theta}[\Omega] - \bar{S}_{FF}^{\mathrm{th}}[\Omega]. \tag{4.1.29}$$

If we consider the ratio of uncertainties for the phase quadrature measurement ($\theta = \pi/2$) and for the measurement at a detuned detuned quadrature θ,

$$\xi_\theta[\Omega] = \frac{\epsilon_{\pi/2}[\Omega]}{\epsilon_\theta[\Omega]} = \frac{\bar{S}_{FF}^{\mathrm{imp},\pi/2}[\Omega] + \bar{S}_{FF}^{\mathrm{QBA}}[\Omega]}{\frac{\bar{S}_{FF}^{\mathrm{imp},\pi/2}[\Omega]}{\sin^2\theta} + \cot\theta \frac{\mathrm{Re}\,\chi_x[\Omega]}{|\chi_x[\Omega]|^2} + \bar{S}_{FF}^{\mathrm{QBA}}[\Omega]}, \tag{4.1.30}$$

the sensitivity enhancement due to back-action cancellation takes place when $\xi_\theta > 1$ for θ such that $\frac{\bar{S}_{FF}^{\mathrm{imp},\pi/2}[\Omega]}{\sin^2\theta} + \cot\theta \frac{\mathrm{Re}\,\chi_x[\Omega]}{|\chi_x[\Omega]|^2} < \bar{S}_{FF}^{\mathrm{imp},\pi/2}[\Omega] < \bar{S}_{FF}^{\mathrm{imp},\pi/2}[\Omega]$.

The enhancement in sensitivity attained for measurement at the frequency-dependent optimal quadrature θ_{opt}, compared to the conventional measurement on phase quadrature, is quantified by,

$$\xi_\theta[\Omega] = \frac{\epsilon_{\pi/2}[\Omega]}{\epsilon_{\theta_{\mathrm{opt}}}[\Omega]} = \frac{\bar{S}_{FF}^{\mathrm{imp},\pi/2}[\Omega] + \bar{S}_{FF}^{\mathrm{QBA}}[\Omega]}{\bar{S}_{FF}^{\mathrm{imp},\pi/2}[\Omega] + \bar{S}_{FF}^{\mathrm{QBA}}[\Omega]\left[1 - \eta\left(\mathrm{Re}\,\chi_x[\Omega]/\left|\chi_x[\Omega]\right|\right)^2\right]} \approx \left[1 - \eta\left(\frac{\mathrm{Re}\,\chi_x[\Omega]}{\left|\chi_x[\Omega]\right|}\right)^2\right]^{-1}, \tag{4.1.31}$$

where the last approximation is valid when $\bar{S}_{FF}^{\mathrm{QBA}}[\Omega] \gg \bar{S}_{FF}^{\mathrm{imp},\pi/2}[\Omega]$, i.e. in the limit of large cooperativity $C \gg 1$ and for frequency offsets around the mechanical resonance $|\Omega - \Omega_{\mathrm{m}}|/\Gamma_{\mathrm{m}} \ll 2\sqrt{\eta}C$. In this regime $\xi_\theta > 1$ and quantum-enhanced force sensitivity can be realized, with the enhancement factor being limited by the finite detection efficiency η and the imaginary part of the mechanical susceptibility. The back-estimated factors $\xi_\theta[\Omega]$ for the parameters of our experiment are shown at the Figure 4.2 and demonstrate thermal force sensitivity enhancement up to 25%.

The ability to better estimate the thermal force over a broad range of frequencies may open up opportunities for probing the structure of the weak thermal environment that the oscillator is coupled to.

Correlation enhanced external force sensing

If an optomechancial system is used for external incoherent force detection, the thermal force itself becomes a part of the noise background. We now consider the sensitivity enhancement

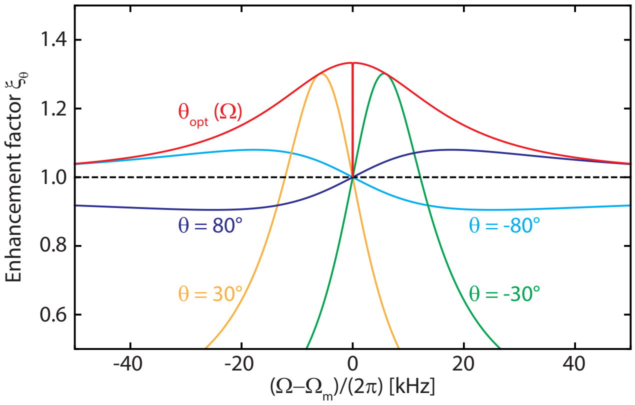

Figure 4.2 – **Theoretical quantum-enhanced sensitivity to thermal force:** Quantum-enhanced sensitivity to thermal force for the parameters realized in the current experiment, assuming input power = 25 μW. Plot shows the enhancement factor $\xi_\theta[\Omega]$, defined in eq. (4.1.30) and eq. (4.1.31), as a function of Fourier frequency and homodyne angle θ. The dashed black line corresponds to $\xi_{\pi/2}[\Omega]$, where force is estimated by phase quadrature detection, where back-action-imprecision correlations are absent. As the homodyne angle is detuned from phase quadrature, enhancement of up to 25% can be observed, limited by the detection efficiency of similar magnitude. The yellow curve shows the theoretically ideal detection scheme, where the homodyne angle is frequency dependent (eq. (4.1.25)), so that broadband enhancement is realized.

in such a case, i.e. $\bar{S}_{FF} = \bar{S}_{FF}^{\text{ext}} + \bar{S}_{FF}^{\text{th}}$, and the error is,

$$\epsilon_\theta[\Omega] \equiv \bar{S}_{FF}^{\text{est}}[\Omega] - \bar{S}_{FF}^{\text{ext}}[\Omega]. \tag{4.1.32}$$

The corresponding expression for the sensitivity enhancement,

$$\xi_{\text{ext}}[\Omega] = \frac{\epsilon_{\pi/2}[\Omega]}{\epsilon_{\theta_{\text{opt}}}[\Omega]} = \frac{\bar{S}_{FF}^{\text{imp},\pi/2}[\Omega] + \bar{S}_{FF}^{\text{th}}[\Omega] + \bar{S}_{FF}^{\text{QBA}}[\Omega]}{\bar{S}_{FF}^{\text{imp},\pi/2}[\Omega] + \bar{S}_{FF}^{\text{th}}[\Omega] + \bar{S}_{FF}^{\text{QBA}}[\Omega]\left[1-\eta\left(\operatorname{Re}\chi_x[\Omega]/\left|\chi_x[\Omega]\right|\right)^2\right]}, \tag{4.1.33}$$

indicates an additional constraint to be met due to the presence of the thermal force – the quantum back-action force needs to be comparable to the thermal force.

For room temperature experiments to date, the regime $n_{\text{QBA}}/n_{\text{th}} \ll 1$ (with $n_{\text{th}} \gg 1$) has been relevant, so, again for the case $\bar{S}_{FF}^{\text{QBA}} \gg \bar{S}_{FF}^{\text{imp},\pi/2}$,

$$\xi_{\text{ext}}[\Omega] \approx 1 + \eta \frac{n_{\text{QBA}}}{n_{\text{th}}} \left(\frac{\operatorname{Re}\chi_x[\Omega]}{\left|\chi_x[\Omega]\right|} \right)^2, \tag{4.1.34}$$

and quantum-enhanced sensitivity to external force can be realized far off resonance, if QBA is significant compared to thermal noise.

In future experiments, where $n_{\text{QBA}}/n_{\text{th}} \gg 1$ may be achieved, the improvement for external force sensitivity scales as,

$$\xi_{\text{ext}}[\Omega] \approx \frac{1}{1-\eta(\operatorname{Re}\chi_x/\left|\chi_x\right|)^2}\left[1 - \mathcal{O}\left(\frac{n_{\text{th}}}{n_{\text{QBA}}}\right)\right], \tag{4.1.35}$$

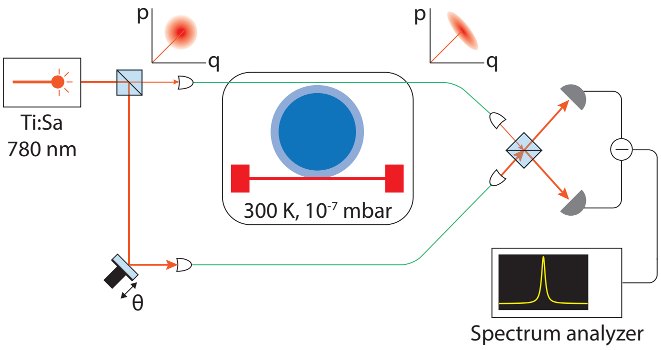

Figure 4.3 – **Optomechanical quantum correlations.** (A) Schematic of the experiment: The optomechanical system is formed by a Si_3N_4 nanobeam oscillator (red) evanescently coupled to a SiO_2 microdisk cavity (blue). Both are maintained at room temperature ($T \approx 300\,K$) in a low pressure ($\approx 10^{-7}$ mbar) vacuum chamber. The cavity is probed on resonance with 780 nm light from a Ti:Sa laser. The transmitted field is read out with a homodyne detector with variable local oscillator phase θ. Amplitude and phase fluctuations of the light field are correlated after passing through the cavity; here represented as squashing in a phase space cartoon.

so that arbitrarily large enhancement may be realized far off resonance, limited by the detection efficiency.

4.2 Experimental results

This section presents the results of the observation of quantum correlations of light generated by reflection from a room temperature nanomechanical oscillator coupled to a high finesse broadband optical microcavity and discusses how to use these correlations to realize a quantum-enhanced mechanical force sensor. To this end, the large bandwidth of the cavity and the exceptionally high Q/mass of the oscillator allows us to operate in a novel regime where the magnitude of quantum correlations is comparable to both sources of quantum noise – imprecision and back-action – at Fourier frequencies detuned as much as an octave from mechanical resonance. In a suitably chosen field quadrature, correlations manifest as a reduction or enhancement in the fluctuation spectrum at Fourier frequencies detuned from mechanical resonance. Though the fluctuations are contaminated by thermal noise and do not drop below the vacuum level – the condition for ponderomotive squeezing – their reduction provides a metrological advantage, since its origin is a coherent cancellation of quantum noises. Counter-intuitively, as a result of this coherence, we observe a 10% noise reduction despite the fact that back-action is 20 dB smaller, in equivalent phonon units (n_{QBA}), than thermal noise ($n_{\mathrm{th}} \approx k_B T/\hbar\Omega_{\mathrm{m}} \approx 10^6$). Indeed, at optimal Fourier frequencies, the fractional noise reduction scales as $\sqrt{n_{\mathrm{QBA}}/n_{\mathrm{th}}}$, distinguishing it from classical noise correlations, and enabling an enhanced estimate of the quantum back-action force relative to standard 'calorimetric' measurements [73–75]. Finally, we demonstrate how quantum correlations can be used to improve the signal-to-noise ratio for the estimation of an off-resonant force.

4.2.1 Concept of the experiment

Accessing the above physics requires the ability to resolve back-action-driven motion far from mechanical resonance, a regime traditionally studied for gravitational wave detectors, but only recently accessed experimentally, using high-cooperativity cryogenic micro-cavity optomechanical systems operating deep in the so-called bad cavity limit [73, 150]. Our system was optimized for achieving this regime at room temperature and is detailed in chapter 3. As illustrated in fig. 4.3, it consists of a Si_3N_4 nanomechanical beam coupled dispersively to a whispering gallery mode of a silica microdisk. The beam has an exceptionally high room temperature Q/mass factor due to its high stress and quasi-1D geometry. To enhance its optomechanical coupling, it is suspended ≈ 50 nm from the surface of the disk and profiled to increase its overlap with the optical mode (see section 4.3.1). This results in a vacuum optomechanical coupling rate of $g_0 \approx 2\pi \cdot 60$ kHz for the fundamental, $\Omega_\mathrm{m} = 2\pi \cdot 3.4$ MHz flexural beam mode – a three-fold increase over previous implementations of the device [73, 150]. In conjunction with the high room temperature mechanical quality factor, $Q_\mathrm{m} \approx 3 \cdot 10^5$ (giving a damping rate of $\Gamma_\mathrm{m} = \Omega_\mathrm{m}/Q_m \approx 2\pi \cdot 12$ Hz), and a critically coupled cavity decay rate of $\kappa \approx 2\pi \cdot 4.5$ GHz, a near-unity single photon cooperativity of $C_0 = 4g_0^2/\kappa\Gamma_\mathrm{m} \approx 0.27$ is attained. Importantly, the system operates in the broadband regime (bad-cavity limit), i.e. $\kappa \gg \Omega_\mathrm{m}$.

In the experiment, as illustrated in the scheme in fig. 4.3, the optomechanical device is placed in a high-vacuum chamber and probed on resonance using a Ti:Sa laser. As in detail shown in section 4.1.1, the motion of the oscillator, characterized by the Fourier transform of its displacement fluctuation $\delta x[\Omega]$, is imprinted on the transmitted phase quadrature as,

$$\delta p_\mathrm{out}[\Omega] = -\delta p_\mathrm{in}[\Omega] + \sqrt{2C\Gamma_\mathrm{m}}\frac{\delta x[\Omega]}{x_\mathrm{zp}}, \tag{4.2.1}$$

where p_in is the phase quadrature of the input field, $x_\mathrm{zp} = \sqrt{\hbar/2m\Omega_\mathrm{m}}$ is the zero-point motion of the oscillator, and $C = C_0 n_c$ is the multi-photon cooperativity for the mean intracavity photon number n_c. The displacement has components from the ambient thermal environment, and quantum back-action,

$$\delta x[\Omega] = \delta x_\mathrm{th}[\Omega] + \delta x_\mathrm{QBA}[\Omega] \tag{4.2.2}$$

The thermal motion,

$$\delta x_\mathrm{th}[\Omega] = 2x_\mathrm{zp}\chi[\Omega]\sqrt{(n_\mathrm{th} + \tfrac{1}{2})/\Gamma_\mathrm{m}}\,\delta\xi[\Omega], \tag{4.2.3}$$

is due to a Langevin force of intensity proportional to the average thermal occupation n_th, and fluctuating as a white noise $\delta\xi$, characterized by,

$$\langle\delta\xi(t)\delta\xi(t')\rangle = \delta(t - t'). \tag{4.2.4}$$

The force fluctuations are transduced into displacement fluctuations via the dimensionless susceptibility of the oscillator,

$$\chi[\Omega] \equiv \frac{\Omega_\mathrm{m}\Gamma_\mathrm{m}}{\Omega_\mathrm{m}^2 - \Omega^2 - i\Omega\Gamma_\mathrm{m}} = \chi_x[\Omega]\, m\Omega_\mathrm{m}\Gamma_\mathrm{m}, \tag{4.2.5}$$

where χ_x is the conventional susceptibility. The back-action driven motion,

$$\delta x_\mathrm{QBA}[\Omega] = 2x_\mathrm{zp}\chi[\Omega]\sqrt{2n_\mathrm{QBA}/\Gamma_\mathrm{m}}\,\delta q_\mathrm{in}[\Omega], \tag{4.2.6}$$

arises from quantum fluctuations in the amplitude quadrature of the input field, δq_in, characterized by,

$$\langle \delta q_\mathrm{in}(t)\delta q_\mathrm{in}(t')\rangle = \frac{1}{2}\delta(t-t'), \tag{4.2.7}$$

and leads to an additional phonon occupation, $n_\mathrm{QBA} = C$. Note that here, we adopt the definition, $\delta q_\mathrm{in} = (\delta a_\mathrm{in} + \delta a_\mathrm{in}^\dagger)/\sqrt{2}$, for the amplitude quadrature. This, in conjunction with the conventional correlator for the photon flux $\langle \delta a_\mathrm{in}^\dagger(t)\delta a_\mathrm{in}(t')\rangle = \delta(t-t')$, gives a factor of $1/2$ in the correlator for the amplitude quadrature.

Because δq_in is written onto the output optical phase vis-a-vis back-action, the amplitude and phase quantum fluctuations of the output field are correlated. The magnitude of these quantum correlations is characterized by the symmetrized cross-correlation spectrum (see section 4.1.1),

$$\begin{aligned} \bar{S}_{pq}^\mathrm{out}[\Omega] &\equiv \int \langle \tfrac{1}{2}\{\delta p_\mathrm{out}(t), \delta q_\mathrm{out}(0)\}\rangle e^{i\Omega t}\, dt \\ &= 2\eta\, n_\mathrm{QBA}\,\mathrm{Re}\,\chi[\Omega], \end{aligned} \tag{4.2.8}$$

which is proportional to the back-action occupation, and the overall detection efficiency η. The correlation changes sign across the mechanical resonance frequency because of the 180° phase change in the response of the oscillator to the quantum back-action force.

Phase-amplitude correlations can be experimentally accessed by measuring a linear superposition of both the amplitude and phase of the transmitted field. Proper choice of the superposition, exemplified by a homodyne detector, allows for a quantum-limited measurement of both quadratures. Specifically, the transmitted field is interfered at a beam-splitter with a strong local oscillator field at a fixed phase offset θ, followed by balanced detection of the two output of the beam-splitter. In this case, the photocurrent I_θ, is proportional to the rotated field quadrature, $\delta q_\theta = \delta q \cos\theta + \delta p \sin\theta$. Its spectrum therefore contains contributions due to amplitude/phase vacuum noise, oscillator motion, and quantum correlations,

$$\bar{S}_{II}^\theta[\Omega] \propto \cos^2\theta\, \bar{S}_{qq}^\mathrm{out}[\Omega] + \sin^2\theta\, \bar{S}_{pp}^\mathrm{out}[\Omega] + \sin(2\theta)\, \bar{S}_{pq}^\mathrm{out}[\Omega], \tag{4.2.9}$$

where,

$$\bar{S}^{\text{out}}_{qq}[\Omega] = \tfrac{1}{2}, \tag{4.2.10}$$

$$\bar{S}^{\text{out}}_{pp}[\Omega] = \tfrac{1}{2} + 8\eta C \left|\chi[\Omega]\right|^2 (n_{\text{tot}} + \tfrac{1}{2}), \tag{4.2.11}$$

are, respectively, the transmitted amplitude quadrature spectrum (containing a copy of the incident vacuum fluctuations) and the transmitted phase quadrature spectrum (carrying in addition, the total motion of the oscillator transduced via the optomechanical interaction). Here, $n_{\text{tot}} = n_{\text{th}} + n_{\text{QBA}}$ is the phonon occupation of the oscillator due to the combined effect of the thermal and back-action forces.

The homodyne photocurrent spectrum (in eq. (4.2.9)), expressed in terms of the mechanical response,

$$\bar{S}^{\theta}_{II}[\Omega] \propto 1 + 16\eta C \left|\chi[\Omega]\right|^2 \left(n_{\text{tot}} + \tfrac{1}{2}\right) \sin^2\theta + 4\eta C \operatorname{Re}\chi[\Omega] \sin 2\theta, \tag{4.2.12}$$

consists of a measurement imprecision due to vacuum fluctuations of the detected quadrature, a component due to the motion of the oscillator diminished by a $\sin^2\theta$ factor, and a component due to correlations between the imprecision and the quantum back-action ($\propto \sin 2\theta$). By exploiting its different dependence on the homodyne angle and Fourier frequency, the correlation term may be detected despite the large thermal motion of the oscillator at room-temperature. Specifically, near the amplitude quadrature ($\theta = 0°$) and at Fourier frequencies detuned from mechanical resonance ($|\Omega - \Omega_{\text{m}}| \gtrsim \Gamma_{\text{m}}$), the contribution of thermal and back-action forces is suppressed relative to the correlation term. Closer inspection shows that a necessary requirement for the correlation term to dominate eq. (4.2.12) is that the back-action force dominates the thermal force: $n_{\text{QBA}} \gtrsim n_{\text{th}}$.

The large thermal occupation of room temperature mechanical oscillators makes it technically challenging to achieve $n_{\text{QBA}} > n_{\text{th}}$. Nevertheless, even when $n_{\text{QBA}} \ll n_{\text{th}}$, the signature of quantum correlations can still be discerned in the homodyne photocurrent spectrum at frequencies far detuned from mechanical resonance (alternate detection techniques have been demonstrated [150, 197], and proposed [206], to detect back-action-induced quantum correlations on mechanical resonance). To wit, for a detuning $\delta \equiv \Omega - \Omega_{\text{m}}$ which is larger than Γ_{m}, the homodyne photocurrent spectrum takes on a characteristic anti-symmetry with respect to both δ and θ [201, 202]

$$\bar{S}^{\theta}_{II}[\Omega_{\text{m}} + \delta]_{|\delta| \gg \Gamma_{\text{m}}} \approx 1 + 4\eta C \left(\frac{\Gamma_{\text{m}}}{\delta}\right)^2 \sin^2\theta \left(n_{\text{th}} + n_{\text{QBA}} - \frac{\delta}{\Gamma_{\text{m}}} \cot\theta\right). \tag{4.2.13}$$

Note that such an anti-symmetry can also arise from quantum correlations established by injecting squeezed light into the optical cavity [207] (or indeed, classical correlations established by injecting a laser field with classical amplitude fluctuations [123, 208]). Figure 4.1 shows a model of the homodyne photocurrent spectrum for a quadrature close to the amplitude (i.e., $\theta \approx 0°$): the red trace represents the asymmetric spectrum observed at sufficiently large optical powers and the blue and green traces represent contributions due to thermal motion

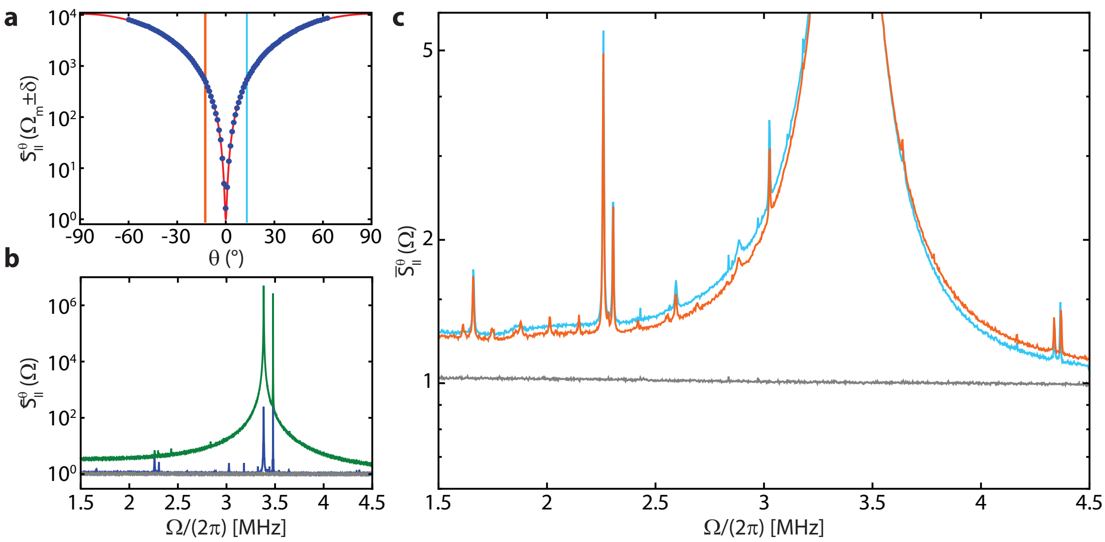

Figure 4.4 – **Asymmetry in homodyne spectrum.** (a) Resonant magnitude of the photocurrent signal, $\bar{S}^{\theta}_{II}[\Omega_\mathrm{m}]$ (normalized to shot-noise), as the homodyne angle, θ, is varied. Blue points are measurements. Red line is a fit to eq. (4.2.12). 40 dB suppression of the signal is achieved on the amplitude quadrature, limited by residual fluctuations in the homodyne angle ($\theta_\mathrm{RMS} < 0.01\,\mathrm{rad}$). (b) Example spectra taken near the phase (green) and amplitude (blue) quadratures. Also plotted is the background with the meter laser blocked (gray), dominated by LO shot noise (detector electronic noise is 10 dB below shot noise). For all measurements, feedback is used to stabilize the mechanical mode, as discussed in section 4.3.2. Note that the sharp peak at 3.5 MHz is due to thermal motion of the fundamental in-plane beam mode. (c) Magnified image of the spectrum at two quadratures, $\theta = \pm 13°$, highlighted with vertical lines in (A) (blue = +13°, yellow = −13°). The ~ 10% asymmetry between the two spectra at Fourier frequency detuning away from mechanical resonance ($\Omega_\mathrm{m} \approx 2\pi \cdot 3.5\,\mathrm{MHz}$) arises due to the quantum correlation term in eq. (4.2.12). Larger asymmetry is observed at Fourier frequencies further from mechanical resonance, as predicted by eq. (4.2.13). The spectra are measured at an injected power of, $P_\mathrm{in} = 280\,\mu\mathrm{W}$. The measurements in this figure were taken with sample AE/L2/B1/34.

and quantum correlations, respectively.

4.2.2 Observation of quantum correlations

In the following, we discuss homodyne measurements of a rotated quadrature of the field transmitted through our room temperature nanobeam-microdisk optomechanical system, with powers sufficient to resolve the asymmetry due to quantum correlations. In order to mitigate optomechanical instabilities, active radiation pressure feedback is used to damp the mechanical mode [73, 209]. For this purpose we employ an auxiliary 850 nm laser side-locked to an independent cavity mode (see section 4.3.2). Cold-damping of this sort changes the mechanical susceptibility within the feedback bandwidth (1 kHz in this instance); nevertheless, the total decoherence rate, and the ratio $n_\mathrm{QBA}/n_\mathrm{th}$, remains unchanged. Figure 4.4a shows the sensitivity of the homodyne interferometer as a function of the local oscillator phase θ. By operating with a modest input power of 280μW, we measure thermal motion of the oscillator with a phonon-equivalent imprecision, $n_\mathrm{imp} = (16\eta C)^{-1} \approx 4 \cdot 10^{-5}$, that is approximately 50 dB below that at the SQL (corresponding to $n_\mathrm{imp} = 1/4$) while operating on phase quadrature

($\theta = 90°$). As the local oscillator phase is swept towards the amplitude quadrature ($|\theta| \to 0°$), the apparent thermal motion is suppressed by about 40 dB. Figure 4.4b shows example photocurrent spectra measured close to the phase (green) and amplitude (blue) quadratures; the gray trace shows shot-noise of the homodyne detector, recorded by blocking the meter field. Excess amplitude noise in the output field is measured to be ≈ 1% for the largest powers used in our experiments ($P \approx 300\mu\mathrm{W}$), which we attribute to thermally driven fluctuations of the tapered fiber.

In order to visualize the asymmetry in the photocurrent spectra as predicted by eq. (4.2.13), we compare two spectra at homodyne angles symmetric about the amplitude quadrature, indicated by the blue (at angle $+\theta$) and yellow (at angle $-\theta$) vertical lines in fig. 4.4a. The corresponding spectra are shown in fig. 4.4c. An asymmetry of approximately 10% with respect to Fourier frequency, is observed at a detuning $\delta \gtrsim 2\pi \cdot 1\,\mathrm{kHz}$, consistent with the theoretically predicted effect due to quantum correlations. Qualitatively, the observed asymmetry over a broad range of frequencies – more than a MHz on either side of resonance – indicates that the magnitude of quantum-noise-induced correlations is comparable to all sources of quantum noise at these frequencies.

The asymmetry in the observed spectrum (red in fig. 4.4c) traces its root to the detuning dependence of quantum correlations (green in fig. 4.1, and third term in eq. (4.2.13)). In order to systematically investigate this asymmetry, we consider the ratio of the homodyne photocurrents at frequency offsets at $\pm\delta$ from mechanical resonance,

$$R_\theta \equiv \frac{\bar{S}^\theta_{II}[\Omega_\mathrm{m} + \delta]}{\bar{S}^\theta_{II}[\Omega_\mathrm{m} - \delta]}. \tag{4.2.14}$$

Following eq. (4.2.13),

$$R_\theta = \frac{1 + 4\eta C n_\mathrm{tot} (\Gamma_\mathrm{m} \sin\theta/\delta)^2 \,(1 - (\delta/n_\mathrm{tot}\Gamma_\mathrm{m}) \cot\theta)}{1 + 4\eta C n_\mathrm{tot} (\Gamma_\mathrm{m} \sin\theta/\delta)^2 \,(1 + (\delta/n_\mathrm{tot}\Gamma_\mathrm{m}) \cot\theta)}. \tag{4.2.15}$$

Note that quantum correlations render R_θ anti-symmetric in θ about amplitude quadrature ($\theta = 0°$), i.e.,

$$R_\theta - 1 \approx -(R_{-\theta} - 1). \tag{4.2.16}$$

It is thus a robust experimental signature for the presence of quantum correlations, provided that excess amplitude and phase noise of the meter laser is sufficiently small (see section 4.3.4). R_θ is measured by recording the spectral power in windows of finite bandwidth symmetric about resonance ($\delta = \pm 2\pi \cdot 21\,\mathrm{kHz}$, also see section 4.3.3), as a function of the homodyne angle θ. Figure 4.5 shows R_θ for several probe powers. At low probe powers (i.e. low cooperativity, $C \approx 1 \cdot 10^2$), shown in the top panel of fig. 4.5, the anti-symmetric feature around the amplitude quadrature (i.e. $R_\theta - 1$) is relatively small due to the large measurement imprecision. As the probe power is increased, shown in the two subsequent panels of fig. 4.5, the relative contribution of quantum correlation increases, leading to a progressively larger anti-symmetry near amplitude quadrature. We note that classical sources of noise may also affect the anti-

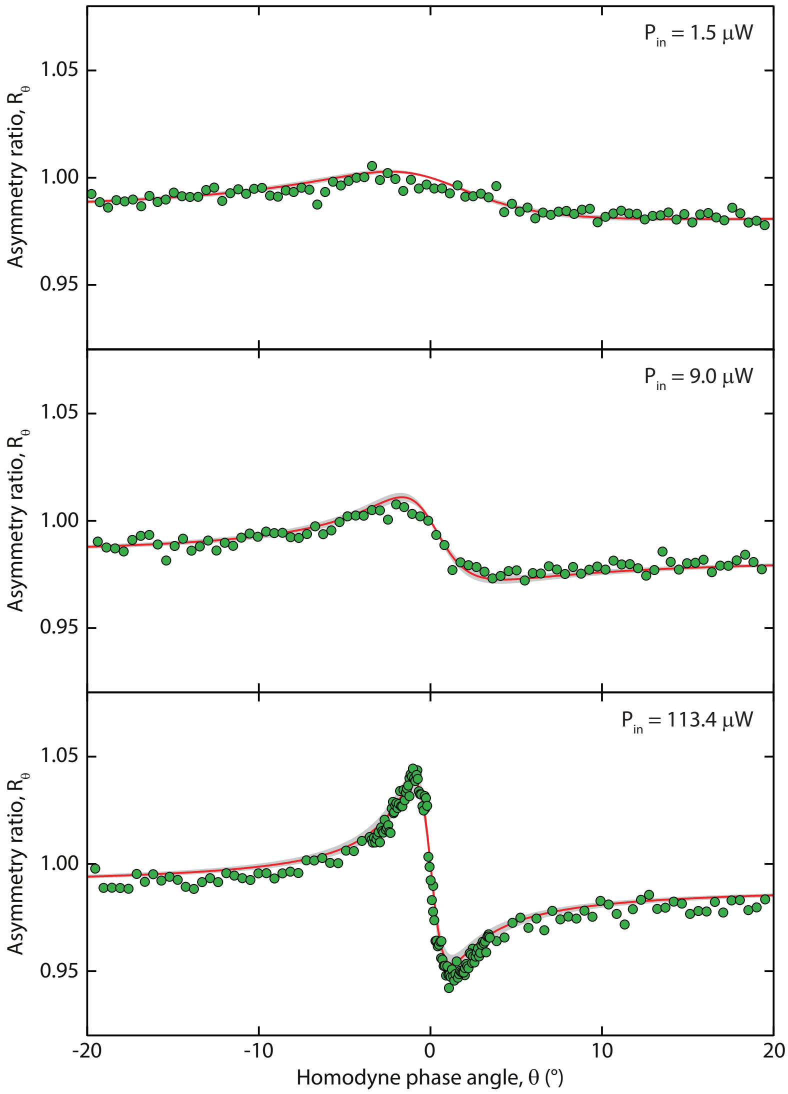

Figure 4.5 – **Asymmetry in homodyne spectrum as a function of quadrature angle.** Each plot shows asymmetry of the homodyne spectra, R_θ (eq. (4.2.15)), as a function of the homodyne angle. From top to bottom, R_θ is plotted as the probe power (mean intracavity photon number) is increased, $P_{\text{in}} = 1.5, 9, 113.4\,\mu W$ ($n_\text{c} \approx 4\cdot 10^2, 2.5\cdot 10^3, 3.1\cdot 10^4$). Red lines are a model employing only quantum noises and independently inferred values of the effective single-photon cooperativity, ηC_0; gray band shows interval corresponding to uncertainties in either parameter. All measurements were taken with sample AE/L2/B1/34.

symmetric feature: laser amplitude noise can establish classical amplitude-phase correlations leading to excess anti-symmetry [208], or anharmonicity of the mechanical oscillator can lead to structured thermal noise which at large Fourier frequency detuning modify the anti-symmetry [179]. These and various other sources of systematics were found to be negligible in our experiment (see section 4.3.4).

For the scenario in our experiments, where the back-action is large, but does not overwhelm thermal motion, i.e. $n_\text{th} \gg n_\text{QBA} \gg 1$, the visibility of the anti-symmetric feature in $R_{\theta\approx 0^\circ}$, is

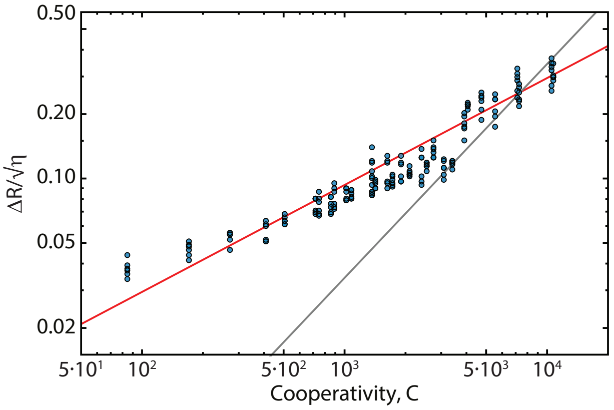

Figure 4.6 – **Visibility of quantum correlations versus laser power.** Blue points are measurements of ΔR (eq. (4.2.17)) of sample AE/L2/B1/34 as a function of laser power (referred to the optomechanical cooperativity, C). At each value of the injected power, the various blue points show ΔR inferred from various choices of the detuning δ. The red line is a prediction based on eq. (4.2.17), with a notably square-root dependence on power. The gray line is a linear fit to the data, which would apply if the correlations were entirely due to classical noise in the laser (see eq. (4.2.18)).

given by (cf. eq. (4.1.20)),

$$\Delta R \equiv \max R_\theta - \min R_\theta \approx 4\sqrt{\eta \frac{n_{\mathrm{QBA}}}{n_{\mathrm{th}}}}. \tag{4.2.17}$$

Here the extrema are calculated with respect to both the readout angle θ and for detuning, $\delta \in (\Gamma_{\mathrm{m}}, 2\Gamma_{\mathrm{m}}\sqrt{\eta C n_{\mathrm{th}}})$. The square-root scaling of ΔR is unique to quantum correlations (as opposed to correlations produced by classical noise), and makes possible the 10% asymmetry despite the relatively small magnitude of quantum back-action in our room temperature experiment $n_{\mathrm{QBA}}/n_{\mathrm{th}} \approx 10^{-2}$. In fig. 4.6 we show measurements of ΔR versus power by analyzing a series of quadrature sweeps as shown in Figure 4.5. For all data, ΔR is extracted from the asymmetry in the same spectral window around $|\delta| \approx 2\pi \cdot 2 \cdot 10^3 \cdot \Gamma_{\mathrm{m}}$. The observed scaling agrees well with the square-root scaling predicted by eq. (4.2.17), shown as a red line in fig. 4.6 with parameters for C, η and n_{th} determined independently.

For comparison, it can be shown that for a laser with excess classical amplitude noise, characterized by an average thermal photon occupation C_{qq} in excess of shot-noise, the visibility of the anti-symmetric feature is given by (see section 4.3.4),

$$\Delta R = 4\sqrt{\eta \frac{n_{\mathrm{QBA}}}{n_{\mathrm{th}}}(1 + 2C_{qq})}. \tag{4.2.18}$$

Phenomenologically, when optical power is changed by attenuating the laser beam (as done in our experiment), excess amplitude noise scales as $C_{qq} \propto P$, leading to $\Delta R \propto P$. This linear scaling is in qualitative disagreement with the observations in fig. 4.6.

4.2.3 Quantum-noise cancellation for force sensing

Quantum correlations are a generic resource for enhancing the precision with which parameters of a system can be estimated [210]. In the context of force estimation using interferometric methods, two techniques – injection of external correlations [81, 83, 191], and back-action evasion [190, 211, 212] – have been conventionally employed to surpass limits imposed by quantum noise of the optical field. A third alternative – correlations developed in-situ – can be directly used to derive a metrological advantage [83, 192]. For example, by performing a rotated-quadrature measurement of the cavity output field, an off-resonant external force (F_{ext}) applied to the mechanical oscillator, can be estimated with a precision better than that achievable with a phase quadrature measurement. As inferred from the homodyne photocurrent (eq. (4.2.12)), the apparent force experienced by the oscillator (i.e., the force estimator, $F^{\theta}_{\mathrm{est}}$) has a spectral density (as detailed in section 4.1.3),

$$\bar{S}^{\mathrm{est},\theta}_{FF}[\Omega] = \bar{S}^{\mathrm{ext}}_{FF}[\Omega] + \bar{S}^{\mathrm{th}}_{FF}[\Omega] + \bar{S}^{\mathrm{imp},\theta}_{FF}[\Omega] + \bar{S}^{\mathrm{QBA}}_{FF}[\Omega] + \hbar \cot\theta \frac{\mathrm{Re}\,\chi_x[\Omega]}{|\chi_x[\Omega]|^2}, \tag{4.2.19}$$

where we now employ the conventional susceptibility, $\chi_x[\Omega] \equiv [m(\Omega_{\mathrm{m}}^2 - \Omega^2 - i\Omega\Gamma_{\mathrm{m}})]^{-1}$. Equation (4.2.19) shows that the uncertainty in the estimate of F_{ext} has a classical component due to thermomechanical noise $\left(\bar{S}^{\mathrm{th}}_{FF}\right)$ and a quantum component (last three terms in eq. (4.2.19)) due to phase quantum noise (imprecision), amplitude shot noise (back-action), and correlations between the two. By detecting a rotated field quadrature ($\theta \neq 90°$), phase-amplitude correlations ($\propto \cot\theta$) can be used to reduce the uncertainty due to quantum noise, which has to be weighed against a concomitant reduction of the signal. In the limit of strong back-action $\bar{S}^{\mathrm{QBA}}_{FF} \gg \bar{S}^{\mathrm{imp},90^\circ}_{FF}$ (i.e. $C \gg 1$), and at an optimal measurement quadrature at angle θ_{opt}, this trade-off reduces to the simplified form (cf section 4.1.3),

$$\bar{S}^{\mathrm{est},\theta_{\mathrm{opt}}}_{FF}[\Omega] = \bar{S}^{\mathrm{ext}}_{FF}[\Omega] + \bar{S}^{\mathrm{th}}_{FF}[\Omega] + \bar{S}^{\mathrm{imp},90^\circ}_{FF}[\Omega] + \left[1 - \eta\left(\frac{\mathrm{Re}\,\chi_x[\Omega]}{\left|\chi_x[\Omega]\right|}\right)^2\right] \bar{S}^{\mathrm{QBA}}_{FF}[\Omega]. \tag{4.2.20}$$

Equation (4.2.20) shows that measurement back-action can be “erased” from the measured photocurrent at frequencies offset from mechanical resonance. The efficacy of this back-action erasure is limited by the detection efficiency, η. Note that, by contrast, *physical* back-action is suppressed in back-action evasion schemes [190].

In the presence of thermal noise, the signal-to-noise enhancement afforded by quantum correlations in eq. (4.2.20) is diminished by a factor of approximately $n_{\mathrm{th}}/n_{\mathrm{QBA}}$. We nevertheless observe the principle behind this quantum-enhancement, by applying a detuned radiation force $F_{\mathrm{ext}}[\Omega_{\mathrm{ext}}]$ via an auxiliary cavity field, as described in section 4.3.3, and recording the signal-to-noise ratio,

$$\mathrm{SN}^{\theta}[\Omega_{\mathrm{ext}}] \equiv \frac{\bar{S}^{\mathrm{est},\theta}_{FF}[\Omega_{\mathrm{ext}}]}{\bar{S}^{\mathrm{est},\theta}_{FF}[\Omega_{\mathrm{ext}}] - \bar{S}^{\mathrm{ext}}_{FF}[\Omega_{\mathrm{ext}}]} \tag{4.2.21}$$

in the homodyne photocurrent versus θ. In the experiment, we choose a two-tone force of the

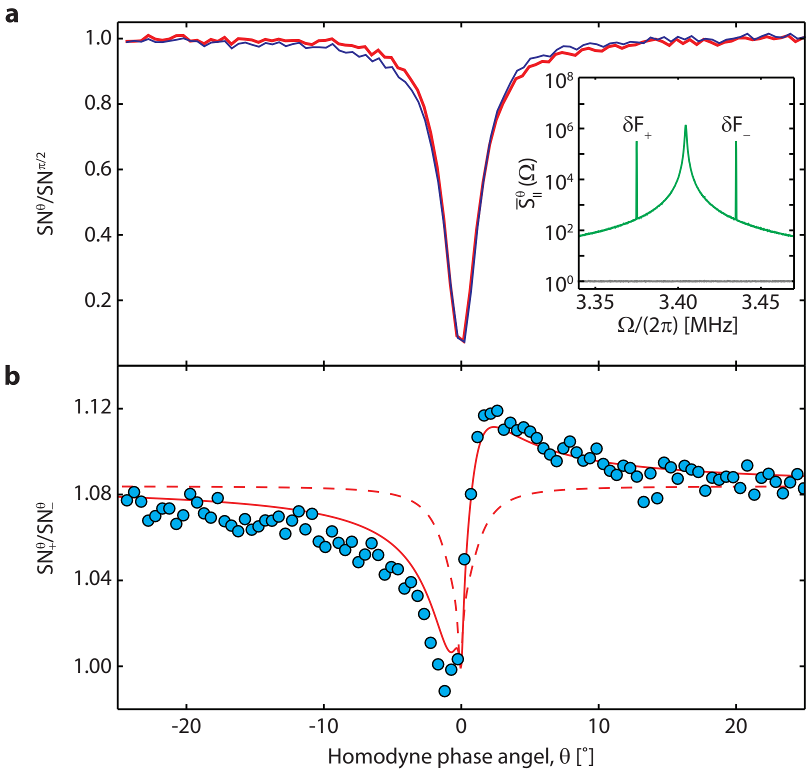

Figure 4.7 – **Quantum-enhanced external force estimation.** (a) Inset: Green shows homodyne photocurrent spectrum near phase quadrature showing the two balanced forces applied on the mechanical oscillator (AE/L2/B1/34) via radiation pressure from the auxiliary laser; grey is the shot noise background. Main: Red (blue) shows the signal-to-noise ratio of the force F_+ (F_-) normalized to its value for phase quadrature detection, i.e. $\mathrm{SN}^{\theta}_{+(-)}/\mathrm{SN}^{\pi/2}_{+(-)}$. The asymmetry between the two traces at $\theta \approx \pm 10°$ is due to quantum noise cancellation. Here the laser input power is $P_{\mathrm{in}} = 110\,\mu\mathrm{W}$. (b) Blue shows $\mathrm{SN}^{\theta}_{+}/\mathrm{SN}^{\theta}_{-}$, extracted as a ratio of the blue and red traces in panel (a). For a force balanced in intensity and frequency offset from resonance, eq. (4.2.23) predicts that $\mathrm{SN}^{\theta}_{+}/\mathrm{SN}^{\theta}_{-} \propto R_\theta$. The solid red line is a prediction based on eq. (4.2.23) in conjunction with eq. (4.1.21), while red dashed shows the same model excluding the contribution from quantum correlations.

form,

$$F_{\mathrm{ext}}[\Omega] = F_+\delta[\Omega_{\mathrm{m}} + \delta] + F_-\delta[\Omega_{\mathrm{m}} - \delta], \tag{4.2.22}$$

centered around resonance, so that one of the forces provides a reference for the signal-to-noise ratio. We denote by $\mathrm{SN}^{\theta}_{\pm}$, the definition of the signal-to-noise ratio in eq. (4.2.21) applied to each of the two force components ($F_\pm$). Figure 4.7a shows the variation of $\mathrm{SN}^{\theta}_{\pm}$ for each of the forces $F_\pm$ (carefully balanced, as shown in inset) as the homodyne readout angle is varied. The effect of quantum correlations in the optical field is to cancel back-action at intermediate measurement quadratures ($0° < |\theta| < 90°$), leading to an enhancement or suppression of $\mathrm{SN}^{\theta}_{\pm}$ at these optimal quadratures. For a fixed measurement setting (i.e. fixed value of C, θ, δ), it can be seen that quantum noise cancellation leads to an enhanced signal-to-noise ratio for F_+ relative to F_-, or visa versa. The absolute value of the enhancement is given by the ratio,

$$\frac{\mathrm{SN}^{\theta}[\Omega_{\mathrm{m}} + \delta]}{\mathrm{SN}^{\theta}[\Omega_{\mathrm{m}} - \delta]} \approx \frac{1}{R_\theta}\frac{|\chi_x[\Omega_{\mathrm{m}} + \delta]|^2}{|\chi_x[\Omega_{\mathrm{m}} - \delta]|^2}\frac{\langle F_+^2\rangle}{\langle F_-^2\rangle}, \tag{4.2.23}$$

and is plotted in fig. 4.7b. The observed anti-symmetric dependence on θ is directly related to R_θ (eq. (4.1.21)). The offset from unity at $\theta = \pm 90°$ is due to imperfect balance of the two forces. The maximum deviation (at $\theta \approx \pm 2°$) of approximately 12% is less than the absolute signal loss shown in fig. 4.7a. It nevertheless provides a measure of the improvement obtained in the ability to estimate a force with and without quantum noise cancellation.

4.3 Experimental details

In this section, we describe details of the experiment. In detail, section 4.3.1 presents the optomechanical device used to generate quantum correlations, section 4.3.2 describes the experimental setup, and section 4.3.3 outlines the process of data acquisition and analysis. Finally, we estimate the magnitude and impact of laser noise (section 4.3.4) and homodyne phase fluctuations (section 4.3.5).

4.3.1 Experimental platform

The characteristics and fabrication details of the device measured in this work are in detail described in chapter 3. To summarize, the device consists of an SiO_2 whispering gallery mode microdisk with a high-stress Si_3N_4 nanobeam centered in the near-field of the microdisk. The sample has been fabricated by a monolithic wafer-scale process that utilizes a sacrificial layer to define a ~ 50 nm gap between the microdisk and nanobeam, as detailed in [160]. Similar devices have also been used for recent cryogenic experiments [73, 150]. However, in contrast to those devices, here both the mechanical and optical resonator shapes are defined by electron-beam lithography. The bare microdisks exhibit a very high finesse of $\sim 10^5$ – nearly an order of magnitude higher than microdisks produced by photo-lithography. However, in this work we do not access this high finesse regime when the nanobeam is placed in the near-field of the disk. We attribute this to the 80 nm thickness of the Si_3N_4, which is conjectured to lead to excessive scattering and/or waveguiding. The microdisk is 40 μm in diameter, ~ 350 nm thick, and has a gently sloping sidewall of ~ 10° which results from the use of thin photoresist during the wet-etching process.

In previous work [73, 150] the mechanical resonator was formed by a beam with a homogeneous transverse profile. However, the present device has been designed with a central defect that allows for increased overlap with the optical mode while minimizing the effective mass ($m_{\mathrm{eff}} \approx 1.94$ pg). The optical mode of the microdisk samples approximately 9 μm of the beam at its center (see [160]), however we utilize a defect that is tapered within the sampling region as this results in lower optical loss and overall higher C_0 than longer defects. This effect may be attributed to the reduced scattering loss on account of a softer dielectric boundary seen by the optical mode, in combination with less optical waveguiding inside the beam. The latter effect can especially be observed by a significant reduction of scattered light at the beam's clamping points. Figure 4.8B shows the defect geometry and the effect of defect length on the effective mass of the fundamental out-of-plane mode. The beam is 70 μm long and consists of

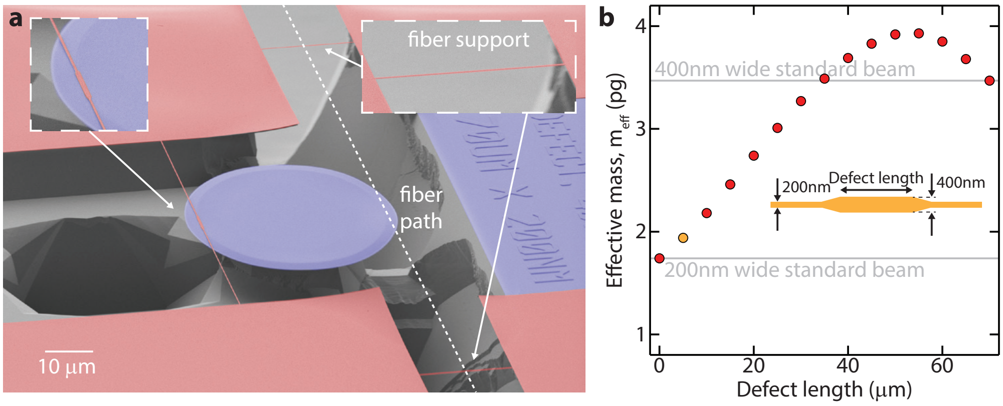

Figure 4.8 – **Experimental device:** (a) False colored scanning electron micrograph of the device design used in this work. Si_3N_4 is indicated in red and SiO_2 in blue. (b) Finite element calculation of effective mass for defect beam design, as a function of the defect length. The data point in orange indicates the defect length (5 μm) of the experimental device; see text for details.

a narrow (200 nm) beam with a wider (400 nm) rectangular defect at the center which tapers linearly into the thin beam at an angle of ~ 12°. The defect length of the device used here is 5 μm, which exhibits an effective mass only 11% larger than that of a standard 200 nm wide beam.

As shown in Figure 4.8a, two short beams of Si_3N_4 with dimensions $20 \times 0.2 \times 0.08\,\mu$m are also placed across the channel on either side of the microdisk to support the tapered optical fiber and increase the overall mechanical stability of the experiment.

4.3.2 Measurement setup

The essential layout of the experiment is shown in fig. 4.9. The sample is placed in a high vacuum chamber, at a pressure of $\sim 10^{-7}$ mbar, and room temperature. Light is coupled in and out of the microdisk cavity using a tapered optical fiber, the position of which is adjusted using piezo actuators to achieve critical coupling into the cavity (i.e. $\eta_c \approx 0.5$).

Two lasers are employed in the experiment – a Ti:Sa laser (MSquared Solstis) with wavelength centered around 780 nm which is the *meter* beam, and an auxiliary 850 nm external cavity diode laser (NewFocus Velocity) which is the *feedback* beam. Both beams are combined before the cavity and separated after it using dichroic beamsplitters. The feedback beam is detected on an avalanche photodetector (APD), while the meter beam is fed into a length- and power-balanced homodyne detector. A small portion of the meter beam – stray reflection from the dichroic beam-splitter – is directed onto an APD.

Both lasers are actively locked to their independent cavity resonances using the APD signals. For the meter beam, a lock on cavity resonance ($|\Delta| \lesssim 0.1 \cdot \kappa$) is implemented using the Pound-Drever-Hall technique [146]. For the feedback beam, a part of the APD signal is used directly

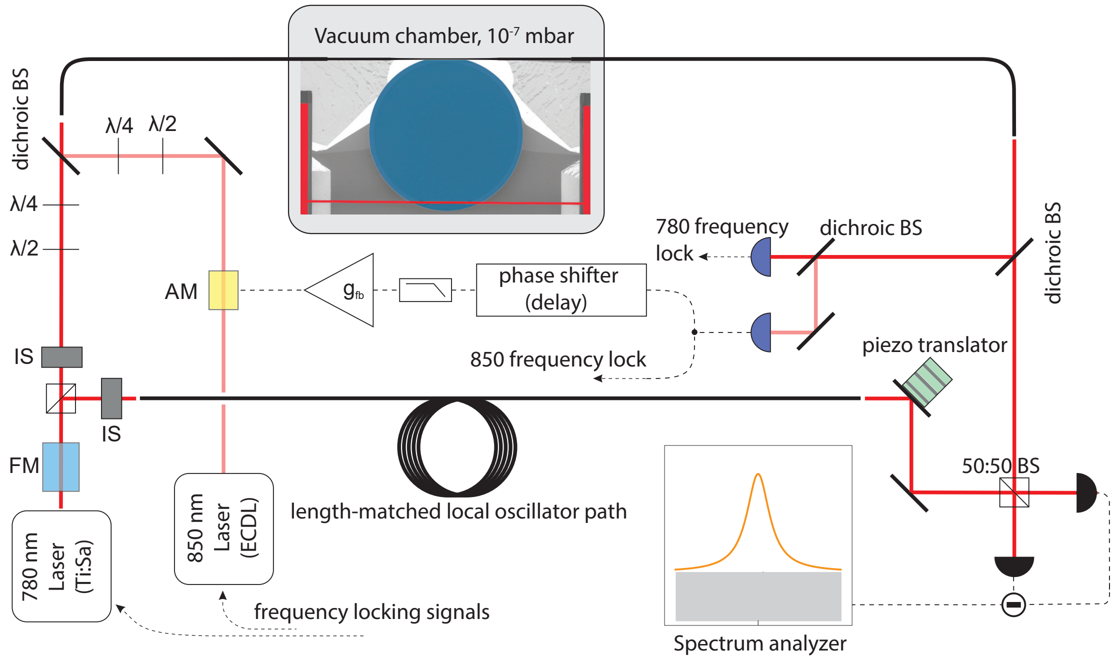
Vacuum chamber, 10^{-7} mbar
dichroic BS
λ/4
λ/2
λ/4
λ/2
AM
g_{fb}
phase shifter
(delay)
780 frequency
lock
dichroic BS
dichroic BS
850 frequency lock
piezo translator
IS
IS
FM
780 nm
Laser
(Ti:Sa)
850 nm
Laser
(ECDL)
length-matched local oscillator path
frequency locking signals
50:50 BS
Spectrum analyzer

Figure 4.9 – **Schematic of the experimental setup.** A Ti:Sa at 780 nm, acting as the meter beam, and an ECDL at 850 nm, providing moderate feedback damping to avoid optomechanical instabilities, are locked to cavity resonances of the optomechanical system. The desired quadrature of the meter beam is read out in a power and length balanced homodyne interferometer, in which the phase of the local oscillator can be adjusted. Abbreviations: AM – amplitude modulator, FM – frequency modulator, BS – beam splitter, IS – intensity stabilizer.

to implement a lock red-detuned from cavity resonance.

The other part of the feedback beam APD signal is used to perform moderate feedback cooling of the mechanical oscillator. Specifically, the photosignal is amplified, low-pass filtered and phase-shifted, before using it to amplitude modulate the same laser. As in conventional cold damping [209], the phase-shift in the feedback loop is adjusted to synthesize an out-of-phase radiation pressure force that damps the mechanical oscillator. This effect is described by an effective mechanical linewidth, $\Gamma_{\mathrm{eff}} = \Gamma_{\mathrm{m}} + \Gamma_{\mathrm{fb}} = (1 + g_{\mathrm{fb}})\Gamma_{\mathrm{m}}$ with the feedback damping rate Γ_{fb} and the dimensionless feedback gain g_{fb}. At the nominal feedback laser power of $5\,\mu$W, a damping rate of $\Gamma_{\mathrm{fb}} = 2\pi \cdot 1\,$kHz is realized; the associated increase in the mechanical decoherence rate due to injected imprecision noise was measured to be below 5%.

The path length difference of the homodyne interferometer is actively stabilized using a two-branch piezo translation system. Demodulation of the homodyne signal at PDH frequency also produced interference fringes suitable for locking the homodyne angle near the amplitude quadrature (i.e. $\theta = 0$). The residual homodyne angle fluctuations could be estimated $\theta_{\mathrm{RMS}} \lesssim 1° \approx 0.017\,$rad, inferred from the suppression of thermomechanical signal-to-noise ratio on amplitude quadrature of ≈ 40 dB compared to the phase quadrature. An offset DC voltage is applied to the homodyne error signal for deterministic choice of detection quadrature.

Since the feedback cooling exclusively relies on the auxiliary diode laser, the homodyne measurements on the 780 nm meter beam are completely out-of-loop and do not contain electronically-induced correlations.

For the external force estimation measurement, the light of the auxiliary laser is intensity modulated at a frequency $\Omega = \Omega_\mathrm{m} + \delta$ to induce an external radiation-pressure force.

4.3.3 Data acquisition and analysis

In each experimental run, corresponding to the data presented in section 4.2, the meter laser is locked to cavity resonance at fixed input power, and a series of homodyne photocurrent spectra are taken at various settings of the homodyne angle θ. From independently measured mechanical and optical parameters of the sample, together with the known input power, the homodyne detection efficiency is inferred in each run by the thermomechanical signal-to-shot-noise ratio. For this, the shot noise level was measured by blocking the signal interferometer arm. To account for a small quadrature rotation by the cavity the nominal $\theta = 0$ quadrature was inferred from the minimum in the transduction of thermomechanical noise.

In order to experimentally access the asymmetry ratio R_θ discussed earlier within this section, R_θ is estimated from an integral over a finite bandwidth $\Delta\Omega$, i.e.,

$$R_\theta = \int_{\Omega_\mathrm{m}+\delta-\Delta\Omega/2}^{\Omega_\mathrm{m}+\delta+\Delta\Omega/2} \bar{S}^\theta_{II}[\Omega]\, d\Omega \bigg/ \int_{\Omega_\mathrm{m}-\delta-\Delta\Omega/2}^{\Omega_\mathrm{m}-\delta+\Delta\Omega/2} \bar{S}^\theta_{II}[\Omega]\, d\Omega\,. \tag{4.3.1}$$

Theoretically, there is some freedom in the choice of the detuning offset δ and integration bandwidth $\Delta\Omega$, since the relative contribution of the quantum interference term to the detected signal is maximum within a broad range of detunings $\Gamma_\mathrm{eff} \ll \delta \ll 2\Gamma_\mathrm{m}\sqrt{\eta C\, n_\mathrm{th}}$; here $\Gamma_\mathrm{eff} \approx 2\pi\cdot 1\,\mathrm{kHz}$ is the effective damping rate due to feedback. For typical experimental conditions in this work $1\ \mathrm{kHz} \ll \delta/2\pi \ll 500\,\mathrm{kHz}$. Figure 4.10 shows the ratio R_θ extracted for various choices of the detuning offset and integration bandwidth. The results presented in section 4.2 in fig. 4.5 depict data extracted for the choice $\delta = 2\pi\cdot 21\,\mathrm{kHz}$ and $\Delta\Omega = 2\pi\cdot 20\,\mathrm{kHz}$.

In the demonstration of external force estimation (see sections 4.1.3 and 4.2), the signal-to-noise ratio for the applied force δF_ext is defined by,

$$\mathrm{SN}^\theta_\pm \equiv \bar{S}^\theta_{II}[\Omega_\mathrm{F} \pm \delta] \big/ \bar{S}_{II}[\Omega_\mathrm{F} \pm \delta]|_{\delta F_\mathrm{ext}=0}\,; \tag{4.3.2}$$

i.e., the signal is the photocurrent noise at the frequencies where the force is applied ($\Omega_\mathrm{F} \pm \delta$), while the noise is the photocurrent noise at the same frequencies without the force. Practically, we estimate both contributions from finite bandwidth integrals over the relevant part of the photocurrent spectrum: for the signal, the photocurrent signal is integrated over a finite bandwidth $\Delta\Omega_\mathrm{F}$ around the applied force, while to estimate the noise, we choose to take averages of the photocurrent spectrum over finite bandwidth $\Delta\Omega_\mathrm{N}$, on either side of the

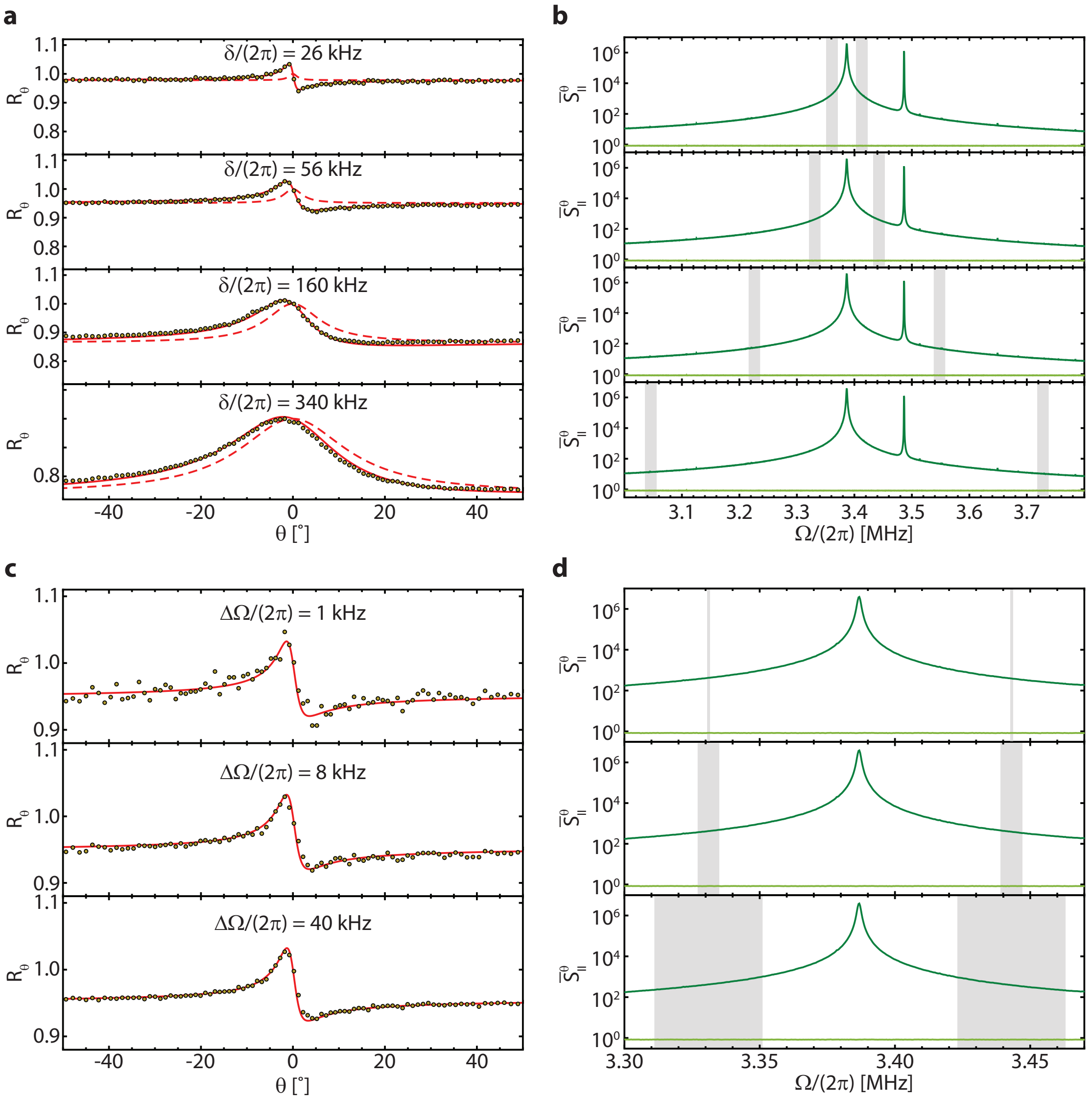

Figure 4.10 – **Asymmetry ratio for different offsets and integration bandwidths:** (a,c) Illustration of the variation of the experimental asymmetry ratio R_θ for different offsets δ at fixed integration bandwidth $\Delta\Omega/2\pi = 20$ kHz (a) and for different integration bandwidths $\Delta\Omega$ at fixed offset $\delta/2\pi = 56$ kHz (c). Solid and dashed red curves show theoretical predictions accounting and not accounting for the quantum back-action-imprecision correlations. (b,d) Plots show the integration bands used for calculation of $R(\theta)$ on the left (shaded gray regions). Dark green is a mechanical spectrum at an intermediate homodyne quadrature and light green is the local oscillator trace showing the shot noise level. The data was taken at $P_{\mathrm{in}} = 200\ \mu$W. All measurements were taken with sample AE/L2/B1/34.

applied force, without turning off the force. Specifically,

$$\mathrm{SN}^{\theta}_{\pm} = \int_{\Omega_{\mathrm{F}}\pm\delta-\Delta\Omega_{\mathrm{F}}/2}^{\Omega_{\mathrm{F}}\pm\delta+\Delta\Omega_{\mathrm{F}}/2} \bar{S}^{\theta}_{II}[\Omega]d\Omega \Big/ \frac{1}{2}\left(\int_{\Omega_{\mathrm{F}}\pm\delta+\delta\Omega_{\mathrm{N}}-\Delta\Omega_{\mathrm{N}}/2}^{\Omega_{\mathrm{F}}\pm\delta+\delta\Omega_{\mathrm{N}}+\Delta\Omega_{\mathrm{N}}/2} \bar{S}^{\theta}_{II}[\Omega]d\Omega + \int_{\Omega_{\mathrm{F}}\pm\delta-\delta\Omega_{\mathrm{N}}-\Delta\Omega_{\mathrm{N}}/2}^{\Omega_{\mathrm{F}}\pm\delta-\delta\Omega_{\mathrm{N}}+\Delta\Omega_{\mathrm{N}}/2} \bar{S}^{\theta}_{II}[\Omega]d\Omega\right). \tag{4.3.3}$$

The integration bands used for main results are shown in figure 4.11.

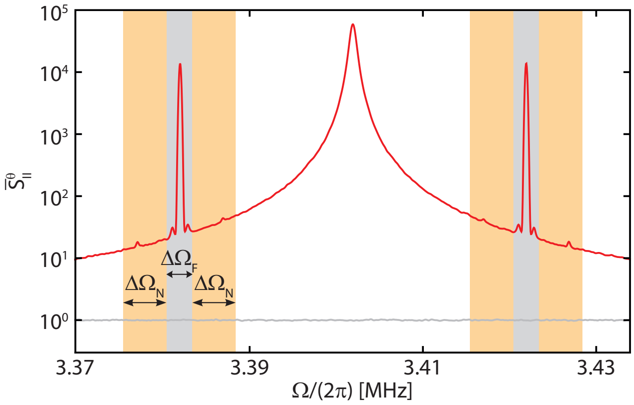

Figure 4.11 – **Choice of integration bands:** Integration bands used in the definition of the signal-to-noise ratio SN^{θ} in section 4.2. The signal bands are shaded gray ($\Delta\Omega_\mathrm{F} = 3\,\mathrm{kHz}$), the bands for noise estimation are shaded orange ($\Delta\Omega_\mathrm{N} = 5\,\mathrm{kHz}$).

Role of broadband mechanical susceptibility

Within the theoretical description that relies on single-pole Lorentzian mechanical susceptibility and white thermal noise, the variation of the asymmetry ratio, $\Delta R = \max_\theta R_\theta - \min_\theta R_\theta$, can be directly related to the $n_\mathrm{QBA}/n_\mathrm{th}$ as given by the eq. (4.1.20). In the present experiment, however, backaction-imprecision correlations are produced in the broad span of frequencies on the order of hundreds of kHz, which makes eq. (4.1.20) not directly applicable at large detunings δ. As is illustrated by the fig. 4.10a, at large δ the experimental $R_\theta - 1$ shows deviations from the antisymmetric shape given by eq. (4.1.19) and should be described by the eq. (4.1.21) containing a contribution symmetric in θ. In order to make the data analysis more transparent we choose $\delta = 21$ kHz, which is small enough so that eq. (4.1.20) holds with sufficient accuracy.

4.3.4 Laser noise

In addition to vacuum fluctuations in the input amplitude quadrature, classical fluctuations in the amplitude quadrature can lead to phase-amplitude correlations in the cavity transmission [150]. Additionally, detuning deviations causing a finite Δ/κ can transduce classical phase fluctuations in the input to excess phase-amplitude correlations in the output.

In order to analyze the two possible classical contributions on the same footing, we consider the quadratures of the cavity transmission, $\delta q_\mathrm{out}, \delta p_\mathrm{out}$ for the case of a finite detuning $|\Delta| \ll \kappa$.

In this regime, eq. (4.1.9) contains corrections of order Δ/κ, in particular,

$$
\begin{aligned}
\delta q_{\mathrm{out}}[\Omega] =& (1-2\eta_{\mathrm{c}})\delta q_{\mathrm{in}}[\Omega] - 2\sqrt{\eta_{\mathrm{c}}(1-\eta_{\mathrm{c}})}\delta q_0[\Omega] \\
&+ \frac{2\Delta}{\kappa}\Big(\sqrt{2\eta_{\mathrm{c}}C\Gamma_{\mathrm{m}}}\delta z[\Omega] \\
&+ 2\eta_{\mathrm{c}}\delta p_{\mathrm{in}}[\Omega] + 2\sqrt{\eta_{\mathrm{c}}(1-\eta_{\mathrm{c}})}\delta p_0[\Omega]\Big) \\
\delta p_{\mathrm{out}}[\Omega] =& (1-2\eta_{\mathrm{c}})\delta p_{\mathrm{in}}[\Omega] - 2\sqrt{\eta_{\mathrm{c}}(1-\eta_{\mathrm{c}})}\delta p_0[\Omega] \\
&- \sqrt{2\eta_{\mathrm{c}}C\Gamma_{\mathrm{m}}}\delta z[\Omega] \\
&- \frac{2\Delta}{\kappa}\Big(2\eta_{\mathrm{c}}\delta q_{\mathrm{in}}[\Omega] + 2\sqrt{\eta_{\mathrm{c}}(1-\eta_{\mathrm{c}})}\delta q_0[\Omega]\Big),
\end{aligned}
\tag{4.3.4}
$$

where $\delta z = \delta z_{\mathrm{th}} + \delta z_{\mathrm{BA}}$ is the total motion. The back-action component in this case,

$$
\begin{aligned}
\delta z_{\mathrm{BA}}[\Omega] =& \sqrt{2C\Gamma_{\mathrm{m}}}\Big[\Big(\sqrt{\eta_{\mathrm{c}}}\delta q_{\mathrm{in}}[\Omega] + \sqrt{1-\eta_{\mathrm{c}}}\delta q_0[\Omega]\Big) \\
&+ 4i\frac{\Omega\Delta}{\kappa^2}\Big(\sqrt{\eta_{\mathrm{c}}}\delta p_{\mathrm{in}}[\Omega] + \sqrt{1-\eta_{\mathrm{c}}}\delta p_0[\Omega]\Big)\Big],
\end{aligned}
\tag{4.3.5}
$$

consists of the motion induced by the quantum and the classical fluctuations in the input laser field. Excess noise in the input amplitude and phase quadratures is modeled by white noise with intensity C_{qq} and C_{pp} respectively, so that,

$$
\bar{S}^{\mathrm{in}}_{qq}[\Omega] = \frac{1}{2} + C_{qq}, \qquad \bar{S}^{\mathrm{in}}_{pp}[\Omega] = \frac{1}{2} + C_{pp}. \tag{4.3.6}
$$

Using eqs. (4.3.4) and (4.3.5) in the definition of the homodyne spectrum (eq. (4.1.12)) to leading order in Δ/κ, the shot-noise normalized balanced homodyne spectrum is:

$$
\begin{aligned}
\bar{S}^{\theta}_{II}[\Omega] \approx& 1 + 4\eta C\Gamma_{\mathrm{m}}\Big[\Big(\bar{S}^{\mathrm{th+QBA}}_{zz}[\Omega] + \bar{S}^{\mathrm{CBA,q}}_{zz}[\Omega] + \bar{S}^{\mathrm{CBA,p}}_{zz}[\Omega]\Big)\sin(\theta')^2 + \frac{1}{2}\sin(2\theta')\mathrm{Re}\,\chi_z[\Omega] \\
&+ \sin(2\theta')\sqrt{\eta_c}(1-2\eta_c)C_{qq}\mathrm{Re}\,\chi_z[\Omega] + 2\sin(\theta')^2\sqrt{\eta_c}(1-2\eta_c)\frac{4\Omega_{\mathrm{m}}\Delta}{\kappa^2}C_{pp}\mathrm{Im}\,\chi_z[\Omega]\Big],
\end{aligned}
\tag{4.3.7}
$$

where $\theta' \approx \theta - 4\Delta/\kappa$ is the quadrature angle rotated by the cavity. The effect of excess noise is two-fold. Firstly, classical amplitude (phase) noise C_{qq} (C_{pp}) causes additional classical back-action motion $\bar{S}^{\mathrm{CBA,q}}_{xx}$ ($\bar{S}^{\mathrm{CBA,p}}_{xx}$), leading to excess back-action occupations,

$$
n_{\mathrm{CBA,q}} = C_0 n_c C_{qq}, \qquad n_{\mathrm{CBA,p}} = C_0 n_c \left(\frac{4\Omega_{\mathrm{m}}\Delta}{\kappa^2}\right)^2 C_{pp}. \tag{4.3.8}
$$

Secondly, classical amplitude noise, and phase noise transduced via finite detuning, establish excess correlations, as can be seen from the last two terms in the eq. (4.3.7). It is important to note that the contribution of excess phase noise C_{pp} to the measured homodyne signal is effectively suppressed for the current experimental parameters since $\Delta \cdot \Omega_{\mathrm{m}}/\kappa^2 = \mathcal{O}(10^{-4})$. Finally, when laser noise is insignificant, the role of a residual detuning from the cavity, i.e. $\Delta \neq 0$, is to rotate the detected quadrature by an angle $\arctan(4\Delta/\kappa)$, without leading to any artificial asymmetry.

Classical amplitude noise leads to excess correlations, which results in a larger anti-symmetry in R. The size of the anti-symmetry is quantified by ΔR. Following the definition in eq. (4.1.20), and using the expression for the homodyne spectrum in the presence of laser noise (eq. (4.3.7)), it can be shown that,

$$\Delta R(\delta) = 4\sqrt{\frac{\eta C}{n_{\mathrm{th}}}(1+2C_{qq})} \text{ for } \Gamma_{\mathrm{m}} \ll \delta \ll 2\Gamma_{\mathrm{m}}\sqrt{\eta C n_{\mathrm{th}}}, \tag{4.3.9}$$

and for an overcoupled cavity ($\eta_c \approx 1$). Thus, the magnitude of the anti-symmetric feature in R is increased by the average thermal photon occupation of the amplitude quadrature.

In addition, the overall scaling of ΔR with probe power is qualitatively different. In order to see this, we consider an arrangement (as in the experiment) where the laser field a_{las} is attenuated by a variable beam-splitter of transmissivity η_{bs}, to derive the field that excites the optical cavity, a_{in}. Thus,

$$\delta a_{\mathrm{in}}[\Omega] = \sqrt{\eta_{\mathrm{bs}}}\,\delta a_{\mathrm{las}}[\Omega] + \sqrt{1-\eta_{\mathrm{bs}}}\,\delta a_{\mathrm{bs}}, \tag{4.3.10}$$

where, δa_{bs}, is the vacuum noise from the remaining open input port of the beam-splitter. This equation, together with the definition of C_{qq} (eq. (4.3.6)), allows us to relate the amplitude quadrature excess noise in the cavity input field to that of the laser, in particular,

$$C_{qq}^{\mathrm{in}} = \eta_{\mathrm{bs}} C_{qq}^{\mathrm{las}} = \frac{P_{\mathrm{in}}}{P_{\mathrm{las}}} C_{qq}^{\mathrm{las}}, \tag{4.3.11}$$

$P_{\mathrm{in}}(P_{\mathrm{las}})$ is the mean optical power of the input (laser) field. Thus, when the cavity input power (P_{in}) is varied by attenuating a laser operating at a fixed output power (P_{las}), the amplitude noise at the cavity input scales proportional to the power. Inserting this in eq. (4.3.9) shows that in this case, $\Delta R \propto P_{\mathrm{in}}$, when $C_{qq}^{\mathrm{in}} \gg \frac{1}{2}$.

For the experiments presented in this chapter, an MSquared Solstis Ti:Sa laser was used for all measurements. The amplitude noise of the laser was characterized via direct photo-detection. In a 3 MHz wide frequency band around the mechanical frequency, $\Omega_{\mathrm{m}} = 2\pi \cdot 3.4\,\mathrm{MHz}$ at the highest employed power of $150\,\mu$W, the classical amplitude noise level was < 1% of the shot noise (see fig. 4.12b). This means that $C_{qq} < 1 \cdot 10^{-3}$, implying a negligible contribution due to excess classical correlations and a negligible fraction of classical back-action motion, $n_{\mathrm{CBA,q}} < 0.001 \cdot n_{\mathrm{QBA}}$, compared to quantum back-action.

Laser phase noise on the other hand was upper-bounded using a self-heterodyne measurement [213] with a 400 m fiber delay line. The self-heterodyne signal can be described by (after shifting the beat-note to zero frequency),

$$\bar{S}_{II}[\Omega] \propto \frac{\pi}{2}\delta[\Omega] + \sin^2\left(\frac{\Omega\tau_0}{2}\right)\bar{S}_{\phi\phi}[\Omega], \tag{4.3.12}$$

where τ_0 is the delay and $\bar{S}_{\phi\phi}[\Omega]$ is the laser phase noise spectral density. The measured signal for the laser is compared to an external cavity diode laser and is shown in figure 4.12a, where the vertical scale is calibrated using the known mean photon flux in the beat note carrier. For the Ti:Sa laser (blue trace in fig. 4.12a) the absence of the characteristic $\sin^2(\Omega\tau_0)$ interference pattern suggests that laser phase noise is below the sensitivity of the measurement. Although the laser is expected to be quantum-noise-limited at frequencies well above the relaxation oscillation frequency ($\approx 400\,\mathrm{kHz}$), our measurements can only provide a conservative upper-bound for the frequency noise to be at the level of $2\,\mathrm{Hz}^2/\mathrm{Hz}$ (in comparison, frequency noise of a commercial external cavity diode laser, also shown in fig. 4.12a, is 20 dB larger). This upper bound on the excess phase noise, together with large optical linewidth (κ) strongly suppresses the influence of C_{pp} and leads to an estimated back-action motion that is below a factor 0.0025 compared to the quantum mechanical contribution. Intrinsic cavity frequency noise, for example from thermoelastic [214] or thermorefractive [215] processes, can also lead to a finite value of C_{pp}. In the current experiments, broadband measurements of cavity transmission on phase quadrature suggest a conservative upper bound of $C_{pp} < 10$ at frequencies around Ω_m. Using a length-balanced homodyne interferometer, classical phase noise in the measurement imprecision is also bounded at 0.1%.

4.3.5 Effect of homodyne phase fluctuations

The measured dependence $R(\theta)$ for $\delta/2\pi = 21$ kHz exhibit sharp variation with θ around amplitude quadrature, with maxima and minima of the high-power measurements being as close as 1-2° to $\theta = 0$. Correspondingly, in order to be able to resolve these features ensuring low residual fluctuations of the homodyne angle is essential.

In order to see the effect of homodyne angle instability on $R(\theta)$, consider the homodyne detection with θ fluctuating as $\theta(t) = \theta_0 + \delta\theta(t)$

$$\begin{aligned} \delta q^{\theta}(t) &= \delta q(t)\cos(\theta(t)) + \delta p(t)\sin(\theta(t)) \\ &\approx \delta q^{\theta_0}(t) + \delta\theta(t)\delta q^{\theta_0+\pi/2}(t), \end{aligned} \tag{4.3.13}$$

where $\delta q^{\theta_0}(t)$ is the signal of a perfectly stable homodyne at the angle θ_0 and $\delta q^{\theta_0+\pi/2}(t)$ is such signal at the orthogonal quadrature. The signal spectral density

$$\bar{S}^{\theta}_{II}[\Omega] = \bar{S}^{\theta_0}_{II}[\Omega] + \bar{S}^{\theta_0+\pi/2}_{II}[\Omega] * S_{\delta\theta}[\Omega], \tag{4.3.14}$$

where $S_{\delta\theta}[\Omega]$ is the homodyne angle fluctuations spectrum and $*$ denotes the convolution,

$$\bar{S}^{\theta_0+\pi/2}_{II}[\Omega] * S_{\delta\theta}[\Omega] = \frac{1}{2\pi}\int d\Omega' \bar{S}^{\theta_0+\pi/2}_{II}[\Omega-\Omega'] S_{\delta\theta}[\Omega']. \tag{4.3.15}$$

In the presented experiment, the homodyne angle fluctuations were mainly confined to low frequency (suppressed within the bandwidth of 300 Hz by feedback loop), so $S_{\delta\theta}[\Omega']$ can be

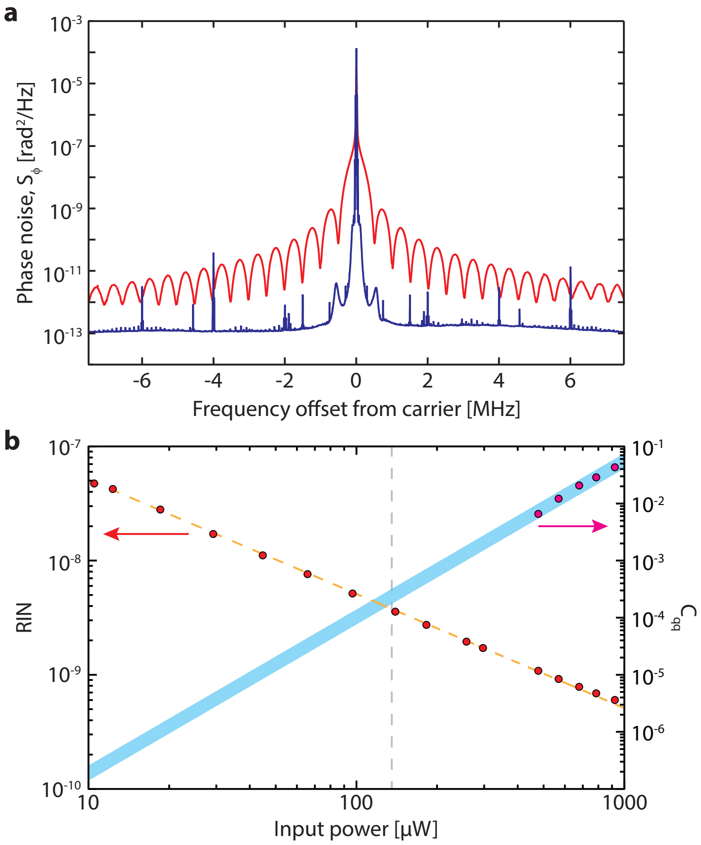

Figure 4.12 – **Phase and amplitude noise of the lasers used in the experiments:** (a) Phase noise about the carrier, measured using an imbalanced Mach-Zehnder interferometer (self-heterodyning). The blue trace shows the measurement for the employed Ti:Sa, whose phase noise contribution can be estimated to be $\le 2\cdot 10^{-13}\,\mathrm{rad}^2/\mathrm{Hz}$ around the mechanical frequency $\approx 3.4\,\mathrm{MHz}$, corresponding to frequency noise $\le 2\mathrm{Hz}^2/\mathrm{Hz}$. The noise peaks at ca. 250 kHz are attributed to the laser's relaxation oscillation frequency. Red shows a commercial external-cavity diode laser (NewFocus Velocity) for comparison, exhibiting at least 20 dB times more phase noise at similar frequencies. The noise measurement for the Ti:Sa laser clearly indicates absence of the $\sin^2(\Omega\tau_0)$ pattern, visible in the measurement for the diode laser and expected for the classical laser noise interference, showing that the phase noise of the Ti:Sa lasers was not observed. (b) Red data shows the amplitude noise measurement of the Ti:Sa characterized as relative intensity noise integrated over a 3 MHz bandwidth around the mechanical frequency. The dashed orange line shows a fit with $1/P$ dependence, characteristic of shot noise limited behavior. The deviation from this model provides C_{qq}, which can be extrapolated to $< 1\cdot 10^{-3}$ for the highest employed powers $\sim 150\,\mu$W, marked by the dashed gray line.

treated as a delta-function

$$\bar{S}_{II}^{\theta_0+\pi/2}[\Omega] * S_{\delta\theta}[\Omega] \approx \langle\delta\theta^2\rangle \bar{S}_{II}^{\theta_0+\pi/2}[\Omega]. \tag{4.3.16}$$

Neglecting terms of order $\langle\delta\theta^2\rangle$, eq. (4.1.16) is modified as,

$$\bar{S}_{II}^{\theta}[\Omega] = 1 + 4\eta C\Gamma_{\mathrm{m}}\left(\bar{S}_{zz}[\Omega](\sin^2\theta + \langle\delta\theta^2\rangle\cos^2\theta) + \frac{1}{2}\sin(2\theta)\,\mathrm{Re}\,\chi_z[\Omega]\right). \tag{4.3.17}$$

Correspondingly, due to the impossibility to completely suppress thermal noise on amplitude

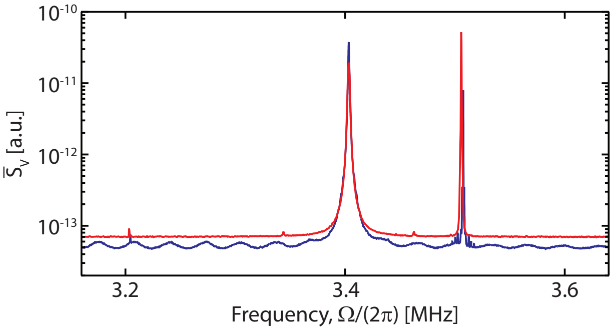

Figure 4.13 – **Excess noise due to taper vibrations:** Blue trace shows a measurement (sample AE/L2/B1/34) with the tapered fiber in contact with the nanobridges (see section 4.3.1). The red trace is a measurement of the same samples with the nanobridges removed and the tapered fiber in contact with the microdisk. For better visualization, the two datasets have been slightly offset.

quadrature, ΔR is diminished by the fraction $\langle\delta\theta^2\rangle/(\theta_{opt})^2$, where $\theta_{opt} \ll 1$ is the angle at which R reaches maximum. For the data presented here, $\sqrt{\langle\delta\theta^2\rangle} \approx 0.4°$, $\theta_{opt} \approx 1.2°$, resulting in the homodyne instability effect on R as $\langle\delta\theta^2\rangle/(\theta_{opt})^2 < 10\%$. Larger δ or smaller input power result in larger θ_{opt} and improve this constraint further.

4.3.6 Excess detection noise due to taper vibrations

While the amplitude quadrature of the employed Ti:Sa laser is quantum limited at Fourier frequencies around the mechanical oscillator, analysis of the initially measured displacement spectra revealed an additional background present in the measurement, that reaches 15% of the shot noise level around the mechanical oscillator Fourier frequencies for the largest powers used in the experiment. An example of a measured spectrum showing this noise is shown as the blue trace in fig. 4.13. In the measurement window, this structured background, extrinsic to the laser, is revealed around the amplitude quadrature where sensitivity to broadband thermomechanical noise is significantly reduced.

Investigating broadband spectra of this excess noise, as shown in fig. 4.14, lets us analyze its spectral dependence. We find evidence that its origin are mechanical vibrations of the tapered fiber, as the noise includes a series of peaks that we associate with vibrational resonances. The inset of fig. 4.14 plots the free spectral range of the noise peaks as a function of frequency, indicated with red data points, which is seen to follow a power law $\propto \Omega^{0.31}$. Such a power law scaling is consistent with phase velocity dispersion of the lateral vibrations of an elastic cylinder [216, 217].

As a second check of the hypothesis that the excess noise originates from fiber vibrations, the eigenmodes of a realistic tapered fiber geometry are computed using finite element modeling (blue data points). The model incorporates the known geometry of the taper, which is ca. 25 mm long and 80 μm in diameter at the clamping points. The taper profile is modeled as exponential in cross-section, as expected for a taper pulled with a uniform heat source [218].

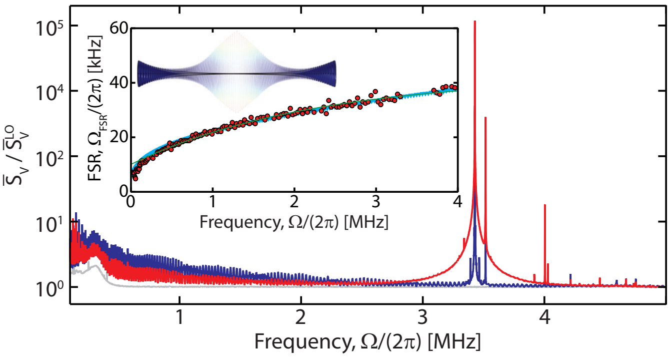

Figure 4.14 – **Broadband measurement of taper excess noise:** Broadband homodyne spectrum in phase and amplitude quadrature (red and blue respectively) normalized to the local oscillator shot noise level, shown in gray. The inset shows the measured free spectral range (FSR) of the noise peaks as a function of frequency (red data points), with a power law fit $\propto \Omega^{0.31}$ (green trace). The data shows excellent agreement with a finite element model calculation, shown in blue. The image shows the FEM solution of a fiber harmonic near 3.5 MHz. The measurements were taken with sample AE/L2/B1/34.

The model assumes the center of the taper is 1 μm in diameter. The prediction of this mode, shown as blue data point in Figure 4.14 inset, closely matches the measured data.

As for the case of guided-acoustic wave Brillouin scattering (GAWBS) in optical fiber[219], we ascribe the motion to the thermal excitation of the vibrational taper modes for the analysis frequencies in the MHz domain, as this frequency band is far outside the acoustic noise disturbance bands. In contrast to GAWBS, the vibrational noise peaks are only present when the taper is coupled to the microcavity. Therefore we attribute the excess amplitude and phase noise due to reactive and dispersive coupling of the tapered fiber to the cavity, which transduces taper fluctuations to both amplitude and phase fluctuations.

To solve is problem and attain a clean spectrum, we removed the fiber supports. This was achieved by loading them with a dummy tapered fiber and apply as much force as necessary to break these nanobridges without harming the sample. For the main results presented in the following section, we instead operate with the tapered optical fiber in contact with the microdisk. This eliminates any vibration in the sampling region of the optical resonator and results in complete suppression of this excess noise, as shown as the red trace in fig. 4.13.

4.4 Conclusion

The experiments reported in this chapter demonstrate how quantum effects of radiation pressure at ambient temperature become both, measurable and useful. Firstly, we were able to observe broadband quantum correlations in a light field detected after reflection off of a nanomechanical oscillator. By overcoming daunting levels of thermomechanical noise that has plagued all such attempts to date, we were able to show how the in-situ generated quantum correlations are a valuable resource for quantum-enhanced sensing in interferometry. Our demonstration is equivalent and complementary to the injection of squeezed states of light.

In a second experiment, we further showed how these correlations can be taken advantage of in order to realize a quantum-enhanced measurement of an (off-resonant) external force. By applying an external force to the oscillator, we demonstrated how quantum noise cancellation leads to an increase in the relative signal-to-noise ratio for the external force.

In conclusion, despite being subtle, the observed effects are unprecedented, and are the first broadband demonstration of long-standing theoretical predictions made in the gravitational-wave community. In fact, the techniques presented here have been adopted by the LIGO community to test for quantum correlations in the interferometer [220]. Further increasing the system's performance will eventually lead to ponderomotive squeezing [60, 61, 150, 195] and sideband asymmetry [150, 197, 199] observable at room temperature, as the quantum correlations are the basis for these effects.

In future room-temperature optomechanics experiments, in which back-action is the dominant force noise, the "variational" measurement technique here described can be used to surpass the standard quantum limit for a linear force measurement. This remains a long-standing pursuit in the gravitational wave community, and was only very recently demonstrated in a micro-cavity optomechanical system at dilution refrigerator temperatures to obtain a displacement sensitivity beyond the finite-efficiency standard quantum limit [221]. As discussed in chapter 1, optomechanically generated squeezed light at room-temperature would be extremely advantageous for further enhancement of the sensitivity in gravitational wave interferometers. Limited by radiation-pressure shot noise, the ponderomotive squeezing would improve the sensitivity beyond usual quantum limits by enhancing the measurement of the same mechanical object that generated it.

5 Outlook

The work reported in this thesis accessed an entirely new regime of cavity optomechanics at room temperature. Utilizing a near-field optomechanical transducer with exceptionally high single-photon cooperativity, we were able to observe the effects of quantum measurement back-action despite the large thermal phonon occupation at room temperature. Even though the thermal motion dominated the measurement back-action induced motion by two orders of magnitude at the highest optical powers used in the experiment, we successfully measured the correlations created between the optomechanical system and the probing light. Around the amplitude quadrature, the displacement noise due to thermal motion is suppressed by 40 dB and hence the correlated signal becomes comparable in magnitude. We therefore pursued a variational measurement strategy [79] allowing us to discern the correlations at the level of 10% over a frequency range of more than an octave around the mechanical resonance frequency. In addition, we demonstrated how to use these correlations to achieve quantum-noise cancellation, leading to an enhanced detection ability of signal-to-noise of an off-resonant external force.

Enhancing the performance of our optomechanical system to further increase the quantum back-action contribution in the total motion of a mechanical oscillator will allow for the investigation of related quantum-mechanical effects at room temperature, such as the generation of ponderomotive squeezing or motional sideband-asymmetry. Another elusive goal that remains is the feedback-cooling of a room-temperature nanomechanical oscillator close to its quantum mechanical ground state.

5.1 Future directions

For the experiments mentioned above, it is essential to further enhance the single-photon cooperativity $C_0 = 4g_0^2/(\kappa\Gamma_\mathrm{m})$ of our optomechanical devices. To achieve this, we attempted to move the beam closer to the disk in order to achieve higher optomechanical coupling as C_0 scales quadratically in this manner. As the intrinsic optical quality factor is already deteriorated by the presence of the beam in the near-field, our observations showed a further dramatic increase of the optical linewidth when positioning the beam further into the optical mode. Part of this can also be attributed to the fact that additional loss occurs due to the nanobeam itself becoming an optical waveguide. The latter also means a physical heating of the beam which is intuitively counterproductive when trying to achieve a large quantum back-action to thermal noise ratio,

$$\frac{n_{\mathrm{QBA}}}{n_{\mathrm{th}}} = C_0 n_{\mathrm{c}} \left(\frac{k_{\mathrm{B}} T}{\hbar\Omega_{\mathrm{m}}}\right)^{-1} = \frac{4g_0^2}{\kappa} n_{\mathrm{c}} \frac{\hbar Q_{\mathrm{m}}}{k_{\mathrm{B}} T}. \tag{5.1.1}$$

The only remaining parameter that can independently optimized in order to achieve a higher cooperativity is the mechanical quality factor.

The efforts currently undertaken to enhance the mechanical quality factor are detailed in the following sections.

5.1.1 Phononic crystal nanobeams

The boundary conditions of the vibrational mode-shape of a doubly-clamped beam require that the displacement profile exhibits curvature close to the supports. Following the approach of anelastic theory, we find that the loss dilution of the mechanical quality factor due to stress for a nanobeam can be expressed as (see eq. (3.1.1)) [162, 164],

$$\frac{Q_{\mathrm{m}}^{(n)}}{Q_{\mathrm{int}}} = (\underbrace{2\lambda}_{\text{clamping}} + \underbrace{\pi^2 n^2 \lambda^2}_{\text{antinodes}})^{-1}, \tag{5.1.2}$$

with $\lambda = \frac{t}{l}\sqrt{E/(12\sigma)}$. Here, Q_{int} is the intrinsic quality factor of the unstressed oscillator, n is the mode number, E is Young's modulus, t (l) is the thickness (length) of the mechanical resonator and σ is the tensile stress. An enhancement of the dilution factor can be achieved by increasing the aspect ratio l/t and/or the tensile stress.

Another approach recently demonstrated is the localization of the displacement profile around an engineered defect by micro-patterning the nanobeam [222]. Since the first term in eq. (5.1.2) is caused by the curvature at the clamping points, while the second term depends on the mode number and describes the curvature at the antinodes [164], a localization of a specific mechanical mode can significantly reduce its bending at the supports. As in general $\lambda \ll 1$, meaning that the contribution due to the bending at the clamped ends of the beam dominates, isolation of the displacement profile away from the clamping points leads to a strong enhancement of the loss dilution.

Inspired by this ”soft-clamping" technique, we have fabricated micro-patterned nanobeams (phononic crystals) with stress $\sigma \sim 800$ MPa, as shown in fig. 5.1a (manuscript in preparation [223]). The beams are between 2 – 6 mm long and 20 – 100 nm thick. The size of the unit cells determines the localized mode number n, and is in this case chosen to localize the mechanical mode around $\Omega_{\mathrm{m}} \approx 2\pi \cdot 2.5$ MHz. The fabricated sample is placed in a high-vacuum environment at ~ 10^{-7} mbar to suppress gas damping of the mechanical quality factor. We estimate the ultimate measurable quality factor, Q_{lim}, at a given pressure by $Q_{\mathrm{lim}}^{-1} = Q_{\mathrm{m}}^{-1} + Q_{\mathrm{gas}}^{-1}$ (see section 2.2.1) and use a simple model to find the contribution due to gas damping [224],

$$Q_{\mathrm{gas}} = 4.2 \cdot 10^{8} \left(\frac{10^{-6}\,\mathrm{mbar}}{p}\right)\left(\frac{\Omega_{\mathrm{m}}}{2\pi \cdot 1\,\mathrm{MHz}}\right)\left(\frac{t}{20\,\mathrm{nm}}\right), \tag{5.1.3}$$

with the pressure p.

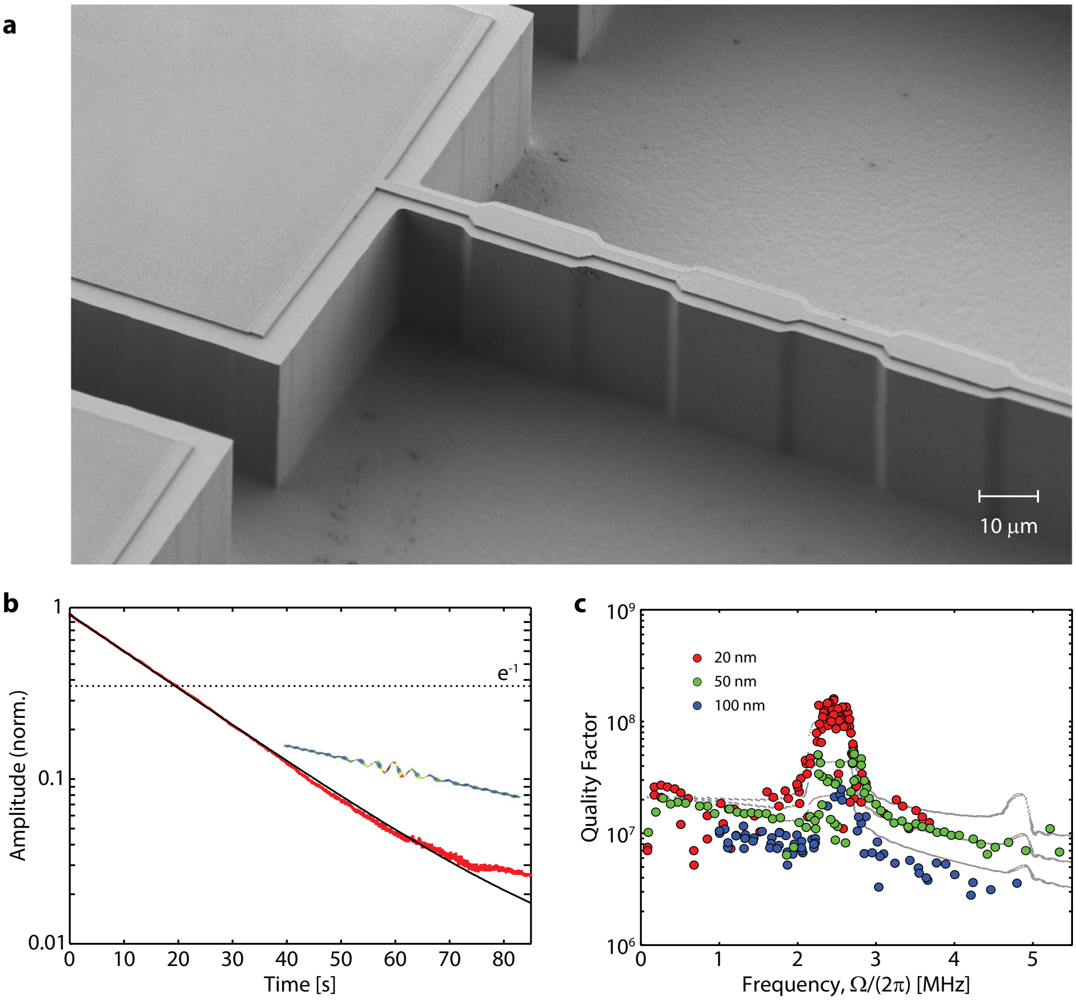

Figure 5.1 – **Quality factor measurements of micropatterned nanobeams:** (a) Scanning electron micrograph of patterned nanobeam with total length $l = 3$ mm. Image is taken before the release of the Si_3N_4 (b) Amplitude ring-down measurement to determine the mechanical quality factor. We compare the ring-down times of a normal beam (blue trace) with that of a patterned beam (red trace) for the same mechanical mode. (c) Quality factor versus frequency for patterned beams with varying corrugation lengths and different thicknesses. Clearly visible is the enhancement in Q_{m} by a factor of 10 for the localized mechanical mode. Note that the localized mode slightly shifts when varying the thickness t.

The measurement results of the quality factors for different beams are shown in fig. 5.1b and c. The beams are measured in a fiber interferometer [225] using the ring-down method, in

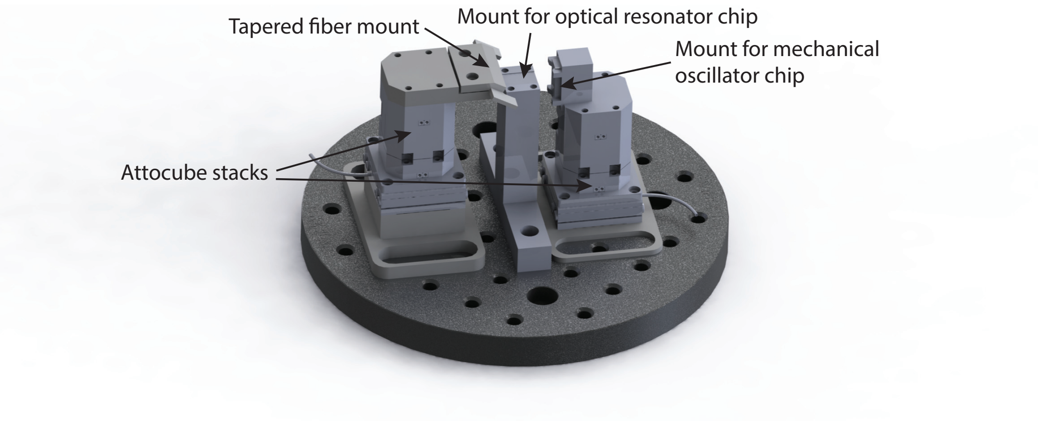
Tapered fiber mount
Mount for optical resonator chip
Mount for mechanical oscillator chip
Attocube stacks

Figure 5.2 – **Near-field setup:** Rendered CAD design of the planned near-field setup. For description, refer to the text.

which laser light from a lensed fiber is focused onto the beam and the substrate underneath, and then reflected back into the fiber. The motion of the nanobeam shifts the phase of the light, allowing for the detection of the reflected light through a homodyne interferometer to access the mechanical spectrum. For the measurement of the mechanical quality factor, the motion of the beam is briefly actuated at the target mode's frequency using a piezo, which is placed underneath the sample chip. We then record the time trace of the ring-down and fit an exponential function to it in order to extract the quality factor. The result of measurements of different order modes on different beams with sweeps in unit cell size (to find the ideal localization conditions) is shown in fig. 5.1c. We were able to measure quality factors of $1.5 \cdot 10^8$ for a 2.5 MHz localized mechanical mode which means a gain of a factor 10 compared to unpatterned beams.

As these long beams are very difficult to integrate with an optical microdisk without the beam collapsing and sticking to the disk during the fabrication process, we are currently developing a *near-field setup* in which mechanical oscillator and optical resonator are on separate chips. The CAD drawing is shown in fig. 5.2. The chip with the optical resonator (silica microsphere) will be placed on the fixed center pedestal. The tapered optical fiber and the chip with the mechanical oscillators can then be brought into the near field of the optical cavity independently by three-dimensional nanopositioners (attocubes). The entire setup will then also be placed into a high-vacuum environment at 10^{-7} mbar. To ensure mechanical stability, the whole setup will be placed onto a dedicated vibration-isolated table, similar to the present setup (see appendix A). We emphasize that experiments in the near-field setup will be performed at lower optomechanical coupling rates due to the limitation in positioning the two elements with respect to each other. The ultimate goal will be to integrate these patterned beams into the existing device to achieve the aforementioned enhancement in cooperativity.

As seen in fig. 5.1a, we have so far studied unit cell designs of rectangular shape with the sole purpose of localizing the mechanical mode. Calculations and simulations of different unit cell shapes, for example a tapering of the beam towards its center, have shown that this can lead to increased stress in regions of maximum displacement [223]. Adding this method of ”stress-engineering" to the nanobeams could eventually lead to another increase in mechanical Q by a factor of $\sim 1.5-2$.

5.1.2 Nanobeams with ultra-high stress

Another possibility to enhance the mechanical quality factor (in addition to the discussion above) is to increase the tensile stress in the film (see eq. (5.1.2)) as the ultimate yield strength of silicon nitride is reached for a stress 6.4 GPa [226].

The deposition method (described in section 3.2.3) for silicon nitride used up to this point is the low pressure chemical vapor deposition (LPCVD). Here, the relaxed silicon nitride film is deposited at a temperature 800°C resulting in a stressed film at room temperature of $\sigma \sim$ 800 MPa. The advantage of this method is that the silicon nitride film is highly stoichiometric, i.e. no further treatment is necessary to purify and clean the Si_3N_4, and therefore no further enhancement in intrinsic stress can be achieved.

As a different approach, a plasma-enhanced chemical vapor deposition (PECVD). Here, the film is deposited at lower temperatures around 300°C. The deposition process can be controlled such that tensile stress $\sigma \sim 400$ MPa of the film at room temperature can be achieved [227]. Films deposited with PECVD are known not to be very stoichiometric as they possess a significant amount of hydrogen, requiring an annealing step in order to achieve a purified Si_3N_4 film. It has been demonstrated that annealing of the film by performing ultraviolet thermal processing (UVTP) leads to breaking of hydrogen bonds, as shown in fig. 5.3a, and removal of these impurities. In particular, the stress of thin films ($t < 100$ nm) can be increased by up to 1 GPa this way [228, 229]. Figure 5.3b shows measurement results of this stress increase in dependence of UV irradiation time from [228].

Due to the rapid deposition of water (within seconds) under ambient conditions [100], we chose to implement an ”in-situ" solution, which is shown in fig. 5.4. To realize this UVTP treatment of the nanobeam samples, as the first element, we have equipped the measurement setup inside the vacuum chamber with a high-power (1mW), 250 nm UV LED, which can be positioned close to the nanobeams using the nanopositioners. With this, the necessary intensity for efficient UV irradiation with intensities of up to 100 mW/cm^2 [228] can be achieved. To complete the UVTP setup, the sample stage is equipped with a micro heater that can be heated to up to temperatures ~450°C. The first PECVD nanobeams are currently under development and will be processed soon after submission of this thesis.

5.2 Conclusion

With the approaches described in this chapter, we hope to be able to enhance the cooperativity of our optomechanical system with the aim to observe stronger quantum back-action and

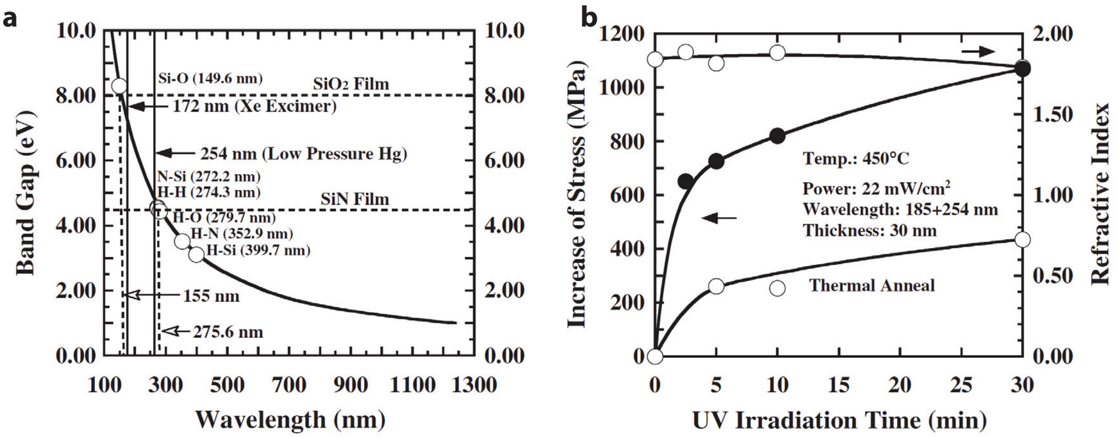

Figure 5.3 – **Ultraviolet thermal processing:** (a) Band gap versus wavelength. Photons of wavelength 250 nm provide sufficient energy to break H-Si and H-N bonds as well as N-Si. The latter can then recombine in order to enhance the stoichiometry of the film and achieve higher stress. (b) Increase of stress versus UV irradiation time. A clear improvement in stress enhancement is visible when exposing the samples to strong UV light (center curve, filled circles) compared to a pure thermal anneal (bottom curce, open circles). The top curve shows the change in refractive index (right axis). Images adapted from [228].

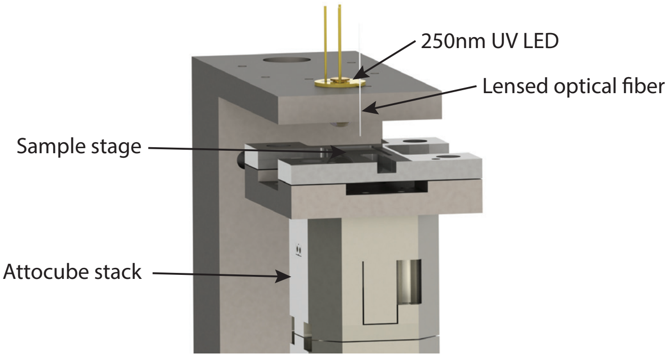

Figure 5.4 – **Ultraviolet thermal processing setup:** Rendered CAD design of the fiber interferometer setup for measurement of mechanical quality factors. For UV thermal processing, a ceramic micro heater underneath the sample stage and a 250 nm UV LED are implemented.

eventually the creation of ponderomotive squeezing at room temperature. For this, the ultimate goal is the engineering of an integrated structure with a micro-patterned nanobeam, potentially in combination with the stress-enhancement for PECV-deposited silicon nitride.

In the near-field setup, where lower optomechanical coupling rates are expected, the plan is to demonstrate room-temperature feedback cooling of the mechanical oscillator to its quantum-mechanical ground state, analogous to the work presented in [73].

A Experimental setup

The schematic of the setup, showing the essential components, is shown in fig. A.2. Key element is the vacuum chamber which contains a chip with a number of optomechanical samples. Using nanopositioners, the desired device can be probed by coupling a tapered optical fiber to the microdisk cavity. Three available lasers constitute the light sources for the experiments: two tunable external cavity diode laser (ECDL) at 780 nm and 850 nm and a titanium-sapphire (Ti:Sa) laser, which is described in more detail in the following section. For the main experiments presented in this thesis, the Ti:Sa laser at 780 nm acts as the ”meter" beam used for probing the cavity, while the 850 nm ECDL serves as the ”feedback" beam providing moderate feedback cooling of the mechanical oscillator, as described in section 4.3.2. The tunable 780 nm ECDL mainly serves characterizing purposes to determine the parameters of the optomechanical device in terms of resonance frequencies, quality factors and optomechanical coupling rates.

Applying the Pound-Drever-Hall method [146], both lasers are locked to the respective cavity resonance by frequency modulating the light (using EOMs) and demodulation at the drive frequency in the detected transmission signals (by avalanche photodiodes) after the cavity. The optical path through the optomechanical device also constitutes one arm of a balanced homodyne interferometer. After probing the cavity and being combined with a local oscillator, the mechanical motion in an arbitrary quadrature of the light field can be measured, leading to the results presented in chapters 3 and 4.

To minimize the susceptibility to external vibrations, the optical setup is placed on floated optical tables. The vacuum system on the other hand, containing the device under test, is situated on a floated breadboard on top of a massive granite block (as also used in atomic-force microscopy) to guarantee even superior vibration isolation. The chamber is evacuated by an ion pump that ionizes gas particles and employs a high electrical potential to accelerate the ions towards its cathode to subsequently capture them at this point. In contrast to a turbo pump, an ion pump possesses no moving components, such that the pumping is completely free of vibrations. In addition to these measures, a custom-made acoustic shield covers the vacuum setup and further insulation for the acoustic frequency spectrum. The entire isolated

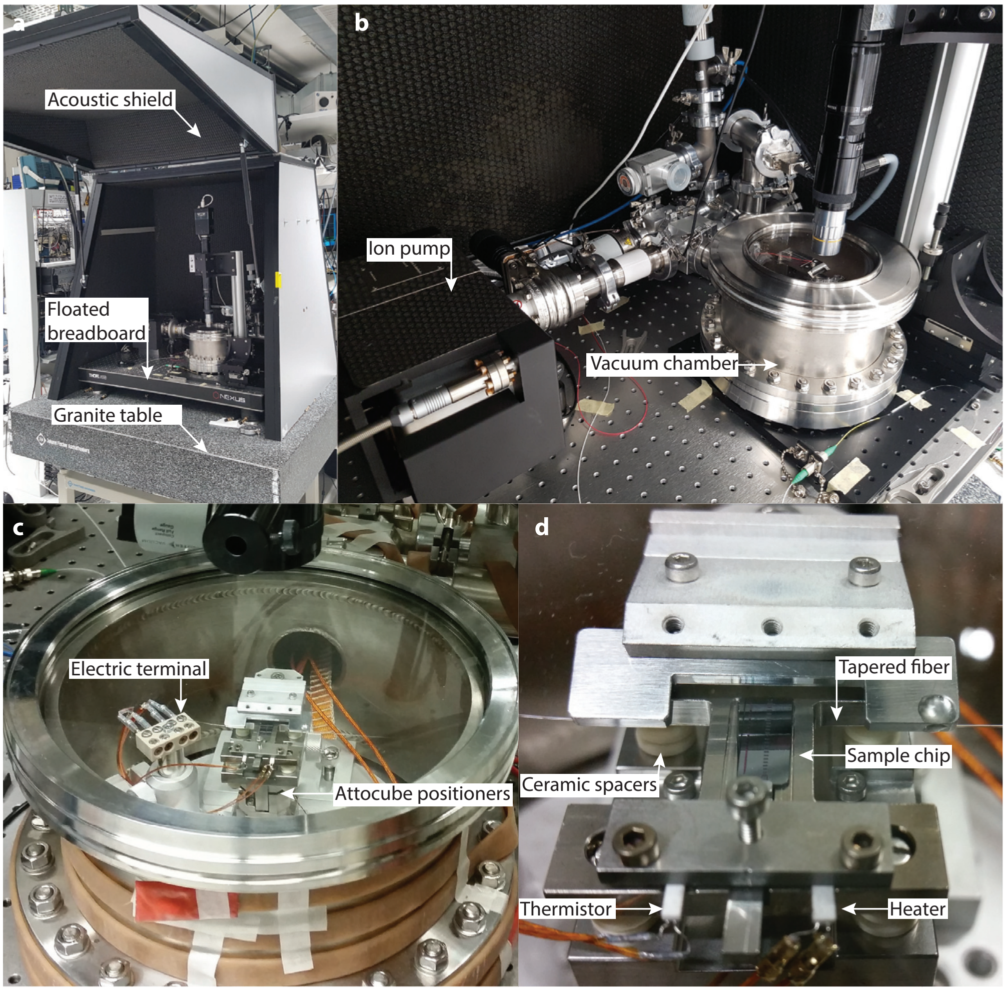
a
b
c
d
Acoustic shield
Floated breadboard
Granite table
Ion pump
Vacuum chamber
Electric terminal
Attocube positioners
Tapered fiber
Sample chip
Ceramic spacers
Thermistor
Heater

Figure A.1 – **Picture of the vacuum setup.** (a)+(b) Vacuum system on a floated breadboard positioned on a granite AFM table. (b) Close-up of the high-vacuum system allowing for operation at 10^{-7} mbar. (c)+(d) Inside the chamber is the optomechanical device under test that is coupled to a tapered optical fiber. The sample is positioned on a stack of nanopositioners allowing for precise three-dimensional alignment with respect to the optical fiber. A heater and thermistor attached to the thermally isolated sample stage allow for sample baking up to 450°C.

vacuum system is shown in fig. A.1.

The following appendices describe the key elements of the entire experiment in more detail. In particular appendix B explains the operation of the MSquared SolsTiS titanium-sapphire laser, appendix C explains the assembly and correct handling of a vacuum system, and appendix D details the setup, balancing and locking procedure of the homodyne detection scheme. Finally, appendix F presents the observation and countermeasures to restore degraded mechanical quality factors due to adsorption of water molecules.

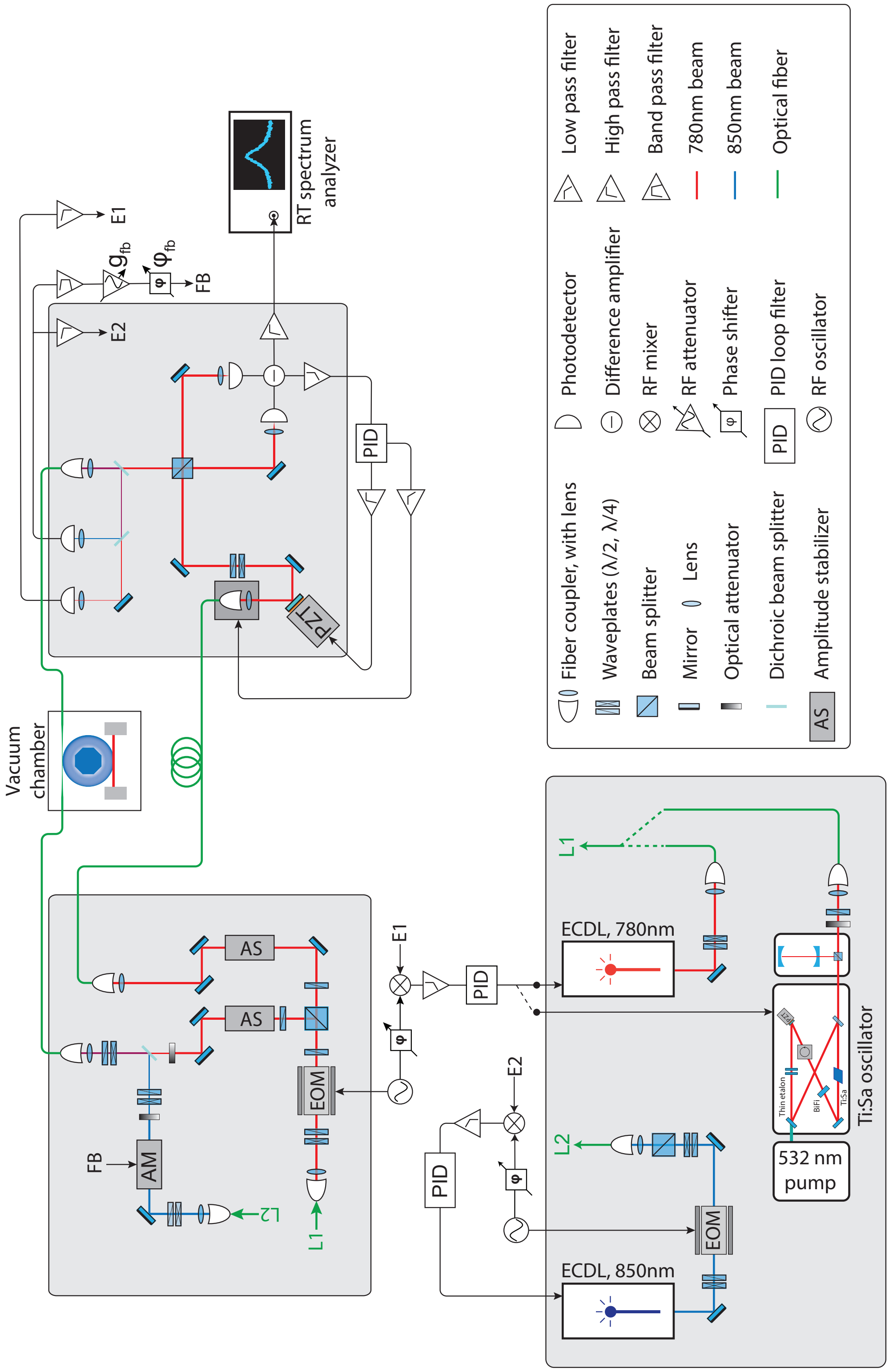
Vacuum chamber
RT spectrum analyzer
E1
E2
g_fb
φ_fb
FB
PID
PZT
AS
AS
AM
FB
EOM
L1
L2
E1
E2
PID
PID
ECDL, 780nm
ECDL, 850nm
EOM
L1
L2
Thin etalon
BiFi
TiSa
532 nm pump
Ti:Sa oscillator
Fiber coupler, with lens
Waveplates (λ/2, λ/4)
Beam splitter
Mirror
Lens
Optical attenuator
Dichroic beam splitter
Amplitude stabilizer
Photodetector
Difference amplifier
RF mixer
RF attenuator
Phase shifter
PID loop filter
RF oscillator
Low pass filter
High pass filter
Band pass filter
780nm beam
850nm beam
Optical fiber

Figure A.2 – **Layout of the experiment.**

B Ti-sapphire laser operation

The quantum correlation measurements presented in this thesis were performed using a MSquared SolsTiS Ti:Sapphire laser. Ti:Sa lasers are widely used in research as they provide wide tuning range and output low amplitude and phase noise (cf. section 4.3.4). Figure B.1a shows an image of the SolsTiS system used in the experiment. The first element in the chain of the laser system is a 532 nm, 10 W laser serving as the pump for the titanium-doped sapphire crystal (Ti:Al_2O_3). Following the pump laser is an optics module for injecting the pump light into the cavity, which contains the Ti:Sa crystal inside the main laser cavity. A small fraction of the laser head's output is injected into a reference cavity, which reduces the laser linewidth down to 50 kHz if locked to.

The laser is controlled via a web interface provided by an Ethernet control unit (ICE – Instrument Control by Ethernet). A screen shot of the interface is shown in fig. B.1b. For locking of the laser to a specific wavelength (e.g. a microresonator mode), the following procedure is followed:

1. Identification of the target wavelength by characterizing the optical spectrum with the diode laser and readout of the wavelength with a calibrated wavelength meter.
2. Coarse adjustment of the target wavelength by rotation of a motorized intracavity birefringent filter.
3. Adjustment and locking of the intracavity thin etalon for stable operation close to the target wavelength.
4. Locking to the temperature-controlled reference cavity at the target wavelength using one of the SolsTiS cavity mirrors, which is mounted on a fast piezo.
5. Finally, a PDH lock is applied by feeding an error signal, which is derived from the science cavity resonance, to the laser controller.

Once locked to the science cavity, the laser operates stably for sufficient periods of time, allowing to perform the experiments without midst falling out of the lock. Typically, the

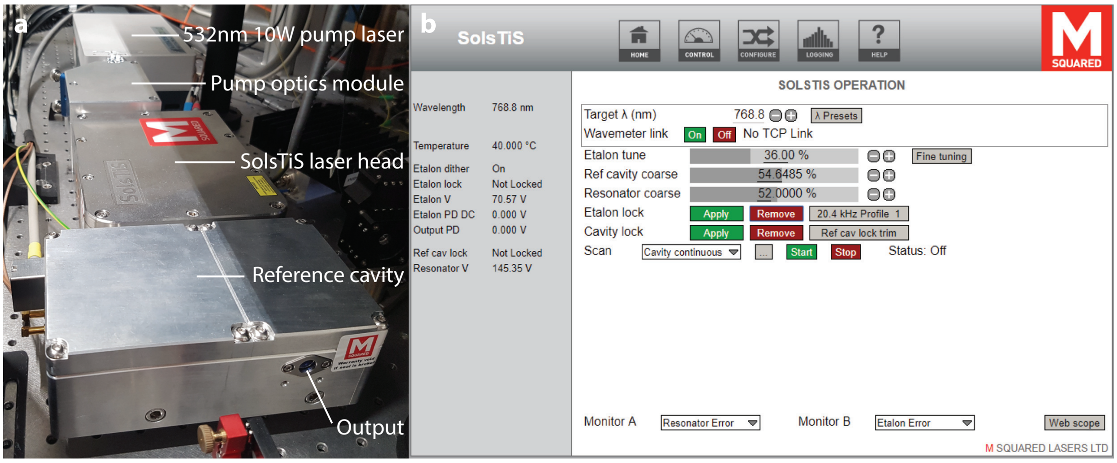
a
532nm 10W pump laser
Pump optics module
SolsTiS laser head
Reference cavity
Output
b
SolsTiS
HOME
CONTROL
CONFIGURE
LOGGING
HELP
M SQUARED
SOLSTIS OPERATION
λ Presets
Fine tuning
Apply
Remove
Start
Stop
Web scope
M SQUARED LASERS LTD

Wavelength 768.8 nm
Temperature 40.000 °C
Etalon dither On
Etalon lock Not Locked
Etalon V 70.57 V
Etalon PD DC 0.000 V
Output PD 0.000 V
Ref cav lock Not Locked
Resonator V 145.35 V

Target λ (nm) 768.8
Wavemeter link On Off No TCP Link
Etalon tune 36.00 %
Ref cavity coarse 54.6485 %
Resonator coarse 52.0000 %
Etalon lock 20.4 kHz Profile 1
Cavity lock Ref cav lock trim
Scan Cavity continuous Status: Off
Monitor A Resonator Error
Monitor B Etalon Error

Figure B.1 – **MSquared SolsTiS laser.** (a) Picture of the Ti:sapphire laser system. (b) Screen shot of the software interface for control of the laser.

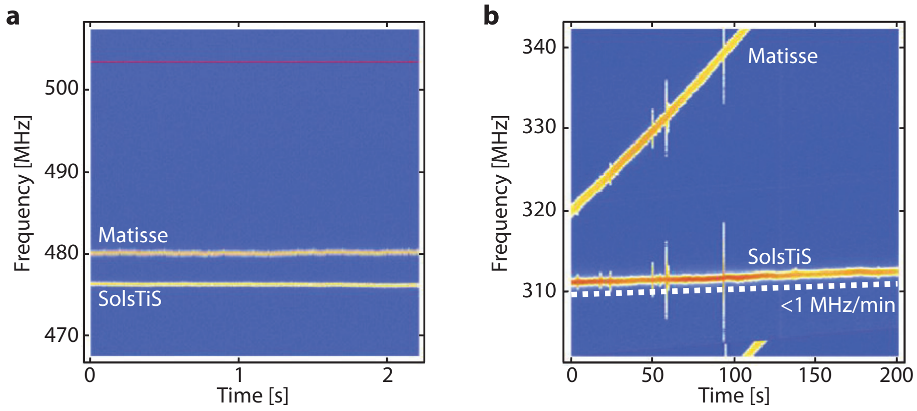

Figure B.2 – **Frequency stability of the SolsTiS laser.** (a) Short and (b) long term measurement of the beat frequency versus time between two Ti:Sa lasers and a Menlo Systems frequency comb, stabilized to an atomic clock. The SolsTis shows little drift $< 1\,\mathrm{MHz\,min}^{-1}$.

laser stays locked for the entire work day. Figure B.2 a and b compare the short and long term frequency stability of the SolsTiS system to that of a Sirah Matisse Ti:Sa system used in previous experiments. The measurements were acquired by beating both lasers with a Menlo Systems frequency comb, which is stabilized to an atomic clock, and monitoring the beat frequency over time. Both the Ti:Sa lasers were hereby locked to their respective reference cavity and left running for a day to equilibrate with the environment. The result shows very stable operation of the SolsTiS with a frequency drift $< 1\,\mathrm{MHz\,min}^{-1}$. Its linewidth was measured to be $\sim 100\,\mathrm{kHz}$, many orders of magnitude below the typical linewidth of the microdisk resonators ($\kappa \approx 2\pi \cdot 1\,\mathrm{GHz}$).

C (Ultra-)High vacuum chambers

The center piece of the experimental setup is the vacuum chamber. Operation in such is essential to alleviate gas damping (see section 3.3.3) of the mechanical oscillator but also to avoid contamination of the sample due to dust particles, adsorption of water molecules, etc. For an optimal result, it is vital to keep the vacuum chamber as clean as possible. For this, we adhere to the following vacuum guidelines:

- Keep the chamber vented for as short as possible. Especially when performing tasks outside the chamber in between (change of samples with air-side mounting steps, modification of the vacuum-side setup, etc.), the chamber should be closed and ideally evacuated, even if with mechanical pumps only. This will keep possible contamination of the chamber's inside to a minimum.
- Vent and purge the chamber with dry nitrogen (N_2) gas instead of air. This helps to reduce the amount of unwanted adsorbate (especially water molecules) introduced into the chamber.
- Only use vacuum compatible components and materials with very low out-gassing rates under vacuum. We use materials that are often considered for vacuum applications, which include (unanodized) metals such as 304(L) stainless steel and aluminum, plastics like Teflon (PTFE) and polyether ether ketone (PEEK), and alumina ceramics for thermal isolation. For electrical connections, Kapton insulated wires and lead-free solder are common choices. Another feature of vacuum compatible components are the polished surfaces minimizing the amount of adsorption of water molecules.
- Any component introduced into the vacuum setup must be thoroughly cleaned in order to remove various residues, e.g. flux from soldering, lubricants from machining, etc.

Following these steps, the experiments of this thesis were performed in a high-vacuum environment at a pressure around 10^{-7} mbar using the setup described in appendix A. The limiting factor in the achievable pressure (besides the ISO-KF flanges that are rated for pressures down

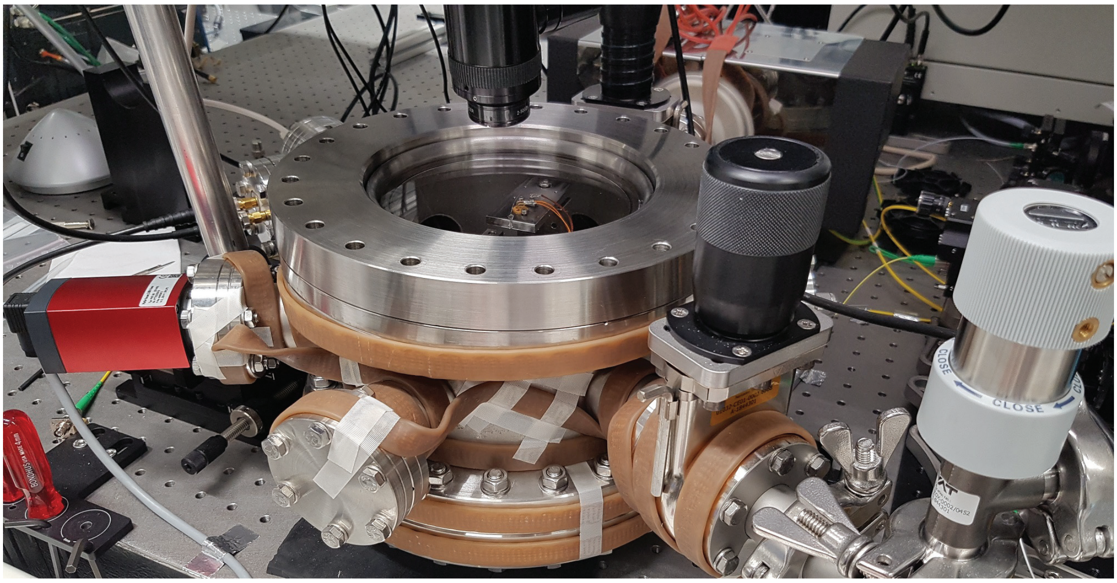

Figure C.1 – **Ultra-high vacuum chamber:** Featuring only CF flanges, this chamber is capable of reaching the UHV regime. The right hand side of the picture shows the port for the mechanical pump (roughing and turbo pump) together with the leak valve used to vent and purge the chamber with nitrogen gas. In the background, the ion pump is placed, guaranteeing vibration-free operation at high-vacuum levels. The chamber and flanges are wrapped in heat ribbons for a potential bake-out, once gas-damping becomes the limiting factor.

to 10^{-8} mbar) is water that is adsorbed onto the surfaces when the chamber is cycled. Under vacuum, this leads to desorption of water vapor limiting the ultimate pressure to $\sim 10^{-8}$ mbar. This limitation can be eluded by heating up the entire vacuum system, also referred to as a bake-out.

For future measurements where gas damping even at high vacuum pressures might become an issue, we have designed a new chamber capable of reaching the ultra-high vacuum (UHV) regime $< 10^{-9}$ mbar. To this end, we created a similar design to the setup already in place with the key difference of using conflat (CF) flange interconnections. The new UHV chamber is shown in fig. C.1.

The following sections detail the cleaning procedure of the components (appendix C.1), assembly advices of the UHV chamber (appendix C.2) and the bake-out process (appendix C.3).

C.1 Cleaning

As mentioned above, all parts that are being placed inside a vacuum system must be extremely clean in order to limit out-gassing, but also reduce the risk of redepositing contaminants onto samples during pump-down and bake-out. Documents are publicly available detailing the cleaning procedures for UHV components in large-scale high-energy physics experiments, such as the Deutsches Elektronen-Synchrotron (DESY) [230] and the European Organization for Nuclear Research (CERN) [231], and also for the Laser Interferometer Gravitational-Wave

Observatory (LIGO) [232].

The essential procedure for cleaning of parts and components is the following:

1. Wearing gloves through the entire procedure, the first step is to wipe off visible grease and dirt (e.g. lubricants from machining) using lint free wipers.
2. In an ultrasonic bath, in which contaminants also in hard-to-reach places are removed, the parts are then cleaned using an appropriate detergent (based on the material, refer to the references given above) for at least 20 minutes. Afterwards, the detergent is replaced first with acetone (if all materials permit), followed by ethanol and finally methanol. For each of these, the parts are sonicated for another 20 minutes minimum. While acetone is very suitable for thorough cleaning, it will leave residues on the surface and hence contaminate the UHV environment. Therefore, ethanol and methanol, solvents with gradually lower molecular weight, are used as the final steps to replace the acetone.
3. The now clean parts should be immediately dried with nitrogen gas to completely evaporate any remaining residues from the solvents.
4. After finishing the cleaning procedure, the components should be immediately implemented into the vacuum system to avoid recontamination. If prior assembly is necessary work on a clean workbench layered with aluminum foil.
5. Before placing a sample into the setup, the vacuum chamber should be evacuated after new components have been added to the system.

Parts and components that are too large for the sonicator (e.g. the vacuum chamber itself) need to be thoroughly cleaned using lint free wipers and the solvents mentioned above in the same order, followed by drying with nitrogen gas.

C.2 Assembly of a UHV system

For UHV applications, it is inevitable to use conflat (CF) matings throughout the entire system. Instead of a Viton o-ring as it is the case for ISO-KF flange connections, each of the two mating CF flanges has a knife edge that cuts into a copper gasket, creating an extremely leak-tight, metal-to-metal seal. As the soft copper is able to forgive small defects in the knife-edges of the flanges, CF in principle allows for an operation down to 10^{-13} mbar. In reality the base pressure will be limited by out-gassing of the materials used inside the chamber.

The key for being able to reach UHV base pressures is a leak-free assembly of the vacuum system. Other than the easy-to-handle ISO-KF flanges, conflat flanges require a careful procedure as the copper gasket must be uniformly clamped. In contrast to the Viton o-rings for the KF system, the copper gaskets cannot be reused, i.e. a new (clean, see procedure

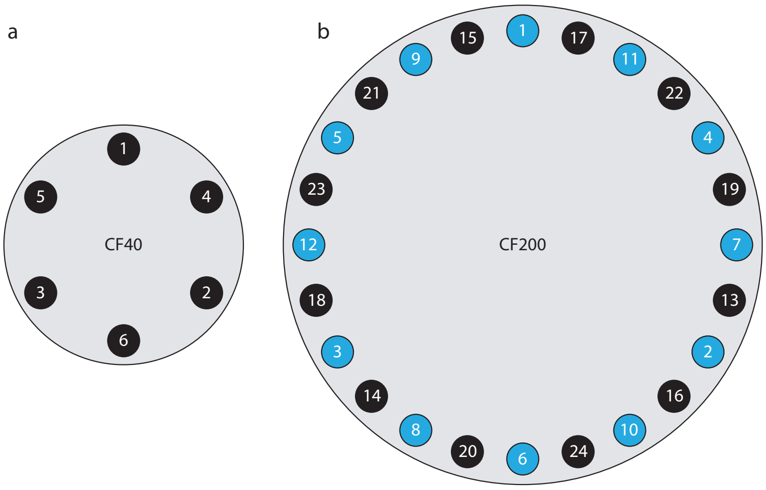

Figure C.2 – **Sequence for CF flanges:** "Triangular-reverse-direction" pattern for sealing CF flanges. For description refer to the text.

in appendix C.1) gasket is necessary each time two flanges are mated. To avoid "see-sawing" and to ensure a leak-free seal, the copper gasket should be clamped evenly.

In the UHV community, a well-established method is the "triangular-reverse-direction" sequence in which the bolts are tightened in triangular patterns with alternating directions. The sequence is illustrated in fig. C.2 for the two common flange sizes in our setup. Ideally with a torque wrench starting from low 6 Nm, at least two rounds of the sequence should be completed each time before gradually increasing the torque in $1-2$ Nm steps to the maximum value of typically 20 Nm. At this torque, the sequence should finally be gone through multiple times until none of the bolts tighten any further. After completion of this entire procedure, an even gap of ~ 1.5 mm between the flanges with the copper gasket remaining barely visible indicates a leak-tight seal. Ultimately, all matings should be checked by performing a leak test.

For convenience, fluorocarbon gaskets are available that provide a reusable seal in non-critical, non-UHV applications, particularly when frequent reassembly is necessary (e.g. frequent changes of samples). These have similar ratings to ISO-KF seals in terms of pressure but cannot be baked out, as the maximum temperature rating is typically $< 100°$C.

Figure C.3 shows measurements of the pressure versus time. The orange trace represents a pump down using only the turbo pump. When comparing to the blue trace, which shows a pressure curve, where the pumping has been switched to an StarCell ion pump after two hours of turbo pumping to $\sim 1 \cdot 10^{-4}$ mbar, a significant improvement in pump speed is observable. The red trace shows the initial pump down after the assembly of the chamber. The pump speed is slower due to evaporating solvent residues etc. A slower pump down is also typical after exposing the chamber to atmosphere for an extended amount of time, as well as after adding freshly cleaned components. With the present setup, we can reach pressures $\sim 8 \cdot 10^{-7}$ mbar when pumping for several days.

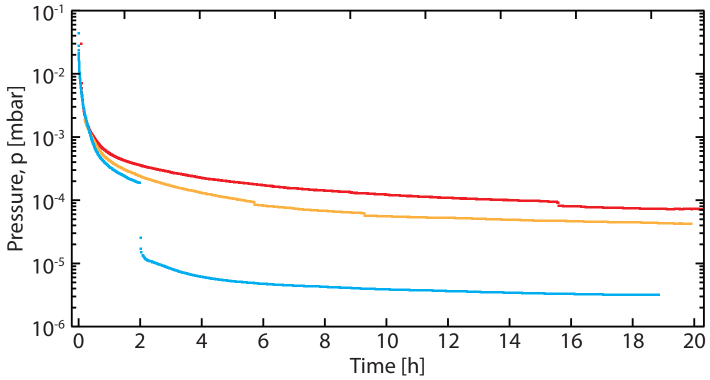

Figure C.3 – **Pumpdown of the vacuum chamber:** Measurement of the pressure inside the vacuum chamber versus time. The orange trace shows a pump down with only the turbo pump. Higher pump power is supplied by the StarCell ion pump which can be switched to at pressures $\sim 1 \cdot 10^{-4}$ mbar (blue trace). The red trace shows the initial pump-down after assembly which is slower due to evaporating solvent residues etc.

For ongoing experiments with nanobeam samples that feature extremely high mechanical quality factors (see the outlook in chapter 5), gas damping might become the limiting factor at these pressures. To reach pressures in the UHV range, a bake out of the chamber is inevitable. The process is detailed in the following section.

C.3 Bake-out of a vacuum chamber

Every time a vacuum system is opened to ambient air with its attendant humidity, the internal surfaces (chamber surfaces as well as other parts inside the chamber) are covered with multiple layers of water molecules. Any subsequent pump-down removes two components from the vacuum system: the permanent gases contained in air (mainly O_2 and N_2) and the water molecules desorbing from the internal surfaces. It turns out that at pressures below 10^{-3} mbar, water makes up 99% of the gas load. As the water-to-water bonds get stronger from the last formed layers towards the chamber walls, the desorption rate Q_{des}, given by [233],

$$Q_{\mathrm{des}} = \frac{q_{\mathrm{des}} A t_0}{t}, \tag{C.3.1}$$

decreases over time t. Here, A denotes the vacuum-side surface of the chamber, q_{des} is a material constant describing the desorption rate per unit area ($q_{\mathrm{des}} = 2.7 \cdot 10^{-4}\,\mathrm{Pa\,m^3\,s^{-1}\,m^{-2}}$ for stainless steel), and $t_0 \sim 1$ h is the time constant. As the pressure p is given by the ratio of desorption rate and pump speed S, one finds for the total pump time,

$$t = \frac{q_{\mathrm{des}} A t_0}{pS}. \tag{C.3.2}$$

At a pumping speed $S = 35\,\mathrm{l/s}$, a valid value for the Agilent StarCell 40 ion pump used in the experiments, and assuming a surface area $A \sim 2\,\mathrm{m}^2$, the pump-down time towards a pressure

$p = 10^{-8}$ mbar $= 10^{-6}$ Pa would be $t \approx 643$ d. In fact, when considering the expression for the mean dwell time of adsorbed particles [234],

$$\tau = \tau_0 \exp\left(\frac{E_{\text{des}}}{RT}\right), \tag{C.3.3}$$

where $\tau_0 = \nu_0^{-1} \approx 10^{-13}$ s denotes the time constant as inverse of the vibration rate $\nu_0 \approx 10^{13}$ s^{-1} of the adsorbed molecules, the desorption energy E_{des} that needs to be exceeded by the kinetic energy of the particles in order for them to desorb, the temperature T and the gas constant $R = 8.314$ J mol^{-1} K^{-1}. The molar desorption energy of H_2O on aluminum or stainless steel is approximately $E_{\text{des}} \approx 90$ kJ mol^{-1} [234] which results in an average dwell time of $\tau = 864$ s at room temperature ($T = 295$ K). Elevating the temperature of the chamber to 200°C, this time reduces to $9 \cdot 10^{-4}$ s, an improvement by six orders of magnitude. The desorption rate follows a similar behavior known from radioactive decay, and the time t required to reduce the number of adsorbed molecules to a fraction f can be calculated as,

$$t = \tau \cdot \ln\left(\frac{1}{f}\right). \tag{C.3.4}$$

The time to achieve $f = 10^{-6}$ at room temperature is $t \approx 10^5$ s, while at 200°C the same calculation yields $t \approx 10$ ms.

This demonstrates the strong dependence of the desorption rate on temperature, and shows the importance of a bake out of a vacuum system when targeting a pressure below 10^{-7} mbar. A common strategy is to heat the vacuum chamber to 200°C for a period of 48 h during the pump-down, such that almost all water molecules are desorbed from the inside surfaces into the vacuum and pumped out of the system.

In fig. C.1, it is shown how the heat ribbons, that are regulated by a PID controller, are wrapped around the chamber. They can heat up the entire system up to 180°C, the temperature limit for the most sensitive components in our system: the attocube nanopositioners. For an efficient bake-out, the entire system needs to be thermally isolated from the environment by wrapping several layers of fiberglass and finally a layer of aluminum foil around the chamber and its connected components. This also ensures a uniform heating to avoid thermal expansion gradients across the system.

D Setup and operation of a balanced homodyne interferometer

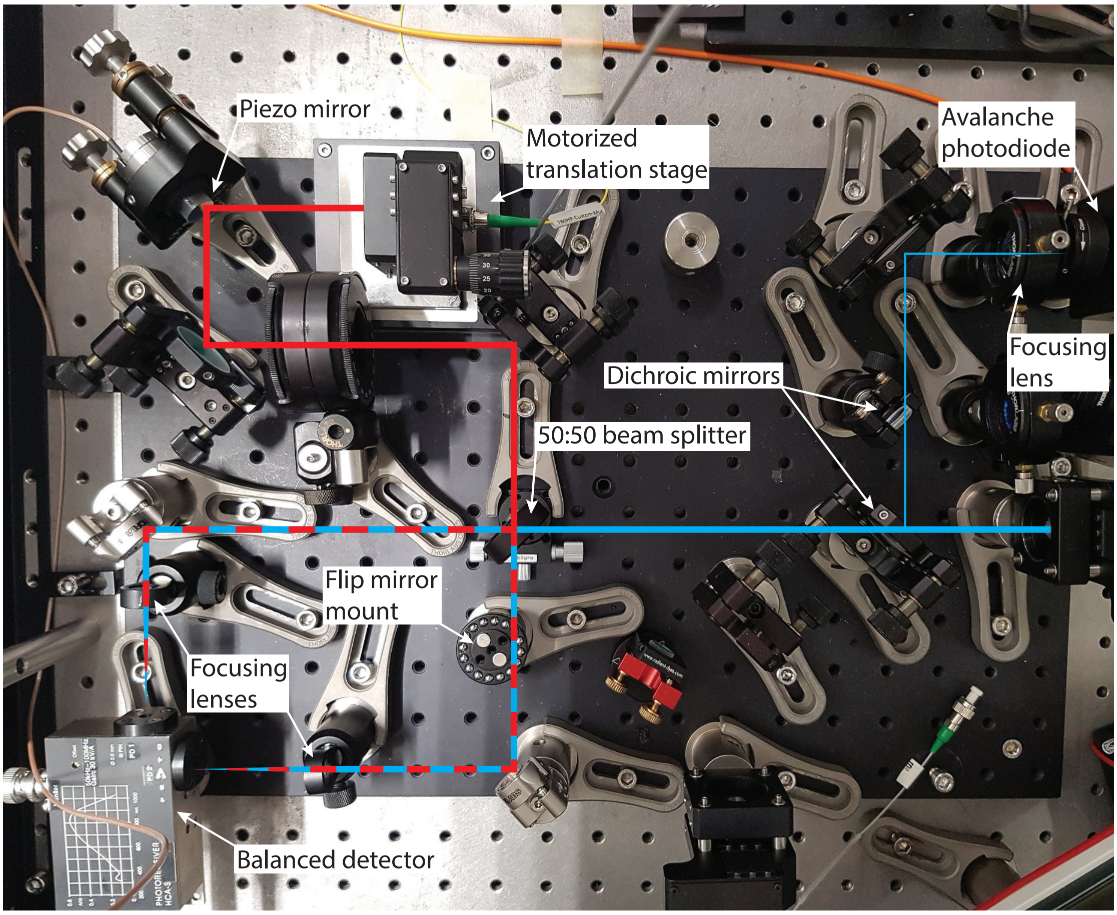
Piezo mirror
Motorized translation stage
Avalanche photodiode
Focusing lens
Dichroic mirrors
50:50 beam splitter
Flip mirror mount
Focusing lenses
Balanced detector

Figure D.1 – **Balanced homodyne detection layout:** Signal beam from the optomechanical device (blue) and local oscillator (red) are combined at a 50:50 beam splitter, such that both are spatially overlapped at the two output ports. Both output beams are then focused onto the two photodiodes of a balanced detector. A piezo mirror and a motorized translation stage in the local oscillator path provide fast and slow feedback channel for the phase lock, respectively. Before entering the interferometer, part of the signal beam is directed to an avalanche photodiode for locking the laser to the cavity resonance using the Pound-Drever-Hall method. For more details, refer to the text.

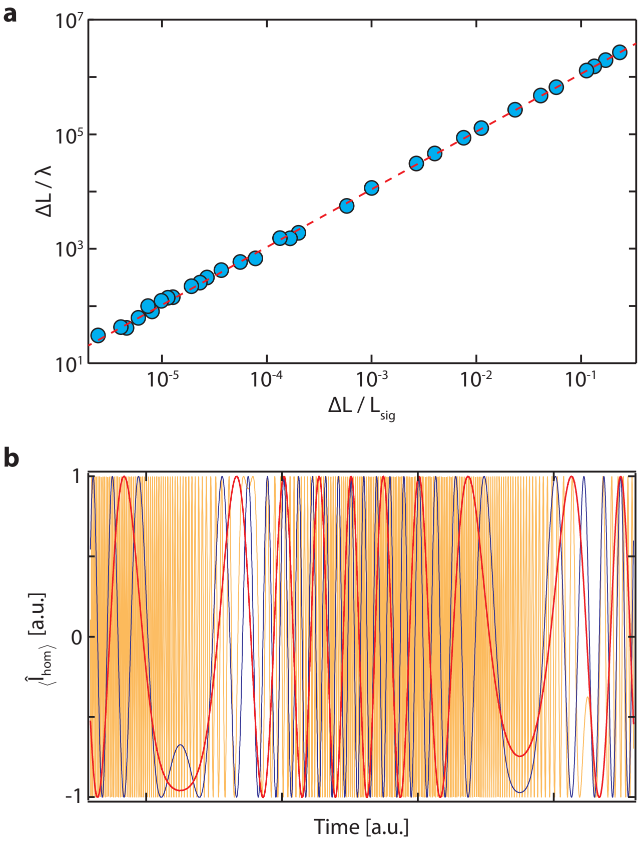

Figure D.2 – **Length balancing of a homodyne interferometer:** (a) Measurement of ω_{fringe} versus length imbalance and converted to relative imbalance $\Delta L/\lambda$. The red dashed line is a linear fit to only the ten points with largest imbalance which demonstrates the robustness of this method. (b) The frequency ω_{fringe} of the interference fringes reduces with decreasing $|\Delta L|$. Shown are three points with large (orange trace), intermediate (blue) and small imbalance (red).

The foundations of a balanced homodyne interferometer are detailed in section 2.4.4. This chapter details the experimental realization of the homodyne setup used in the experiment, as shown in fig. D.1. The signal beam (blue trace) is broken out of the fiber coming from the optomechanical system. It is directed through a dichroic mirror that is transmissive for 780 nm and reflective at 830 nm. Due to its imperfectness, it also reflects a small fraction of the 780 nm light, which is used for Pound-Drever-Hall locking [146] to the resonance of the optomechanical device. The main fraction of the signal is directed to a balanced beam splitter where it is spatially overlapped with a local oscillator beam from the same laser source (hence the term homodyne), which is polarization matched using the quarter- and half-waveplates in its path. The overlap is achieved by using a flip mirror to fiber couple the two beams behind one of the beam splitter's outputs into the same single-mode optical fiber. After this, the flip mirror is removed and both beam-splitter output beams are focused onto the two photodiodes of a balanced detector, that then outputs the subtraction of the two inputs as an electric signal (see section 2.4.4). To avoid back reflections from the photodiodes back into the signal fiber, the balanced detector is slightly rotated.

The fundamental aim of a balanced homodyne detection is the capability to perform a measurement of an arbitrary but constant quadrature of the signal. The challenging aspect under experimental conditions lies hereby in the preservation of a constant relative phase, θ_{hom}, between the signal and local oscillator light fields. For given path lengths $L_{\text{sig(LO)}}$ of the signal (LO) arm, the homodyne phase is found to be,

$$\theta_{\text{hom}} \approx \frac{2\pi}{\lambda_l}\left(\frac{L_{\text{sig}}}{n_{\text{sig}}} - \frac{L_{\text{LO}}}{n_{\text{LO}}}\right) \approx \frac{2\pi}{\lambda_l n_{\text{eff}}}\left(L_{\text{sig}} - L_{\text{LO}}\right), \tag{D.0.1}$$

where λ_l denotes the optical wavelength and $n_{\text{sig(LO)}}$ the refractive index of the signal (LO) path. In the approximation, for both interferometer arms, an effective refractive index $n_{\text{eff}} \approx 1.5$ is assumed, as here the light propagates predominantly inside optical fiber for both. To achieve a desired phase $0 \le \theta_{\text{hom}} \le \pi/2$, the difference in path length, ΔL, relative to the wavelength is required to be of order unity,

$$\frac{\Delta L}{\lambda_l} = \frac{L_{\text{sig}} - L_{\text{LO}}}{\lambda_l} \to 1. \tag{D.0.2}$$

To experimentally realize a length imbalance in the order of the optical wavelength, a two-step process is applied. In the first step, after alignment of the optics, the wavelength of the laser is modulated with $\lambda(t) = \lambda_l + \delta\lambda(t)$. This results in a mean of the homodyne photocurrent (using eqs. (2.4.55) and (D.0.1)),

$$\left\langle \hat{I}_{\text{hom}}(t) \right\rangle \propto \sin\left(\frac{2\pi\Delta L}{n_{\text{eff}}\lambda}\right) \approx \sin\left(\frac{2\pi\Delta L}{n_{\text{eff}}\lambda_0} + \underbrace{\frac{2\pi\Delta L}{n_{\text{eff}}\lambda_0}\frac{1}{\lambda_0}\frac{\mathrm{d}\lambda}{\mathrm{d}t}}_{:=\omega_{\text{fringe}}} t\right). \tag{D.0.3}$$

The frequency ω_{fringe} of the interference fringes therefore depends on the imbalance and can be monitored using an oscilloscope. By repeatedly shortening and re-splicing the local oscillator optical fiber (which is prepared intentionally at a length exceeding the signal path), the frequency ω_{fringe} is reduced for decreasing length imbalance between signal and local oscillator. Practically, with this method an imbalance of ~ 1 cm can be achieved, ultimately limited by the precision with which the optical fiber can be cut and spliced. The reduction in $\omega_{\text{fringe}} \propto \Delta L/\lambda$ is shown in fig. D.2a for decreasing the imbalance following this technique. Figure D.2b shows the measured fringes during the process for large (light blue trace, large ω_{fringe}), intermediate (blue) and small imbalance (dark blue). The remaining path difference is balanced with a micrometer translation stage supporting the input fiber coupler of the signal beam. In the end, around $\Delta L \approx 10\lambda$, the interference fringes start to become sensitive to minimal external disturbances implying that at this point, the homodyne imbalance has to be actively stabilized.

To generate an error signal from $\left\langle \hat{I}_{\text{hom}}(t) \right\rangle$, the length imbalance is modulated by dithering a piezo-mounted mirror in the local oscillator path (see fig. D.1). An example of an error signal is shown as the red trace in fig. D.3a. Using a PID controller, a fast branch (10-300 Hz bandpass) actuates the mirror piezo to suppress the corresponding high-frequency fluctuations in path length, while a slow branch (1 Hz low-pass) at the same time feeds back on the motorized stage

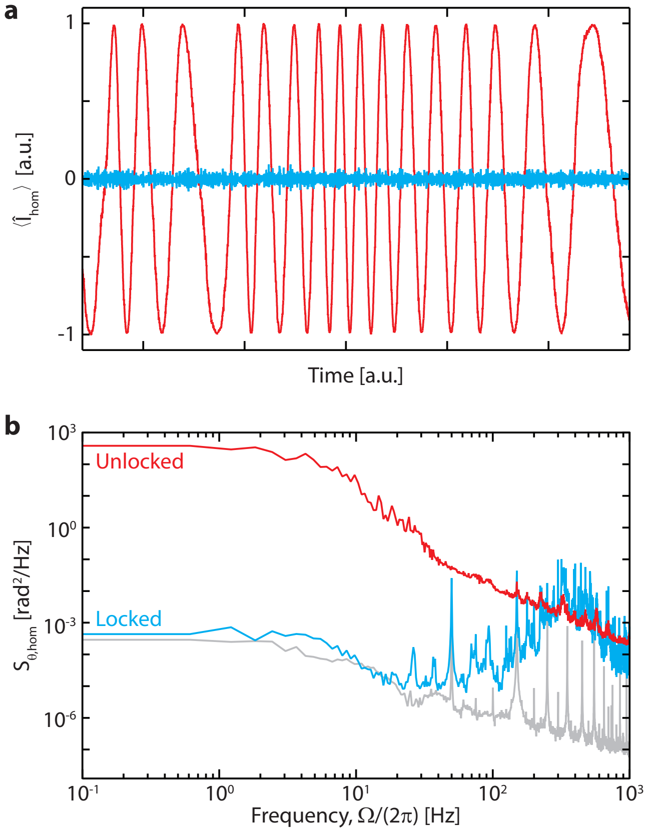

Figure D.3 – **Homodyne lock and residual phase noise:** (a) Homodyne error signal $\langle \hat{I}_{\text{hom}}(t) \rangle$ when scanning the piezo mirror (red trace) and in the locked case with activated PID controller (blue trace). (b) Spectral analysis of the homodyne signal showing residual noise in the phase θ_{hom} in the unlocked (red) and locked (green) case. The gray trace is the electronic noise limiting the ultimate stability.

underneath the output coupler of the LO (also marked in fig. D.1) to account for slow drifts, e.g. due to temperature fluctuations or seismic activity. The homodyne interferometer can hence be locked to an arbitrary quadrature by choosing the corresponding position on the fringe, and activating the PID controller. The locked homodyne signal is shown as the blue trace in fig. D.3a. The zero-crossing of the fringes – also acting as the lock point in this example – corresponds to the phase quadrature and the minimum and maximum to the amplitude quadrature. For a measurement close to the amplitude quadrature, the error signal is demodulated at the EOM frequency which is also used to PDH lock the laser to the cavity. This facilitates the locking as the derivation of the error signal then oscillates around the zero-crossing of the fringe error signal, which in this case corresponds to the amplitude quadrature. Spectral analysis of the error signal of the locked homodyne interferometer provides an estimation of the noise in the homodyne phase due to imperfect locking. Figure D.3b shows the residual noise in the homodyne phase θ_{hom} for both when the homodyne is locked and free-running. For low frequencies, an upper-bound of $\text{Var}\left[\theta^2_{\text{hom}}\right]^{1/2} < 100$ mrad for the locked homodyne can be extracted from the data. For frequencies in the kHz regime, the presence of piezo resonances limits the gain that can be applied.

E Sample design and characterization

The fabrication process of the integrated near-field devices is detailed in section 3.2. Figure E.1 shows a photograph of a finalized chip, which contains 40 integrated near-field samples. This large number allows for the sweep of sample parameters, such as beam geometry and width, its position, or different disk sizes. This way, the behavior of the sample specifications for varying design parameters, which are presented in section 3.3.5, can be easily investigated. A sweep of e.g. the beam position can also be used to account for uncertainties during the fabrication process and hence guarantee the fabrication of at least one sample on the chip with the desired optimal design parameters. Top and bottom of each chip are used for placing a unique labeling, indicating the wafer (top label) and chip (bottom). Figure E.2a shows a sketch

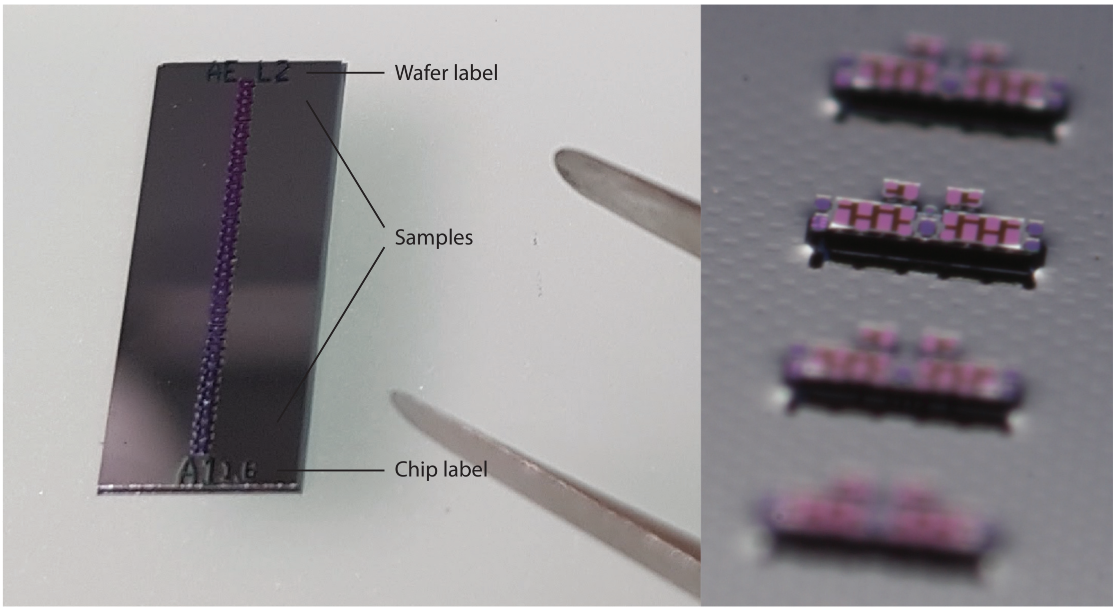

Figure E.1 – **Sample chip:** Left: photograph of a chip after finalized micro fabrication. The chip is 16 mm x 5 mm in size and holds 40 optomechanical near-field devices, consisting of an Si_3N_4 nanobeam placed in the evanescent near-field of a SiO_2 microdisk optical resonator. Each chip carries a unique label identifying the wafer (top label) as well as the chip (bottom). Right: Close-up photograph of the individual devices.

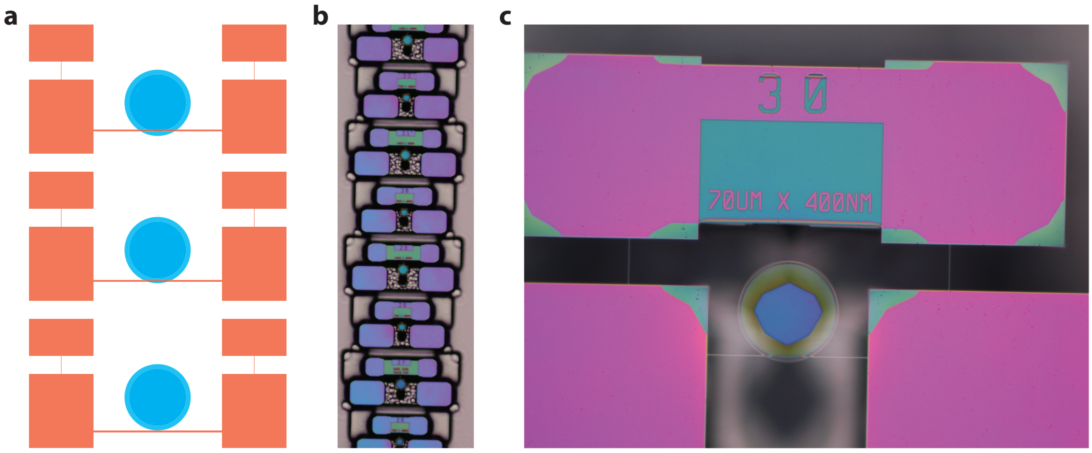

Figure E.2 – **Sample chip:** (a) Design sketch illustrating a parameter sweep of the lateral beam position in this case. (b) Optical microscope image of the finalized samples on a ship. (c) Close-up of a single optomechanical device. The label at the top, but also the actual device components (nanobeam, microdisk, fiber supports) are discernible.

illustrating a sweep of the lateral beam position in discrete steps across adjacent samples. Figure E.2b shows a microscope image of adjacent samples. The close proximity between the individual devices ensures a large variety across the entire chip. Finally, fig. E.2c shows a close-up of a single optomechanical device. At this magnification, the sample number as well as a description of the beam geometry are easily readable, facilitating the identification during a measurement. Concerning the actual sample, the nanobeam above the microdisk as well as the support bridges for the tapered optical fiber are discernible.

After fabrication, the samples are measured one-by-one for characterization of their optical and mechanical properties. An example of a measurement result is shown in fig. E.3a and b. From these values, the cooperativity C_0 can be calculated to gain an estimate of the device's performance in the desired experiment. Typically, the highest cooperativity is achieved for the beam position with the highest coupling g_0, in this case for sample -1 with $C_0 = 0.64$.

Besides characterization, the measurement results are also useful to reveal possible design flaws that can be optimized for the following fabricated runs. Encountered examples for this include excessive optical linewidths due to limited optical confinement because of too thin microdisks, and misplaced nanobeams resulting in no available sample with a peak in C_0 across the chip.

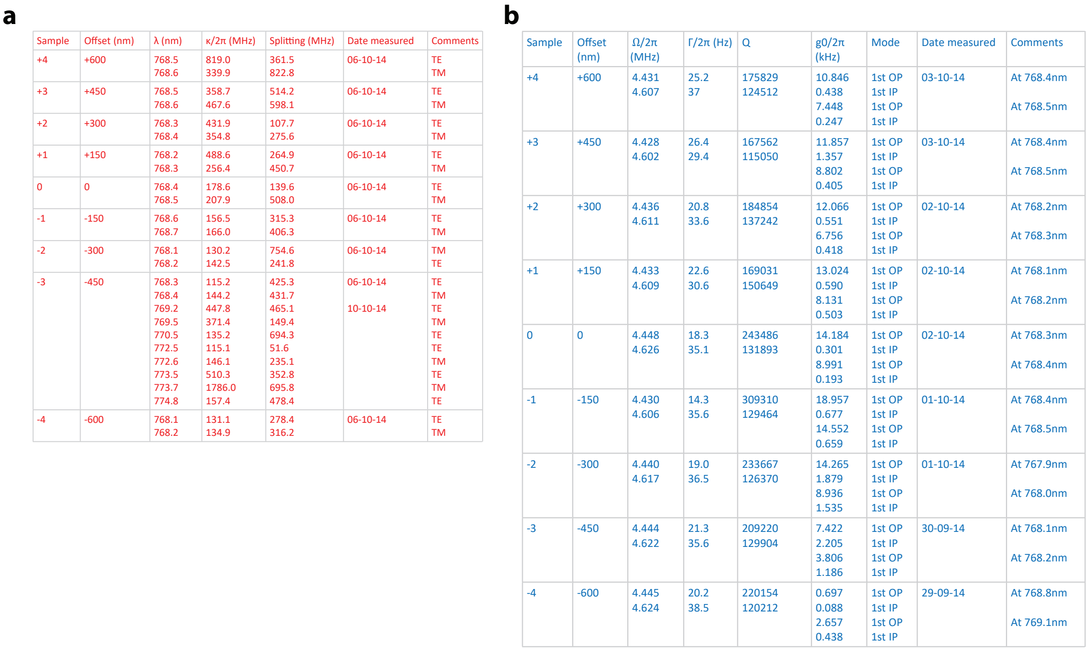

Sample	Offset (nm)	λ (nm)	κ/2π (MHz)	Splitting (MHz)	Date measured	Comments
+4	+600	768.5 768.6	819.0 339.9	361.5 822.8	06-10-14	TE TM
+3	+450	768.5 768.6	358.7 467.6	514.2 598.1	06-10-14	TE TM
+2	+300	768.3 768.4	431.9 354.8	107.7 275.6	06-10-14	TE TM
+1	+150	768.2 768.3	488.6 256.4	264.9 450.7	06-10-14	TE TM
0	0	768.4 768.5	178.6 207.9	139.6 508.0	06-10-14	TE TM
-1	-150	768.6 768.7	156.5 166.0	315.3 406.3	06-10-14	TE TM
-2	-300	768.1 768.2	130.2 142.5	754.6 241.8	06-10-14	TM TE
-3	-450	768.3 768.4 769.2 769.5 770.5 772.5 772.6 773.5 773.7 774.8	115.2 144.2 447.8 371.4 135.2 115.1 146.1 510.3 1786.0 157.4	425.3 431.7 465.1 149.4 694.3 51.6 235.1 352.8 695.8 478.4	06-10-14 10-10-14	TE TM TE TM TE TE TM TE TM TE
-4	-600	768.1 768.2	131.1 134.9	278.4 316.2	06-10-14	TE TM

Sample	Offset (nm)	Ω/2π (MHz)	Γ/2π (Hz)	Q	g0/2π (kHz)	Mode	Date measured	Comments
+4	+600	4.431 4.607	25.2 37	175829 124512	10.846 0.438 7.448 0.247	1st OP 1st IP 1st OP 1st IP	03-10-14	At 768.4nm At 768.5nm
+3	+450	4.428 4.602	26.4 29.4	167562 115050	11.857 1.357 8.802 0.405	1st OP 1st IP 1st OP 1st IP	03-10-14	At 768.4nm At 768.5nm
+2	+300	4.436 4.611	20.8 33.6	184854 137242	12.066 0.551 6.756 0.418	1st OP 1st IP 1st OP 1st IP	02-10-14	At 768.2nm At 768.3nm
+1	+150	4.433 4.609	22.6 30.6	169031 150649	13.024 0.590 8.131 0.503	1st OP 1st IP 1st OP 1st IP	02-10-14	At 768.1nm At 768.2nm
0	0	4.448 4.626	18.3 35.1	243486 131893	14.184 0.301 8.991 0.193	1st OP 1st IP 1st OP 1st IP	02-10-14	At 768.3nm At 768.4nm
-1	-150	4.430 4.606	14.3 35.6	309310 129464	18.957 0.677 14.552 0.659	1st OP 1st IP 1st OP 1st IP	01-10-14	At 768.4nm At 768.5nm
-2	-300	4.440 4.617	19.0 36.5	233667 126370	14.265 1.879 8.936 1.535	1st OP 1st IP 1st OP 1st IP	01-10-14	At 767.9nm At 768.0nm
-3	-450	4.444 4.622	21.3 35.6	209220 129904	7.422 2.205 3.806 1.186	1st OP 1st IP 1st OP 1st IP	30-09-14	At 768.1nm At 768.2nm
-4	-600	4.445 4.624	20.2 38.5	220154 120212	0.697 0.088 2.657 0.438	1st OP 1st IP 1st OP 1st IP	29-09-14	At 768.8nm At 769.1nm

Figure E.3 – **Characterization data:** Characterization data for chip M2 A Up Top. (a) shows the optical properties, in particular the wavelength λ of the measured resonance, its linewidth κ, mode splitting as well as the polarization direction. (b) shows the measured mechanical resonance frequency Ω_m, linewidth Γ_m and single-photon coupling strength g_0 for the respective optical modes from (a).

F Degradation of the mechanical quality factor

As mentioned in section 2.1.2 for the optical quality factors of silica microresonators, the hygroscopic nature of Si_3N_4 likewise causes the nanobeams to adsorb water molecules on their surface when exposed to moist air. This process can occur when samples are kept outside of flow boxes that serve the purpose of surround the samples in a dry nitrogen atmosphere, but also in vacuum chambers that either have leaks or have been left at atmosphere for long periods of time [235]. We investigated the degradation of the mechanical quality factor over time by leaving samples exposed to normal air while periodically measuring Q_m inside the vacuum chamber. The result of these measurements is shown in fig. F.1a. First immediately measured after the finalized fabrication, the mechanical quality factor shows rapid exponential degradation by almost an order of magnitude within several days. An indicator that the degradation is indeed caused by adsorption is the also exponentially decreasing resonance frequency Ω_m, a clear proof for an increased effective mass due to deposited particles.

However, it has been found that this process is reversible. The initial mechanical properties of the samples can be fully restored by heating them on a hot plate to a temperature around 400°C for the duration of an hour [235]. Our applied solution is an *in-situ* heating without the need to vent the chamber and move the sample. This is realized by attaching a ceramic microheater (and thermocouple) to the thermally isolated chip mount. We observe that this in-situ baking of the chip for around half an hour could fully recover the mechanical quality factors, as well as the resonance frequency to its original value, as shown in fig. F.1b.

Figure F.1c shows the measured noise spectra of sample 2 before (red) and after the bake (blue), from which a clear improvement in mechanical quality factor is apparent. For easier visualization, the shift in resonance frequency after baking is corrected for in this figure. Following the assembly and cleaning procedures described in appendix C, the samples now no longer experience any degradation due to redistribution of water molecules inside the chamber when left in vacuum. In conclusion, the in-situ heating enables the restoration of the mechanical quality factors, allowing for experiments on long time scales without any degradation. In addition, the revised vacuum setups eliminate the previously observed problem of degrading mechanics due to particle redistribution inside the chamber when under vacuum.

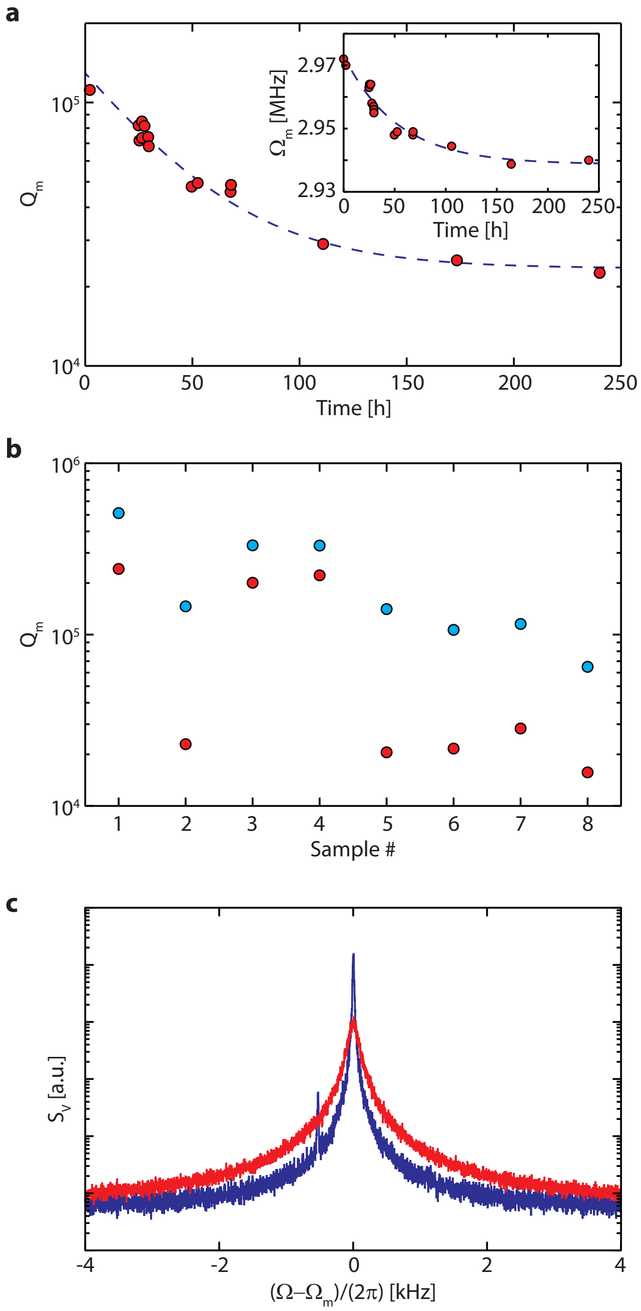

Figure F.1 – **Degradation of mechanical quality factor:** (a) Measurement of Q_m versus time of a sample when left exposed to atmosphere (red data points). The blue dashed trace is an exponential fit to the data. The inset shows a likewise exponential decrease in the mechanical resonance frequency Ω_m, indicating an increased mass through particle deposition. (b) Measurements of Q_m for different samples, that were left exposed to atmosphere, before (red data) and immediately after baking at $400^\circ C$ for half an hour (blue data). (c) Measured noise spectra of sample 2 before (red) and after (blue) heating the sample. For better visualization, the change in resonance frequency has been corrected for. These measurements were taken with sample M8/CD/B/+1.

G Two-level systems in cavity optomechanical systems

Optomechanical systems provide an excellent platform for the investigation of mechanical dissipation mechanisms in materials such as silicon nitride and silicon dioxide. Due to their amorphous structure, these glass materials inherit defects that can be described as intrinsic two-level systems (TLS) with tunnel splitting $\hbar\Delta_0$ and asymmetry energy $\hbar\Delta$, such that the eigenstates are split by $\Delta_\mathrm{T} = \sqrt{\Delta^2 + \Delta_0^2}$ (fig. G.1b) [236]. These TLS embody the dominant decoherence channel at low operation temperatures that can be studied in a regime in which the interaction between phonons and TLS becomes resonant, i.e. the dissipation rate is dominated by resonant phonon absorption. The resonator-phonon interaction can be approximated by the Jaynes–Cummings Hamiltonian [237],

$$H_\mathrm{JC} = \left(\frac{\hbar\Delta_\mathrm{T}}{2}\right)\sigma_z + \hbar\Omega_\mathrm{m} b^\dagger b + \hbar\lambda\left(\sigma_+ b + \sigma_- b^\dagger\right). \tag{G.0.1}$$

Here, σ_i denote the Pauli matrices and λ the TLS-phonon coupling rate,

$$\lambda \approx \frac{D_\mathrm{T}}{\hbar}\frac{\Delta_0}{\Delta_\mathrm{T}}\sqrt{\frac{\hbar\Omega_\mathrm{m}}{2EV_\mathrm{m}}}, \tag{G.0.2}$$

with the deformation potential D_T, Young's modulus E of the material, the mechanical mode volume V_m, and the assumption that $\lambda \ll \Delta_\mathrm{T} \approx \Omega_\mathrm{m}$ [237]. From the above expression follows that a high mechanical resonance frequency together with a small modal volume is desirable. Silica ($\mathrm{SiO_2}$) microsphere resonators on needle support pillars, as shown in fig. G.1c, turn out to be very suitable candidates for the observation of the direct phonon absorption, as for them a regime can be achieved in which this process dominates the other loss channels, such as losses introduced by the clamping to a support. The theoretical TLS model and parameters for the amorphous SiO2 have been subjects of studies for a long time [238, 239]. At temperatures below 10 K and for mechanical frequencies in the MHz regime, the level transition process is dominated by tunneling of the phonon through the barrier. This can be approximated by two asymptotic behaviors. At typically a few Kelvin, this process is independent of the temperature T and results in a plateau value $Q^{-1}_\mathrm{tun,plateau}$. For lower temperatures, the mechanical absorption

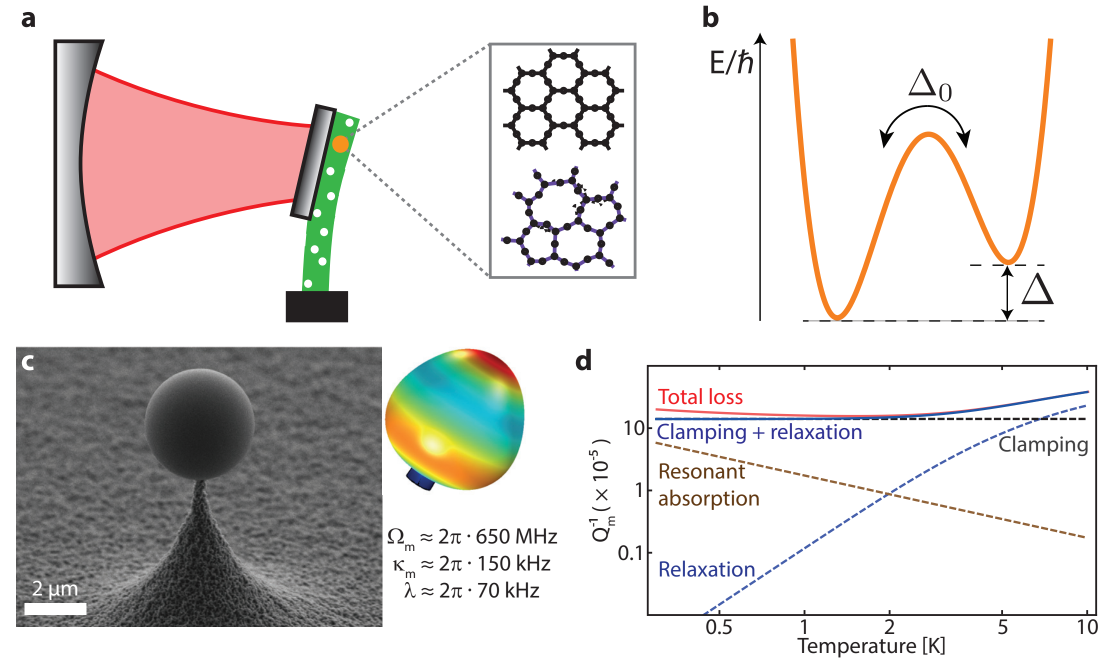

Figure G.1 – **Two-level systems in optomechanical systems:** (a) Glasses such as SiO_2 and Si_3N_4 are amorphous materials where atoms at certain lattice positions can have more than one equilibrium state. (b) At low temperature, the defect can be effectively described by two states in a double-well potential, where Δ_0 is the tunnel splitting frequency and Δ the asymmetry frequency. (c) Scanning electron micrograph of an SiO_2 microsphere (Sample 32/10S/G0B/18) with ~ 6.5 μm diameter on a silicon needle pillar (~ 500 nm diameter). Also shown is an FEM simulation of the displacement profile for the fundamental radial breathing mode of such a sphere with a mechanical resonance frequency of in this case $\Omega_m \approx 2\pi \cdot 650$ MHz. (d) Estimation of the loss channels of a silica microsphere resonator. For the sample parameters used, a dominating contribution due to resonant phonon absorption is expected below the temperature of 1 K.

decreases with T, yielding $Q^{-1}_{\text{tun,slope}}(T)$. When working at even lower temperatures (and/or higher mechanical frequencies), the so-called resonant absorption regime (given by $Q^{-1}_{\text{res}}(T)$) can be reached, in which the phonon energy corresponds to the TLS energy such that coherent processes take place. The expressions for these three contributions are given by,

$$Q^{-1}_{\text{tun,slope}}(T) = \frac{9\zeta(3)}{\pi}\frac{\Omega_m \bar{P} B^4}{\rho^2 c_s^7 \hbar^4}(k_B T)^3, \tag{G.0.3}$$

$$Q^{-1}_{\text{tun,plateau}} = \frac{\pi \bar{P} B^2}{2\rho c_s^2}, \tag{G.0.4}$$

$$Q^{-1}_{\text{res}}(T) = \frac{\pi \bar{P} B^2}{\rho c_s^2}\tanh\left(\frac{\hbar\Omega_m}{2k_B T}\right). \tag{G.0.5}$$

Here, $\bar{P}$ denotes the TLS distribution parameter, B the parameter linking a deformation to a change in energy splitting, ρ the mass density, c_s the speed of sound and $\zeta(s)$ is the Riemann zeta function of s. Evaluating these expressions for specifically fabricated microsphere samples, as shown in fig. G.1c, combined with their derived clamping loss rate suggests a measurable increase of total dissipation at temperatures below 1 K, according to the resonant

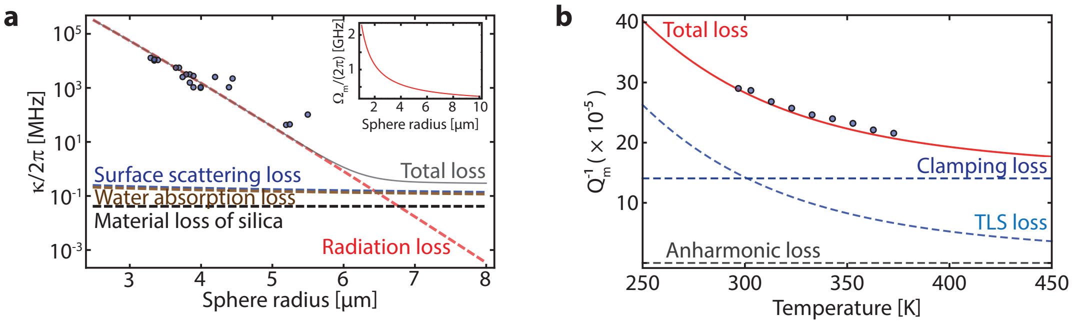

Figure G.2 – **Optical and mechanical properties of microsphere resonators:** (a) Measurement of the optical linewidth versus sphere diameter. Spheres with a radius less than ~ 6 μm are radiation loss limited, as the good agreement to the model suggests. The inset shows a model for the mechanical resonance frequency of the fundamental breathing mode, following a r_s^{-1} dependence. (b) Measurement of the mechanical quality factor for an elevated temperature. The data shows good agreement with the model, combining the losses due to relaxation and estimated clamping losses from an FEM simulation.

absorption process (cf. fig. G.1d). This environment can be achieved inside a Helium-3 cryostat that condenses to temperatures as low as 500 mK. As the mechanical resonance frequency scales inversely with the sphere radius, i.e. $\Omega_\mathrm{m} \propto r_\mathrm{s}^{-1}$ (see inset of fig. G.2a), one might suggest to work with sphere radii as small as possible. However, this comes at the expense of rapidly increasing radiation losses for the optical modes (cf. section 2.1.2), rendering a sensitive measurement of the mechanical resonance difficult. A measurement of κ vs. sphere size is shown in fig. G.2a, based on which a sphere size of $r_\mathrm{s} \approx 3.5$ μm has been chosen as a trade-off between decent optical quality factor and expected contribution of the resonant phonon absorption. A measurement of the mechanical quality factor versus temperature between room temperature and 100°C (fig. G.2b) shows good agreement with the theoretical TLS model (dominated by relaxation processes in this regime). A measurement at cryogenic temperatures has not yet been conducted but a recent similar experiment focusing on acoustic fiber modes could successfully observe the resonant phonon absorption [240].

In addition to strain, it has been found that TLS are also susceptible to classical electromagnetic fields [236, 241]. In particular, the two-level systems interact with a coherent microwave drive at Rabi frequency Ω_μ according to the Hamiltonian,

$$H_{\mathrm{TLS},\mu} = \hbar\Omega_\mu e^{i\omega_\mu t}\sigma_- + \hbar\omega_\mu^* e^{-i\Omega_\mu t}\sigma_+. \tag{G.0.6}$$

Applying such a microwave drive to the optomechanical system, the TLS can be driven into their excited state and thus the resonant phonon absorption be suppressed. This would lead to higher mechanical quality factors by removing the loss channel due to the TLS absorption. This would be especially interesting for experiments with optomechanical systems close to their quantum-mechanical ground state that consist of amorphous materials and operate at high mechanical resonance frequencies. One example is the silica microtoroid in a Helium-3 cryostat that is placed in a $T \sim 500$ mK environment, a regime close to the dominating resonant absorption [187]. Further, the ability to drive the defect with a resonant microwave field enables the realization of a phonon blockade, and eventually the preparation of non-classical states of the mechanical oscillator [237].

Bibliography

[1] J. Kepler, *De Cometis Libelli Tres* (1619).

[2] H. Hertz, Annalen der Physik **267**, 983 (1887).

[3] A. Einstein, Annalen der Physik **322**, 132 (1905).

[4] P. A. M. Dirac, *The Principles of Quantum Mechanics*, 4th ed. (Clarendon Press, 1982).

[5] E. F. Nichols and G. F. Hull, Physical Review (Series I) **17**, 26 (1903).

[6] W. Crookes, Philosophical Transactions of the Royal Society of London **164**, 501 (1874).

[7] H. Cavendish, Philosophical Transactions of the Royal Society of London **88**, 469 (1798).

[8] P. Lebedew, Annalen der Physik **311**, 433 (1901).

[9] H. P. Robertson and H. N. Russell, Monthly Notices of the Royal Astronomical Society **97**, 423 (1937).

[10] P. Musen, Journal of Geophysical Research **65**, 1391 (1960).

[11] J. A. Burns, P. L. Lamy, and S. Soter, Icarus **40**, 1 (1979).

[12] C. H. Townes, in *A Century of Nature: Twenty-One Discoveries That Changed Science and the World* (The University of Chicago Press, 2003).

[13] A. Einstein, Annalen der Physik **322**, 549 (1905).

[14] A. Ashkin, Physical Review Letters **24**, 156 (1970).

[15] T. W. Hänsch and A. L. Schawlow, Optics Communications **13**, 68 (1975).

[16] D. J. Wineland, R. E. Drullinger, and F. L. Walls, Physical Review Letters **40**, 1639 (1978).

[17] A. Ashkin, Science **210**, 1081 (1980).

[18] V. Braginsky and A. Manukin, Sov. Phys. JETP **25**, 653 (1967).

[19] V. B. Braginsky, A. B. Manukin, and M. Y. Tikhonov, Sov. Phys. JETP **31**, 829 (1970).

[20] V. B. Braginsky, A. B. Manukin, and D. H. E. Douglass, *Measurement of Weak Forces in Physics Experiments*, 1st ed. (Univ. of Chicago Press, 1977).

[21] V. B. Braginsky and F. Y. Khalili, *Quantum measurement* (Cambridge University Press, 1992).

[22] C. M. Caves, Phys. Rev. Lett. **45**, 75 (1980).

[23] M. T. Jaekel and S. Reynaud, Journal de Physique I **1**, 1395 (1991).

[24] A. F. Pace, M. J. Collett, and D. F. Walls, Physical Review A **47**, 3173 (1993).

[25] M. Aspelmeyer, T. J. Kippenberg, and F. Marquardt, Rev. Mod. Phys. **86**, 1391 (2014).

[26] LIGO Scientific Collaboration and Virgo Collaboration, Physical Review Letters **116**, 061102 (2016).

[27] A. Glinsky, *Theremin: Ether Music and Espionage* (University of Illinois Press, 2000).

[28] T. J. Kippenberg and K. J. Vahala, Science **321**, 1172 (2008).

[29] B. D. Cuthbertson, M. E. Tobar, E. N. Ivanov, and D. G. Blair, Review of Scientific Instruments **67**, 2435 (1996).

[30] F. Massel, T. T. Heikkilä, J.-M. Pirkkalainen, S. U. Cho, H. Saloniemi, P. J. Hakonen, and M. A. Sillanpää, Nature **480**, 351 (2011).

[31] C. A. Regal, J. D. Teufel, and K. W. Lehnert, Nat. Phys. **4**, 555 (2008).

[32] T. Rocheleau, T. Ndukum, C. Macklin, J. B. Hertzberg, A. A. Clerk, and K. C. Schwab, Nature **463**, 72 (2009).

[33] J. D. Teufel, T. Donner, D. Li, J. W. Harlow, M. S. Allman, K. Cicak, A. J. Sirois, J. D. Whittaker, K. W. Lehnert, and R. W. Simmonds, Nature **475**, 359 (2011).

[34] J. Chan, T. P. M. Alegre, A. H. Safavi-Naeini, J. T. Hill, A. Krause, S. Groeblacher, M. Aspelmeyer, and O. Painter, Nature **478**, 89 (2011).

[35] E. Gavartin, R. Braive, I. Sagnes, O. Arcizet, A. Beveratos, T. J. Kippenberg, and I. Robert-Philip, Physical Review Letters **106** (2011), 10.1103/physrevlett.106.203902.

[36] J. D. Thompson, B. M. Zwickl, A. M. Jayich, F. Marquardt, S. M. Girvin, and J. G. E. Harris, Nature **452**, 72 (2008).

[37] D. Wilson, C. Regal, S. Papp, and H. Kimble, Phys. Rev. Lett. **103**, 207204 (2009).

[38] X. Jiang, Q. Lin, J. Rosenberg, K. Vahala, and O. Painter, Optics Express **17**, 20911 (2009).

[39] Q. Lin, J. Rosenberg, X. Jiang, K. J. Vahala, and O. Painter, Physical Review Letters **103** (2009), 10.1103/physrevlett.103.103601.

[40] G. S. Wiederhecker, L. Chen, A. Gondarenko, and M. Lipson, Nature **462**, 633 (2009).

[41] M. Eichenfield, R. Camacho, J. Chan, K. J. Vahala, and O. Painter, Nature **459**, 550 (2009).

[42] L. Ding, C. Baker, P. Senellart, A. Lemaitre, S. Ducci, G. Leo, and I. Favero, Applied Physics Letters **98**, 113108 (2011).

[43] Y.-S. Park and H. Wang, Nature Physics **5**, 489 (2009).

[44] A. Schliesser, G. Anetsberger, R. RiviÃ¨re, O. Arcizet, and T. J. Kippenberg, New J. Phys. **10**, 095015 (2008).

[45] E. Verhagen, S. Deléglise, S. Weis, A. Schliesser, and T. J. Kippenberg, Nature **482**, 63 (2012).

[46] A. Schliesser, O. Arcizet, R. Rivière, G. Anetsberger, and T. J. Kippenberg, Nature Physics **5**, 509 (2009).

[47] O. Arcizet, P.-F. Cohadon, T. Briant, M. Pinard, A. Heidmann, J.-M. Mackowski, C. Michel, L. Pinard, O. Français, and L. Rousseau, Physical Review Letters **97** (2006), 10.1103/physrevlett.97.133601.

[48] I. Favero, C. Metzger, S. Camerer, D. König, H. Lorenz, J. P. Kotthaus, and K. Karrai, Applied Physics Letters **90**, 104101 (2007).

[49] S. Gigan, H. R. Böhm, M. Paternostro, F. Blaser, G. Langer, J. B. Hertzberg, K. C. Schwab, D. Bäuerle, M. Aspelmeyer, and A. Zeilinger, Nature **444**, 67 (2006).

[50] S. Gröblacher, J. B. Hertzberg, M. R. Vanner, G. D. Cole, S. Gigan, K. C. Schwab, and M. Aspelmeyer, Nature Physics **5**, 485 (2009).

[51] D. Kleckner and D. Bouwmeester, Nature **444**, 75 (2006).

[52] C. M. Mow-Lowry, A. J. Mullavey, S. Goßler, M. B. Gray, and D. E. McClelland, Physical Review Letters **100** (2008), 10.1103/physrevlett.100.010801.

[53] D. Kleckner, B. Pepper, E. Jeffrey, P. Sonin, S. M. Thon, and D. Bouwmeester, Optics Express **19**, 19708 (2011).

[54] S. Gröblacher, K. Hammerer, M. R. Vanner, and M. Aspelmeyer, Nature **460**, 724 (2009).

[55] M. H. Schleier-Smith, I. D. Leroux, H. Zhang, M. A. V. Camp, and V. Vuletić, Physical Review Letters **107** (2011), 10.1103/physrevlett.107.143005.

[56] K. W. Murch, K. L. Moore, S. Gupta, and D. M. Stamper-Kurn, Nature Physics **4**, 561 (2008).

[57] F. Brennecke, S. Ritter, T. Donner, and T. Esslinger, Science **322**, 235 (2008).

[58] P. Verlot, A. Tavernarakis, T. Briant, P.-F. Cohadon, and A. Heidmann, Phys. Rev. Lett. **102**, 103601 (2009).

[59] A. G. Krause, T. D. Blasius, and O. Painter, arXiv preprint arXiv:1506.01249 (2015).

[60] A. H. Safavi-Naeini, S. Gröblacher, J. T. Hill, J. Chan, M. Aspelmeyer, and O. Painter, Nature **500**, 185 (2013).

[61] T. P. Purdy, P. Yu, R. W. Peterson, N. S. Kampel, and C. A. Regal, Physical Review X **3**, 031012 (2013).

[62] R. Leijssen and E. Verhagen, Scientific Reports **5** (2015), 10.1038/srep15974.

[63] E. E. Wollman, C. Lei, A. Weinstein, J. Suh, A. Kronwald, F. Marquardt, A. Clerk, and K. Schwab, Science **349**, 952 (2015).

[64] T. Palomaki, J. Harlow, J. Teufel, R. Simmonds, and K. Lehnert, Nature **495**, 210 (2013).

[65] M. Wu, A. C. Hryciw, C. Healey, D. P. Lake, H. Jayakumar, M. R. Freeman, J. P. Davis, and P. E. Barclay, Phys. Rev. X **4**, 021052 (2014).

[66] N. Matsumoto, K. Komori, Y. Michimura, G. Hayase, Y. Aso, and K. Tsubono, Phys. Rev. A **92**, 033825 (2015).

[67] T. P. Purdy, K. E. Grutter, K. Srinivasan, and J. M. Taylor, Science **356**, 1265 (2017).

[68] LIGO Scientific Collaboration, Classical and Quantum Gravity **32**, 074001 (2015).

[69] M. Eichenfield, J. Chan, R. M. Camacho, K. J. Vahala, and O. Painter, Nature **462**, 78 (2009).

[70] T. P. Purdy, D. W. C. Brooks, T. Botter, N. Brahms, Z.-Y. Ma, and D. M. Stamper-Kurn, Physical Review Letters **105** (2010), 10.1103/physrevlett.105.133602.

[71] Teufel, J. D. et. al., Nature **475**, 359 (2011).

[72] I. Wilson-Rae, N. Nooshi, W. Zwerger, and T. J. Kippenberg, Phys. Rev. Lett. **99**, 093901 (2007).

[73] D. J. Wilson, V. Sudhir, N. Piro, R. Schilling, A. Ghadimi, and T. J. Kippenberg, Nature **524**, 325 (2015).

[74] T. P. Purdy, R. W. Peterson, and C. A. Regal, Science **339**, 801 (2013).

[75] J. D. Teufel, F. Lecocq, and R. W. Simmonds, Phys. Rev. Lett. **116**, 013602 (2016).

[76] J.-M. Courty, A. Heidmann, and M. Pinard, Eur. Phys. J. D **17**, 399â€“408 (2001).

[77] A. Szorkovszky, A. C. Doherty, G. I. Harris, and W. P. Bowen, Phys. Rev. Lett. **107**, 213603 (2011).

[78] D. Van Thourhout and J. Roels, Nat. Phot. **4**, 211 (2010).

[79] S. P. Vyatchanin and E. A. Zubova, Phys. Lett. A **201**, 269 (1995).

[80] LIGO Scientific Collaboration, Nature Phys. **7**, 962 (2011).

[81] LIGO Scientific Collaboration, Nature Phot. **7**, 613 (2013).

[82] A. Heidmann, Y. Hadjar, and M. Pinard, Applied Physics B: Lasers and Optics **64**, 173 (1997).

[83] H. J. Kimble, Y. Levin, A. B. Matsko, K. S. Thorne, and S. P. Vyatchanin, Phys. Rev. D **65**, 022002 (2001).

[84] V. Braginsky, M. Gorodetsky, and V. Ilchenko, Physics Letters A **137**, 393 (1989).

[85] L. Collot, V. Lefèvre-Seguin, M. Brune, J. M. Raimond, and S. Haroche, Europhysics Letters (EPL) **23**, 327 (1993).

[86] D. W. Vernooy, V. S. Ilchenko, H. Mabuchi, E. W. Streed, and H. J. Kimble, Optics Letters **23**, 247 (1998).

[87] S. M. Spillane, T. J. Kippenberg, and K. J. Vahala, Nature **415**, 621 (2002).

[88] V. Sandoghdar, F. Treussart, J. Hare, V. Lefèvre-Seguin, J. M. Raimond, and S. Haroche, Physical Review A **54**, R1777 (1996).

[89] B. Min, T. J. Kippenberg, and K. J. Vahala, Optics Letters **28**, 1507 (2003).

[90] D. W. Vernooy, A. Furusawa, N. P. Georgiades, V. S. Ilchenko, and H. J. Kimble, Physical Review A **57**, R2293 (1998).

[91] A. M. Armani, R. P. Kulkarni, S. E. Fraser, R. C. Flagan, and K. J. Vahala, Science **317**, 783 (2007).

[92] F. Vollmer and S. Arnold, Nature Methods **5**, 591 (2008).

[93] F. Vollmer, S. Arnold, and D. Keng, Proceedings of the National Academy of Sciences **105**, 20701 (2008).

[94] D. K. Armani, T. J. Kippenberg, S. M. Spillane, and K. J. Vahala, Nature **421**, 925 (2003).

[95] J. W. S. L. Rayleigh), *Theory of Sound*, 1st ed., Vol. II (1878).

[96] L. Rayleigh, Philosophical Magazine Series 6 **20**, 1001 (1910).

[97] M. R. Foreman, J. D. Swaim, and F. Vollmer, Advances in Optics and Photonics **7**, 168 (2015).

[98] G. Mie, Annalen der Physik **330**, 377 (1908).

[99] A. Chiasera, Y. Dumeige, P. Féron, M. Ferrari, Y. Jestin, G. N. Conti, S. Pelli, S. Soria, and G. Righini, Laser & Photonics Reviews **4**, 457 (2010).

[100] M. L. Gorodetsky, A. A. Savchenkov, and V. S. Ilchenko, Optics Letters **21**, 453 (1996).

[101] M. L. Gorodetsky, A. D. Pryamikov, and V. S. Ilchenko, Journal of the Optical Society of America B **17**, 1051 (2000).

[102] P. K. Tien, Applied Optics **10**, 2395 (1971).

[103] H. Rokhsari, S. M. Spillane, and K. J. Vahala, Applied Physics Letters **85**, 3029 (2004).

[104] B. Min, L. Yang, and K. Vahala, Physical Review A **76** (2007), 10.1103/physreva.76.013823.

[105] H. A. Haus, *Waves and Fields in Optoelectronics* (Prentice-Hall, Inc., 1984).

[106] C. Gardiner and M. Collett, Phys. Rev. A **31**, 3761 (1985).

[107] M. Cai, O. Painter, and K. J. Vahala, Physical Review Letters **85**, 74 (2000).

[108] D. S. Weiss, V. Sandoghdar, J. Hare, V. Lefèvre-Seguin, J.-M. Raimond, and S. Haroche, Optics Letters **20**, 1835 (1995).

[109] T. J. Kippenberg, S. M. Spillane, and K. J. Vahala, Optics Letters **27**, 1669 (2002).

[110] A. N. Cleland and M. L. Roukes, Nature **392**, 160 (1998).

[111] H. Mamin and D. Rugar, App. Phys. Lett. **79**, 3358 (2001).

[112] K. Jensen, K. Kim, and A. Zettl, Nature Nano. **3**, 533 (2008).

[113] K. C. Schwab and M. L. Roukes, Physics Today **58**, 36 (2005).

[114] M. D. LaHaye, Science **304**, 74 (2004).

[115] N. Flowers-Jacobs, D. Schmidt, and K. Lehnert, Phys. Rev. Lett. **98**, 096804 (2007).

[116] A. N. Cleland, *Foundations of Nanomechanics* (Springer, 2003).

[117] K. Ekinci and M. Roukes, Rev. Sci. Instru. **76**, 061101 (2005).

[118] N. Wiener, Acta Mathematica **55**, 117 (1930).

[119] H. Nyquist, Physical Review **32**, 110 (1928).

[120] H. B. Callen and T. A. Welton, Physical Review **83**, 34 (1951).

[121] P. R. Saulson, Phys. Rev. D **42**, 2437 (1990).

[122] M. Imboden and P. Mohanty, Physics Reports **534**, 89 (2014).

[123] T. Caniard, P. Verlot, T. Briant, P.-F. Cohadon, and A. Heidmann, Physical Review Letters **99** (2007), 10.1103/physrevlett.99.110801.

[124] T. Faust, J. Rieger, M. J. Seitner, P. Krenn, J. P. Kotthaus, and E. M. Weig, Physical Review Letters **109** (2012), 10.1103/physrevlett.109.037205.

[125] H. G. Craighead, Science **290**, 1532 (2000).

[126] Y. T. Yang, K. L. Ekinci, X. M. H. Huang, L. M. Schiavone, M. L. Roukes, C. A. Zorman, and M. Mehregany, Applied Physics Letters **78**, 162 (2001).

[127] M. Li, H. X. Tang, and M. L. Roukes, Nature Nanotechnology **2**, 114 (2007).

[128] V. Sazonova, Y. Yaish, H. Üstünel, D. Roundy, T. A. Arias, and P. L. McEuen, Nature **431**, 284 (2004).

[129] S. S. Verbridge, J. M. Parpia, R. B. Reichenbach, L. M. Bellan, and H. G. Craighead, J. Appl. Phys. **99**, 124304 (2006).

[130] S. S. Verbridge, H. G. Craighead, and J. M. Parpia, Applied Physics Letters **92**, 013112 (2008).

[131] A. Schliesser, R. Rivière, G. Anetsberger, O. Arcizet, and T. J. Kippenberg, Nature Physics **4**, 415 (2008).

[132] T. J. Kippenberg and K. J. Vahala, Optics Express **15**, 17172 (2007).

[133] A. M. Jayich, J. C. Sankey, B. M. Zwickl, C. Yang, J. D. Thompson, S. M. Girvin, A. A. Clerk, F. Marquardt, and J. G. E. Harris, New Journal of Physics **10**, 095008 (2008).

[134] D. E. Chang, C. A. Regal, S. B. Papp, D. J. Wilson, J. Ye, O. Painter, H. J. Kimble, and P. Zoller, Proceedings of the National Academy of Sciences **107**, 1005 (2009).

[135] G. Anetsberger, O. Arcizet, Q. P. Unterreithmeier, R. RiviÃ¨re, A. Schliesser, E. M. Weig, J. P. Kotthaus, and T. J. Kippenberg, Nat. Phys. **5**, 909 (2009).

[136] A. Dorsel, J. D. McCullen, P. Meystre, E. Vignes, and H. Walther, Physical Review Letters **51**, 1550 (1983).

[137] A. Schliesser, P. Del'Haye, N. Nooshi, K. J. Vahala, and T. J. Kippenberg, Physical Review Letters **97** (2006), 10.1103/physrevlett.97.243905.

[138] C. K. Law, Physical Review A **51**, 2537 (1995).

[139] V. Giovannetti and D. Vitali, Physical Review A **63** (2001), 10.1103/physreva.63.023812.

[140] P. Zoller and C. Gardiner, *Quantum Noise* (Springer, 2004).

[141] F. Marquardt, J. P. Chen, A. A. Clerk, and S. M. Girvin, Physical Review Letters **99** (2007), 10.1103/physrevlett.99.093902.

[142] A. A. Clerk, M. H. Devoret, S. M. Girvin, F. Marquardt, and R. J. Schoelkopf, Reviews of Modern Physics **82**, 1155 (2010).

[143] F. Marquardt, J. G. E. Harris, and S. M. Girvin, Physical Review Letters **96** (2006), 10.1103/physrevlett.96.103901.

[144] T. J. Kippenberg, H. Rokhsari, T. Carmon, A. Scherer, and K. J. Vahala, Physical Review Letters **95** (2005), 10.1103/physrevlett.95.033901.

[145] R. W. P. Drever, J. L. Hall, F. V. Kowalski, J. Hough, G. M. Ford, A. J. Munley, and H. Ward, Applied Physics B Photophysics and Laser Chemistry **31**, 97 (1983).

[146] E. D. Black, American Journal of Physics **69**, 79 (2001).

[147] O. Arcizet, P.-F. Cohadon, T. Briant, M. Pinard, and A. Heidmann, Nature **444**, 71 (2006).

[148] D. W. C. Brooks, T. Botter, S. Schreppler, T. P. Purdy, N. Brahms, and D. M. Stamper-Kurn, Nature **488**, 476 (2012).

[149] W. Heitler, *The Quantum Theory of Radiation*, 3rd ed. (Clarendon Press, 1954).

[150] V. Sudhir, D. Wilson, R. Schilling, H. Schütz, S. Fedorov, A. Ghadimi, A. Nunnenkamp, and T. Kippenberg, Physical Review X **7**, 011001 (2017).

[151] U. Leonhardt, Reports on Progress in Physics **66**, 1207 (2003).

[152] M. Collett, R. Loudon, and C. Gardiner, Journal of Modern Optics **34**, 881 (1987).

[153] H. P. Yuen and V. W. S. Chan, Optics Letters **8**, 345 (1983).

[154] S. Spillane, T. Kippenberg, O. Painter, and K. Vahala, Phys. Rev. Lett. **91**, 043902 (2003).

[155] C. Doolin, P. Kim, B. Hauer, A. MacDonald, and J. Davis, New J. Phys. **16**, 035001 (2014).

[156] R. M. Cole, G. A. Brawley, V. P. Adiga, R. De Alba, J. M. Parpia, B. Ilic, H. G. Craighead, and W. P. Bowen, Phys. Rev. App. **3**, 024004 (2015).

[157] L. Neuhaus, E. van Brackel, E. Gavartin, P. Verlot, and T. Kippenberg, in *CLEO: Science and Innovations* (Optical Society of America, 2012) pp. CW3M–2.

[158] E. Gavartin, P. Verlot, and T. J. Kippenberg, Nat. Nano. **7**, 509 (2012).

[159] G. Anetsberger, E. Gavartin, O. Arcizet, Q. P. Unterreithmeier, E. M. Weig, M. L. Gorodetsky, J. P. Kotthaus, and T. J. Kippenberg, Phys. Rev. A **82** (2010).

[160] R. Schilling, H. Schütz, A. Ghadimi, V. Sudhir, D. Wilson, and T. Kippenberg, Phys. Rev. Applied **5**, 054019 (2016).

[161] J. Rieger, A. Isacsson, M. J. Seitner, J. P. Kotthaus, and E. M. Weig, Nature Communications **5** (2014), 10.1038/ncomms4345.

[162] G. I. González and P. R. Saulson, The Journal of the Acoustical Society of America **96**, 207 (1994).

[163] Q. P. Unterreithmeier, T. Faust, and J. P. Kotthaus, Phys. Rev. Lett. **105**, 027205 (2010).

[164] L. G. Villanueva and S. Schmid, Phys. Rev. Lett. **113**, 227201 (2014).

[165] J. D. Teufel, T. Donner, M. A. Castellanos-Beltran, J. W. Harlow, and K. W. Lehnert, Nat. Nano. **4**, 820 (2009).

[166] S. S. Verbridge, R. Ilic, H. Craighead, and J. M. Parpia, App. Phys. Lett. **93**, 013101 (2008).

[167] B. M. Zwickl, W. E. Shanks, A. M. Jayich, C. Yang, A. C. Bleszynski Jayich, J. D. Thompson, and J. G. E. Harris, Appl. Phys. Lett. **92**, 103125 (2008).

[168] T. Kippenberg, J. Kalkman, A. Polman, and K. Vahala, Phys. Rev. A **74** (2006).

[169] H. Lee, T. Chen, J. Li, K. Y. Yang, S. Jeon, O. Painter, and K. J. Vahala, Nat. Phot. **6**, 369 (2012).

[170] M. Oxborrow, in *Lasers and Applications in Science and Engineering* (International Society for Optics and Photonics, 2007) pp. 64520J–64520J.

[171] M. Borselli, T. Johnson, and O. Painter, Opt. Express **13**, 1515 (2005).

[172] M. L. Povinelli, M. Loncar, M. Ibanescu, E. J. Smythe, S. G. Johnson, F. Capasso, and J. D. Joannopoulos, Opt. Lett. **30**, 3042 (2005).

[173] G. Anetsberger, *Novel cavity optomechanical systems at the micro-and nanoscale and quantum measurements of nanomechanical oscillators*, Ph.D. thesis, lmu (2010).

[174] R. Riviere, O. Arcizet, A. Schliesser, and T. J. Kippenberg, Rev. Sci. Instrum. **84**, 043108 (2013).

[175] M. L. Gorodetsky, A. Schliesser, G. Anetsberger, S. Deleglise, and T. J. Kippenberg, Opt. Exp. **18**, 23236 (2010).

[176] W. Zhang, M. Martin, C. Benko, J. Hall, J. Ye, C. Hagemann, T. Legero, U. Sterr, F. Riehle, G. Cole, *et al.*, Opt. Lett. **39**, 1980 (2014).

[177] T. G. Thomas and S. C. Sekhar, *Communication Theory* (Tata-McGraw Hill, 2005).

[178] C. H. Metzger and K. Karrai, Nature **432**, 1002 (2004).

[179] S. Fedorov, V. Sudhir, R. Schilling, H. Schütz, D. Wilson, and T. Kippenberg, Physics Letters A (2017), 10.1016/j.physleta.2017.05.046.

[180] G. I. González and P. R. Saulson, Phys. Lett. A **201**, 12 (1995).

[181] A. Bernardini, E. Majorana, Y. Ogawa, P. Puppo, P. Rapagnani, F. Ricci, and G. Testi, Physics Letters A **255**, 142 (1999).

[182] A. R. Neben, T. P. Bodiya, C. Wipf, E. Oelker, T. Corbitt, and N. Mavalvala, New Journal of Physics **14**, 115008 (2012).

[183] M. L. Gorodetsky and I. S. Grudinin, Journal of the Optical Society of America B **21**, 697 (2004).

[184] N. Kondratiev and M. Gorodetsky, Physics Letters A (2017), 10.1016/j.physleta.2017.04.043.

[185] C. Fabre, M. Pinard, S. Bourzeix, A. Heidmann, E. Giacobino, and S. Reynaud, Phys. Rev. A **49**, 1337 (1994).

[186] S. Mancini and P. Tombesi, Phys. Rev. A **49**, 4055 (1994).

[187] O. Arcizet, R. Rivière, A. Schliesser, G. Anetsberger, and T. J. Kippenberg, Phys. Rev. A **80**, 021803 (2009).

[188] R. O. Pohl, X. Liu, and E. Thompson, Rev. Mod. Phys. **74**, 991 (2002).

[189] M. Metcalfe, Applied Physics Reviews **1**, 031105 (2014).

[190] C. M. Caves, M. Zimmermann, K. S. Thorne, and R. W. Drever, Rev. Mod. Phys. **52**, 341 (1980).

[191] M. Jaekel and S. Reynaud, Europhys. Lett. **13**, 301 (1990).

[192] A. Buonanno and Y. Chen, Phys. Rev. D **64**, 042006 (2001).

[193] Y. Chen, S. L. Danilishin, F. Y. Khalili, and H. Müller-Ebhardt, General Relativity and Gravitation **43**, 671 (2011).

[194] H. Vahlbruch, M. Mehmet, K. Danzmann, and R. Schnabel, Phys. Rev. Lett. **117**, 110801 (2016).

[195] W. H. P. Nielsen, Y. Tsaturyan, C. B. Møller, E. S. Polzik, and A. Schliesser, Proc. Natl. Acad. Sci. **114**, 62 (2017).

[196] F. Y. Khalili, H. Miao, H. Yang, A. H. Safavi-Naeini, O. Painter, and Y. Chen, Phys. Rev. A **86**, 033840 (2012).

[197] A. Weinstein, C. Lei, E. Wollman, J. Suh, A. Metelmann, A. Clerk, and K. Schwab, Phys. Rev. X **4**, 041003 (2014).

[198] T. P. Purdy, P.-L. Yu, N. S. Kampel, R. W. Peterson, K. Cicak, R. W. Simmonds, and C. A. Regal, Phys. Rev. A **92**, 031802 (2015).

[199] M. Underwood, D. Mason, D. Lee, H. Xu, L. Jiang, A. B. Shkarin, K. Børkje, S. M. Girvin, and J. G. E. Harris, Phys. Rev. A **92**, 061801 (2015).

[200] M. Evans *et al.*, Phys. Rev. Lett. **114**, 161102 (2015).

[201] P. Verlot, A. Tavernarakis, T. Briant, P.-F. Cohadon, and A. Heidmann, Phys. Rev. Lett. **104**, 133602 (2010).

[202] K. Borkje, A. Nunnenkamp, B. Zwickl, C. Yang, J. Harris, and S. Girvin, Phys. Rev. A **82**, 13818 (2010).

[203] V. B. Braginsky, M. L. Gorodetsky, F. Y. Khalili, and K. S. Thorne, Phys. Rev. D **61**, 044002 (2000).

[204] T. Corbitt, Y. Chen, F. Khalili, D. Ottaway, S. Vyatchanin, S. Whitcomb, and N. Mavalvala, Phys. Rev. A **73**, 023801 (2006).

[205] V. Sudhir, R. Schilling, S. A. Fedorov, H. Schütz, D. J. Wilson, and T. J. Kippenberg, Physical Review X **7**, 031055 (2017).

[206] L. Buchmann, S. Schreppler, J. Kohler, N. Spethmann, and D. Stamper-Kurn, Phys. Rev. Lett. **117**, 030801 (2016).

[207] J. B. Clark, F. Lecocq, R. W. Simmonds, J. Aumentado, and J. D. Teufel, Nature Physics **12**, 683 (2016).

[208] F. Marino, F. Cataliotti, A. Farsi, M. de Cumis, and F. Marin, Physical Review Letters **104**, 073601 (2010).

[209] P. Cohadon, A. Heidmann, and M. Pinard, Phys. Rev. Lett. **83**, 3174 (1999).

[210] V. Giovannetti, S. Lloyd, and L. Maccone, Science **306**, 1330 (2004).

[211] J. Suh, A. J. Weinstein, C. U. Lei, E. E. Wollman, S. K. Steinke, P. Meystre, A. A. Clerk, and K. C. Schwab, Science **344**, 1262 (2014).

[212] F. Lecocq, J. Clark, R. Simmonds, J. Aumentado, and J. Teufel, Physical Review X **5**, 041037 (2015).

[213] L. B. Mercer, J. Lightwave Tech. **9**, 485 (1991).

[214] V. B. Braginsky, M. L. Gorodetsky, and S. P. Vyatchanin, Phys. Lett. A **264**, 1 (1999).

[215] V. B. Braginsky, M. L. Gorodetsky, and S. P. Vyatchanin, Phys. Lett. A **271**, 303 (2000).

[216] G. E. Hudson, Phys. Rev. **63**, 46 (1943).

[217] J. Zemanek and I. Rudnick, The Journal of the Acoustical Society of America **33**, 1283 (1961).

[218] S. Harun, K. Lim, C. Tio, K. Dimyati, and H. Ahmad, Optik **124**, 538 (2013).

[219] R. M. Shelby, M. D. Levenson, and P. W. Bayer, Phys. Rev. B **31**, 5244 (1985).

[220] LIGO Scientific Collaboration, Physical Review A **95**, 043831 (2017).

[221] N. Kampel, R. Peterson, R. Fischer, P.-L. Yu, K. Cicak, R. Simmonds, K. Lehnert, and C. Regal, Phys. Rev. X **7**, 021008 (2017).

[222] Y. Tsaturyan, A. Barg, E. S. Polzik, and A. Schliesser, Nature Nanotechnology (2017), 10.1038/nnano.2017.101.

[223] A. Ghadimi, S. Fedorov, N. Engelsen, M. Bereyhi, R. Schilling, H. Schütz, D. J. Wilson, and T. J. Kippenberg, "Phononic crystal nanostrings with ultra-high quality factors," .

[224] M. Martin, B. Houston, J. Baldwin, and M. Zalalutdinov, Journal of Microelectromechanical Systems **17**, 503 (2008).

[225] A. Barg, Y. Tsaturyan, E. Belhage, W. H. P. Nielsen, C. B. Møller, and A. Schliesser, Applied Physics B **123** (2016), 10.1007/s00340-016-6585-7.

[226] A. Kaushik, H. Kahn, and A. Heuer, Journal of Microelectromechanical Systems **14**, 359 (2005).

[227] K. Mackenzie, D. Johnson, M. DeVre, R. Westerman, and B. Reelfs, in *Proceedings of the 207th Electrochemical Society Meeting* (2005) pp. 148–159.

[228] Y. Shioya, H. Takagi, R. Maeda, and Y. Kokubun, Japanese Journal of Applied Physics **47**, 7081 (2008).

[229] B. Varadarajan, *Tensile Dielectric Films Using UV Curing*, Patent US 9659769 (2017).

[230] U. Hahn and K. Zapfe, "Guidelines for UHV-Components at DESY," Technical Specification (2010).

[231] M. Taborelli, "Cleaning and surface prperties," CERN (2006).

[232] B. Bland, D. Coyne, and J. Fauver, "LIGO Vacuum Compatibility, Cleaning Methods and Qualification Procedures," LIGO Systems Engineering (2012).

[233] R. Calder and G. Lewin, British Journal of Applied Physics **18**, 1459 (1967).

[234] K. Jousten, ed., *Wutz Handbuch Vakuumtechnik*, 11th ed. (Springer Vieweg, 2013).

[235] S. S. Verbridge, D. F. Shapiro, H. G. Craighead, and J. M. Parpia, Nano Letters **7**, 1728 (2007).

[236] W. A. Phillips, Reports on Progress in Physics **50**, 1657 (1987).

[237] T. Ramos, V. Sudhir, K. Stannigel, P. Zoller, and T. J. Kippenberg, Physical Review Letters **110** (2013), 10.1103/physrevlett.110.193602.

[238] J. Jäckle, Zeitschrift für Physik A Hadrons and nuclei **257**, 212 (1972).

[239] R. Vacher, E. Courtens, and M. Foret, Physical Review B **72** (2005), 10.1103/physrevb.72.214205.

[240] R. O. Behunin, P. Kharel, W. H. Renninger, and P. T. Rakich, Nature Materials **16**, 315 (2016).

[241] H. M. Carruzzo, E. R. Grannan, and C. C. Yu, Physical Review B **50**, 6685 (1994).

Hendrik Schütz

Curriculum Vitae

PERSONAL DETAILS

Birth	August 12, 1985
Address	Rue du Temple, 1304 Cossonay-Ville, Switzerland
Phone	+41 (0)76 466 27 70
Mail	`hschuetz@gmail.com`

EDUCATION

Doctoral studies 2012-2017

École Polytechnique Fédérale de Lausanne, Switzerland

PhD thesis at the Laboratory of Photonics and Quantum Measurements (LPQM) in the group of Prof. Tobias Kippenberg, entitled ”Quantum optomechanics at room temperature”.

Physics studies 2006-2011

University of Hamburg, Germany

Diploma thesis in the group of Prof. Klaus Sengstock, Institute of Laser Physics, entitled ”Conception of a laser system for simultaneous cooling of ^{39}K and ^{40}K and implementation of a 2D-3D-MOT combination for ^{87}Rb”.

Abitur 1996-2005

Johannes-Brahms-Schule, Pinneberg, Germany

TEACHING AND WORK EXPERIENCE

Teaching assistant 2012-2016

École Polytechnique Fédérale de Lausanne, Switzerland

Tutor for different courses.

Research assistant 2011-2012

Institute of Laser Physics, University of Hamburg, Germany

Continuation of the project starting within the frame of the diploma thesis.

Alternative service 2005-2006

Albertinen Hospital, Hamburg, Germany

Assistant work in the diagnostics department, mainly ECG recording and development of X-ray images.

SKILLS

Languages	German (mother tongue) English (fluent) French (conversational)
Software	Matlab, Mathematica, LaTeX, LabView, Solidworks